Statics and dynamics of critical Casimir forces

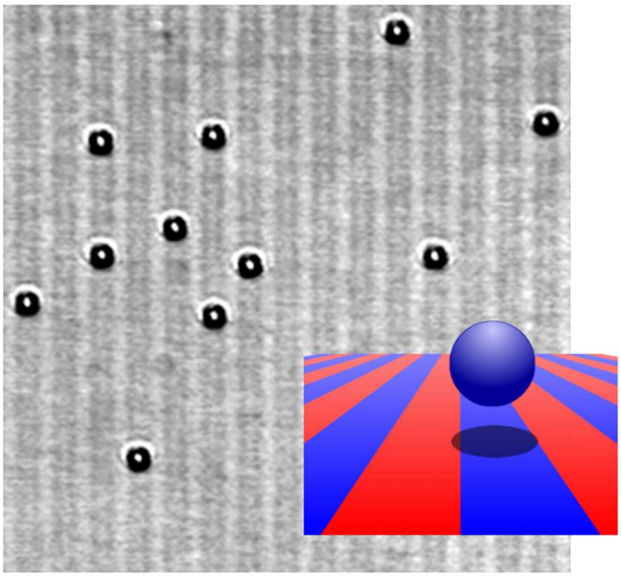

Von der Fakultät Mathematik und Physik der Universität Stuttgart zur
Erlangung der Würde eines Doktors der Naturwissenschaften (Dr. rer. nat.)
genehmigte Abhandlung

vorgelegt von

Matthias Tröndle

aus Lörrach

Hauptberichter: Prof. Dr. Siegfried Dietrich
Mitberichter: Prof. Dr. Clemens Bechinger

Tag der Einreichung: 22.12.2011
Tag der Prüfung: 21.02.2012

Max-Planck-Institut für Intelligente Systeme, Stuttgart &
Institut für Theoretische und Angewandte Physik, Universität Stuttgart

2012

◄ **Title image:** Top view on colloids immersed in a critical water-lutidine mixture in the presence of a flat substrate structured with chemical stripes of alternating adsorption preferences. The colloidal particles are attracted via critical Casimir forces by those stripes which exhibit the same adsorption preference as the colloids via critical Casimir forces. (Experimental snapshot by D. Vogt.)

Zusammenfassung

Statik und Dynamik kritischer Casimir-Kräfte

DIESE Arbeit behandelt *kritische Casimir-Kräfte*, welche in Flüssigkeiten nahe des kritischen Punktes auftreten und auf in der Flüssigkeit gelöste Kolloide — Teilchen der Größe von Nanometern bis wenige Mikrometer — wirken. Solche kolloidalen Suspensionen spielen eine bedeutende Rolle in der Natur sowie in Anwendungen und stellen ein wichtiges Modellsystem dar. Sie werden durch die Statistische Physik beschrieben und können in Experimenten mittels der optischen Mikroskopie direkt beobachtet werden. Wechselwirkungen in kolloidalen Systemen können darüberhinaus zur Nachahmung autonomer Systeme wie Bakterien oder für das Verständnis atomarer Mechanismen eingesetzt werden.

Der kritische Casimir-Effekt entsteht durch die räumliche Einschränkung von Fluktuationen in der Flüssigkeit. Thermische Fluktuationen breiten sich über einen Bereich aus, der durch die charakteristische Längenskala in einem Lösungsmittel, der Korrelationslänge ξ, gegeben ist, und üblicherweise im molekularen Bereich liegt. Nahe des kritischen Punktes des Lösungsmittels wächst ξ jedoch stark an, sodass selbst sichtbares Licht von der Flüssigkeit gestreut wird (*kritische Opaleszenz*). Die Divergenz der Korrelationslänge nahe der kritischen Temperatur $T = T_c$ folgt einem universellen Potenzgesetz $\xi \propto |T - T_c|^{-\nu}$, wobei ν ein *kritischer Exponent* ist. Molekulare Details spielen für die Beschreibung eines kritischen Systems eine untergeordnete Rolle und die theoretische Beschreibung der kritischen Phänomene ist für eine Vielzahl physikalischer Systeme dieselbe. Werden die kritischen Fluktuationen des Lösungsmittels von den Kolloidteilchen sowie den Wänden des Systems eingeschränkt, entstehen effektive Kräften auf die Kolloidteilchen — die kritischen Casimir-Kräfte, deren Stärke stark von der Abweichung von der kritischen Temperatur abhängt.

Während der kritische Punkt von einfachen Flüssigkeiten oft bei hohen Temperaturen und Drücken liegt, ist der kritische Punkt vieler binärer Flüssigkeitsmischungen bei Atmosphärendruck und in der Nähe der Raumtemperatur erreichbar. Die kritischen Casimir-Kräfte, die auf die in binären Flüssigkeitsmischungen gelösten Kolloidteilchen wirken, sind somit experimentell relevant und können direkt gemessen werden.[1]

Je nach chemischen Randbedingungen auf den Oberflächen sind die kritischen Casimir-Kräfte zwischen einem einzelnen Kolloidteilchen und einem planaren Substrat anziehend oder abstoßend. In dieser Arbeit wird untersucht, wie sich eine *Kombination* verschiedener Randbedingungen mittels chemisch strukturierter Substrate auf den kritischen Casimir-Effekt auswirkt. Durch die chemische Strukturierung entstehen auch *laterale* Kräfte auf die Kolloidteilchen, so dass die Kolloide nahe eines bestimmten chemischen Streifens gefangen werden können. Für bestimmte chemische Muster werden die *normalen* kritischen Casimir-Kräfte auf die Teilchen gar derart verändert, dass die Kolloide schweben können.

---

[1] C. Hertlein, L. Helden, A. Gambassi, S. Dietrich, and C. Bechinger, Nature **451**, 172 (2008).

Der Vergleich der hier berechneten theoretischen Vorhersagen für diese Kräfte mit den vorhandenen experimentellen Daten liefert eine sehr gute Übereinstimmung. Kritische Casimir-Kräfte bieten somit eine Möglichkeit, Wechselwirkungen auf Kolloidteilchen gezielt in Stärke und Wirkrichtung mittels der Temperatur des Lösungsmittels und der chemischen Randbedingungen zu beeinflussen.

Während der Großteil der bisherigen Untersuchungen Systeme im thermodynamischen Gleichgewicht betrachtet, gibt es kaum Betrachtungen der kritischen *Dynamik* eingeschränkter Systeme. Durch die Ausweitung der thermischen Fluktuationen am kritischen Punkt wird auch ein starker Anstieg der Relaxationszeiten im Lösungsmittel bewirkt. Die kritische Dynamik kann somit ebenfalls universell beschrieben werden. Diese Arbeit untersucht den Einfluss der gekrümmten Oberflächen von Kolloidteilchen auf die kritische Dynamik des Lösungsmittels in ihrer Umgebung. Es zeigt sich, dass je nach Krümmung und Art der Randbedingung die Dynamik unterschiedliche Charakteristika aufweist.

Im Folgenden werden die einzelnen Kapitel der Arbeit zusammengefasst.

Kapitel 1: Einleitung

Kapitel 1 bietet einen kurzen Überblick der Literatur zu kritischen Phänomenen und zum kritischen Casimir-Effekt. Ein kritischer Punkt tritt im Phasenverhalten einer Vielzahl physikalischer Systeme auf, wie beispielsweise in einfachen Flüssigkeiten [Abbildung 1.1], Ferromagneten [Abb. 1.2] oder binären Flüssigkeitsmischungen [Abb. 1.3]. Diese unterschiedlichen Systeme können einheitlich mittels des Ordnungsparameters ϕ und dimensionslosen Größen wie der reduzierten Temperatur $\tau = \pm|T - T_c|/T_c$ beschrieben werden. Positive Werte $\tau > 0$ entsprechen der homogenen Phase des Systems (verschwindender Ordnungsparameter), während $\tau < 0$ der geordneten Phase des Systems entspricht ($\phi \neq 0$). Die universelle Beschreibung kritischer Phänomene hängt von nur zwei makroskopischen Größen ab, der Dimension des Ordnungsparameters und der Raumdimension d. Für die oben genannten Systeme ist ϕ skalar, weswegen diese allesamt zur *Ising-Universalitätsklasse* gehören.

Da eine Probe eines Materials stets eine endliche Ausdehnung hat, üben Grenzflächen Randbedingungen auf das System aus. In **Abschnitt 1.2.2** wird der Einfluss der Oberflächeneffekte auf kritische Systeme beschrieben. Beispielsweise führt die Adsorptionspräferenz eines Substrats für *eine* der Komponenten einer binären Mischung zu einer Verstärkung der Ordnung im Vergleich zum Volumen, welche sich aufgrund der wachsenden Korrelationslänge nahe des kritischen Punkts weit ausbreitet. Dies entspricht der *normalen* Oberflächen-Universalitätsklasse, welche sich von der *gewöhnlichen* (niedrigere Oberflächenordnung) und der *speziellen* (gleich bleibende Oberflächenordnung) unterscheidet. Wird — wie in kolloidalen Suspensionen — das Material durch mehrere Oberflächen eingegrenzt, führt dies zusätzlich zu den Oberflächeneffekten zu einer Einschränkung der thermischen Fluktuationen des Ordnungsparameters. Sobald die Korrelationslänge nahe des kritischen Punktes dieselbe Größenordnung wie der Abstand zweier begrenzender Objekte annimmt, werden auf diese effektive Kräfte ausgeübt. Dieser **kritische Casimir-Effekt** ist eng verwandt mit dem quantenelektrodynamischen Casimir-Effekt, bei dem Kräfte "aus dem Nichts" durch die Einschränkung von Vakuumfluktuationen entstehen.

In **Abschnitt 1.2.3** wird das **Skalenverhalten** von Systemen endlicher Größe eingeführt. Insbesondere hängt die kritische Casimir-Kraft zwischen zwei planaren Wänden im Abstand L von der Skalenvariablen L/ξ ab und kann mittels einer universellen Skalenfunktion beschrieben werden. **Abschnitt 1.2.4** führt die **Molekularfeldtheorie** (MFT) ein, welche das kritische Verhalten eines Materials oberhalb der Dimension $d = 4$ korrekt beschreibt. Um die universellen MFT-Skalenfunktionen zu erhalten, kann der *Landau-Ginzburg-Wilson-Hamiltonian* [Gl. (1.6)] minimiert werden, indem man das räumliche Ordnungsparameterprofil $\phi(\mathbf{r})$ variiert [Anhang A.1]. Anhand des minimierenden Profils $m(\mathbf{r}) = \langle\phi(\mathbf{r})\rangle$ kann mittels des Spannungstensors [Anhang A.2] die kritische Casimir-Kraft bestimmt werden. Für Systeme mit komplexen Geometrien, wie sie in dieser Arbeit betrachtet werden, kann so die universelle Skalenfunktion für die kritische Casimir-Kraft innerhalb der MFT vollständig numerisch berechnet werden.

Nicht nur die statischen Eigenschaften kritischer Systeme sind durch die Langreichweitigkeit der Fluktuationen geprägt, sondern auch deren Zeitentwicklung. **Abschnitt 1.2.5** führt in **dynamische kritische Phänomene** ein. Diese sind durch eine *kritische Verlangsamung* gekennzeichnet, die sich in der Divergenz der Relaxationszeit $t_R \propto |\tau|^{-\nu z}$ widerspiegelt, wobei z der dynamische Exponent ist. Dynamische Universalitätsklassen hängen von der Unterscheidung ab, ob der Ordnungsparameter eine zeitlich erhaltene Größe ist oder nicht, und ob und wie er an andere physikalische Größen koppelt. Der einfachste Fall, bei dem ϕ nicht erhalten ist und ebenfalls nicht an andere Größen koppelt, wird als *Modell A* bezeichnet und beschreibt die reine Relaxation des Ordnungsparameters in den Gleichgewichtszustand, die durch eine Langevin-Gleichung beschrieben werden kann [Gl. 1.9].

Kapitel 2: Kritische Casimir-Kräfte zwischen Kolloiden und chemisch strukturierten Substraten

In Kapitel 2 werden *normale* und *laterale* kritische Casimir-Kräfte untersucht, die auf kolloidale Teilchen in der Nähe eines chemisch strukturierten Substrats wirken [Abb. 2.1]. Ein chemische Strukturierung erzeugt eine inhomogene Adsorptionspräferenz des Substrats für die Komponenten einer kritischen Flüssigkeitsmischung, in welcher die Kolloidteilchen gelöst sind.[2,3] Neben

---

[2] M. Tröndle, S. Kondrat, A. Gambassi, L. Harnau, and S. Dietrich, EPL **88**, 40004 (2009).

[3] M. Tröndle, S. Kondrat, A. Gambassi, L. Harnau, and S. Dietrich, J. Chem. Phys. **133**, 074702 (2010).

der MFT wird die *Derjaguin-Näherung* [Abb. B.6 im Anhang] angewandt, um die Skalenfunktionen der Kräfte und des kritischen Casimir-Potentials zu erhalten, die auf ein Teilchen gegenüber eines strukturierten Substrats wirken. Mittels der Derjaguin-Näherung können diese anhand der Skalenfunktionen der kritischen Casimir-Kräfte zwischen zwei *homogenen Platten* berechnet werden, die beispielsweise aufgrund von Monte-Carlo-Simulationen in der Raumdimension $d = 3$ vorliegen. Der gültige Anwendungsbereich der Derjaguin-Näherung kann durch entsprechende Vergleiche mit den numerisch berechneten MFT-Funktionen bestimmt werden.

Zunächst wird in **Abschnitt 2.2** ein kugelförmiges Kolloid gegenüber einem chemisch **homogenen Substrats** betrachtet, welches im Vergleich zum Kolloid dieselbe ("$(-)$ Randbedingung") oder eine andere ("$(+)$ Randbedingung") Adsorptionspräferenz aufweist. Die kritische Casimir-Kraft wird durch Skalenfunktionen beschrieben, die vom Oberflächenabstand D zwischen Kolloid und Substrat in Einheiten der Korrelationslänge, $\Theta = \pm D/\xi_\pm$ (wobei ± dem Vorzeichen von τ entspricht), sowie in Einheiten des Kolloidradius, $\Delta = D/R$, abhängen [Gl. (2.1) und (2.2)]. Der Vergleich der Derjaguin-Näherung mit den Ergebnissen der MFT zeigt, dass erstere für Werte $\Delta \lesssim 0.4$ das tatsächliche Verhalten gut beschreibt [Abb. 2.2].

In **Abschnitt 2.3** wird eine **chemische Stufe** betrachtet, die den grundlegenden Baustein strukturierter Substrate darstellt. Aufgrund der verschiedenen Randbedingungen auf beiden Seiten der chemischen Stufe wirkt eine laterale kritische Casimir-Kraft auf das Kolloid [Abb. 2.3], welche von der Skalenvariablen $\Xi = X/\sqrt{RD}$ abhängig ist, die dem lateralen Abstand X des Kugelmittelpunktes von der chemischen Stufe entspricht [Gl. (2.8), (2.10), (2.17)]. Die kritischen Casimir-Kräfte auf ein Kolloid können mittels der Derjaguin-Näherung in $d = 3$ und $d = 4$ bestimmt werden, wobei sich herausstellt, dass diese für kleine Werte von D/R gut mit den numerischen Ergebnissen der MFT übereinstimmt [Abb. 2.3 und 2.4].

In **Abschnitt 2.4** werden die kritischen Casimir-Kräfte betrachtet, die auf ein Kolloid gegenüber eines **chemischen Streifens** wirken. Innerhalb der Derjaguin-Näherung können das kritische Casimir-Potential und die -Kräfte durch die entsprechenden Skalenfunktion einer chemischen *Stufe* ausgedrückt werden [Gl. (2.25) und (2.26)]. Es zeigt sich, dass die endliche Breite $2L$ des Streifens erst für $L \lesssim 3\sqrt{RD}$ bemerkbar wird [Abb. 2.5]. Der Vergleich der Derjaguin-Näherung mit den numerischen MFT-Ergebnissen ergibt, dass selbst für kleine Werte von $L/\sqrt{RD}$ die Derjaguin-Näherung für $\Delta \lesssim 0.4$ das tatsächliche Verhalten gut beschreibt [Abb. 2.6]. Dies gilt nicht mehr allgemein für den Fall eines **periodisch gemusterten Substrats**, welches in **Abschnitt 2.5** behandelt wird. Es stellt sich heraus, dass die Derjaguin-Näherung einerseits die kritische Casimir-Kraft für Werte $\Pi \gtrsim 2$ gut beschreibt, wobei $\Pi = P/\sqrt{RD}$ die der Periode P zugehörige Skalenvariable ist [Gl. 2.31; Abb. 2.7, 2.8(a), 2.10(a)]. Andererseits stimmen für $\Pi \to 0$ [Gl. 2.33] die numerisch berechneten MFT-Funktionen nicht mehr mit der Derjaguin-Näherung überein [Abb. 2.7, 2.8(a), 2.10(b)]. Dies kann darauf zurückgeführt werden, dass für diese Bereiche die Annahme der Additivität der Kräfte, auf welcher die Derjaguin-Näherung basiert, nicht gilt, und nicht-lineare sowie Kanten-Effekte nicht mehr zu vernachlässigen sind [Abb. 2.9]. In den in Kapitel 3 betrachteten Experimenten wurden allerdings solche Streifenbreiten verwendet, für welche die berechnete Derjaguin-Näherung als gültig angenommen werden kann [Abb. 2.11].

Wie in **Abschnitt 2.6** beschrieben wird, ergibt sich für bestimmte geometrische Parameter des Streifen-Musters ein **kritisches Casimir-Schweben** des Kolloids. Aufgrund der Kombination von repulsiven und attraktiven Kräften wird das Kolloidteilchen für Abstände $D < D_0 = D_{0,s}$ vom Substrat abgestoßen, während es für $D > D_0 = D_{0,s}$ von ihm angezogen wird [Abb. 2.12]. Dadurch schwebt das Kolloid stabil im Abstand $D_{0,s}$, welcher mittels des Temperaturabstandes zum kritischen Punkt verändert werden kann. Es stellt sich heraus, dass genau *am* kritischen Punkt ($T = T_c$) solch ein Schweben nicht möglich ist, während für $T \neq T_c$ stets ein geometrisches Streifenmuster gefunden werden kann, das Schweben ermöglicht [Abb. 2.13]. Für eine einmal gewählte Geometrie erscheinen mit Annäherung an die kritische Temperatur ein lokales Maximum und ein lokales Minimum im kritischen Casimir-Potential als Funktion des Kolloidabstandes D [Abb. 2.14]. Die Potential-Tiefe dieses lokalen Minimums kann typischerweise bis zu einigen k_BT betragen, sodass das Schweben stabil gegen die Brownsche Bewegung des Kolloids ist und auch in der Anwesenheit zusätzlicher elektrostatischer Kräfte präsent bleibt [Abb. 2.15].

Das oben beschriebene Verhalten für kugelförmige Kolloide zeigt sich ebenso für **zylindrische Kolloide**, deren Achsen parallel zum Substrat und den Streifen liegen [**Abschnitt 2.7**]. Die wesentlichen Eigenschaften der Skalenfunktionen für die kritischen Casimir-Kräfte und -Potentiale stimmen qualitativ mit denen für ein kugelförmiges Kolloid überein, insbesondere hinsichtlich der Aussagen über die Gültigkeit der Derjaguin-Näherung [Abb. 2.16]. Für ein zylindrisches Teilchen ergibt sich ebenfalls ein kritisches Casimir-Schweben über einem strukturierten Substrat innerhalb eines großen Bereiches geometrischer Parameter [Abb. 2.17].

Kapitel 3: Vergleich mit Experimenten

In Kapitel 3 werden die gewonnenen theoretischen Vorhersagen mit Experimenten verglichen.[2,4] Dabei wird auf Messungen des kritischen Casimir-Potentials von einzelnen Kolloiden in einer kritischen Flüssigkeitsmischung aus Wasser und 2,6-Lutidin nahe eines mit chemischen Streifen strukturierten Substrats zurückgegriffen. Es zeigt sich, dass die experimentellen Beobachtungen und Daten konsistent im Rahmen des kritischen Casimir-Effektes qualitativ und quantitativ interpretiert werden können.

Experimentell lassen sich Muster chemischer Streifen unterschiedlicher Breite und wechselnder Adsorptionspräferenz für Lutidin $(+)$ oder Wasser $(-)$ durch Mikro-Kontakt-Drucken[4] oder mittels eines fokussierten Ionenstrahls[5] herstellen. Durch ihre Oberflächenladung sind die experimentell genutzten Kolloidteilchen (Polystyrol-Kugeln vom Durchmesser $2.4\,\mu$m) hydrophil (entsprechend $(-)$ Randbedingungen). In **Abschnitt 3.2** werden die effektiven Wechselwirkungspotentiale für die Kolloidteilchen unter den experimentellen Bedingungen berechnet. Dazu wurde die Derjaguin-Näherung angewandt, welche — basierend auf Kapitel 2 — für den betrachteten Bereich gültig ist. Somit kann das Potential in voller räumlicher Auflösung theoretisch analysiert werden [Abb. 3.1]. Da die Massendichte der verwendeten Kolloidteilchen kaum größer als die der Flüssigkeit ist, fluktuiert ihr Abstand vom Substrat und ihre laterale Position generell stark [Abb. 3.2]. Nahe T_c führen die kritischen Casimir-Kräfte jedoch zu einer Lokalisierung der Kolloidteilchen nahe der Substratoberfläche und gegenüber Streifen der gleichen Adsorptionspräferenz [Abb. 3.3].

---

[4] M. Tröndle, O. Zvyagolskaya, A. Gambassi, D. Vogt, L. Harnau, C. Bechinger, and S. Dietrich, Molecular Physics **109**, 1169 (2011).

[5] F. Soyka, O. Zvyagolskaya, C. Hertlein, L. Helden, and C. Bechinger, Phys. Rev. Lett. **101**, 208301 (2008).

In **Abschnitt 3.3** werden die theoretischen Vorhersagen mit den gemessenen Daten aus den Experimenten von *Soyka et al.*[5] und *Vogt et al.*[4] verglichen. Experimentell wird das effektiv eindimensionale, auf die laterale Achse projizierte Potential eines einzelnen Kolloids gemessen. Für dessen theoretische Berechnung wird zusätzlich berücksichtigt, dass die chemischen Stufen des Musters in der Realität eine Abweichung von einer idealen Linie aufweisen können. Während der Wert der Potential-*Tiefen* davon nicht beeinflusst ist [Abb. 3.4], erhöht die Berücksichtigung eines "nicht-idealen" Musters jedoch die Übereinstimmung der theoretischen Vorhersagen für das *gesamte* Potential mit den experimentellen Messungen von *Soyka et al.* [Abb. 3.5] signifikant. Im Hinblick darauf lässt sich festhalten, dass kritische Casimir-Kräfte sehr stark von den geometrischen Details der chemischen Struktur abhängen und damit eine Möglichkeit zu deren nachträglicher "Überprüfung" bieten.

Der Vergleich der Theorie mit den Experimenten von *Vogt et al.* liefert eine sehr gute Übereinstimmung sowohl für die Potential-Tiefen bei unterschiedlich breiten Streifenmustern [Abb. 3.6], als auch für den Wert der nicht-universellen Amplitude ξ_0 im Vergleich zur Literatur [Tab. 3.1]. Darüberhinaus zeigen die vollständigen Potentiale als Funktion der lateralen Koordinate des Kolloids eine sehr gute Übereinstimmung der Theorie mit dem Experiment für alle vermessenen Streifenbreiten [Abb. 3.7 und 3.8]. Der durchgeführte Vergleich zeigt somit die quantitative Übereinstimmung der theoretischen Vorhersagen der kritischen Casimir-Kräfte auf kolloidale Teilchen mit den experimentellen Daten. Dies bestätigt die Signifikanz des kritischen Casimir-Effekts für kolloidale Suspensionen und weist auf neue Möglichkeiten der Nutzung von Kolloiden als Modellsysteme oder in Anwendungen in Mikro- oder Nano-Elektromechanischen Systemen hin.

Kapitel 4: Kritische Dynamik an kolloidalen Teilchen

Kapitel 4 behandelt *dynamische* Phänomene in einer Flüssigkeit am kritischen Punkt $T = T_c$. Die betrachtete Dynamik entspricht der reinen Relaxation des Ordnungsparameters (Modell A) und ist innerhalb der Molekularfeldtheorie durch die Langevin-Gleichung (4.1) bestimmt. Die dynamischen Universalitätsklassen teilen sich in endlich ausgedehnten System wiederum je nach Randbedingung weiter auf. In Kapitel 4 wird insbesondere die kritische Dynamik in der nähe einer gekrümmten Oberfläche betrachtet, wie sie bei kolloidalen Teilchen natürlicherweise vorkommt.

Zunächst werden jedoch in **Abschnitt 4.2.1** und **Abschnitt 4.2.2** bekannte Untersuchungen zur kritischen Dynamik in **halbunendlichen Systemen** und der **Film-Geometrie** mit planaren Oberflächen vorgestellt.[6,7] In der Umgebung der Oberfläche wird das Verhalten im Vergleich zum Volumen derart modifiziert, dass die Relaxation des gemittelten Ordnungsparameters m durch einen neuen charakteristischen Exponenten als Funktion der Zeit, $m \propto t^{-\beta_1/z\nu}$, gegeben ist. Dieses Verhalten propagiert im Laufe der Zeit in das Volumen. Für die gewöhnliche Oberflächenklasse (entsprechend Dirichlet-Randbedingungen) für den Ordnungsparameter an der Oberfläche ist damit die Relaxation beschleunigt im Vergleich zum Volumen. Die räumlich-zeitliche Entwicklung des Ordnungsparameters kann mit der Methode der finiten Elemente [Anhang A.3] berechnet werden [Abb. 4.1 und 4.2]. In der Film-Geometrie entwickelt sich durch die räumliche Einschränkung ein charakteristisches Verhalten für späte Zeiten: der Ordnungsparameter relaxiert selbst für $T = T_c$ *exponentiell* [Abb. 4.3 und 4.4]. Innerhalb dieses Bereich nimmt das Ordnungsparameterprofil entlang des Films eine sinusoidale Form an [Abb. 4.5].

In **Abschnitt 4.2.3** wird die **kritische Dynamik an gekrümmten Oberflächen** betrachtet. Dabei werden unterschiedliche gekrümmte Objekte mit Krümmungsradius R mittels einer "Krümmungs-Dimension" d_s unterschieden, wobei $d_s - 1$ die Anzahl der gekrümmten Richtungen der Oberfläche ist. Dabei entspricht $d_s = 1$ einer planaren Wand, $d_s = 2$ einem Zylinder, $d_s = 3$ einer Kugel und $d_s = 4$ einer Hyperkugel [Gl. 4.6]. Nahe des kritischen Punktes nimmt der Ordnungsparameter eine dynamische Skalenform an [Gl. 4.7], die bei $T = T_c$ von den Skalenvariablen $u = (r_\perp/\xi_0^+)(t/t_{R,0}^+)^{-1/z}$ und $v = r_\perp/R$ abhängt,wobei $r_\perp$ der Abstand zur gekrümmten Oberfläche ist und ξ_0^+ sowie $t_{R,0}^+$ die nicht-universellen Amplituden der Korrelationslänge und der Relaxationszeit sind. Für frühe Zeiten der Relaxation hängt der Ordnungsparameter zusätzlich von seinem Anfangsprofil ab [Gl. (4.7)]. In **Abschnitt 4.2.4** wird eine Entwicklung des dynamischen Ordnungsparameterprofils um gekrümmte Oberflächen für kleine Werte von u durchgeführt, was kurzen Abständen oder späten Zeiten entspricht. Der Einfluss der Krümmung wird durch unterschiedliche Skalenfunktionen $g(v)$ beschrieben, die von der Randbedingung und der Krümmungs-Dimension der Oberfläche abhängen [Abb. 4.6 und 4.7]. Während für Randbedingungen, welche die Symmetrie bewahren (gewöhnliche und spezielle Oberflächenklasse), $g(v \to \infty)$ für $d_s > 2$ verschwindet, geschieht dies für die Symmetrie-brechende normale Oberflächenklasse erst für $d_s > 3$.

Abschnitt 4.2.5 betrachtet die Relaxation des Ordnungsparameterprofils nahe gekrümmter Oberflächen mit der Randbedingung der **gewöhnlichen Universalitätsklasse**. Dabei werden zunächst Ergebnisse der Finite-Elemente-Methode für den Fall $d_s = 2$ betrachtet. Für kleine Abstände $r_\perp$ von der Zylinderoberfläche steigt das Ordnungsparameterprofil zunächst linear an

---

[6] H. Riecke, *Nichtlineare Relaxation in halbunendlichen Systemen*, Diplomarbeit, Ludwigs-Maximilian-Universität München (1982).

[7] A. Gambassi and S. Dietrich, J. Stat. Phys. **123**, 929 (2006).

[Abb. 4.8 und 4.9], was mit der Entwicklung für kleine Werte von u aus Abschnitt 4.2.4 übereinstimmt. Es stellt sich heraus, dass die im Rahmen dieser Arbeit verwendete Finite-Elemente-Methode numerisch jedoch nur für die frühe Entwicklung des Ordnungsparameters genutzt werden kann, so dass die vorhergesagte Skalenfunktion $g(v)$ asymptotisch noch nicht erreicht wird [Abb. 4.10]. Um auch späte Zeiten und alle Krümmungs-Dimensionen d_s zu untersuchen, werden im weiteren Verlauf von Abschnitt 4.2.5 effektiv eindimensionale Berechnungen verwendet. Diese bestätigen das vorhergesagte asymptotische Verhalten des Ordnungsparameterprofils für $d_s = 2,3,4$ und späte Zeiten t [Abb. 4.11 und 4.12]. Für $T = T_c$ relaxiert der Ordnungsparameter im betrachteten Bereich für die unterschiedlichen Krümmungs-Dimensionen d_s nach einem jeweils charakteristischen Potenzgesetz $m \propto t^{-(2-y(d_s))/2}$ wobei $0 \leq y(d_s) \leq 1$ [Fig. 4.13]. Während $y(1) = 0$ einer planaren Wand entspricht, werden numerisch die Werte $y(2) = 0.66(5)$ für einen Zylinder, $y(3) = 0.93(5)$ für eine Kugel und $y(4) = 0.99(5)$ für eine Hyperkugel gefunden [Abb. 4.14 und 4.15]. Dies zeigt, dass die Krümmung der Oberfläche nicht nur im statischen Sinn einen Einfluss in Form des Auftretens der Skalenfunktion $g(v)$ hat, sondern dass sich auch die charakteristische Dynamik im Vergleich zu einer planaren Oberfläche ändert.

Die in einem eingeschränkten System auftretenden kritischen Casimir-Kräfte können ebenfalls zeitabhängig sein. In **Abschnitt 4.3** wird ein kurzer Überblick über den aktuellen Stand der Forschung bezüglich der **Dynamik von kritischen Casimir-Kräften** gegeben. Außerhalb des thermodynamischen Gleichgewichts sind diese *definitionsabhängig*, wobei es sich zeigt, dass der Spannungstensor [Anhang A.2] für flüssige Systeme die physikalisch motivierte Wahl darstellt.

Kapitel 5: Ausblick

Kapitel 5 spricht weitere Entwicklungen des Themengebiets an, welches in den letzten Jahren sowohl theoretisch als auch experimentell eine große Dynamik erfahren hat.

Teile dieser Arbeit wurden in den folgenden Publikationen vorab veröffentlicht:

- M. Tröndle, S. Kondrat, A. Gambassi, L. Harnau, and S. Dietrich, *Normal and lateral critical Casimir forces between colloids and patterned substrates*, EPL **88**, 40004 (2009).
- M. Tröndle, S. Kondrat, A. Gambassi, L. Harnau, and S. Dietrich, *Critical Casimir effect for colloids close to chemically patterned substrates*, J. Chem. Phys. **133**, 074702 (2010).
- M. Tröndle, O. Zvyagolskaya, A. Gambassi, D. Vogt, L. Harnau, C. Bechinger, and S. Dietrich, *Trapping colloids near chemical stripes via critical Casimir forces*, Molecular Physics **109**, 1169 (2011).

Levitation is a phenomenon which fascinates mankind ever since thousands of years. In Section 2.6 of Chapter 2 it is shown how critical Casimir forces may levitate colloidal particles above chemically patterned substrates. (This photograph has been taken in the city center of Vienna visited on the occasion of the 8th EPS Liquid Matter Conference. The author admits that the phenomenon shown in the image above is the only one presented in this work which is actually *not* due to the critical Casimir effect.)

Contents

Zusammenfassung 3

1 Introduction **17**

1.1 The critical Casimir effect in soft matter 17

1.2 Theoretical background 20

1.2.1 Critical phenomena 21

1.2.2 Critical Casimir effect 26

1.2.3 Finite-size scaling 29

1.2.4 Mean-field theory 31

1.2.5 Dynamic critical phenomena 32

2 Critical Casimir forces between colloids and patterned substrates **37**

2.1 Introduction 37

2.2 Homogeneous substrate 39

2.2.1 Derjaguin approximation 39

2.2.2 Scaling functions for the normal critical Casimir force and the potential 42

2.3 Chemical step (s) 42

2.3.1 Derjaguin approximation 43

2.3.2 Lateral critical Casimir force 46

2.4 Single chemical lane (ℓ) 46

2.4.1 Derjaguin approximation 47

2.4.2 Scaling function for the critical Casimir potential 48

2.5 Periodic chemical patterns (p) 50

2.5.1 Derjaguin approximation 51

2.5.2 Scaling function for the normal critical Casimir force 51

2.6 Critical Casimir levitation 58

2.6.1 General analysis of geometrical parameters 59

2.6.2 Levitation for experimentally relevant parameters — a case study 64

2.6.3 Comparison with quantum electrodynamic Casimir levitation 68

2.7 Cylindrical colloids 69

2.8 Summary 74

3 Comparison with experiments 79

3.1 Introduction . . . 79
3.2 Theory . . . 80
3.2.1 Critical Casimir potential 80
3.2.2 Background forces 82
3.2.3 Total potential 84
3.2.4 Measured potential 86
3.2.5 Non-ideal stripe patterns 87
3.2.6 Particle-substrate distance 88
3.3 Comparison with the experimental data . . . 92
3.3.1 Description of the experiments 92
3.3.2 Comparison of theory with experiments 93
3.3.3 Experiment by *Soyka et al.* 94
3.3.4 Experiment by *Vogt et al.* 96
3.4 Summary . . . 102

4 Dynamic critical phenomena around colloidal particles 105
4.1 Introduction . . . 105
4.2 Critical dynamics in systems confined by curved surfaces . . . 105
4.2.1 Nonlinear relaxation close to planar walls 107
4.2.2 Critical dynamics in thin films 110
4.2.3 Dynamic critical phenomena around colloidal particles 112
4.2.4 Critical dynamics at curved objects 114
4.2.5 Relaxation phenomena around colloids for the ordinary transition 119
4.3 Dynamic critical Casimir force — state of the art . . . 127
4.4 Summary . . . 128

5 Outlook 131

Appendix 135
A Numerics - `f3dm` . . . 135
A.1 Numerical calculation of static critical behaviour 135
A.2 Stress tensor 139
A.3 Numerical calculation of critical dynamics 142

B **Calculation of the Derjaguin approximation for patterned substrates** . . 146
B.1 Derjaguin approximation for a chemical step 146
B.2 Derjaguin approximation for a single chemical lane 152
B.3 Derjaguin approximation for periodic chemical patterns 152
B.4 Cylinder close to a patterned substrate 154
C **Short distance expansion for critical dynamics** 157

Bibliography 157

Danksagung 173
Lebenslauf 176

1. Introduction

1.1. The critical Casimir effect in soft matter

In 1948, *Hendrik Casimir* predicted a force “out of nothing”, when he realized that two metallic plates placed nearby in vacuum attract each other [1]. The origin of this curious attraction are quantum fluctuations of the electromagnetic field, which are present in any medium and in even in vacuum. These quantum fluctuations are a manifestation of *Heisenberg’s uncertainty principle* [2]; “zero-point” fluctuations occur even in the ground-state of the system and at zero temperature. Thus, surfaces which confine the medium impose boundary conditions to the type of fluctuations inside the cavity formed by the two plates and, therefore, restrict their spectrum. This restriction due to the presence of the bodies amounts to a change of the zero-point energy of the system and leads to a long-ranged effective attraction acting on the metallic plates. This force (see Eq. (1.2) on page 28 below) depends only on the speed of light characterizing the response time of electromagnetic fluctuations between the two plates and *Planck’s constant* [3] which characterizes the quantization of the energy of light as realized later by *Albert Einstein* [4]. The Casimir effect is therefore a macroscopic (or mesoscopic) consequence of a quantum effect. The theoretical prediction of the Casimir force was followed by several experimental investigations, however a verification with high accuracy has been obtained not until 1997 [5, 6].

In statistical physics the analogue of vacuum fluctuations are thermal fluctuations inherent to any medium at finite temperature. Soft matter physics is governed by thermal fluctuations and, accordingly, one of the most prominent phenomena, the *Brownian motion* of *colloidal particles* suspended in a liquid [7], has been identified by *Einstein*, *von Smoluchowski* and *Perrin* as a manifestation of the thermal fluctuations of the liquid molecules [8–11]. The term “colloid” goes back to *Thomas Graham* who considered around 1860 the diffusion of organic and inorganic substances like gum Arabic or gelatine and distinguished these “colloids” from the “crystalloids”, which in their solid state form a crystal [12] (the term colloids stems from the Greek word for “glue”). Today, the definition of a colloidal system is rather broad [13, 14]; according to Ref. [15] it *“can be described as a microscopically heterogeneous system where one component has dimensions in between those of molecules and those of macroscopic* *particles like sand"*[8,9]. Thus, the definition of colloids concerns the size of colloidal particles (in the range of 1 nm to few µm) compared to the size of the solvent molecules, rather than their state of matter or their shape. The distinguishing feature of such *colloidal dispersions* is the relatively large contact area between the disperse particles and the dispersion medium so that the interface chemistry is significant [14]. Indeed, the types of colloidal dispersions are distinguished by the phase of the disperse and the phase of the dispersion medium. For example, dispersions of liquid and solid colloidal particles in a gas form aerosols like smoke, fog or hairspray; gaseous colloidal particles in a liquid form foams; liquid particles in a liquid solvent form emulsions, e.g., milk or mayonnaise [14]. This work focuses on solid colloidal particles immersed in a liquid, which forms sols, colloidal suspensions (dispersions), or paste (high solid content) [15]. These colloidal dispersions are widely used in every day life, e.g., as paint, printing ink, or toothpaste [14, 15]. And it were such colloids — pollen particles suspended in water droplets — observed by *Brown*.

The strength of thermal fluctuations is characterized by the value of k_BT, where k_B is the Boltzmann constant and T is the (absolute) temperature. The transition due to thermal fluctuations between different thermodynamic states of the system characterized by an energy difference of less than or much more than the value of k_BT is highly probable or very improbable, respectively [16, 17]. In contrast to quantum fluctuations in vacuum, thermal fluctuations do generally not occur on any length scale but only on scales up to the *correlation length*, which is in liquids of molecular size. However, upon approaching a critical point in the phase diagram of the medium, the correlation length increases according to an algebraic singularity and attains *macroscopic* values, resulting in critical opalescence discovered by *Thomas Andrews* in 1869 [18]. More than hundred years after *Andrews'* discovery, in 1978, *Michael E. Fisher* and *Pierre-Gilles de Gennes* realized that the confinement of these long-ranged critical fluctuations by macroscopic or mesoscopic bodies immersed in a critical fluid — in analogy to the Casimir effect — leads to a force acting on them [19]. At criticality, this critical Casimir force becomes long-ranged [19].

The first *direct* measurements of critical Casimir forces have been performed only recently at the University of Stuttgart by investigating the Brownian motion of solid, spherical polystyrene colloids immersed in a critical fluid and close to a substrate [20, 21]. These experiments clearly demonstrated that, upon approaching the critical point, the critical Casimir force can modify the effective interaction between the colloid and the substrate by several multiples of k_BT. Since, near the critical point, the correlation length depends strongly on temperature, the strength of the critical Casimir effect does so as well. Consequently, in contrast to the quantum Casimir force, critical Casimir forces can be "tuned" by minute temperature changes [22, 23]. The critical Casimir force depends strongly on the type of boundary conditions at the surfaces of the

---

[8] P. 133 of Ref. [15].

[9] Formally, the whole system consisting of molecules and larger particles is denoted as colloid. Typically, however, (and as used in this work) only the larger particles are called colloids.

bodies immersed in the (near-) critical medium, and it can be attractive or repulsive, depending on the effective type of boundary conditions (see, e.g., Refs. [24–33] and references therein). In binary liquid mixtures, the type of boundary conditions is given by the generic adsorption preference of the surfaces. The sign of the critical Casimir force can be set by suitable surface treatments rather easily [20, 21] (by contrast, the quantum electrodynamic Casimir force is typically attractive and responsible for *stiction*; turning it to be repulsive requires a careful choice of the fluid and of the bulk materials of the confinement [34]).

A striking feature of the critical Casimir effect is the occurrence of a *universal* description. That is, the critical Casimir force expressed in terms of suitable scaling variables depends only on a given universality class of the bulk critical point and on the type of boundary conditions, whereas it is independent of the microscopic structure and of the material properties of the specific fluid medium involved (see, e.g., Refs. [24, 25] and references therein). For theoretical physicists this universality offers the opportunity to investigate the critical Casimir force in representative models (e.g., lattice models). The corresponding predictions can be stringently compared with data measured, e.g., for the experimentally relevant classical binary liquid mixtures and simple fluids because the universal features of the critical Casimir force are preserved, independent of the actual physical system.

Whereas it has turned out to be experimentally rather difficult to align two comparably large plates perfectly parallel at distances on the micro-scale, a break-trough in measuring Casimir forces has been obtained using a large-radius sphere instead of the second plane [6, 20]. Such spherical colloidal particles are not only widely used as model systems in soft matter physics, but they have also applications at the micro- and nanometer scale and are used in micro- and nano-electromechanical devices. As noted above, colloidal particles immersed in a fluid, are subjected to Brownian motion; in turn, this motion can be experimentally used to scan the effective potential acting on the particle via relating the *Boltzmann factor* [16, 17]. In particular, in Refs. [20, 21, 35, 36] the probability distribution of the vertical displacement of a particle from an opposing wall was recorded via *total internal reflection microscopy* (TIRM), and the effective critical Casimir potential of the particle as a function of the displacement has been determined from these data. However, the Brownian motion of colloidal particles can not only be used to let particles explore the normal direction of a wall, but also the *lateral* one. Recently, the critical Casimir potential of a colloid close to a substrate with a *pattern* of parallel chemical stripes with laterally alternating adsorption preference has been measured via an analogous method in Refs. [37–40]: The projected particle distribution along the lateral direction perpendicular to the chemical stripes has been measured via *digital video microscopy*, and the effective potential for a single colloid has been determined via the Boltzmann factor. From these experiments, it turned out that suitably designed substrate patterns consisting of stripes of surface properties, which — in the homogeneous case — correspond to attractive and repulsive (normal) critical Casimir forces, lead to the occurrence of *lateral* critical Casimir forces acting on colloids. Current techniques allow one to endow solid surfaces with precise structures on the nano- and micrometer-scale. Hence, the critical Casimir effect can be used to create laterally confining potentials for a single colloid, which can be tuned by temperature [37]. In order to reap the full benefits of the wide range of possibilities, a thorough theoretical understanding of the underlying physics is essential. In this context theoretical studies of critical Casimir forces have been limited either to colloids facing a *laterally homogeneous* surface [41–46], or to the *parallel plate* geometry involving chemically [47, 48] or geometrically [49, 50] structured substrates for which lateral forces vanish if one of the substrates is homogeneous.

In order to overcome these limitations, in Chapter 2 we[10] study the critical Casimir force acting on spherical and cylindrical colloids close to a substrate with laterally alternating adsorption preferences for the two components of a confined binary liquid mixture. We provide quantitative predictions for the *universal* features of this effective force, pursuing a two-fold approach: a full numerical analysis of the appropriate mean-field theory (MFT) and use of the so-called Derjaguin approximation (DA) together with the knowledge of scaling functions determined by Monte Carlo simulations in three dimensions. A suitable choice of substrate patterns may even lead to levitation of colloids at a stable distance above the substrate due to the critical Casimir effect (Sec. 2.6). In Chapter 3 we compare our theoretical predictions for the critical Casimir potential of single colloids close to patterned substrates with the corresponding available experimental data including two different types of substrate surface preparation: partial removing of a coating via a *focused ion beam* [37] and *microcontact printing* [39, 40]. It turns out that the critical Casimir force is a sensitive probe for the geometrical details of the imprinted structures. Accounting properly for this feature, for all patterned substrates that were investigated, our theoretical predictions agree well with the measured critical Casimir potentials.

Parts of this thesis have been published in advance in Refs. [40, 51, 52].

1.2. Theoretical background

In this Section we present briefly the necessary, well-known theoretical background concerning the statics and dynamics of critical Casimir forces. In Subsec. 1.2.1 the thermodynamic description of equilibrium critical phenomena in bulk systems is reviewed, based on Refs. [53–60] and references therein, which are only a small fraction of the vast amount of literature on this topic. In Subsec. 1.2.2 the description of surface critical phenomena and the Casimir effect in soft matter systems are briefly reviewed, followed by a more thorough description of finite size scaling in Subsec. 1.2.3. Subsection 1.2.4 briefly reviews the field theoretic description of critical phenomena and the mean field theory is presented. Finally, in Subsec. 1.2.5 we shall give a short account of the dynamics of critical phenomena.

---

[10] Throughout this thesis *pluralis auctoris* is used instead of the first person singular.

1.2.1. Critical phenomena

Phases of matter are macroscopic regions in which the physical properties are homogeneous. In thermal equilibrium, most materials form either a solid, liquid, or gaseous phase, determined by external parameters. This is described by an equation of state, which relates few macroscopic quantities, such as pressure p, temperature T and particle number density ρ. This functional relation, e.g., $\rho(p,T)$, defines a surface, where each of the surface points corresponds to a equilibrium state of the system (see, e.g., Refs. [53–55] and references therein). In Fig. 1.1 a phase diagram is shown, which sketches such a surface for a *simple fluid*. At certain values of the relevant parameters, matter can exist in two or more phases, which are separated into different regions. This corresponds to a multivalued relation $\rho(p,T)$ and distinct points on the surface $\rho(p,T)$. In the phase diagram such coexisting phases are represented as regions, which do not belong to the surface of equilibrium states $\rho(p,T)$, but which connect coexisting states. In Fig. 1.1 these coexistence regions are indicated as light shaded areas; lines across the coexistence regions connect distinct phases of different density which may coexist. The triple line connects *three* coexisting phases of matter: solid, liquid, and gas. Across a coexistence region, the transition from one phase to another is discontinuous and corresponds to a jump of the density ρ and involves a latent heat. Coexistence regions may end at a critical point (ρ_c, p_c, T_c), where the phase transition becomes *continuous*. That is, right at the critical point the density changes continuously. Beyond the critical point, there exists only a single fluid phase throughout the system, and there is no difference between the gaseous and the liquid phases, which are two extensions of the fluid phase and share the same symmetry properties. In Fig. 1.1 the coexistence region between the solid and the fluid phase does not end at a critical point because these two phases have different characteristic symmetry properties.

From the viewpoint of statistical physics, the local density $\rho(\mathbf{r})$ exhibits random *thermal fluctuations* on the length scale of the bulk correlation length ξ which is generally of molecular size. However, in the vicinity of the critical point the physical system shows rather special features, known as *critical phenomena* (see, e.g., Refs. [56–60] and references therein). Since the critical isotherm has zero slope at the critical point, the compressibility *diverges*, reflected in an algebraic singularity of the correlation length ξ. This leads to pronounced thermal fluctuations of $\rho(\mathbf{r})$ on macroscopic length scales. Even visible light is scattered by the fluctuating fluid close to criticality, known as *critical opalescence* discovered around 150 years ago [18]. Whereas far from criticality thermal equilibrium favors the separation of two coexisting phases into two macroscopic regions, close to the critical point regions of different phases may form in any size and number. Since close to the critical point ξ is much larger than any microscopic quantity, it is the only relevant length scale in the system; the size of the molecules, the precise form of the molecular interaction potential, or the chemical type of the molecules forming the fluid, are ruled out. Thus, the critical behavior exhibits *universality* in the sense that its features do not depend on microscopic parameters but only on few gross features of the system.

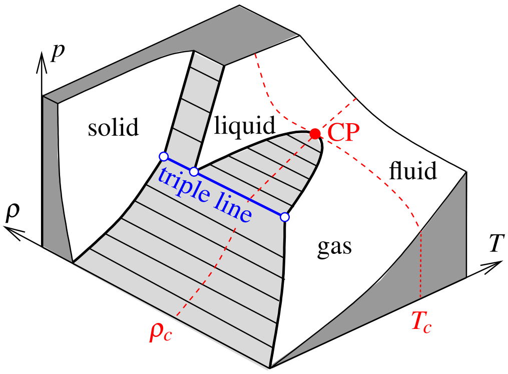

Figure 1.1: Sketch of the phase diagram of a simple fluid. In the space spanned by the three parameters temperature T, pressure p, and density ρ, the states in thermal equilibrium form a surface (white area). Distinct phases of matter may coexist at same temperature and pressure if they are connected by a line across a coexistence region (light shaded areas) which does not belong to the surface of equilibrium states. The triple line connects three coexisting phases: solid, liquid, and gas. The coexistence region of the liquid and the gas phases, which are two extensions of the fluid phase, ends at a critical point (CP) with the critical values T_c, p_c, and ρ_c. Typical representations of a phase diagram are the projections of the surface of equilibrium states onto the pT, $p\rho$, or ρT-plane.

Not only simple fluids exhibit critical phenomena but also many other physical systems. Consider the phase diagram of a *uniaxial ferromagnet* shown in Fig. 1.2. Here, the macroscopic relevant quantities are not density and pressure but the magnetization m and the magnetic field H. The physical state of the system in thermal equilibrium is then described by a surface $m(H,T)$. The phase diagram shows a critical point at $(m = 0, H = 0, T = T_c)$, where T_c is the critical (Curie) temperature of the ferromagnet. Below T_c there are two phases corresponding to spontaneous magnetization oriented in the one or other direction along the easy axis of the uniaxial ferromagnet, and *Weiss domains*, regions of different homogeneous magnetization, may coexist. Above T_c the material forms a paramagnetic phase which is unordered and has a non-zero magnetization only when an external field H is applied. At the critical point, the magnetic susceptibility which measures the ease of magnetizing a system, diverges. This is analogous to the compressibility of a simple fluid, and correspondingly, close to the critical point, the local magnetization $m(\mathbf{r})$ exhibits large-scale fluctuations. Thus, the magnetization for a uniaxial ferromagnet plays the same role as the density for a simple fluid. The correlation length of the magnetic system diverges, and microscopic length scales such as the lattice constant are not relevant for the critical behavior. It turns out that the critical behavior of the ferromagnetic system is the same as for a simple fluid, just with the physical quantities replaced by corresponding ones. The universal features of the critical phenomena for a uniaxial ferromagnet and a simple fluid are identical, which shows that the concept of universality holds for very different physical systems.

In this work we are particularly interested in the experimentally relevant *binary liquid mix-*

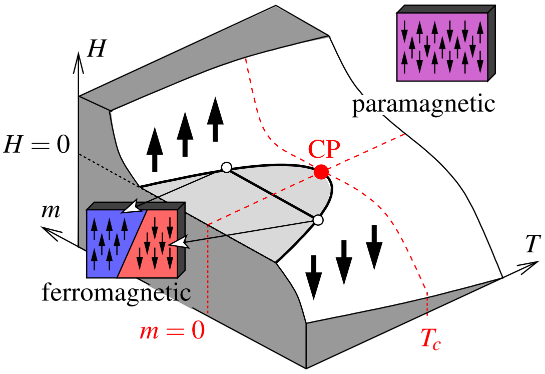

Figure 1.2: Sketch of the phase diagram of a uniaxial ferromagnet. States in thermal equilibrium correspond to points on the white surface in the space of magnetization m, temperature T, and magnetic field H. Below T_c (Curie temperature), ferromagnetic phases of positive or negative magnetization are spontaneously formed and may coexist in Weiss-domains. Above T_c, the system is paramagnetic and the molecular magnetic moments point in random directions along the easy axis of the magnet.

tures. Denoting the two species forming the mixture as "A" and "B", one finds that the thermodynamic description is based on three intensive thermodynamic quantities: temperature T, pressure p, and the concentration c_A of the "A"-particles [54]. At a fixed pressure p, the sum $\mu_A + \mu_B$ of the chemical potentials of the two species is fixed, and the relative concentration determined by the difference $\mu_A - \mu_B$. Figure 1.3 shows the phase diagram of a binary liquid mixture at fixed pressure p chosen such that the mixture is in the liquid phase. The temperature *vs* concentration phase diagram shown in Fig. 1.3 represents a *lower* critical demixing point (or consolute point), which frequently occurs. In addition, binary liquid mixtures have also an upper critical demixing point not shown in Fig. 1.3. For temperatures above the critical one, phase separation, i.e., *demixing* of the two species into a A-rich and a B-rich phase, occurs; in a test tube, the phase corresponding to a higher mass density will be at the bottom of the tube. For $T < T_c$ the binary liquid is always in the unordered, mixed state. The coexistence curve of a binary liquid mixture is similar to the ones for a simple fluid or a uniaxial ferromagnet. Indeed, their critical phenomena are completely analogous: the local concentration $c_A(\mathbf{r})$ exhibits large-scale fluctuations at the critical point because the bulk correlation length diverges.

The features of the critical behavior for simple fluids, uniaxial ferromagnets, and binary liquid mixtures are *universal*. The underlying physical mechanism is the divergence of the length scale of thermal fluctuations close to criticality — molecular details are ruled out. A unified description for these very different systems can be obtained using generalized quantities which represent the system-dependent ones. A general measure for the order of a state is characterized by the *order parameter* $\phi(\mathbf{r})$; it is defined such that its thermal average $\langle\phi(\mathbf{r})\rangle$ vanishes in the disordered state and it is non-zero for ordered states. The order parameter is defined on a *mesoscopic* scale, i.e., ϕ is a coarse-grained (but spatially varying) average of the actual system-dependent physical observable identified with order of the system. For a simple fluid this is

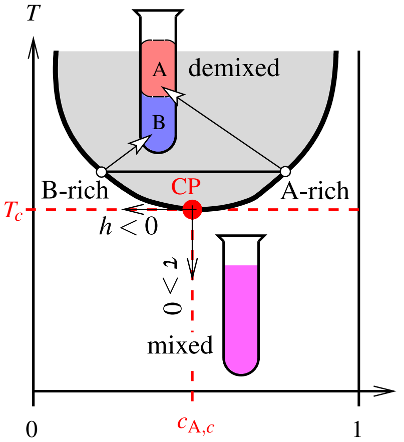

Figure 1.3: Sketch of the region around a lower critical demixing point in the phase diagram of a binary liquid mixture of "A" and "B" particles at fixed pressure. Below the critical temperature $T = T_c$ the binary liquid is in a mixed phase. Above T_c, phase separation into a A-rich phase (corresponding to a high concentration c_A of A-particles) and a B-rich phase (corresponding to low c_A) occurs. The coexistence region ends at the critical point corresponding to the critical concentration $c_{A,c}$. The difference of the concentration from its critical one is steered by the "field" $h = \mu_A - \mu_{A,c}$, i.e., the difference of the chemical potential for species "A" from its critical value. The reduced temperature $\tau = -(T - T_c)/T_c$ measures the temperature difference from the critical point, such that $\tau > 0$ corresponds to the homogeneous, mixed phase.

the difference of the density from its critical value, $\phi(\mathbf{r}) = \rho(\mathbf{r}) - \rho_c$; for a ferromagnet it is given by the magnetization $\phi(\mathbf{r}) = m(\mathbf{r})$; and for a binary liquid mixture it is the concentration difference $\phi(\mathbf{r}) = c_A(\mathbf{r}) - c_{A,c}$. The temperature is generalized as the *reduced temperature* $\tau = \pm(T - T_c)/T_c$, such that $\tau > 0$ corresponds to the homogeneous, unordered phase, and $\tau < 0$ corresponds to the disordered state. The generalized *external field* h conjugate to ϕ is given by the magnetic field H for a ferromagnet; for a simple fluid h is given by a linear combination of $p - p_c$ and τ; and for a binary liquid mixture the field is given by the chemical potential $\mu_A - \mu_{A,c}$. For zero bulk field ($h = 0$) the physical description is symmetric in terms of ϕ, whereas for $h \neq 0$ this symmetry is broken and the thermal average of the order parameter is non-zero also for $\tau > 0$. That is, the critical point at $\tau = 0$ can be only reached exactly for $h = 0$, where the order parameter changes continuously from 0 for $\tau \geq 0$ to non-zero values for $\tau < 0$.

For all systems ϕ exhibits the same behavior for $\tau < 0$: $\langle\phi(\mathbf{r})\rangle = \pm a|\tau|^\beta$, where a is a non-universal amplitude depending on the actual physical system, and $\beta > 0$ is a universal *critical exponent*. Similarly, the behavior of the bulk correlation length ξ is universal. It diverges as $\xi = \xi_0^\pm|\tau|^{-\nu}$ upon approaching the critical point from $\tau \gtrless 0$, where $\nu > 0$ is another critical exponent. The two amplitudes ξ_0^+ and ξ_0^- are system-dependent, however, their ratio ξ_0^+/ξ_0^- is universal. Similarly, close to the critical point all system-dependent, non-universal amplitudes can be universally related to each other, so that one is left with very few independent non-universal amplitudes only. Not only the temperature dependence of critical phenomena is universal but all dependencies; in particular the ones on spatial variables can be expressed in dimensionless *scaled variables*, i.e., quantities divided by its characteristic size.

The universality of critical phenomena allows for a common description of many different physical systems which can be classified into few *universality classes*. Their universal critical behavior depends only on few gross features of the systems [61]:

- the spatial dimensionality d of the system,
- the symmetry properties of the order parameter ϕ, characterized by its dimensionality n,
- the range of the intermolecular interactions, which are classified into either short-ranged, intermediate-ranged, or long-ranged interactions.

Here, we consider short-ranged intermolecular interactions only, which are characterized by a spatial decay which is stronger than one with a power law behavior with an exponent of $-(d+2)$ [56]; this is the generic case for most physical systems. Thus, the set $(d;n)$ characterizes completely a universality class for the critical behavior of systems with short-ranged interactions. The physically relevant dimensions are $d \leq 3$, however, it turned out to be very useful to consider also higher dimensions.

The systems considered above have in common that there are basically two ordered phases, which can be characterized by a *scalar* order parameter, which is positive for one ordered phase and negative for the other ordered phase. Thus, the symmetry of the order parameter is one-dimensional, $n = 1$, which means that these physical systems belong to the *Ising universality class*. Due to universality, one can use simplified models, which share the key features, in order to theoretically predict the critical behavior for the whole universality class. The Ising model is such a simple lattice model, which consists of spins sitting on the sites of a d-dimensional cubic lattice. The spins can take the values $+1$ or -1 and interact with their nearest neighbors only. Thus, the order parameter measuring the local magnetization is scalar, and the intermolecular interactions are short-ranged. At low temperatures the spins prefer a parallel alignment and form a ferromagnetic state. At high temperatures, thermal fluctuations eventually destroy this order and the spins are arbitrarily aligned and form a paramagnetic state. For $d \geq 2$ a continuous phase transition between the ferromagnetic and the paramagnetic state occurs at $T = T_c$. The meso- and macroscopic features of the critical behavior of the Ising spin model are universal and characterize the behavior of the corresponding d-dimensional Ising universality class. Accordingly, systems with a two component order parameter, i.e., $n = 2$, belong to the *XY universality class* referring to so-called XY-magnets. The critical behavior of normal to superfluid phase transition of liquid helium is a famous example for the XY universality class. The *Heisenberg universality class* corresponds to $n = 3$ inheriting its name from the *Heisenberg model*.

The critical exponents characterizing the critical behavior of the physically relevant observables are different for the various universality classes. Here and in the following we focus on the Ising universality class, which encompasses the binary liquid mixtures. In the Ising universality class for $d = 3$ the critical exponents for the order parameter and the bulk correlation length take the values $\beta \simeq 0.33$ and $\nu \simeq 0.63$ [62].

1.2.2. Critical Casimir effect

Large samples of materials are dominated by bulk effects like the ones described above. However, life at the border is the most interesting. Finite size of a real sample, confinements of fluids, and surfaces and interfaces of matter cause remarkable physical effects. Generically, the surfaces which confine a binary liquid mixture preferentially adsorb one of its two components (or the gas or liquid phase in the case of a one-component fluid). This amounts to the presence of effective, symmetry-breaking *surface fields* coupling to the order parameter. Thus, either positive or negative values of the scalar order parameter ϕ, which is the difference between the local concentrations of the two species, are favored. The extension of the spatial region in the direction normal to the surfaces, within which the local structural properties of the fluid deviate from the bulk ones, is given by the bulk correlation length, which diverges upon approaching the critical point. Thus, a macroscopic layer of the preferentially adsorbed material forms next to the confining surface, known as *critical adsorption* [19, 63, 64].

More generally, the spatial profile of the order parameter depends on the boundary conditions of the confining surfaces. As a consequence, the universality classes of critical phenomena are subdivided into *surface universality classes* which represent the generic cases of boundary conditions. Surface universality classes are characterized by a universal behavior of the influence of the boundary condition on the physical properties of the confined medium close to its critical point. Within the Ising universality class, one finds few surface universality classes. Depending on the boundary conditions (BC), the confined medium falls into one of these cases. These are [63, 65, 66]

- the *ordinary* surface universality class, characterized by a lower ordering at the surface than in the bulk; this is the generic case for magnetic materials due to the effect of “missing bonds”,

- the *special* surface universality class, which is *multicritical* because the continuous phase transition from the unordered to the ordered state occurs in the bulk and at the surface at the same temperature, and

- the *extraordinary* or *normal* surface universality class, which corresponds to the case that even for $\tau > 0$ the material at the surface has a higher order than the one in the bulk; for magnets this might be uncommon, however for fluids and binary liquid mixtures, this is the “normal” case in the laboratory [67–70].

The influence of the surface on the order parameter can be described via two generalized parameters, the surface enhancement c and the surface field h_1. The surface enhancement which accounts for the effect of "missing neighbors" couples in a symmetric way to the order parameter, i.e., independent of the sign of ϕ. On the other hand, h_1 introduces a *symmetry-breaking* surface influence on the order parameter and couples linearly to ϕ. Thus, the surface field accounts for an external influence on the system at the surface, such as chemical properties of the container walls confining a liquid.

Consider the case of binary liquid mixture. The inevitable preference of a surface for one of the two species "A" or "B" results in change of the concentration c_A close to the surface; the symmetry between "A" and "B" particles is broken. The thermodynamic quantities coupling linearly to the concentrations of the species are the corresponding chemical potentials. Thus, the surface influence on a binary liquid mixture can be described via the surface field [71, 72]

$$h_1 = (k_B T)^{-1} \left[(\mu_A - \mu_{A,c})_{\text{surface}} - (\mu_A - \mu_{A,c}) \right] \tag{1.1}$$

because the appropriate order parameter is given by the concentration difference $c_A - c_{A,c}$ of species "A" from its critical value. The strength of the adsorption at the surface is controlled via the value of h_1 and varying it yields a rich behavior of phenomena [33].

Here, we are interested in the generic case of *strong adsorption* at the surface. This corresponds to the *fixed point* value $h_1 \to \pm\infty$, which causes the order parameter formally to diverge at the surface. As the whole concept of the order parameter is based on a coarse-grained point of view, this divergence describes the actual concentration only at scales larger than the molecular one and corresponds to the leading behavior. However, suitably close to the critical point, this leading behavior dominates and therefore describes the actual physics very well. This kind of boundary conditions is denoted as "$(+)$" corresponding to $\phi|_{\text{surface}} \to \infty$ or as "$(-)$" corresponding to $\phi|_{\text{surface}} \to -\infty$ [63, 73]. Close to the critical point and for $\xi \gg y$ the order parameter diverges algebraically as $\phi \propto \pm y^{-\beta/\nu}$, where y is the distance from the surface with $(\pm)$ BC [19]. Critical adsorption is the generic case of boundary conditions exerted by surfaces confining binary liquid mixtures, where $(+)$ and $(-)$ boundary conditions correspond to preferential adsorption of the one or the other species, and has been measured in various experiments (see, e.g., Refs. [63, 64] and references therein).

The *finite size* of systems gives rise to pronounced effects in addition to the effect due to single surfaces and the change of volume. The celebrated *Casimir effect in quantum electrodynamics* is such a finite size effect [1, 5, 74]. The zero-point fluctuations of the electric field in vacuum are affected when two conducting plates limit the size of the system. The spectrum of fluctuations is restricted to modes which vanish at the surfaces plates and therefore the zero-point energy depends on the distance of the two plates. *Hendrik Casimir* has predicted that this leads to an attractive force K between two perfectly conducting plates of area A at distance L in vacuum, which is determined by the natural constants c and $\hbar$ as

$$\frac{K(L)}{A} = -\frac{\pi^2 \hbar c}{240 L^4}. \tag{1.2}$$

Equation (1.2) is a special case of the more general *Lifshitz formula* which describes the force due to quantum electrodynamic fluctuations between two dielectric bodies which are separated by a third dielectric medium [75]. Similarly, the well known van-der-Waals or London dispersion forces are based on quantum electrodynamic fluctuations, as well, and can be described by the Lifshitz formula [76]. Van-der-Waals forces act on separations on a molecular scale, i.e., of few nanometers. Since electrodynamic fluctuations occur on a (infinitely) large scale, they lead to forces between confining media also at large separations. At larger distances, the fluctuation induced forces are affected by retardation effects associated with the speed of light, which shows up in Eq. (1.2). The quantum electrodynamic Casimir force is typically attractive and thus responsible for *stiction* ("static friction") which leads to a standstill of nano-mechanical devices. Depending on the choice of dielectric constants, the Casimir forces can also be repulsive; however, this requires a careful choice of the media (see, e.g., Ref. [34] and references therein).

Fluctuation induced forces lead to manifestations of the Casimir effect in condensed matter in rather different fields across physics, chemistry, and biology due to the confinement of *thermal fluctuations*. Their common feature is that the restriction of the spectrum of fluctuations due to the presence of confining bodies leads to a force between them. For example, the different manifestations of the Casimir effect in soft matter [5] include the director fluctuations of confined liquid crystals [77–80], forces induced by fluctuations of interfaces [81, 82], forces within fluctuating membranes [83–86], or forces induced by charge fluctuations [87–92].

A rather intriguing example for a fluctuation induced force in soft matter is the *critical Casimir effect*, which has been predicted in a seminal work by *Michael Fisher* and *Pierre-Gilles de Gennes* in 1978 [19]. The confinement of the long-ranged *critical* fluctuations of the order parameter leads to forces acting on the confining surfaces even at large distances. The theoretical description of the critical Casimir forces is particularly challenging due to the non-Gaussian character of the order parameter fluctuations, which contrasts with the intrinsically Gaussian nature of the low energy fluctuations of the electromagnetic field. In addition, the critical Casimir effect is also particularly rich as it allows, *inter alia*, symmetry breaking boundary conditions as described above, which do not occur for electromagnetic fields. The critical Casimir force strongly depends on the effective boundary conditions at the walls [24–33]. It is attractive for equal symmetry breaking $(\pm, \pm)$ BC and repulsive for opposing $(\pm, \mp)$ BC. *Inter alia*, this latter feature qualifies critical Casimir forces to be a tool to overcome the problem of *stiction*. As stated above, the critical Casimir effect exhibits universality and can be described in terms of universal functions valid for all systems which are encompassed by the same universality class.

The existence of the critical Casimir effect has been experimentally confirmed and its strength has been first measured indirectly for wetting films [93–97]. The first direct measurement of this effect has been performed at the sub-micrometer scale for a spherical colloid immersed in a (near-) critical binary liquid mixture close to a laterally homogeneous and planar substrate [20, 21]. The corresponding Monte Carlo simulation data are in very good quantitative agreement with all available experimental data [20, 21, 98–107].

Clearly, Casimir forces are strongly affected by the properties of the confining surfaces. In particular, their topological structure has be subject of various investigations concerning the quantum electrodynamic Casimir effect (see, e.g., Ref. [108] and references therein). Critical Casimir forces for geometrically structured confinements have been studied in Refs. [49, 50]. Opposing wedge-like structured surfaces even experience *lateral* critical Casimir forces [49, 50]. Sharing different types of boundary conditions on their surfaces, *chemically* structured substrates strongly influence the effective critical Casimir forces acting on them; for a chemically structured wall opposing another planar wall forming a film geometry, the critical Casimir force has been obtained within mean-field theory (MFT) [47, 48] and from Monte Carlo simulations [109, 110].

This work focuses on colloids opposite to such chemically structured substrates. The geometry of the colloids plays a crucial role for the universal properties of the critical Casimir forces acting on them. Theoretical studies of the critical Casimir effect acting on colloidal particles involve spherically [41–46] or ellipsoidally [111] shaped colloids adjacent to *homogeneous* substrates, the latter ones even experience a critical Casimir torque [111].

1.2.3. Finite-size scaling

According to the theory of finite-size scaling, the critical Casimir force and the corresponding potential can be described by *universal* scaling functions, which are independent of the molecular details of the system but depend only on the gross features of the system, i.e., on the bulk universality class of the associated critical point (see, e.g., Refs. [24, 25, 112, 113] and references therein). This work focuses on the Ising universality class characterized by a scalar order parameter ϕ, which is relevant for simple fluids and binary liquid mixtures, in spatial dimensions $d = 3$ and $d = 4$. The critical Casimir force depends on the type of effective boundary conditions at the walls, which are denoted by (a) and (b), and by the geometry of the confining surfaces. Note that (a) and (b) can represent the various symmetry preserving fixed-point BC (the so-called ordinary, special, periodic, or antiperiodic boundary conditions [24, 25]) in addition to the symmetry breaking cases $(\pm)$.

Inspired by the experiments described in Refs. [20, 21, 35, 37–40], here binary liquid mixtures are considered with their (lower) critical point approached by varying the temperature T towards T_c from below at fixed pressure and critical composition. This corresponds to the case of a zero bulk field, $h = 0$, which is assumed throughout this work. Consider first the *film* geometry in which the fluid undergoing the continuous phase transition is confined between two parallel, infinitely extended walls at distance L. According to renormalization group theory the normal critical Casimir force $f_{(a,b)}$ per unit area which is acting on the walls scales as [26–28]

$$f_{(a,b)}(L,T) = k_B T \frac{1}{L^d} k_{(a,b)}(\mathrm{sign}(\tau) L/\xi_\pm), \tag{1.3}$$

where (a,b) denotes the pair of boundary conditions (a) and (b) characterizing the two walls. The scaling function $k_{(a,b)}$ depends only on a single scaling variable given by the sign of the reduced temperature distance τ from the critical point ($\pm$ for $\tau \gtrless 0$) and the film thickness L in units of the bulk correlation length $\xi_\pm(t \to 0^\pm) = \xi_0^\pm |\tau|^{-\nu}$, where $\nu \simeq 0.63$ in $d = 3$ and $\nu = 1/2$ in $d = 4$ [62]. Clearly, one has $f_{(a,b)}(L,T) = f_{(b,a)}(L,T)$. Positive values of τ, $\tau > 0$, correspond to the disordered (homogeneous) phase of the fluid, whereas negative values of τ, $\tau < 0$, correspond to the ordered (inhomogeneous) phase, where phase separation occurs. The two non-universal amplitudes $\xi_0^\pm$ of the correlation length are of molecular size and characterized by the universal ratio $\xi_0^+/\xi_0^- \simeq 1.9$ in $d = 3$ [62, 114] and $\xi_0^+/\xi_0^- = \sqrt{2}$ in $d = 4$ [115, 116]; $\xi_\pm$ is determined by the exponential spatial decay of the two-point correlation function of the order parameter ϕ in the bulk.

At the critical point $T = T_c$, the correlation length diverges, $\xi_\pm \to \infty$, and the scaling function of the critical Casimir force acting on the two planar walls attains a universal constant value referred to as the critical Casimir amplitude [24, 25]:

$$k_{(a,b)}(L/\xi_\pm = 0) = \Delta_{(a,b)}. \tag{1.4}$$

Away from criticality, the critical Casimir force decays exponentially as a function of $L/\xi_\pm$.

For the specific case of symmetry breaking BC $a,b \in \{+,-\}$, the functions $k_{(+,\pm)}$ have been calculated exactly in $d = 2$ [29], for $d < 4$ using perturbative field-theoretical methods [117] or effective theories [118], and in $d = 3$ numerically via Monte Carlo simulations [99, 100, 104–106]. At present, a quantitatively reliable theoretical determination of both $k_{(+,+)}$ and $k_{(+,-)}$ in $d = 3$ is provided only by Monte Carlo simulations. For $a,b \in \{+,-\}$ and for $\tau > 0$ one expects for $L/\xi_+ \gg 1$ a *pure* exponential decay of $f_{(+,\pm)}$ (see, e.g., Refs. [29, 117, 118], i.e., a decay without an algebraic prefactor to the exponential and without a numerical prefactor to L/ξ_+ in the argument of the exponential[11]) corresponding to

$$k_{(+,\pm)}(L/\xi_+ \gg 1) = A_\pm \left(\frac{L}{\xi_+}\right)^d \exp(-L/\xi_+), \tag{1.5}$$

where $A_\pm$ are universal constants [21]. Note that, in the absence of symmetry-breaking fields inside the film, the scaling functions for $(+,+)$ BC are the same as for $(-,-)$ BC.

---

[11] This purely exponential decay is proven only in $d = 2$ and 4 but it is expected to hold for all spatial dimensions.

1.2.4. Mean-field theory

The standard Landau-Ginzburg-Wilson fixed-point effective Hamiltonian describing critical phenomena of the Ising universality class in the *bulk* is given by [63, 66, 73, 119–125]

$$\mathscr{H}[\phi] = \int\limits_V \mathrm{d}^d r \left\{ \frac{1}{2}(\nabla\phi)^2 + \frac{\hat{\tau}}{2}\phi^2 + \frac{u}{4!}\phi^4 - h\phi \right\}, \tag{1.6}$$

where $\phi(\mathbf{r})$ is the order parameter describing the fluid, which completely fills the volume V in d-dimensional space. The first term in the integral in Eq. (1.6) penalizes local fluctuations of the order parameter. The parameter $\hat{\tau}$ in Eq. (1.6) is proportional to τ, and the coupling constant u is positive and provides stability of the Hamiltonian for $\tau < 0$. The last term in Eq. (1.6) vanishes for the case considered here, $h = 0$, which corresponds to the concentrations of the binary liquid mixture species fixed to their critical values. In a finite-size system the bulk Hamiltonian $\mathscr{H}[\phi]$ is supplemented by appropriate surface and curvature (edge) contributions [63, 66, 73, 126]. The corresponding Hamiltonian for a surface, which adds to Eq. (1.6) is given by [63, 66, 73, 126]

$$\mathscr{H}_\mathrm{s}[\phi] = \int\limits_S \mathrm{d}^{(d-1)} r \left\{ \frac{c}{2}\phi^2 - h_1\phi \right\}, \tag{1.7}$$

where c is the surface enhancement and h_1 is the surface field. In the *strong* adsorption limit [69, 127], these contributions generate boundary conditions for the order parameter such that $\phi\big|_\mathrm{surface} = \pm\infty$. For binary liquid mixtures these fixed-point $(\pm)$ BC are the experimentally relevant ones. (Note that a *weak* adsorption preference might lead to a crossover between various kinds of effective boundary conditions for the order parameter ϕ [21, 32, 33].) Thus, Eq. (1.7) and additional curvature contributions can be replaced by applying the appropriate BC to ϕ and using Eq. (1.6) throughout the bulk. The mean-field order parameter profile $m \equiv (u/3!)^{1/2}\langle\phi\rangle$ minimizes the Hamiltonian, i.e., $\delta\mathscr{H}[\phi]/\delta\phi|_{\phi=(u/3!)^{-1/2}m} = 0$. In the bulk the mean-field order parameter is spatially constant and attains the values $\langle\phi\rangle = \pm a|\tau|^\beta$ for $\tau < 0$ and $\langle\phi\rangle = 0$ for $\tau > 0$, where, besides ξ_0^+, a is the only additional independent non-universal amplitude appearing in the description of bulk critical phenomena, and $\beta(d = 4) = 1/2$ is a standard critical exponent. Within MFT $\hat{\tau} = \tau(\xi_0^+)^{-2}$ and $u = 6a^{-2}(\xi_0^+)^{-2}$.

In Chapter 2 we present MFT results which we have calculated by minimizing numerically $\mathscr{H}[\phi]$ using a $3d$ finite element method in order to obtain the (spatially inhomogeneous) profile $m(\mathbf{r})$ for the geometries under consideration. The normal and the lateral critical Casimir forces are calculated directly from these mean-field order parameter profiles using the stress tensor [111, 117].[12] This allows one to infer the universal scaling functions of the critical Casimir forces at the upper critical dimension $d = 4$ up to an overall prefactor $\propto u^{-1}$ and logarithmic corrections (for a general description of the field theory for critical phenomena, see, e.g., Ref. [128]). The corresponding critical Casimir potential is obtained by the appropriate integration of the normal or of the lateral critical Casimir forces.

---

[12] The details of the numerical method are described in Appendix A.1.

In the case of planar walls the MFT scaling functions for the critical Casimir force can be determined analytically [117] and one finds [see Eq. (1.4)] for the case of symmetry breaking boundary conditions the following critical Casimir amplitudes: $\Delta_{(+,+)} = \Delta_{(-,-)} = 24[K(1/\sqrt{2})]^4/u \simeq -283.61 \times u^{-1}$, where K is the complete elliptic integral of the first kind, and $\Delta_{(+,-)} = -4\Delta_{(+,+)}$ (see Ref. [117] and Eq. (27) and Ref. [49] in Ref. [100]).

1.2.5. Dynamic critical phenomena

The critical phenomena described above are static, i.e., the time-independent equilibrium behavior of the system. However, also the dynamics of the system is altered close to a critical point. Due to the divergence of the correlation length $\xi = \xi_0^{\pm}|\tau|^{-\nu}$, collective behavior of the molecules and thermal fluctuations of the order parameter occur on a large length scale. Thus, the associated dynamic time scales grow as well, known as *critical slowing down*. (see, e.g., Refs. [129–133] and references therein).

Critical slowing down of the order parameter dynamics is expressed in terms of the dynamic scaling hypothesis [134–137]. Accordingly, the relaxation time t_R, which characterizes the temporal persistence of order parameter fluctuations, *diverges* upon approaching criticality as

$$t_R = t_{R,0}^{\pm}|\tau|^{-\nu z} \tag{1.8}$$

upon approaching the critical point from $\tau \gtrless 0$, where $\tau = \pm(T - T_c)/T_c$ is the reduced temperature, ν is the bulk critical exponent as above, z is the universal *dynamical critical exponent*, and $t_{R,0}^{\pm}$ are non-universal amplitudes (the amplitude ratio $t_{R,0}^{+}/t_{R,0}^{-}$ is a universal quantity). Thus, close to the critical point, time scales which are much larger than the microscopic ones are important and the dynamics can be effectively described by means of stochastic equations for the spatio-temporal evolution of the order parameter (see, e.g., Refs. [130, 131] for a review). It is convenient to use field-theoretic models which allow for a systematic analysis of the dynamic critical behavior and yield predictions for the scaling behavior of the time-dependent correlation functions [130, 131]. Quantitatively, due to the critical slowing down, the dynamics of a continuous phase transition is determined by "slow" system variables, i.e., quantities which change on a much larger time scale than the microscopic ones. These slow variables — including the order parameter of the system — are related to macroscopic observables. On the other hand, "fast" microscopic variables are usually treated as *noise*, which mimics stochastic forces acting on the slow variables. The description of critical dynamics is formulated in terms of coupled non-linear Langevin equations, which include the noise stemming from the non-critical fast variables, as well as dissipative terms corresponding to relaxation or diffusion, and eventually terms which are reversible in time [130, 131].

As for the static case, *universality* occurs also for the dynamic behavior of the system. The static universality classes described above are subdivided into several dynamic universality classes, which are represented by stochastic models denoted by capital letters introduced in Ref. [130]. The different dynamic universality classes are characterized by the structure of the dynamical equations describing the system [130, 131]. As stated in Ref. [131] for distinguishing the different universality classes one has to consider the following questions:

(1) Is the order parameter a *conserved* physical quantity?

(2) Does the order parameter *couple* to other conserved quantities?
    - If yes, *how* do they couple?

Consequently, several dynamical universality classes appear, and the static universality classes split up into sub-classes corresponding to different physical situations [130, 131]. For example, whereas the static Ising universality class encompasses altogether uniaxial ferromagnets, simple fluids, and binary liquid mixtures, as discussed above, the characteristic dynamical behaviors of these three physical systems belong to different dynamical universality classes.

The *uniaxial ferromagnets* shown in Fig. 1.2 may be described by the simplest dynamical model called *Model A* [138, 139]. Instead of studying the *Glauber dynamics* for the individual spin flips on a lattice, it is convenient to study the corresponding field theory with the suitable dynamical model for the relaxation of the system into its equilibrium state corresponding to the static Hamiltonian of the system. Model A describes the dissipative *(purely) relaxational dynamics* from a non-equilibrium to an equilibrium state [130, 131]. The order parameter in Model A is non-conserved and does not couple to other conserved quantities. The dynamical critical exponent for the static Ising universality class with Model A dynamics is $z \simeq 2.021$ in spatial dimensions $d = 3$ and $z = 2$ in $d = 4$ [131].

For the gas liquid transition of simple fluids (Fig. 1.1) the scalar order parameter, which represents the density difference between the gas and the liquid phase, is conserved [130, 140–143]. Moreover, due to conservation of momentum in an incompressible fluid, the momentum current appears as a secondary conserved vector field in the appropriate dynamical description [130, 140–142]. Whereas the longitudinal component of the momentum density ("sound mode") can be neglected for the critical dynamics, the transverse components of the momentum density are left as independent hydrodynamic slow variables which couple to the order parameter [130, 131, 133]. The dynamical model describing these features is known as *Model H* [130]. The asymptotic universality class of a *binary liquid mixture* (Fig. 1.3) is the same as for a simple fluid [130]. A simplified form of the actual dynamics of fluid mixtures is given by *Model B*, which includes the diffusive dynamics of a conserved order parameter, but not its coupling to other conserved quantities [130, 131]. The dynamical critical exponent for the universality class with Model B dynamics is $z = 4 - \eta$ in all dimensions, where η is a static critical exponent [131]. For the Ising universality class $\eta \simeq 0.036$ in $d = 3$ [62] and $\eta = 0$ in $d = 4$ [57].

Great interest has been paid also to *surface-directed spinodal decomposition*, i.e., the demixing process of a binary liquid mixture "quenched" into the miscibility gap and close to a surface with an adsorption preference for one of the species (see, e.g., Refs. [144–148] and references therein). Thus, regarding questions (1) and (2) on the preceding page for the characterization of the dynamic universality classes, Model A corresponds to the answers (1) "No", (2) "No", and Model B corresponds to the answers (1) "Yes", (2) "No".

In the following, we will mainly consider a space- and time-dependent scalar order parameter $\phi(\mathbf{r},t)$ (static Ising universality class) within the universality classes of Model A dynamics. Then, in general the stochastic Langevin equation for the order parameter is given by [132, 133, 149]

$$\partial_t \phi(\mathbf{r},t) = -\hat{\Omega}\frac{\delta \mathscr{H}[\phi]}{\delta \phi(\mathbf{r},t)} + \zeta(\mathbf{r},t), \tag{1.9}$$

where $\hat{\Omega}$ is the *kinetic coefficient* and $\mathscr{H}$ is the (static) Hamiltonian of the system. The first term on the RHS of Eq. (1.9) corresponds to the deterministic evolution of the order parameter, whereas the second term corresponds to the stochastic nature characterized by ζ which is a so-called *Gaussian white noise* with vanishing average $\langle \zeta(\mathbf{r},t)\rangle = 0$. Moreover, the noise is correlated only over microscopic time and length scales, so that [132, 133]

$$\langle \zeta(\mathbf{r},t)\zeta(\mathbf{r}',t')\rangle = 2k_BT\hat{\Omega}\delta(\mathbf{r}-\mathbf{r}')\delta(t-t'). \tag{1.10}$$

The prefactor in Eq. (1.10) is determined by the Einstein relation [132, 133, 149]. For the study of dynamic critical phenomena the Hamiltonian is given by Eq. (1.6), so that, in the absence of noise, the time-dependent Ginzburg-Landau (TDGL) model [Eq. (1.9)] relaxes back to a state which minimizes $\mathscr{H}$ [132]. The kinetic coefficient $\hat{\Omega}$ depends on the character of the dynamics of the system; for Model A dynamics $\hat{\Omega} = \Omega$ is simply a constant relaxation rate, whereas for Model B dynamics $\hat{\Omega} = D\nabla^2$ with the diffusion constant D [132, 133].

In order to obtain averaged expressions for macroscopic observables, such as correlation and response functions, one has to solve the (non-linear) Langevin equation given in Eq. (1.9) and average over the noise. The *response functional formalism* provides an equivalent alternative representation from which one can directly obtain observable quantities from a dynamical functional [128, 130–133, 150–155]. For the Langevin equation in Eq. (1.9) the corresponding dynamical functional is given by

$$S[\phi,\tilde{\phi}] = \int \mathrm{d}t \int \mathrm{d}\mathbf{r} \left\{ \tilde{\phi}\partial_t\phi + \hat{\Omega}\tilde{\phi}\frac{\delta \mathscr{H}[\phi]}{\delta \phi} - \tilde{\phi}\hat{\Omega}\tilde{\phi}, \right\} \tag{1.11}$$

where $\tilde{\phi}$ is the auxiliary *response field*, which is conjugate to an external field h (see above). Then, the average of observable $\mathscr{O}$ can be obtained from Eq. (1.11) by standard means when treating e^{-S/k_BT} in a formal sense as a "probability distribution" with the path-integral measure $\mathscr{D}$ [132, 133]:

$$\langle \mathscr{O}\rangle = \int \mathscr{D}[\phi,\tilde{\phi}]\mathscr{O}e^{-S[\phi,\tilde{\phi}]/k_BT}. \tag{1.12}$$

However, S is not real and e^{-S/k_BT} may not be strictly interpreted as a probability distribution [132]. Thus, although S plays the role of a "Hamiltonian" in a formal sense, its "partition function" $\int \mathscr{D}[\phi, \tilde{\phi}]e^{-S[\phi,\tilde{\phi}]/k_BT} = 1$ and therefore the corresponding "free energy" $-k_BT\log(\int \mathscr{D}[\phi, \tilde{\phi}]e^{-S[\phi,\tilde{\phi}]/k_BT})$ always vanishes [133].

The response field formulation provides the basis for straightforward application of the field-theoretic "machinery", like perturbation theory and renormalization group, available from statics [133] and has been widely used for the field-theoretic treatment of critical phenomena [131]. The mean field theory (MFT), corresponding to a "zero loop" perturbation, amounts to taking the averages of the terms in Eq. (1.9), i.e., dropping the noise term [156, 157].

In this work, our aim is to gradually extend previous studies on dynamic critical phenomena. In particular, in Chap. 4 we provide a calculation of the Model A dynamics of the mean field order parameter profile *beyond* the simple film geometry. From an experimental point of view, the critical Casimir force acting on colloidal particles immersed in a critical binary liquid mixture and involving *curved* surfaces is highly relevant [20, 21]. Accordingly, in Sec. 4.2 we theoretically study the dynamic evolution of the order parameter close to spherical and cylindrical particles. Finally, in Sec. 4.3 the current literature concerning the issue of the suitable definition of the dynamic critical Casimir force is briefly addressed.

2. Critical Casimir forces between colloids and patterned substrates

2.1. Introduction

COLLOIDS can be used not only as model systems in soft matter physics but also in applications on the nano- and micrometer scale which take advantage of their interaction with chemically structured solid surfaces. Such systems can be useful in integrated nano-devices provided that one is able to exert active control over these interactions. Critical Casimir forces provide such a tool, because their *strength* and *direction* can be tuned via minute temperature changes and surface treatments of the substrate. Surfaces might be designed as to provide temperature-controlled laterally confining potentials for single colloids, offering novel means of self-assembly processes [37].

Here,[13] we study the normal and lateral critical Casimir forces acting on colloidal particles immersed in (near-) critical binary liquid mixtures close to a substrate with laterally alternating adsorption preferences for the two components of the confined liquid. We provide quantitative predictions for the *universal* features of these effective forces for various substrate patterns, i.e., in excess to regular, nonuniversal background contributions. In particular, we study the critical Casimir effect for a three-dimensional sphere close to a homogeneous substrate [Sec. 2.2], a chemical step [Sec. 2.3], a single chemical lane [Sec. 2.4], and periodic patterns of chemical stripes of alternating adsorption preference [Sec. 2.5] (see Fig. 2.1). For completeness, we also consider a *cylinder* which is aligned with the chemical pattern [Sec. 2.7]. We provide quantitative predictions for the scaling functions of the critical Casimir forces, pursuing a two-pronged approach:

(i) We calculate the force using the full three-dimensional numerical analysis of the appropriate mean-field theory (MFT) as described in Sec. 1.2.4 and Appendix A.1.

(ii) We use the so-called Derjaguin approximation (DA) based on the scaling functions for the critical Casimir force in the film geometry either obtained analytically within MFT [117] or obtained from Monte Carlo simulations [99, 100], which allows us to predict the critical Casimir force in the physically relevant three-dimensional case.

---

[13] This chapter has been published in advance in Refs. [51, 52].

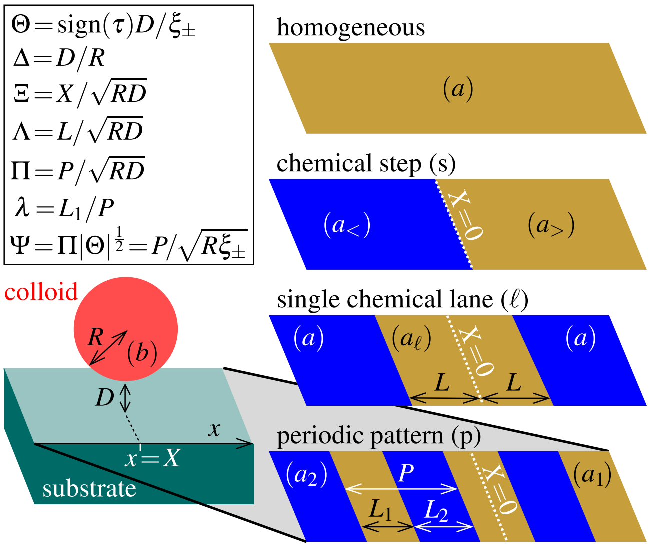

Figure 2.1: Sketch of a spherical colloid immersed in a (near-) critical binary liquid mixture (not shown) and close to a (patterned) planar substrate. The sphere with (b) boundary condition (BC) and radius R is located at a surface-to-surface distance D from the substrate and its center has a lateral coordinate $x = X$ with the substrate pattern being translationally invariant in all other directions. The following four different types of substrate surfaces are considered: homogeneous substrate [Sec. 2.2], a chemical step [s; Sec. 2.3], a single chemical lane [ℓ; Sec. 2.4], and a periodically patterned substrate [p; Sec. 2.5]. (Note that for a four-dimensional system, which we also consider, this is a three-dimensional cut of the system, which is invariant along the fourth direction; the sphere thus corresponds to a hypercylinder in four dimensions.) For later reference, the box on the left side summarizes the definitions of the various scaling variables which the scaling functions of the critical Casimir force depend on for the listed geometrical configurations. On the right, (a), $(a_\gtrless)$, (a_ℓ), (a_1), and (a_2) indicate the boundary conditions corresponding to the various chemical patterns.

Inter alia, we determine the range of validity of the DA within MFT, which provides guidance concerning its applicability in three spatial dimensions $d = 3$. This is an important information because presently available Monte Carlo simulations are far from being able to capture complex geometries [99, 100].

Currently, the possibility of realizing stable levitation of particles by means of the electrodynamic Casimir forces has been the subject of intense theoretical investigation [158–164]. Our results presented in Secs. 2.6 and 2.7 show that for suitable choices of the geometry of the chemical pattern of the substrate, the critical Casimir forces can be used to levitate a colloid above the substrate at a height which can be tuned by temperature. .This levitation is stable against perturbations because it corresponds to a minimum of the potential of the critical Casimir force acting on the colloid.

Section 2.2 is devoted to the well-studied case of a colloid close to a homogeneous substrate. As mentioned above, the various patterns and setups are considered in Secs. 2.3–2.7. Certain important technical details concerning the calculation of the Derjaguin approximation are presented in the Appendices B.1–B.4.

In $d = 4$, as appropriate for MFT, the three-dimensional colloid is extended to the fourth dimension as a hypercylinder, for which we also present the results of our analysis. For this case, the physical properties are invariant along the fourth dimension. Accordingly, the MFT results for the forces and the potentials given below are those per length along this additional direction.

2.2. Homogeneous substrate

We first consider a three-dimensional sphere of radius R with (b) boundary condition (BC) facing a chemically *homogeneous* substrate with (a) BC at a surface-to-surface distance D as shown in Fig. 2.1, denoting this combination by (a,b). The critical Casimir force $F_{(a,b)}(D,R,T)$ *normal* to the substrate surface and the corresponding critical Casimir potential $\Phi_{(a,b)}(D,R,T) = \int_D^\infty \mathrm{d}z\, F_{(a,b)}(z,R,T)$ take the scaling forms [20, 21, 43–45]

$$F_{(a,b)}(D,R,T) = k_B T \frac{R}{D^{d-1}} K_{(a,b)}(\Theta,\Delta) \tag{2.1}$$

and

$$\Phi_{(a,b)}(D,R,T) = k_B T \frac{R}{D^{d-2}} \vartheta_{(a,b)}(\Theta,\Delta), \tag{2.2}$$

where $\Delta = D/R$ and $\Theta = \mathrm{sign}(\tau) D/\xi_\pm$ (for $\tau \gtrless 0$) are the scaling variables corresponding to the distance D in units of the radius R of the colloid and of the correlation length $\xi_\pm$, respectively. The case $d = 4$ corresponds to the MFT solution up to logarithmic corrections, which we shall neglect here. Equations (2.1) and (2.2) describe a force and an energy, respectively, per D^{d-3}, which for $d = 4$ corresponds to considering $F_{(a,b)}$ and $\Phi_{(a,b)}$ per length L_4 of the extra translationally invariant direction of the hypercylinder.

2.2.1. Derjaguin approximation

The Derjaguin approximation (DA) [165] is based on the idea of decomposing the surface of the spherical colloid into infinitely thin circular rings of radius ρ and area $\mathrm{d}S(\rho) = 2\pi\rho\mathrm{d}\rho$ which are parallel to the opposing substrate surface [20, 21, 43]. (Here we do not multiply $2\pi\rho\mathrm{d}\rho$ by the linear extension L_4 of the hypercylinder along its axis in the fourth dimension, because the critical Casimir force is eventually expressed in units of L_4, which therefore drops out from the final expressions.) The distance L of a ring with radius $\rho \le R$ from the substrate is given by

$$L(\rho) = D + R\left(1 - \sqrt{1 - \rho^2/R^2}\right). \tag{2.3}$$

Assuming *additivity* of the forces and neglecting edge effects, the normal critical Casimir forces $\mathrm{d}F(\rho)$ acting on these rings can be expressed in terms of the force acting on parallel plates [Eq. (1.3)]:

$$\frac{\mathrm{d}F(\rho)}{k_B T} = \frac{\mathrm{d}S}{[L(\rho)]^d} k_{(a,b)}(\mathrm{sign}(\tau)\, L(\rho)/\xi_{\pm}). \tag{2.4}$$

Finally, in order to calculate the total force $F_{(a,b)}$ acting on the colloid, one sums up the contributions of the rings, which yields

$$\frac{F_{(a,b)}(D,R,T)}{k_B T} \simeq 2\pi \int_0^R \mathrm{d}\rho \rho \, [L(\rho)]^{-d} \, k_{(a,b)}(\mathrm{sign}(\tau)\, L(\rho)/\xi_{\pm}). \tag{2.5}$$

(For $d = 3$, $F_{(a,b)}$ is the force on a sphere whereas in $d = 4$ it is the force on a hypercylinder per length of its axis.)

One expects the DA to describe the actual behavior accurately if the colloid is very close to the substrate, i.e., for $\Delta = D/R \to 0$. In this limit, Eq. (2.3) can be approximated by $L(\rho) = D\alpha$ where $\alpha = 1 + \rho^2/(2RD)$, so that one finds for the scaling function of the force [21, 43]

$$K_{(a,b)}(\Theta, \Delta \to 0) = 2\pi \int_1^\infty \mathrm{d}\alpha \alpha^{-d} k_{(a,b)}(\alpha\Theta), \tag{2.6}$$

and, accordingly, for the scaling function of the potential [20, 21]

$$\vartheta_{(a,b)}(\Theta, \Delta \to 0) = 2\pi \int_1^\infty \mathrm{d}\beta \left(\frac{1}{\beta^{d-1}} - \frac{1}{\beta^d} \right) k_{(a,b)}(\beta\Theta). \tag{2.7}$$

At the bulk critical point, using Eq. (1.4), one finds the well known values $K_{(a,b)}(0,0) = 2\pi\Delta_{(a,b)}/(d-1)$ and $\vartheta_{(a,b)}(0,0) = 2\pi\Delta_{(a,b)}/[(d-2)(d-1)]$. We note that the DA implies that the dependence of $F_{(a,b)}$ and $\Phi_{(a,b)}$ on the size R of the sphere reduces to the proportionality $\propto R$ indicated explicitly in Eqs. (2.1) and (2.2).

Before proceeding further one first has to assess the accuracy of the DA, which will carried out below within MFT ($d = 4$). We expect the range of validity of the DA to be similar for $d = 3$, so that within that range one can use the DA based on scaling functions for the film geometry obtained from Monte Carlo simulations[14] in order to calculate the critical Casimir force acting on a colloid in $d = 3$.

---

[14] For the scaling function in $d = 3$ of the critical Casimir force acting on two parallel planar walls with $(\pm)$ BC, we use the approximation denoted by (i) in Figs. 9 and 10 of Ref. [100]. The uncertainty of the overall amplitude of the scaling functions is about 10% to 20% as indicated by the different results obtained by the various approximations used in Ref. [100]. Correspondingly, this uncertainty affects our predictions for the scaling functions based on such Monte Carlo simulation data. However, the normalized scaling functions are affected less leading to an uncertainty of at most 3%.

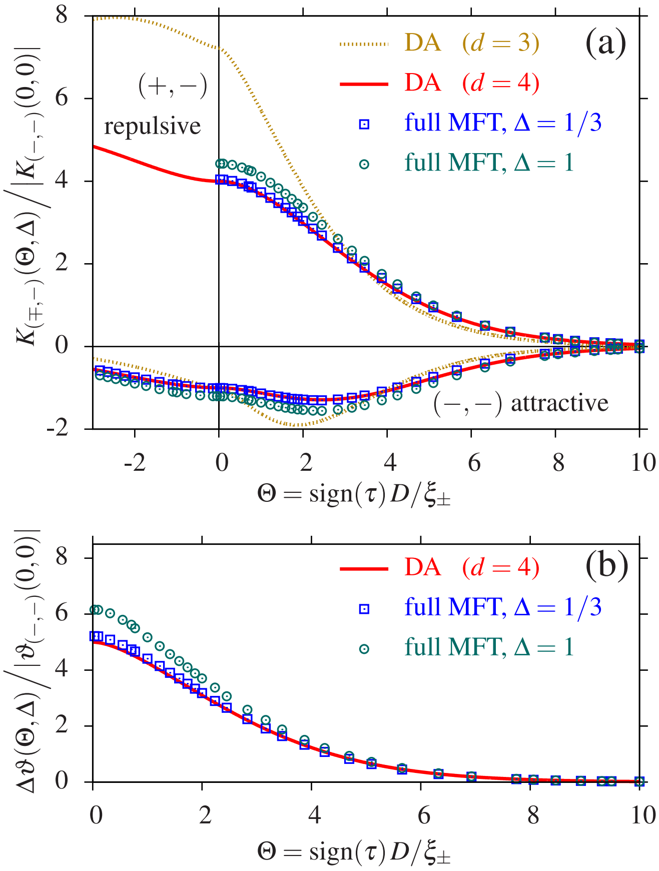

Figure 2.2: (a) Scaling functions $K_{(\mp,-)}$ for the normal critical Casimir force [Eq. (2.1)] acting on a three-dimensional sphere with $(b) = (-)$ BC close to a homogeneous substrate with $(a) = (\mp)$ BC [Fig. 2.1]. The suitably normalized scaling functions $K_{(\mp,-)}$ are shown as a function of the scaling variable $\Theta = \mathrm{sign}(\tau)D/\xi_{\pm}$ for $\tau \gtrless 0$, where τ is the reduced deviation from the critical temperature and $K_{(-,-)}(0,0)$ is the value of the critical Casimir force scaling function within the DA at $T = T_c$ for $(-,-)$ BC. The solid lines correspond to the Derjaguin approximation (DA, $\Delta = D/R \to 0$) within mean-field theory (MFT, $d = 4$) whereas the dotted lines correspond to the DA obtained by using Monte Carlo (MC) results for films in $d = 3$ the systematic uncertainties of which are not indicated (see footnote 14). The normalization implies that at $\Theta = 0$ both the solid and dotted lines pass through -1 for $(-,-)$ BC whereas the solid line passes through 4 for $(+,-)$ BC. The symbols correspond to the full numerical MFT results obtained for $\Delta = 1/3$ and $\Delta = 1$, the size of which indicates the estimated numerical error. (For $(+,-)$ BC and $\tau < 0$ we have not been able to calculate the corresponding scaling functions with adequate precision due to severe numerical difficulties in obtaining the full three-dimensional order parameter profile in the presence of two "competing" bulk values.) Since within the DA the dependence of $K_{(\mp,-)}$ on Δ drops out, the difference between the symbols $\boxdot$ and $\odot$ and the solid lines measures the accuracy of the DA in $d = 4$. (b) Difference $\Delta\vartheta = \vartheta_{(+,-)} - \vartheta_{(-,-)}$ of the scaling functions for the Casimir potentials [Eq. (2.2)] for $(+,-)$ and $(-,-)$ BC, suitably normalized by $\vartheta_{(-,-)}(0,0)$. The solid line corresponds to the DA within MFT and the symbols correspond to the full MFT results for $\Delta = 1/3$ and $\Delta = 1$; the dotted line is the DA for $d = 3$. Due to the normalization the solid line reaches 5 for $\Theta = 0$.

2.2.2. Scaling functions for the normal critical Casimir force and the potential

The expressions obtained above within the DA hold for general boundary conditions (a) and (b) and are valid beyond the cases we consider in the following, i.e., $a \in \{+,-\}$ and $b = -$. Figure 2.2(a) shows the full numerical MFT ($d = 4$) results for the scaling functions $K_{(\pm,-)}$ with $\Delta = 1$ and $1/3$ compared with the corresponding DA results based on the suitable numerical integration [Eq. (2.6)] of the analytic (MFT) expression for $k_{(\pm,-)}$ [117]. Moreover, in Fig. 2.2, the corresponding DA results for $d = 3$ are shown; they are obtained from the film scaling functions determined by MC simulations (see footnote 14 on page 40) and by using the corresponding ratio of the correlation lengths above and below T_c [62]. In Fig. 2.2(b) we report the difference $\Delta\vartheta(\Theta,\Delta) \equiv \vartheta_{(+,-)}(\Theta,\Delta) - \vartheta_{(-,-)}(\Theta,\Delta)$ computed for the various cases reported in Fig. 2.2(a), which will be useful for describing the case of a chemically patterned substrate. The scaling functions in $d = 4$ are reasonably well reproduced by the DA for $\Delta \lesssim 0.4$ and we expect this to hold for $d = 3$ as well. The fact that for increasing values of Δ the magnitude of the actual scaling functions becomes larger compared with those within the DA (corresponding to $\Delta \to 0$) is in agreement with earlier results obtained for a d-dimensional hypersphere (see, e.g., Ref. [43]).

It has been shown that the scaling functions obtained within the DA for $d = 3$ agree very well — within the experimental accuracy — with the ones obtained from direct measurements of the critical Casimir potential [20, 21] corresponding to $\Delta \lesssim 0.35$ (see also Ref. [48] in Ref. [100]).

2.3. Chemical step (s)

The basic building block of a chemically patterned substrate of the type we consider here, i.e., with translational invariance in all directions but one (x), is a chemical step (s) realized by a substrate with $(a_{\gtrless})$ BC for $x \gtrless 0$ at its surface. In this section we analyze the critical Casimir force if such a substrate is approached by a colloid with (b) BC with its center located at the lateral position $x = X$ (see Fig. 2.1 and Ref. [37] for experimental realizations). We denote this configuration by $(a_<|a_>,b)$. The normal critical Casimir force F_s is described by the scaling form

$$F_\mathrm{s}(X,D,R,T) = k_B T \frac{R}{D^{d-1}} K_\mathrm{s}(\Xi,\Theta,\Delta), \tag{2.8}$$

where $\Xi = X/\sqrt{RD}$ is the scaling variable corresponding to the lateral position of the colloid. It is useful to write the scaling function K_s as

$$K_\mathrm{s}(\Xi,\Theta,\Delta) = \frac{K_{(a_<,b)} + K_{(a_>,b)}}{2} + \frac{K_{(a_<,b)} - K_{(a_>,b)}}{2} \psi_{(a_<|a_>,b)}(\Xi,\Theta,\Delta), \tag{2.9}$$

where the scaling functions of the laterally homogeneous substrates $K_{(a_{\gtrless},b)}$ depend on Θ and Δ only [Eq. (2.1)], and the scaling function $\psi_{(a_<|a_>,b)}$ varies from $+1$ at $\Xi \to -\infty$ to -1 at $\Xi \to +\infty$, such that the laterally homogeneous cases are recovered far from the step. Accordingly, the corresponding critical Casimir potential $\Phi_{\mathrm{s}}(X,D,R,T) = \int_D^\infty \mathrm{d}z\, F_{\mathrm{s}}(X,z,R,T)$ can be cast in the form

$$\Phi_{\mathrm{s}}(X,D,R,T) = k_B T \frac{R}{D^{d-2}} \vartheta_{\mathrm{s}}(\Xi,\Theta,\Delta), \tag{2.10}$$

and

$$\vartheta_{\mathrm{s}}(\Xi,\Theta,\Delta) = \frac{\vartheta_{(a_<,b)} + \vartheta_{(a_>,b)}}{2} + \frac{\vartheta_{(a_<,b)} - \vartheta_{(a_>,b)}}{2} \omega_{(a_<|a_>,b)}(\Xi,\Theta,\Delta), \tag{2.11}$$

where $\vartheta_{(a_{\gtrless},b)}$ depend on Θ and Δ only [Eq. (2.2)], and $\omega_{(a_<|a_>,b)}(\Xi = \pm\infty,\Theta,\Delta) = \mp 1$. Note that the scaling functions $\psi_{(a_<|a_>,b)}$ and $\omega_{(a_<|a_>,b)}$ are independent of the common prefactor $\propto u^{-1}$ [see Sec. 1.2.4], which is left undetermined by the analytical and numerical mean-field calculation of K_{s} and ϑ_{s}.

2.3.1. Derjaguin approximation

If the sphere is close to the substrate, i.e., $\Delta \to 0$, the DA can be applied, and one finds for the scaling function of the critical Casimir force [see Appendix B.1]

$$\psi_{(a_<|a_>,b)}(\Xi \gtrless 0,\Theta,\Delta \to 0) = \mp 1 \pm \frac{4\int_{1+\Xi^2/2}^{\infty} \mathrm{d}\alpha\, \alpha^{-d} \arccos\left(|\Xi|(2\alpha-2)^{-1/2}\right) \Delta k(\alpha\Theta)}{K_{(a_<,b)}(\Theta,\Delta\to 0) - K_{(a_>,b)}(\Theta,\Delta\to 0)}, \tag{2.12}$$

where $\Delta k(\Theta) = k_{(a_<,b)}(\Theta) - k_{(a_>,b)}(\Theta)$ is the difference between the scaling functions for the critical Casimir forces acting on two planar walls with $(a_<,b)$ and with $(a_>,b)$ boundary conditions, respectively. We note that according to Eqs. (2.12) and (2.6) within the DA $\psi_{(a_<|a_>,b)}$ can be determined from the knowledge of the film scaling functions $k_{(a,b)}(\Theta)$ [Eq. (1.3)] only. Due to the assumption of additivity which underlies the DA, (i) $\psi_{(a_<|a_>,b)}$ vanishes at $\Xi = 0$ for all Θ and it is an antisymmetric function of Ξ and (ii) $\psi_{(a_<|a_>,b)} = \psi_{(a_>|a_<,b)}$; within the DA both of these properties are valid irrespective of the type of boundary conditions on both sides of the chemical step. (However, the actual scaling function $\psi_{(a_<|a_>,b)}$ as, e.g., obtained from full numerical MFT calculations may violate this symmetry because the actual critical Casimir forces are non-additive.) At the bulk critical point one has $\Theta = 0$ so that [see Appendix B.1],

$$\psi_{(a_<|a_>,b)}(\Xi,\Theta=0,\Delta\to 0) = \Xi^{2d-7}\left(\tfrac{15}{2}(3-d) + (3-2d)\Xi^2 - \Xi^4\right)\left(2+\Xi^2\right)^{-(d-\frac{3}{2})} \tag{2.13}$$

independent of $k_{(a_{\gtrless},b)}$. Similarly, within the DA one finds for the scaling function ω of the critical Casimir potential [see Appendix B.1]

$$\omega_{(a_<|a_>,b)}(\Xi \gtrless 0,\Theta,\Delta\to 0) = \mp 1 \pm \frac{\Xi^4 \int_1^\infty \mathrm{d}s \frac{s\arccos\left(s^{-1/2}\right) - \sqrt{s-1}}{(1+\Xi^2 s/2)^d} \Delta k\left(\Theta[1+\Xi^2 s/2]\right)}{\vartheta_{(a_<,b)}(\Theta,\Delta\to 0) - \vartheta_{(a_>,b)}(\Theta,\Delta\to 0)}. \tag{2.14}$$

This yields $\omega_{(a_<|a_>,b)}(\Xi = 0,\Theta,\Delta\to 0) = 0$, as expected from the underlying assumption of additivity; within full MFT this only holds in the limit $\Delta \to 0$. At the critical point we find [see Appendix B.1]

$$\omega_{(a_<|a_>,b)}(\Xi,\Theta=0,\Delta\to 0) = \Xi\left(1-d-\Xi^2\right)\left(\Xi^2+2\right)^{-3/2}. \tag{2.15}$$

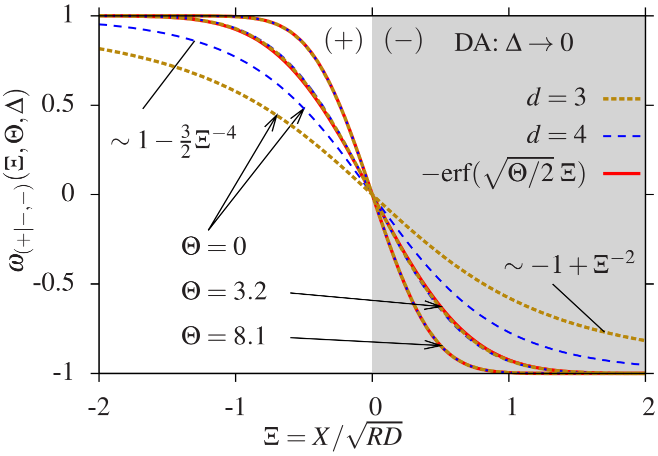

Figure 2.3: Scaling function $\omega_{(+|-,-)}$ [Eq. (2.11)] within DA (i.e., $\Delta \to 0$) for the critical Casimir potential of a sphere $(-)$ facing a chemical step $(+|-)$. The dotted and dashed lines refer to $d=3$ and $d=4$ (MFT), respectively. At bulk criticality ($\Theta=0$), $\omega_{(+|-,-)}$ is given by Eq. (2.15), whereas for $\Theta \neq 0$ it is calculated on the basis of the scaling functions for the film geometry [see the main text]. For $\Theta \gtrsim 3$, $\omega_{(+|-,-)}$ becomes practically independent of d and coincides with the expression for $\Theta \gg 1$ [Eq. (2.16), solid lines, barely distinguishable from the corresponding dashed and dotted ones].

Note that Eqs. (2.12) — (2.15) are valid beyond the symmetry breaking BC we consider in the following, i.e., $a_{\gtrless} \in \{+,-\}$ and $b=-$. For $(\mp,-)$ BC the critical Casimir force $f_{(\mp,-)}(D,T)$ between two planar walls decays $\propto \exp(-\Theta)$ for $\Theta \gg 1$ [29, 117, 118] (see also footnote 11 on page 30), which leads to a *d-independent* result for the scaling functions $\psi_{(+|-,-)}$ and $\omega_{(+|-,-)}$ [see Appendix B.1]:

$$\psi_{(+|-,-)}(\Xi,\Theta \gg 1,\Delta \to 0) = \omega_{(+|-,-)}(\Xi,\Theta \gg 1,\Delta \to 0) = -\,\mathrm{erf}\left(\sqrt{\Theta/2}\,\Xi\right), \qquad (2.16)$$

where erf is the error function.

In Fig. 2.3 we compare the behavior of $\omega_{(+|-,-)}$ calculated within the DA in $d=4$ and 3; the required scaling functions $k_{(\pm,-)}$ for the film geometry are obtained analytically in $d=4$ within MFT [117] and in $d=3$ from Monte Carlo simulation data [99, 100]. The systematic uncertainty of the latter does not affect significantly (at most by 3%) the estimate of $\omega_{(+|-,-)}$ shown in Fig. 2.3. For $\Theta \to 0$ the Casimir potential for $d=3$ as a function of the lateral coordinate varies more smoothly than the corresponding MFT function [see Eq. (2.15)]. However, for $\Theta \gtrsim 3$ the scaling functions $\omega_{(+|-,-)}$ for $d=3$ and $d=4$ (MFT) practically coincide with Eq. (2.16) valid for $\Theta \gg 1$.

Figure 2.4(a) compares the scaling function $\omega_{(a_<|a_>,b)}$ for the critical Casimir potential of a sphere with $(-)$ BC in front of a $(+|-)$ step, as obtained within the DA for $d=4$ [Eq. (2.14)], with the one obtained numerically within full MFT for $\Delta = 1/3$. For $\Delta \lesssim 1/3$ the DA captures the scaling function very well, in particular for $\Theta \gtrsim 3$.

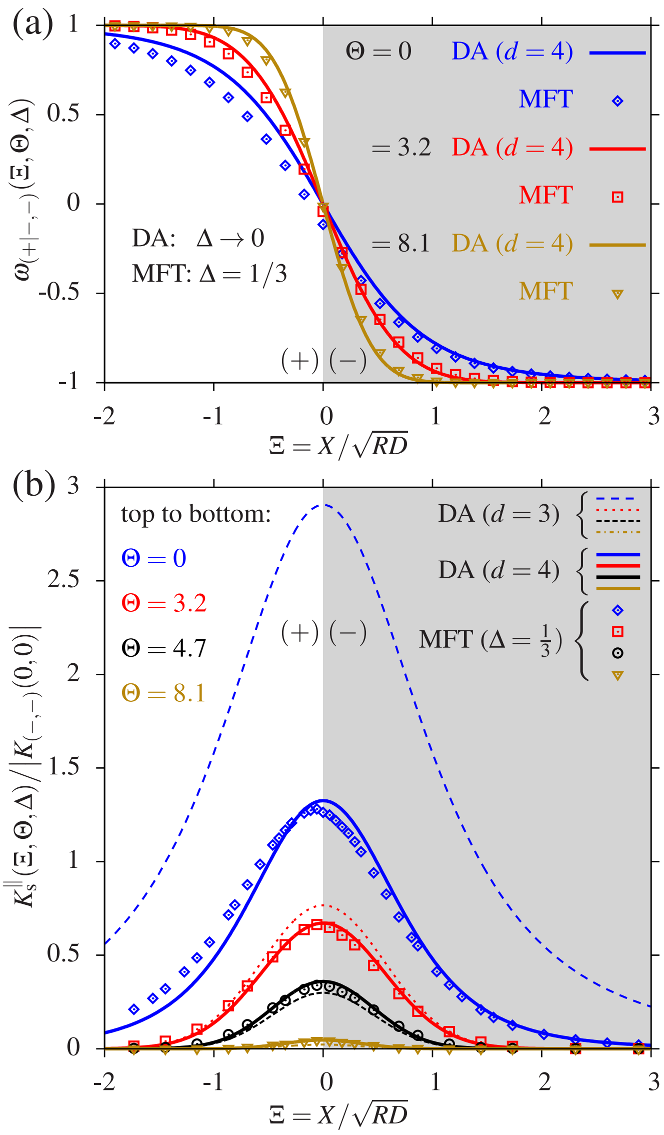

Figure 2.4: (a) Scaling function $\omega_{(+|-,-)}$ [Eq. (2.11)] for the critical Casimir potential of a spherical colloid with $(-)$ BC across a chemical step $(+|-)$ as a function of $\Xi \equiv X/\sqrt{RD}$ for various (positive) values of $\Theta = D/\xi_+$. Within the DA $\omega_{(+|-,-)}$ is an antisymmetric function of Ξ [Eq. (2.14)] whereas within full MFT this antisymmetry is slightly violated, in particular for small Θ. (b) Corresponding scaling function $K_s^{\parallel}$ [Eq. (2.17)] of the *lateral* critical Casimir force, normalized by the amplitude $K_{(-,-)}(0,0) = 2\pi\Delta_{(-,-)}/(d-1)$ of the normal critical Casimir force at $T = T_c$ acting on a colloid with $(-)$ BC close to a homogeneous substrate with $(-)$ BC within the DA [Sec. 2.2.1]. For both (a) and (b) the full numerical MFT results obtained for $\Delta = 1/3$ are shown as symbols (the symbol size represents the estimated numerical error) whereas the lines show the corresponding results obtained within the DA (i.e., $\Delta \to 0$); the dotted lines refer to $d = 3$ and are obtained by using Monte Carlo simulation data (see footnote 14 on page 40) and the solid lines refer to $d = 4$. The lines for $\Theta = 0$ are obtained by using Eq. (2.15) and Eq. (2.19), respectively; for $\Theta = 3.2, 4.7, 8.1$ the DA lines de facto coincide with the asymptotic results obtained for symmetry breaking BC and $\Theta \gg 1$ [Eq. (2.16) and Eq. (2.20), respectively] and thus are indeed independent of d. The DA ($d = 4$) provides a good approximation for the full numerical MFT data, in particular for $\Theta \gtrsim 3$. $K_s^{\parallel} > 0$ implies that the colloid moves to the right where it enjoys an attractive potential versus a repulsive one for $\Xi < 0$. Within the DA $K_s^{\parallel}$ is a symmetric function of Ξ [Eqs. (2.14) and (2.18)] whereas within full MFT this symmetry is slightly violated, in particular for small Θ.

2.3.2. Lateral critical Casimir force

The *lateral* critical Casimir force is given by $F_s^{\|} = -\partial_X \Phi_s$ and can be cast in the scaling form

$$F_s^{\|}(X,D,R,T) = k_B T \frac{R}{D^{d-1}} \left(\frac{D}{R}\right)^{1/2} K_s^{\|}(\Xi,\Theta,\Delta), \tag{2.17}$$

where $K_s^{\|}$ is a universal scaling function. $F_s^{\|}$ and $K_s^{\|}$ vanish far from the chemical step, i.e., for $|\Xi| \to \infty$. In Eq. (2.17) the prefactors in terms of R and D and their exponents are chosen such that $K_s^{\|}$ is regular and non-vanishing for $\Delta \to 0$. We note that the same holds for the normal critical Casimir forces and the corresponding potentials [see Eqs. (2.1), (2.2), (2.8), (2.10), and the considerations following below].

Within the DA $K_s^{\|}$ can be calculated from Eqs. (2.11) and (2.14):

$$K_s^{\|}(\Xi,\Theta,\Delta\to 0) = -\frac{1}{2}\left[\vartheta_{(a_<,b)}(\Theta,\Delta\to 0) - \vartheta_{(a_>,b)}(\Theta,\Delta\to 0)\right] \partial_\Xi \omega_{(a_<|a_>,b)}(\Xi,\Theta,\Delta\to 0). \tag{2.18}$$

At bulk criticality $\Theta = 0$ one finds with Eq. (2.15) [see Eq. (2.12)]

$$K_s^{\|}(\Xi,\Theta=0,\Delta\to 0) = \pi\Delta k(0)\left(2+\Xi^2\right)^{-(d-\frac{3}{2})}. \tag{2.19}$$

For $(\mp,-)$ BC and $\Theta \gg 1$ Eqs. (2.10), (2.11), and (2.16) lead to

$$K_s^{\|}(\Xi,\Theta\gg 1,\Delta\to 0) = \left[\vartheta_{(+,-)}(\Theta,\Delta) - \vartheta_{(-,-)}(\Theta,\Delta)\right]\sqrt{\frac{\Theta}{2\pi}}\exp\left\{-\frac{\Theta\Xi^2}{2}\right\}, \tag{2.20}$$

for *both* $d = 3$ and $d = 4$. [The prefactor $\Delta\vartheta(\Theta,\Delta) = \vartheta_{(+,-)}(\Theta,\Delta) - \vartheta_{(-,-)}(\Theta,\Delta)$ in Eq. (2.20) is shown in Fig. 2.2(b).]

Figure 2.4(b) shows the comparison between the normalized lateral critical Casimir force obtained within the DA (solid lines) and the full MFT data obtained for $\Delta = 1/3$ (symbols). We infer that not only the shape of $K_s^{\|}$ as a function of Ξ but also its *amplitude* is described well by the DA [Eqs. (2.19) and (2.20)] for $\Delta \lesssim 1/3$, and in particular for $\Theta \gtrsim 3$. We expect this feature to hold in $d = 3$, too, as well as for the normal critical Casimir force and the critical Casimir potential. The lateral critical Casimir forces for $d = 3$ obtained within the DA on the basis of Monte Carlo simulation data for the film geometry (see footnote 14 on page 40) are shown in Fig. 2.4(b) as dashed lines. Compared with the previous curves, these ones have similar shapes but their overall amplitudes in units of the normal critical Casimir force at $\Theta = 0$ are significantly different for $\Theta = 0$ and $\Theta = 3.2$. This difference reflects the analogous one observed in the normalized difference between the corresponding critical Casimir potentials for $(+,-)$ and $(-,-)$ BC, reported in Fig. 2.2(b).

2.4. Single chemical lane (ℓ)

In this section we consider the case of a colloid with (b) BC close to a substrate with a single chemical lane (ℓ) with (a_ℓ) BC and width $2L$ in the lateral x direction and which is invariant along the other lateral direction(s). The remaining parts of the substrate are two semi-infinite planes at $|x| > L$ with (a) BC [see Fig. 2.1]. The lateral coordinate X of the center of mass of the sphere along the x direction is chosen to vanish in the center of the chemical lane. One expects that for "broad" lanes a description in terms of two subsequent chemical steps is appropriate [Sec. 2.3], whereas for "narrow" lanes the effects of the two subsequent chemical steps interfere. We find that in addition to the variables characterizing the chemical step [Eq. (2.8)], a further scaling variable $\Lambda = L/\sqrt{RD}$ emerges naturally, which corresponds to the width of the lane. Accordingly, the normal critical Casimir force F_ℓ acting on the colloid can be cast in the form

$$F_\ell(L,X,D,R,T) = k_B T \frac{R}{D^{d-1}} K_\ell\,(\Lambda,\Xi,\Theta,\Delta)\,, \tag{2.21}$$

where K_ℓ is the corresponding universal scaling function. The critical Casimir potential scales as

$$\Phi_\ell(L,X,D,R,T) = k_B T \frac{R}{D^{d-2}} \vartheta_\ell\,(\Lambda,\Xi,\Theta,\Delta)\,, \tag{2.22}$$

with ϑ_ℓ as the universal scaling function for the potential of a sphere close to a single chemical lane. Analogously to Eqs. (2.9) and (2.11) we define ψ_ℓ and ω_ℓ according to

$$K_\ell(\Lambda,\Xi,\Theta,\Delta) = \frac{K_{(a,b)} + K_{(a_\ell,b)}}{2} + \frac{K_{(a,b)} - K_{(a_\ell,b)}}{2} \psi_\ell(\Lambda,\Xi,\Theta,\Delta), \tag{2.23}$$

and

$$\vartheta_\ell(\Lambda,\Xi,\Theta,\Delta) = \frac{\vartheta_{(a,b)} + \vartheta_{(a_\ell,b)}}{2} + \frac{\vartheta_{(a,b)} - \vartheta_{(a_\ell,b)}}{2} \omega_\ell(\Lambda,\Xi,\Theta,\Delta), \tag{2.24}$$

so that far from the lane $\psi_\ell\,(\Lambda, |\Xi| \gg \Lambda, \Theta, \Delta) = \omega_\ell\,(\Lambda, |\Xi| \gg \Lambda, \Theta, \Delta) = 1$. On the other hand, only for a "broad" lane the scaling functions at the center of the chemical lane approach their limiting value $\psi_\ell\,(\Lambda \to \infty, \Xi = 0, \Theta, \Delta) = -1 = \omega_\ell\,(\Lambda \to \infty, \Xi = 0, \Theta, \Delta)$, corresponding to the homogeneous case with (a_ℓ, b) BC.

2.4.1. Derjaguin approximation

Using the underlying assumption of additivity of the forces, within the DA ($\Delta \to 0$) we find for the scaling functions of the critical Casimir force and of the critical Casimir potential [see Appendix B.2]

$$\psi_\ell(\Lambda,\Xi,\Theta,\Delta \to 0) = 1 + \psi_{(a_\ell|a,b)}(\Xi+\Lambda,\Theta,\Delta \to 0) - \psi_{(a_\ell|a,b)}(\Xi-\Lambda,\Theta,\Delta \to 0) \tag{2.25}$$

and

$$\omega_\ell(\Lambda,\Xi,\Theta,\Delta \to 0) = 1 + \omega_{(a_\ell|a,b)}(\Xi+\Lambda,\Theta,\Delta \to 0) - \omega_{(a_\ell|a,b)}(\Xi-\Lambda,\Theta,\Delta \to 0), \tag{2.26}$$

respectively. Thus, within the DA, from the knowledge of the scaling functions $\psi_{(a_\ell|a,b)}$ [Eq. (2.12)] and $\omega_{(a_\ell|a,b)}$ [Eq. (2.14)] for the chemical step with the appropriate BC, one can directly calculate the corresponding scaling functions for the chemical lane configuration. Accordingly, in the limit $\Delta \to 0$ and for symmetry breaking BC, ψ_ℓ and ω_ℓ can be analytically calculated on the basis of Eqs. (2.25) and (2.26) by taking advantage of Eqs. (2.13), (2.15), and (2.16).

2.4.2. Scaling function for the critical Casimir potential

In Fig. 2.5(a) we show the scaling function ω_ℓ for the critical Casimir potential obtained within the DA for $d = 3$ and $d = 4$ (MFT) at the bulk critical point $T = T_c$ [Eqs. (2.26) and (2.15)] for various values of $\Lambda = L/\sqrt{RD}$ as a function of the lateral coordinate of the colloid. One can infer from Fig. 2.5 that, at bulk criticality, the critical Casimir potential varies less pronounced in $d = 3$ than in $d = 4$. As expected, for small values of Λ (i.e., "narrow" chemical lanes), the potential does not reach the limiting homogeneous value -1 in the center of the chemical lane. On the other hand for large values of the scaling variable Λ (i.e., "broad" chemical lanes), ω_ℓ does attain the value -1 in the center of the chemical lane and the critical Casimir potential flattens. In this case the potential is adequately described by two independent chemical steps. However, the criterion for being a sufficiently "broad" lane depends sensitively on Θ and d. Indeed, from Eqs. (2.26) and (2.15) we find that at criticality ($\Theta = 0$) the critical Casimir potential at the center of the chemical lane ($\Xi = 0$) reaches the limiting value corresponding to the colloid facing a homogeneous substrate by up to 1% for $\Lambda \gtrsim 3.3$ in $d = 4$ and for $\Lambda \gtrsim 10$ in $d = 3$. We note that the curves in Fig. 2.5(a) as well as these bounds are *independent* of the actual boundary conditions because for all kinds of BC the scaling function of the normal critical Casimir force is constant at the critical point [see Eq. (1.4)].

Below we shall discuss some properties which are specific for BC with $a, a_\ell, b \in \{+,-\}$, which exhibit the feature that the normal critical Casimir force $f_{(\mp,-)}$ acting on two planar walls decays *purely* exponentially [see the text preceding Eq. (1.5)] as a function of their distance expressed in units of the bulk correlation length [see Eqs. (1.3) and (1.5)]. In Fig. 2.5(b) the scaling functions ω_ℓ in $d = 3$ and $d = 4$ obtained from Monte Carlo simulation data (see footnote 14 on page 40) and analytic MFT results [117], respectively, within the DA [see Eqs. (2.26) and (2.16)] are shown for the same values of Λ as in Fig. 2.5(a) but off criticality. For $\Theta = 7.7$ the curves for $d = 3$ and $d = 4$ are indistinguishable from each other and from their common asymptotic expression given in Eq. (2.16). For $\Theta \gg 1$, the critical Casimir potential attains its limiting homogeneous value in the center of the lane for values of Λ which are smaller than the ones for $\Theta = 0$ due to the shorter range of the forces. That is, for both $d = 3$ and $d = 4$ the single chemical lane is almost equally well approximated by two independent chemical steps for $\Lambda \gtrsim 1.5$ at $\Theta = 3.3$ (data not shown) and for $\Lambda \gtrsim 1.0$ at $\Theta = 7.7$ [Fig. 2.5(b)].

In Fig. 2.6 we compare the MFT ω_ℓ obtained within the DA ($\Delta \to 0$) at $\Theta = 0$ [Eqs. (2.26) and (2.15)] with the scaling function obtained from the full numerical MFT calculations for $\Delta = 1/3$. We find a rather good agreement even for small values of Λ (i.e., "narrow" chemical lanes). This shows that for the geometry of a colloid close to a single chemical lane, nonlinearities, which are actually present in the critical Casimir effect and potentially invalidate the assumption of additivity underlying the DA, do not affect the resulting potential for small values of Δ. We expect this property to hold beyond MFT in $d = 3$ as well, in particular off criticality, i.e., for $\Theta \neq 0$.

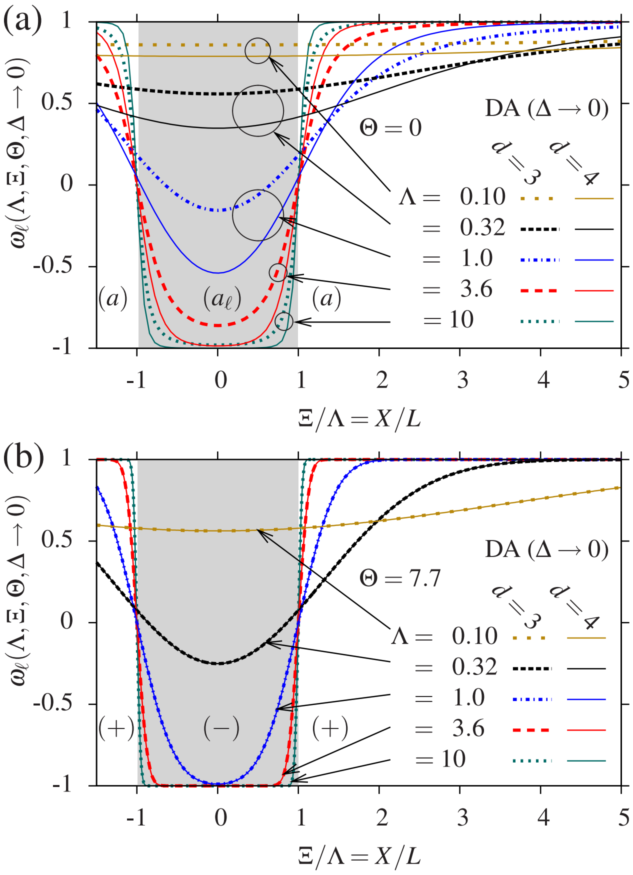

Figure 2.5: Scaling function ω_ℓ [Eq. (2.24)] describing the lateral variation of the critical Casimir potential of a colloid across a single chemical lane of width $2L$ as a function of the lateral position X of the colloid in units of the half width of the lane [see Fig. 2.1; $\Xi = X/\sqrt{RD}$, $\Lambda = L/\sqrt{RD}$, $\Theta = D/\xi_+$]. Here, ω_ℓ has been obtained within the DA ($\Delta \to 0$) in $d=3$ and 4 [Eq. (2.26)]. In (a) the curves correspond to $\Theta = 0$ [Eq. (2.15)], whereas in (b) they correspond to $\Theta = 7.7$ and $a, a_\ell, b \in \{+,-\}$ BC [Fig. 2.1]. For $\Theta \gg 1$ [(b)] the corresponding scaling functions obtained from Monte Carlo simulation data (see footnote 14 on page 40) in $d=3$ and from analytic MFT results [117] in $d=4$ de facto coincide and their asymptotic expressions are given by Eqs. (2.16) and (2.26). $\omega_\ell = 1$ corresponds to the laterally homogeneous critical Casimir potential for (a,b) BC outside the chemical lane, whereas $\omega_\ell = -1$ corresponds to the value of the critical Casimir potential for the homogeneous case with (a_ℓ, b) BC as within the chemical lane. For large values of Λ the critical Casimir potential is the same as for two independent chemical steps, and ω_ℓ reaches its limiting value -1 in the center of the lane at $\Xi = 0$ [see the main text]. In (b), for $\Theta \gg 1$, ω_ℓ attains -1 in the center of the chemical lane already for smaller values of Λ due to the exponential decay of the critical Casimir force. We note that the DA results for $\Theta = 0$ (i.e., at the critical point) are independent of the actual boundary conditions which, accordingly, were not specified in (a).

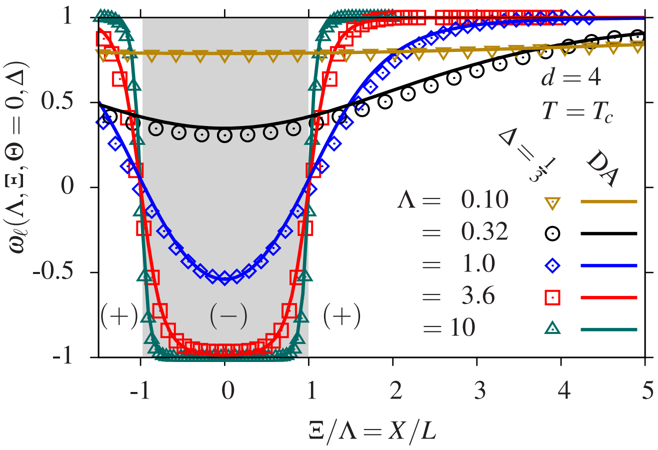

Figure 2.6: Test of the performance of the DA for the scaling function ω_ℓ [Eq. (2.24)] of the critical Casimir potential for a sphere with $(-)$ BC close to a single chemical lane with $(-)$ BC embedded in a substrate with $(+)$ BC. The MFT ω_ℓ is evaluated at bulk criticality $\Theta=0$ in $d=4$ both on the basis of the DA (lines, $\Delta\to 0$) and of the full numerical MFT (symbols, $\Delta = 1/3$). There is good agreement between the DA and the full MFT results, even for small values of $\Lambda = L/\sqrt{RD}$. Nonlinear effects, which are inherently present in the theory, do not strongly affect the potential. For $\Delta \to 0$ the assumption of additivity of the critical Casimir forces underlying the DA is reliable even for small Λ.

2.5. Periodic chemical patterns (p)

In this section we consider a pattern of chemical stripes which are alternating *periodically* along the x direction. The pattern consists of stripes of width L_1 with (a_1) BC joined with stripes of width L_2 with (a_2) BC, such that the periodicity is given by $P = L_1 + L_2$. Thus, the geometry of the substrate pattern is characterized by the two variables L_1 and P [see Fig. 2.1]. The coordinate system is chosen such that the lateral coordinate X of the center of the sphere is zero at the center of a (a_1) stripe. The normal critical Casimir force F_p acting on the colloidal particle and its corresponding potential Φ_p take on the following scaling forms:

$$F_\mathrm{p}(L_1,P,X,D,R,T) = k_BT\frac{R}{D^{d-1}}K_\mathrm{p}(\lambda,\Pi,\Xi,\Theta,\Delta) \tag{2.27}$$

and

$$\Phi_\mathrm{p}(L_1,P,X,D,R,T) = k_BT\frac{R}{D^{d-2}}\vartheta_\mathrm{p}(\lambda,\Pi,\Xi,\Theta,\Delta), \tag{2.28}$$

where $\Pi = P/\sqrt{RD}$ is the scaling variable characterizing the periodicity of the pattern and $\lambda = L_1/P$ is the scaling variable chosen to correspond to the relative width of the stripe with (a_1) BC. K_p and ϑ_p are universal scaling functions for the normal critical Casimir force and the critical Casimir potential, respectively. For $\lambda = 1$ or 0 the force and the potential correspond to the homogeneous cases with (a_1,b) BC or (a_2,b) BC, respectively [see Sec. 2.2]. As before it is useful to define scaling functions ψ_p and ω_p which vary for $\lambda \in [0,1]$ within the range $[-1,1]$ and describe the lateral behavior of the critical Casimir effect:

$$K_\mathrm{p}(\lambda,\Pi,\Xi,\Theta,\Delta) = \frac{K_{(a_2,b)}+K_{(a_1,b)}}{2} + \frac{K_{(a_2,b)}-K_{(a_1,b)}}{2}\psi_\mathrm{p}(\lambda,\Pi,\Xi,\Theta,\Delta) \tag{2.29}$$

and

$$\vartheta_\mathrm{p}(\lambda,\Pi,\Xi,\Theta,\Delta) = \frac{\vartheta_{(a_2,b)}+\vartheta_{(a_1,b)}}{2} + \frac{\vartheta_{(a_2,b)}-\vartheta_{(a_1,b)}}{2}\omega_\mathrm{p}(\lambda,\Pi,\Xi,\Theta,\Delta). \tag{2.30}$$

2.5.1. Derjaguin approximation

Taking advantage of the assumption of additivity of the forces underlying the DA, one finds for the scaling function of the normal critical Casimir force in the limit $\Delta \to 0$ [see Appendix B.3]

$$\begin{aligned}&\psi_\mathrm{p}(\lambda,\Pi,\Xi,\Theta,\Delta\to 0) = \\ &1+\sum_{n=-\infty}^{\infty}\left\{\psi_{(a_1|a_2,b)}(\Xi+\Pi(n+\tfrac{\lambda}{2}),\Theta,\Delta\to 0)-\psi_{(a_1|a_2,b)}(\Xi+\Pi(n-\tfrac{\lambda}{2}),\Theta,\Delta\to 0)\right\}.\end{aligned} \tag{2.31}$$

Thus, the knowledge of the scaling function $\psi_{(a_1|a_2,b)}$ for a single chemical step with the appropriate BC [Sec. 2.3] is sufficient to calculate directly the corresponding scaling function of the critical Casimir force acting on a colloid close to a periodic pattern of chemical stripes. As expected, from Eq. (2.31) one recovers the values $\psi_\mathrm{p}(\lambda=0,\Pi,\Xi,\Theta,\Delta)=1$ and $\psi_\mathrm{p}(\lambda=1,\Pi,\Xi,\Theta,\Delta)=-1$, i.e., the cases of a colloid with (b) BC facing a homogeneous substrate with (a_2) BC and (a_1) BC, respectively [see Appendix B.3].

In the limit $\Pi \to 0$, i.e., for a pattern with a very fine structure compared to the size of the colloid, the sum in Eq. (2.31) turns into an integral [see Appendix B.3] and, as expected, ψ_p becomes independent of Ξ, i.e., of the lateral position of the colloid:

$$\psi_\mathrm{p}(\lambda,\Pi\to 0,\Xi,\Theta,\Delta\to 0) = 1-2\lambda. \tag{2.32}$$

Accordingly, in the limit $\Pi \to 0$ the force acting on the colloid — within the DA — is the average of the ones corresponding to the two boundary conditions weighted by the corresponding relative stripe width [see Eqs. (2.32) and (2.29)]:

$$K_\mathrm{p}(\lambda,\Pi\to 0,\Xi,\Theta,\Delta\to 0) = \frac{L_1}{L_1+L_2}K_{(a_1,b)}(\Theta,\Delta\to 0)+\frac{L_2}{L_1+L_2}K_{(a_2,b)}(\Theta,\Delta\to 0). \tag{2.33}$$

For the scaling function of the critical Casimir potential the results are completely analogous to Eqs. (2.31)–(2.33) [see Appendix B.3].

2.5.2. Scaling function for the normal critical Casimir force

Figure 2.7 shows the scaling function ψ_p [Eq. (2.29)] as a function of $\Xi/\Pi = X/P$, describing the lateral variation of the normal critical Casimir force at $\Theta = 0$ as obtained within the DA

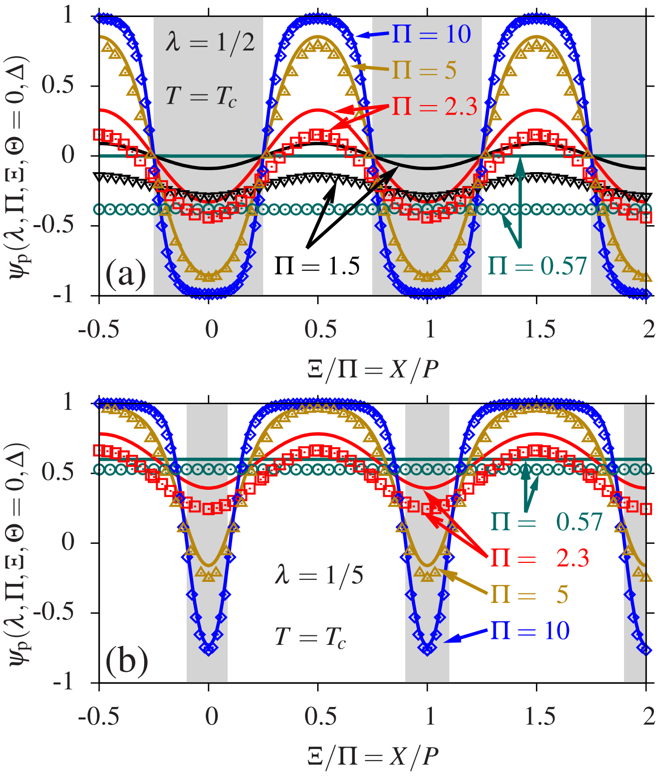

Figure 2.7: MFT ($d = 4$) scaling function ψ_p [Eq. (2.29)] of the normal critical Casimir force acting on a colloidal sphere with $(b) = (-)$ BC which is close to a periodically patterned substrate [Fig. 2.1] with $(a_1) = (-)$ BC on one kind of stripes [shaded areas] and $(a_2) = (+)$ BC on the other kind of stripes. Due to this choice of the BC the colloid is attracted by the shaded stripes and repelled by the others. ψ_p is shown as a function of the lateral position of the colloid X/P with $P = L_1 + L_2$ and at the bulk critical point $\Theta = 0$. The geometry of the pattern is characterized by $\Pi = P/\sqrt{RD}$ and $\lambda = L_1/P$, for which we have chosen the values (a) $\lambda = 0.5$ and (b) $\lambda = 0.2$. The lines are the results for ψ_p as obtained within the DA for $d = 4$ [Eqs. (2.31) and (2.13)], whereas the symbols represent the full numerical data obtained within MFT for $\Delta = 1/3$ for various values of Π. For patterns which are finely structured on the scale of the colloid size, i.e., $\Pi \lesssim 2$, the actual results deviate from the approximate ones obtained within the DA due to the strong influence (in this context) of the inherent nonlinear effects.

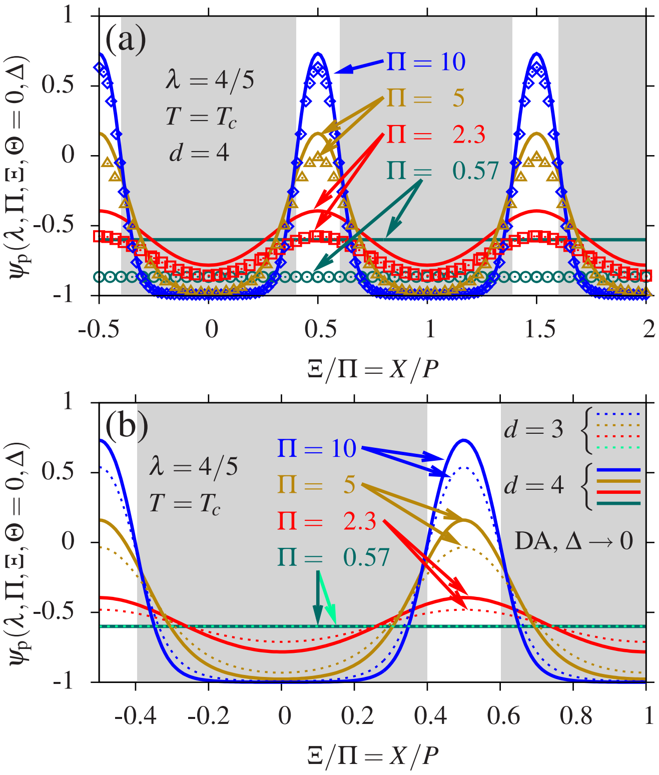

Figure 2.8: (a) The same as in Fig. 2.7, but for $\lambda = 0.8$. Also in this case, the DA turns out to be accurate for $\Pi \gtrsim 2$ while it fails to describe quantitatively the full numerical data for smaller values of Π. (b) Comparison between the scaling functions ψ_p in $d = 3$ (dotted lines) and $d = 4$ (solid lines), at $T = T_c$, for $\lambda = 0.8$, and within the DA. At the critical point the expression for this scaling function ψ_p is known analytically [see Eqs. (2.31) and (2.13)], and the corresponding plot presented here shows that the lateral variation of the normal critical Casimir force is less pronounced in $d = 3$ than in $d = 4$. (We note that for $\Pi \to 0$ we expect that also in $d = 3$ the DA fails to describe quantitatively the actual behavior; however, we nonetheless present the curve for $\Pi = 0.57$ in order to show that the critical Casimir force obtained within the DA practically does not change laterally for such small values of Π.)

for $d = 4$ [Eq. (2.31) with Eq. (2.13); solid lines] compared with the one obtained from the full numerical MFT calculation [$\Delta = 1/3$; symbols] for symmetry breaking boundary conditions $(a_1) = (-)$, $(a_2) = (+)$, and $(b) = (-)$ [Fig. 2.1]. From this comparison for $\lambda = 0.5$ [Fig. 2.7(a)] and $\lambda = 0.2$ [Fig. 2.7(b)] and for various values of Π one can infer that for $\Delta \to 0$ and $\Pi \gg 1$, i.e., $L_1 + L_2 \gg \sqrt{RD}$ the DA describes well the actual behavior of the scaling function, even if the force scaling function does not attain its limiting homogeneous values $\psi_p = \pm 1$ in the center of the stripes. However, for $\Pi \lesssim 2$ (in $d = 4$ at $T = T_c$) the DA does not quantitatively describe the actual behavior and the scaling function ψ_p obtained from the full numerical MFT calculations deviates from the one obtained within the DA. Within both the DA and the full numerical MFT calculation, for $\Pi \to 0$ the normal critical Casimir force loses its lateral dependence on Ξ. But from the full numerical calculation we find that the corresponding constant value which is attained by $\psi_{\rm p}$ differs from the one obtained within DA [Eq. (2.32)]. This shows that for small periodicities $P \lesssim \sqrt{RD}$ nonlinearities inherent in the critical Casimir effect strongly affect the resulting scaling functions of the force and the potential, so that in this respect the assumption of additivity of the force and thus the use of the DA are not justified.

Figure 2.8(a) shows the same comparison as Fig. 2.7 but for $\lambda = 0.8$, which corresponds to an areal occupation of 80% of the substrate surface with $(-)$ BC and 20% with $(+)$ BC. Due to the fact that at the critical point $\psi_{(a_1|a_2,b)}(\Xi,\Theta=0,\Delta\to 0)$ is actually independent of the BC, $\psi_{\rm p}(\lambda=0.8,\Pi,\Xi,\Theta=0,\Delta\to 0)$ in Fig. 2.8(a) is, within the DA, complementary to the one for $\lambda = 0.2$ in Fig. 2.7(b), i.e., it is obtained from the latter by a reflection with respect to $\psi_{\rm p} = 0$ followed by a shift in Ξ/Π of 0.5. Instead, the full numerical data in Fig. 2.8(a) and Fig. 2.7(b) show a different behavior as they clearly tend to assume the value -1 corresponding to the homogeneous case with $(-,-)$ BC. By contrast, for the case $\lambda = 0.2$ shown in Fig. 2.7(b), the full numerical data do not reach as closely the value $+1$ corresponding to $(+,-)$ BC, although the substrate area is covered by 80% with $(+)$ BC. This feature is addressed in more detail in Sec. 2.7. Figure 2.8(b) compares the scaling function $\psi_{\rm p}$ of the normal critical Casimir force at $T = T_c$ and for $\lambda = 0.2$ as obtained within the DA for $d = 4$ (solid lines) with the corresponding one for $d = 3$ (dotted lines). At $T = T_c$, $\psi_{\rm p}$ is determined by Eqs. (2.31) and (2.13) from which one can infer that the lateral variation of the normal Casimir force is less pronounced for $d = 3$ than for $d = 4$. This qualitative feature holds for all values of λ (not shown). However, off criticality, $\Theta \gg 1$, [according to Eqs. (2.31) and (2.16)] the DA scaling functions both for $d = 3$ as obtained from MC simulation data and for $d = 4$ as obtained from MFT de facto coincide (not shown), similarly to the case of a single chemical lane in Fig. 2.5(b).

Although one would expect the DA to be valid for large radii R, the lateral variation of the boundary conditions at the surface of the patterned substrate on a scale $P \lesssim \sqrt{RD}$ — corresponding to the limit $\Pi \to 0$ — renders the DA less accurate, as it clearly emerges from the numerical data presented in Figs. 2.7 and 2.8. The fact that a large colloid radius R does not guarantee the validity of the DA can be understood by noting that such a discrepancy between the full numerical calculation and the result of the DA approximation already emerges in the *film* geometry (formally corresponding to the limit $R \to \infty$), i.e., for a chemically *p*atterned wall opposite to a laterally *h*omogeneous flat wall. This "*ph*" configuration has been studied in Ref. [47] within MFT for laterally alternating chemical stripes of width $L_1 = S_+$ and $L_2 = S_-$ with $(+)$ and $(-)$ BC, respectively, opposite to a homogeneous substrate with $(+)$ BC a distance L apart [see Fig. 2.1 and the inset of Fig. 2.9]. Indeed, by using the assumption of additivity of the critical Casimir forces underlying the DA and neglecting edge effects, the normal critical Casimir force $f^{ph}_{(\rm DA)}(S_+,S_-,L,T)$ per unit area acting on the walls is predicted to be given by

$$f^{ph}_{(\rm DA)}(S_+,S_-,L,T) = \frac{S_+}{S_+ + S_-} f_{(+,+)}(L,T) + \frac{S_-}{S_+ + S_-} f_{(+,-)}(L,T), \tag{2.34}$$

where $f_{(+,\pm)}$ refer to homogeneous parallel walls, as in Eq. (1.3). At the bulk critical point the

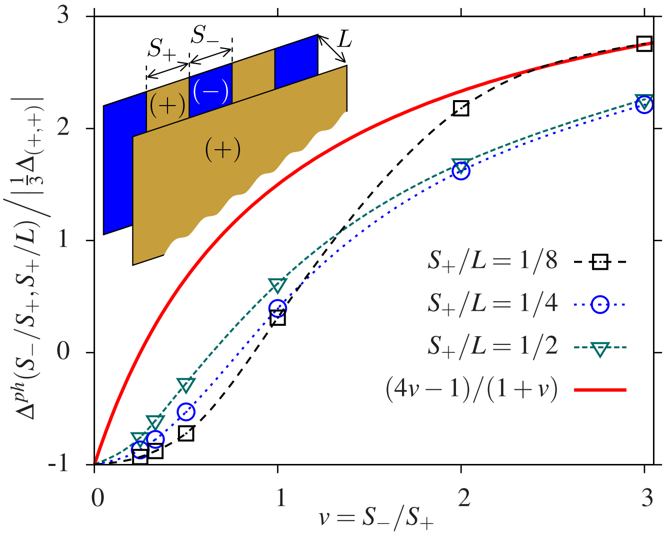

Figure 2.9: Normalized scaling function Δ^{ph} of the critical Casimir force at criticality acting on a homogeneous *planar* wall with $(+)$ BC opposite to a periodically patterned planar substrate with stripes of alternating $(+)$ and $(-)$ BC as a function of $v = S_-/S_+$, where S_+ and S_- are the respective widths. The symbols correspond to the MFT ($d = 4$) data presented in Fig. 12 of Ref. [47] for various values of S_+/L (note that $\Delta_0^{++} = \Delta_{(+,+)}/(d-1)$ in Fig. 12 of Ref. [47]). The dashed and dotted lines which join the data points are a guide to the eye. The solid line corresponds to the DA result given in Eq. (2.37) which assumes additivity of the forces and turns out to be independent of the ratio S_+/L. One can immediately infer from the graph that here the assumption of additivity is not justified, which is the limiting configuration of the sphere-wall geometry for $\Pi \to 0$.

critical Casimir force is given in general by [47]

$$f^{ph}(S_+,S_-,L,T=T_c)=k_BT_c\frac{d-1}{L^d}\Delta^{ph}\left(v=\frac{S_-}{S_+},\frac{S_+}{L}\right). \tag{2.35}$$

Using Eq. (2.34) together with Eqs. (1.3) and (1.4) one finds within the DA that

$$(d-1)\Delta^{ph}_{(\mathrm{DA})}\left(v,\frac{S_+}{L}\right)=\frac{v\Delta_{(+,-)}+\Delta_{(+,+)}}{1+v}, \tag{2.36}$$

which renders the rhs of Eq. (2.36) to be independent of the scaling variable S_+/L. Within MFT as studied in Ref. [47] ($d=4$), one has $\Delta_{(+,-)}=-4\Delta_{(+,+)}>0$ [see the end of Sec. 1.2.4] so that

$$\Delta^{ph}_{(\mathrm{DA})}\left(v,\frac{S_+}{L}\right)=\frac{|\Delta_{(+,+)}|}{3}\,\frac{4v-1}{1+v}. \tag{2.37}$$

In Fig. 2.9 we show the comparison between the actual scaling function Δ^{ph} (data points, obtained numerically as reported in Fig. 12 of Ref. [47]) and $\Delta^{ph}_{(\mathrm{DA})}$ (Eq. (2.37), solid line) derived by assuming additivity of the forces and neglecting edge effects. Figure 2.9 clearly shows that the actual behavior of the critical Casimir force in the film geometry is not properly predicted within these assumptions. This is expected to be due to the presence of nonlinear effects and of edge effects in this context. This explains why in the limit $\Pi\to 0$ the DA ($R\gg D$) used here does not capture the behavior of the critical Casimir force acting on a colloid close to periodically patterned substrate.

In Fig. 2.10 we show the behavior of scaling function K_p [Eq. (2.27)] of the normal critical Casimir force acting on the colloid in $d=4$ with $(b)=(-)$ BC as a function of $\Theta=D/\xi_+$ (i.e., as a function of the normal distance of the colloid from the substrate in units of the bulk correlation length) and for various values of λ and Π. In Fig. 2.10 the scaling function K_p is evaluated at $X=0$ [see Fig. 2.1] which corresponds to the most preferred lateral position of the colloid in which the normal force is least repulsive or most attractive [see Fig. 2.7]. From Fig. 2.10 one can infer that the DA does not provide an accurate estimate of K_p in the whole range of Θ for $\Pi=0.57$ [panel (b)], whereas it does so for $\Pi=2.3$ [panel (a)]. Indeed, for $\Pi=0.57$ the discrepancy between the DA and the numerical data is already significant for $\Theta\lesssim 4$ and $0.3\lesssim\lambda\lesssim 0.9$, whereas for $\Pi=2.3$ agreement is found for all values of λ except for $\Theta\lesssim 1$ [Fig. 2.10(a)]. This fact suggests that for relatively small periodicities $\Pi\lesssim 2$ non-additive and edge effects become important. On the other hand, for large values of $\Theta\gg 1$ the DA describes the behavior of K_p rather well for all values of Π due to the exponential decay of the critical Casimir force for $\Theta\gg 1$ [Eq. (1.5)]. Figure 2.11 shows the scaling function K_p for $d=3$ within the DA as obtained from Monte Carlo simulation data for the film geometry (see footnote 14 on page 40). The qualitative features of the behavior of K_p in $d=3$ and $d=4$ are similar.

From our analysis in $d=4$ we conclude that the DA describes quantitatively well the behavior of the actual critical Casimir force for $\Pi\gtrsim 2$ for all values of Θ. For smaller values of Π, the DA

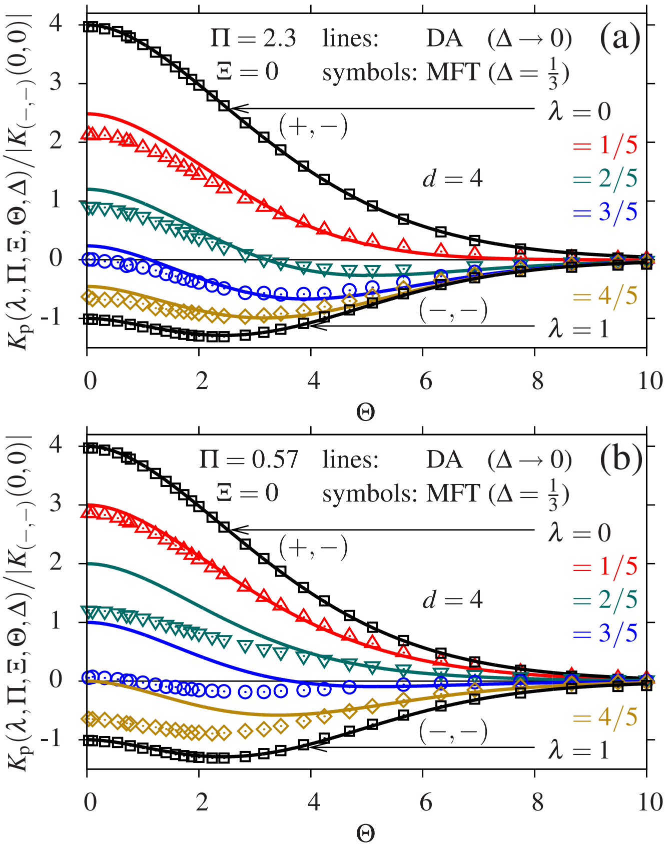

Figure 2.10: Scaling function K_{p} [Eq. (2.27)] of the normal critical Casimir force acting on a spherical colloid with $(-)$ BC located at $X = 0$ ($\Xi = X/\sqrt{RD}$) close to a periodically chemically patterned substrate [see Fig. 2.1]. K_{p} is suitably normalized by the absolute value of the force scaling function $K_{(-,-)}(0,0) = 2\pi\Delta_{(-,-)}/(d-1)$ for the homogeneous $(-,-)$ case at criticality and within the DA [Sec. 2.2.1]. The lateral position of the center of the colloid is fixed at the center of a stripe with $(a_1) = (-)$ BC and width $L_1 = \lambda P$, which it is attracted to, in contrast to the second type of stripes with $(a_2) = (+)$ BC and width $L_2 = (1-\lambda)P$, which it is repelled from. The scaling variable corresponding to the periodicity of the substrate pattern is (a) $\Pi = P/\sqrt{RD} = 2.7$ and (b) $\Pi = 0.57$, whereas the relative area fraction of the $(-)$ stripes changes from $\lambda = L_1/(L_1+L_2) = 0$ to $\lambda = 1$ (top to bottom: fully repulsive to fully attractive). In (a) and (b) the lines represent the result for the MFT critical Casimir force within the DA [$\Delta \to 0$, $d = 4$, see Eq. (2.31)], whereas the symbols represent the full numerical MFT data obtained for $\Delta = 1/3$. The DA agrees reasonably well with the full data for $\Pi = 2.3$ [(a)] and $\Theta \gtrsim 1$, but for $\Pi = 0.57$ [(b)] it fails to describe the actual behavior within the ranges $\Theta \lesssim 4$ and $0.3 \lesssim \lambda \lesssim 0.9$ where the nonlinear effects strongly affect the resulting scaling function.

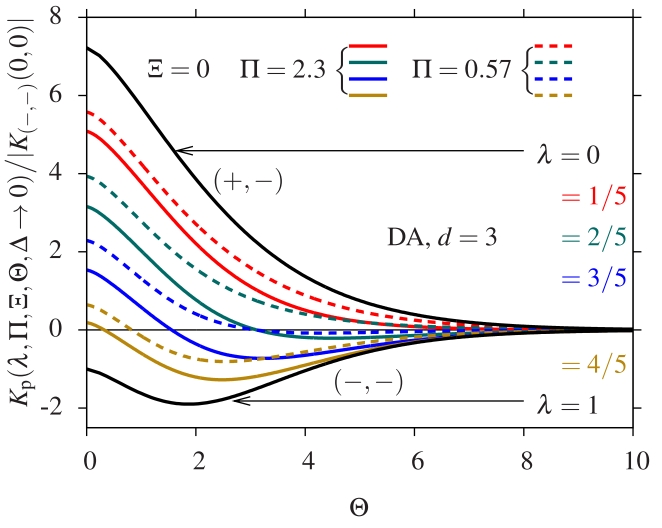

Figure 2.11: Scaling function K_p [Eq. (2.27)] shown for $\Pi = 0.57$ and 2.3, as obtained for $d = 3$ within the DA on the basis of the Monte Carlo simulation data for the film geometry (see footnote 14 on page 40). (We note, however, that we do not expect that the curves shown for $\Pi = 0.57$ are quantitatively reliable.)

is only quantitatively reliable for large values of Θ (at which the force decays exponentially). For example, for $\Pi \gtrsim 0.5$ the DA result is quantitatively correct for $\Theta \gtrsim 4$. We expect these properties to be carried over to $d = 3$.

2.6. Critical Casimir levitation

Rather remarkably, within a certain range of values of λ, K_p *changes sign* as a function of $\Theta = D/\xi_+$ (see Figs. 2.10 and 2.11). In this context it is convenient to introduce for later purposes another scaling variable $\Psi = \Pi|\Theta|^{1/2} = P/\sqrt{R\xi_\pm}$ which is independent of D and therefore does not vanish in the DA limit $D \ll R$ (i.e., $\Delta \to 0$). Due to this change of sign of K_p, there exists a certain value $\Theta = \Theta_0(\Psi,\lambda,\Xi,\Delta)$ at which the normal critical Casimir force F_p acting on the colloid vanishes. This implies that in the absence of additional forces the colloid levitates at a height D_0 determined by Θ_0 and ξ_+, which can be tuned by changing the temperature. Since for fixed geometrical parameters R, X, and P the scaling variables Θ, Π, Ξ, and Δ depend on D, one has to consider the behavior of F_p as a function of D near D_0 in order to assess whether the levitation is stable against perturbations of D or not. Stability requires $\partial_D F_p|_{D=D_0} < 0$ (so that for $D < D_0$ the colloid is repelled from the patterned substrate, whereas for for $D > D_0$ it is attracted). According to Eq. (2.27) one has

$$\partial_D F_p = k_B T \frac{R}{D^d} \left\{-(d-1) - \tfrac{1}{2}\Pi\partial_\Pi - \tfrac{1}{2}\Xi\partial_\Xi + \Theta\partial_\Theta + \Delta\partial_\Delta\right\} K_p(\lambda,\Pi,\Xi,\Theta,\Delta). \qquad (2.38)$$

The laterally preferred position is always at $X = X_0 = 0$, corresponding to $\Xi = \Xi_0 = 0$, so that within the DA ($\Delta \to 0$) one has

$$\operatorname{sign}\left(\partial_D F_\mathrm{p}\big|_{D=D_0, X=X_0, \mathrm{DA}}\right) = \operatorname{sign}\left(\left\{-\tfrac{1}{2}\Pi\partial_\Pi + \Theta\partial_\Theta\right\} K_\mathrm{p}(\lambda, \Pi, \Xi = 0, \Theta, \Delta \to 0)\big|_{\Theta=\Theta_0}\right), \tag{2.39}$$

where we have used the implicit equation $F_\mathrm{p}|_{D=D_0} = 0$ so that $K_\mathrm{p}|_{D=D_0} = 0$. (Equation (2.39) assumes that $\partial_\Delta K_\mathrm{p}$ does not diverge $\propto \Delta^{-1}$ for $\Delta \to 0$.) In the following we only consider $\Theta \geq 0$ and BC $(a_1) = (-)$, $(a_2) = (+)$, and $(b) = (-)$.

Within the DA we find that both $\partial_\Pi K_\mathrm{p}|_{\Theta=\Theta_0, \Xi=\Xi_0}$ and $\partial_\Theta K_\mathrm{p}|_{\Theta=\Theta_0, \Xi=\Xi_0}$ are negative, so that according to Eq. (2.39) the sign of $\partial_D F_\mathrm{p}|_{D=D_0, X=X_0, \mathrm{DA}}$ can vary and depends on their values as well as on Θ_0 and Π. However, at criticality ($\Theta = 0$) the second term of the rhs of Eq. (2.39) vanishes. Thus, at the bulk critical point $T = T_c$ the derivative $\partial_D F_\mathrm{p}$ evaluated at $D = D_0$ and $X = X_0 = 0$ is always positive so that one cannot achieve stable levitation. On the other hand, for $\Theta > 0$ it is always possible to find geometrical configurations for which the colloid exhibits stable levitation, as described in the following.

2.6.1. General analysis of geometrical parameters

Figure 2.12 shows the values of Θ_0 at which the normal critical Casimir force acting on a colloid vanishes as a function of the new scaling variable Ψ introduced at the beginning of this subsection, for various λ, for $\Xi = 0$, and within the DA ($\Delta \to 0$) for (a) $d = 4$ and (b) $d = 3$. The corresponding sign of $\partial_D F_\mathrm{p}\big|_{D=D_0}$ [according to Eq. (2.39)] is also indicated: Θ_0 drawn as a solid line indicates $\partial_D F_\mathrm{p}\big|_{D=D_0} < 0$, i.e., stable levitation of the colloid; a dashed line, instead, indicates $\partial_D F_\mathrm{p}\big|_{D=D_0} > 0$ and therefore a local maximum of the critical Casimir potential with respect to D, which occurs within the shaded regions in Fig. 2.12. For a given value of λ (with $\lambda_1 < \lambda < \lambda_0$ as we shall discuss in detail further below), e.g., $\lambda = 0.60$ in Fig. 2.12(a), the corresponding curve for Θ_0 shows a bifurcation at $\Psi = \Psi^*(\lambda)$ such that a vertical line drawn in Fig. 2.12 at a certain Ψ intersects this curve in two points $\Theta_{0,u}$ and $\Theta_{0,s} > \Theta_{0,u}$ if $\Psi < \Psi^*(\lambda)$, whereas it has no intersection for $\Psi > \Psi^*(\lambda)$. In the former case $\Theta_{0,u}$ and $\Theta_{0,s}$ correspond to a local maximum and to a local minimum of the critical Casimir potential at distances $D_{0,u} = \xi_+\Theta_{0,u}$ and $D_{0,s} = \xi_+\Theta_{0,s}$, respectively, i.e., to an *u*nstable and a *s*table levitation point for the colloid, respectively. Instead, for $\Psi > \Psi^*(\lambda)$, the critical Casimir force has no zero at any finite value of D. We note that $D = 0$ (stiction) and thus $\Theta = 0$ always corresponds to the global minimum of the potential because for $D \to 0$ the critical Casimir potential is strongly attractive. The corresponding geometrical configuration into which the colloid is finally attracted by the substrate [due to $(a_1) = (-)$, $(b) = (-)$, and $X = 0$, see Fig. 2.1] is stabilized by the steric repulsion of the wall.

We note that within the DA the critical Casimir potential for $X = 0$ is attractive at sufficiently small distances, even if the major part of the substrate is characterized by $(+)$ BC, i.e., even if $0 \neq \lambda \ll 1$. Indeed, in this case the potential of the colloid at $X = 0$ and close to a periodically

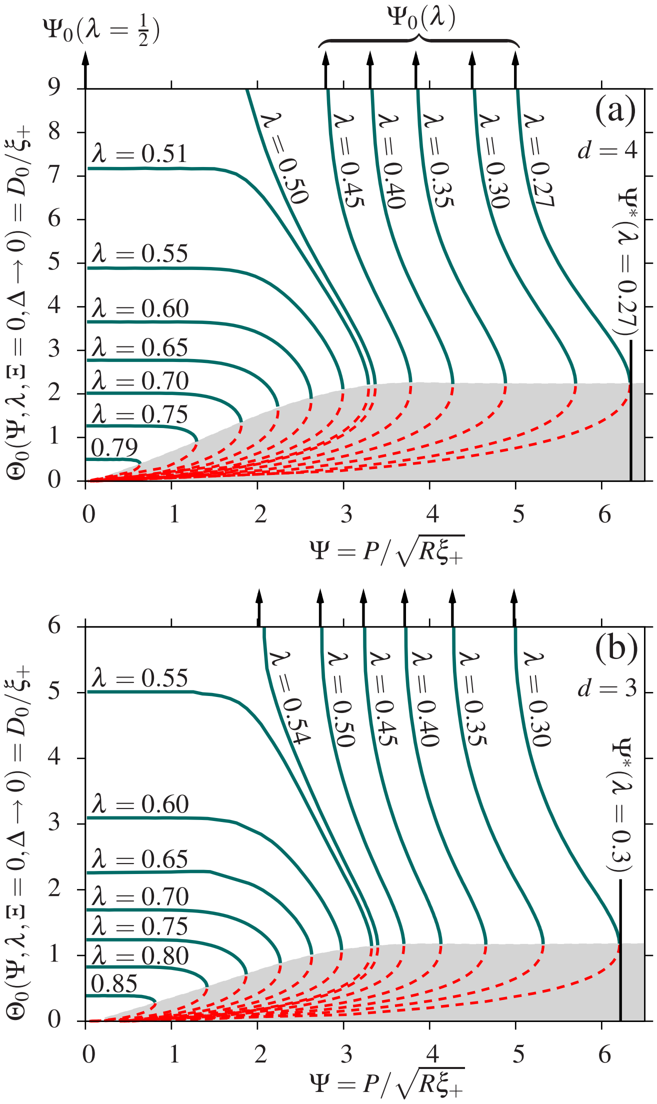

Figure 2.12: Values of the scaling variable Θ_0 at which within the DA ($\Delta \to 0$) the normal critical Casimir force K_p shown in Figs. 2.10 and 2.11 vanishes as a function of Ψ for (a) $d = 4$ and (b) $d = 3$ on the basis of Monte Carlo simulation data (see footnote 14 on page 40) and for various values of $\lambda = L_1/P$. The solid lines correspond to values of Θ_0 for which the levitation of the colloid at a height D_0 above the substrate is *stable* against perturbations of D [$\partial_D F_\text{p}|_{D=D_0} < 0$, see Eq. (2.39)]. The shaded region and the dashed lines indicate those values of Θ_0 for which $\partial_D F_\text{p}|_{D=D_0} > 0$ and thus do *not* correspond to stable levitation. For $\lambda > \lambda_0$ with $\lambda_0(d=4) = 4/5$ and $\lambda_0(d=3) \simeq 0.88$, Θ_0 ceases to exist, i.e., K_p does not exhibit a zero. For $\lambda < \lambda_1$ with $\lambda_1(d=4) = 1/2$ and $\lambda_1(d=3) \simeq 0.545$, $\Theta_0(\Psi \searrow \Psi_0(\lambda))$ diverges. (The values for $\Psi_0(\lambda)$ are indicated by upward arrows.) For any $\lambda < \lambda_0$, Θ_0 exists for $\Psi < \Psi^*(\lambda)$. (From the analysis in Fig. 2.10 we expect the DA to be quantitatively reliable only for $\Psi \gtrsim 2\sqrt{\Theta_0}$ for $\Theta_0 \lesssim 4$ and for $\Psi \gtrsim 0.5\sqrt{\Theta_0}$ for $\Theta_0 \gtrsim 4$, which implies $\lambda \lesssim 0.7$ in $d = 3$ and $\lambda \lesssim 0.6$ in $d = 4$.)

patterned substrate can be approximated by the one due to a single chemical lane centered at $X = 0$, which has been discussed in Sec. 2.4. For given colloid radius R and width $L_l = \lambda P > 0$ of the attractive stripe, the scaling variable $\Lambda = L_l/(2\sqrt{RD})$ diverges as $D \to 0$, so that the scaling function $\omega_\ell(\Lambda, \Xi, \Theta, \Delta)$ which characterizes the potential of the lane [see Eq. (2.24)] attains the value -1 corresponding to the case of homogeneous, attractive $(-,-)$ BC [see Fig. 2.5]. Within this approximation and for $D \ll \xi_\pm$ the critical Casimir force becomes attractive if $\vartheta_\mathrm{p} \simeq \vartheta_\ell < 0$ which, due to Eqs. (2.24), (2.7), and (1.4), yields the condition $\omega_\ell(\Lambda, \Xi = 0, \Theta \to 0, \Delta \to 0) < 1 - 2\Delta_{(+,-)}/(\Delta_{(+,-)} - \Delta_{(+,+)})$, i.e., $\omega_\ell < -0.6$ in $d = 4$ [117] and $\omega_\ell \lesssim -0.76$ in $d = 3$ (see footnote 14 on page 40); this occurs for $\Lambda > \Lambda_0 = 1.1$ in $d = 4$, and $\Lambda > \Lambda_0 = 2.7$ in $d = 3$, respectively [see also Fig. 2.5(a)]. Accordingly, at distances $D < \lambda^2 P^2/(4R\Lambda_0^2)$ (together with $D \ll \xi_\pm$) the critical Casimir potential Φ_p is negative and diverges to $-\infty$ for $D \to 0$. (However, for very small values of λ this would occur at distances of microscopic scale such that the scaling limit and thus the form of Φ_p do no longer hold). Thus the bifurcation of Θ_0 at $\Psi^*(\lambda)$ corresponds to a transition from (metastable) levitation at $D = D_{0,s}$ for $\Psi < \Psi^*(\lambda)$ to stiction at $D = 0$ for $\Psi > \Psi^*(\lambda)$. For $\Psi < \Psi^*(\lambda)$ the metastable levitation minimum at $D_{0,s}$ is shielded from the global minimum at $D = 0$ by a potential barrier the height of which vanishes for $\Psi \nearrow \Psi^*(\lambda)$ [see Fig. 2.14].

Experimentally, one typically varies the value of ξ_+ by changing the temperature [20, 21, 35, 37] and leaves the geometry (λ, P, and R) unchanged, which results in a change of Ψ via varying T. Thus, experimentally, the transition at $\Psi^*(\lambda)$ corresponds to a de facto irreversible transition from separation to stiction of the colloid as a function of temperature.

Moreover, from Fig. 2.12 one can infer that for both $d = 3$ and $d = 4$ there is a λ_0 such that, for $1 \geq \lambda > \lambda_0$, K_p has no zero for any choice of Ψ (i.e., there is no solution Θ_0) and the critical Casimir force is attractive at all distances. Within the DA, $\lambda_0 = \Delta_{(+,-)}/(\Delta_{(+,-)} - \Delta_{(-,-)})$ [see also Eq. (2.33)], which renders the values $\lambda_0 = 0.80$ in $d = 4$ [117] and $\lambda_0 \simeq 0.88$ in $d = 3$ (see footnote 14 on page 40).

In addition, from Fig. 2.12 one can infer that for $\lambda_0 > \lambda > \lambda_1 \simeq 0.5$ and $\Psi \lesssim 1$, $\Theta_{0,s}$ effectively does no longer depend on Ψ but solely on λ. Accordingly, the distance $D_{0,s} \propto \xi_+$ at which the colloid stably levitates can be tuned by temperature upon approaching criticality. However, for $\lambda < \lambda_1 \simeq 0.5$, $\Theta_{0,s}$ diverges at $\Psi = \Psi_0(\lambda) < \Psi^*(\lambda)$ such that for $\Psi_0(\lambda) < \Psi < \Psi^*(\lambda)$ the colloid exhibits critical Casimir levitation at a local minimum of the potential, whereas within this range of λ values for $\Psi < \Psi_0(\lambda)$ the critical Casimir potential has only a local (positive) maximum at $D_{0,u}$; it is repulsive for $D > D_{0,u}$ and therefore for large values of D (i.e., $\Theta \gg 1$ and $\Pi \ll 1$) it approaches zero from positive values. This qualitative change in the behavior of the critical Casimir potential occurs at $\lambda = \lambda_1$. The value of λ_1 is close to 0.5 because the repulsive and attractive forces for $(+,-)$ and $(-,-)$ BC, respectively, have similar strengths but opposite signs for $\Theta \gg 1$, i.e., $k_{(+,-)}(\Theta \gg 1) \simeq -k_{(-,-)}(\Theta \gg 1)$ for both $d = 3$ and $d = 4$ [see Eq. (1.5), where $|A_-/A_+| \simeq 1.2$ in $d = 3$ [21] and $|A_-/A_+| = 1$ in $d = 4$ [117]]. Accordingly, depending on λ being larger or smaller than $\lambda_1 \simeq 0.5$, the area covered by one of the two BC prevails and the resulting force is asymptotically (i.e., $\Theta \gg 1$) attractive or repulsive, respectively [see the remark at the end of Sec. 2.5.1 and Eqs. (2.33) and (B.29)]. Taking into account the slight difference in the strength of the asymptotic forces for $(+,-)$ and $(-,-)$ BC one finds $\lambda_1 = (1 - A_+/A_-)^{-1}$ which renders $\lambda_1 = 1/2$ in $d = 4$ and $\lambda_1 \simeq 0.545$ in $d = 3$. The asymptotic behavior of the force at large distances can be inferred from the asymptotic behavior of $K_{\mathrm{p}}(\lambda, \Pi = \Psi\Theta^{-1/2}, \Xi = 0, \Theta \gg 1, \Delta \to 0) \simeq \mathscr{A}(\Psi,\lambda)\ \Theta^{d-1}e^{-\Theta}$, which can be obtained from Eqs. (2.31), (2.29), (B.29), (2.16), and (1.5) . Accordingly, the value $\Psi_0(\lambda)$ at which $\Theta_{0,s}$ diverges is characterized by the fact that $\mathscr{A}(\Psi \lesseqgtr \Psi_0(\lambda),\lambda) \gtreqless 0$ so that the force approaches zero from above or from below depending on having $\Psi < \Psi_0(\lambda)$ or $\Psi > \Psi_0(\lambda)$, respectively. The condition $\mathscr{A}(\Psi_0(\lambda),\lambda) = 0$ yields the following implicit equation for $\Psi_0(\lambda)$:

$$2\lambda_1 = \sum_{n=-\infty}^{\infty} \operatorname{erf}\left\{\frac{\Psi_0(\lambda)}{\sqrt{2}}\left(n + \frac{\lambda}{2}\right)\right\} - \operatorname{erf}\left\{\frac{\Psi_0(\lambda)}{\sqrt{2}}\left(n - \frac{\lambda}{2}\right)\right\}. \tag{2.40}$$

For $\lambda \ll 1$ the sum on the rhs of Eq. (2.40) can be approximated by the term $n = 0$ alone and one finds $\Psi_0(\lambda \ll 1) \simeq 2^{3/2}\lambda^{-1}\operatorname{erf}^{-1}(\lambda_1)$, where erf^{-1} is the inverse error function, which yields the relations $\Psi_0(\lambda \ll 1) \simeq 1.49/\lambda$ for $d = 3$ and $\Psi_0(\lambda \ll 1) \simeq 1.35/\lambda$ for $d = 4$. On the other hand, in the marginal case one expects $\Psi_0(\lambda = \lambda_1) = 0$. However, as argued above, *at* the critical point ($\Theta = 0$) the colloid does not exhibit stable levitation for any geometrical configuration; this is in accordance with Fig. 2.12 because for $T \to T_c$, the levitation minimum of the potential moves to large D ($D_{0,s} = \Theta_{0,s}\xi_+ \to \infty$) and disappears at $T = T_c$.

In summary, as function of λ there are three distinct levitation regimes:

(i) $\lambda > \lambda_0$ with $\lambda_0(d=3) \simeq 0.88$ and $\lambda_0(d=4) = 4/5$: There is no levitation and the critical Casimir force is attractive at all distances for any temperature.

(ii) $\lambda_0 > \lambda > \lambda_1$ with $\lambda_1(d = 3) \simeq 0.545$ and $\lambda_1(d = 4) = 1/2$: Sufficiently close to T_c, i.e., for $\Psi = P/\sqrt{R\xi_+} < \Psi^*(\lambda)$ there is a local critical Casimir levitation minimum. Upon approaching T_c its position $D_{0,s} = \Theta_{0,s}\xi_+$, with $\Theta_{0,s}(\xi_+ \to \infty)$ finite, moves to macroscopic values proportional to the bulk correlation length.

(iii) $\lambda_1 > \lambda$: As in (ii) there is a local critical Casimir levitation minimum sufficiently close to T_c, i.e., for $\Psi < \Psi^*(\lambda)$. In general the onset of its appearance occurs further away from T_c upon lowering λ. Upon approaching T_c the position $D_{0,s}$ of this minimum diverges at a distinct nonzero reduced temperature given by $\Psi_0(\lambda)$, i.e., at $\xi_+ = P^2/[R\Psi_0^2(\lambda)]$: $D_{0,s} = \Theta_{0,s}\xi_+$ with $\Theta_{0,s}(\Psi \searrow \Psi_0(\lambda)) \to \infty$.

The behavior of the critical Casimir force acting on the colloid for these three cases is sketched in Fig. 2.13.

We note that, according to Figs. 2.7, 2.8, 2.9 and 2.10, we expect that for $\Pi \lesssim 2$ and $\Theta \lesssim 4$ and for $\Pi \lesssim 0.5$ and $\Theta \gtrsim 4$, the DA does not provide a quantitatively reliable description of the actual behavior of K_{p} and therefore of F_{p}; thus, for values of $\Psi \lesssim 2\sqrt{\Theta_0}$ for $\Theta_0 \lesssim 4$, and

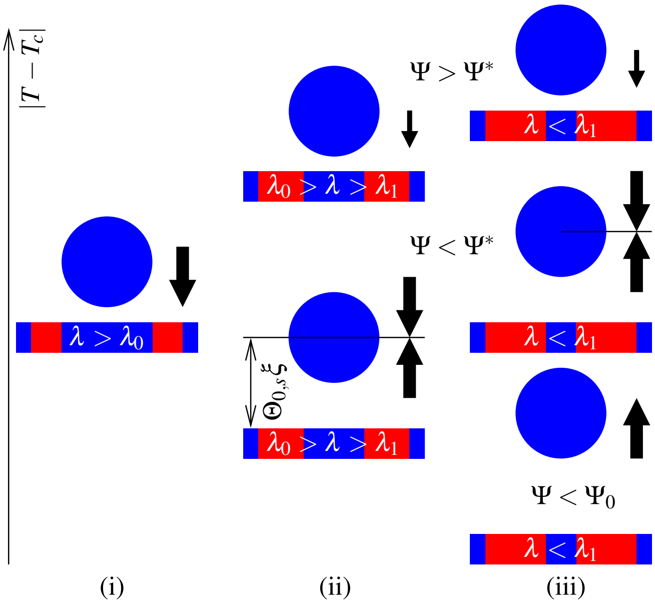
$|T-T_c|$
$\lambda > \lambda_0$
$\lambda_0 > \lambda > \lambda_1$
$\Theta_{0,s}\xi$
$\lambda_0 > \lambda > \lambda_1$
$\Psi > \Psi^*$
$\lambda < \lambda_1$
$\Psi < \Psi^*$
$\lambda < \lambda_1$
$\Psi < \Psi_0$
$\lambda < \lambda_1$
(i)
(ii)
(iii)

Figure 2.13: Sketch of the normal critical Casimir forces acting on a colloid with $(-)$ BC opposite to a substrate patterned with stripes with $(\pm)$ BC.. For the three distinct cases (i) $\lambda > \lambda_0$, (ii) $\lambda_0 > \lambda > \lambda_1$, and (iii) $\lambda < \lambda_1$, one obtains characteristic behavior of the forces as indicated in the figure (see the main text). For $\Psi < \Psi^*(\lambda)$ and $\lambda < \lambda_0$ the particle eventually exhibits leviatation at a stable distance from the substrate. For $\lambda < \lambda_1$, levitation occurs only at values $\Psi^*(\lambda) > \Psi > \Psi_0(\lambda)$.

$\Psi \lesssim 0.5\sqrt{\Theta_0}$ for $\Theta_0 \gtrsim 4$, we expect quantitative discrepancies between the actual behavior and the one predicted by the DA shown in Fig. 2.12. Nonetheless our results demonstrate that the geometric arrangement of the chemical patterns allows one to design the normal critical Casimir force over a wide range.

2.6.2. Levitation for experimentally relevant parameters — a case study

Figures 2.14(a) and (b) show the critical Casimir potential Φ_p as a function of D in $d = 3$ within the DA based on Monte Carlo simulation data for the film geometry (see footnote 14 on page 40) for a variety of specifically chosen values of the parameters P, L_1, R, and ξ. The choice of these values is motivated by the typical experimental parameters which characterize recent investigations of the critical Casimir force acting on colloids immersed in binary liquid mixtures [20, 21, 35, 37]. In particular, concerning the colloid radius we focus on the data of Ref. [35], corresponding to $R = 1.35\,\mu\mathrm{m}$, while for the pattern we have chosen a periodicity $P = 1\,\mu\mathrm{m}$ with $\lambda = 0.4$ (i.e., $L_1 = 400\,\mathrm{nm}$ and $L_2 = 600\,\mathrm{nm}$) [Fig. 2.14(a)], or $P = 0.4\,\mu\mathrm{m}$ with $\lambda = 0.65$ (i.e., $L_1 = 260\,\mathrm{nm}$ and $L_2 = 140\,\mathrm{nm}$) [Fig. 2.14(b)]. A chemically patterned substrate with these characteristics appears to be realizable with presently available preparation techniques [37, 39, 40]. [We note that Φ_p as shown in Fig. 2.14(a) and (b) is expected to describe the actual interaction potential in the scaling regime characterized by values of D and ξ_+ much larger than microscopic length scales (such as $\xi_0^+ \simeq 0.2\,\mathrm{nm}$ [20, 21]) so that this prediction for Φ_p is valid only for $D, \xi_+ \gtrsim 5\,\mathrm{nm}$.] With this choice of parameters we have calculated Φ_p for various values of ξ_+ within an experimentally accessible range [20, 21, 35, 37].

From Figs. 2.14(a) and 2.14(b) one can infer that for small values of ξ_+ (corresponding to large values of $\Psi > \Psi^*(\lambda)$) the critical Casimir potential is always attractive with a monotonic dependence on D [see also Fig. 2.12]. Upon approaching criticality, i.e., for increasing values of ξ_+ and decreasing values of $\Psi < \Psi^*(\lambda)$, a local maximum and a local minimum of the potential develop, so that for very small as well as for large D the colloid is attracted to the patterned substrate, whereas within an intermediate range of values for D it is repelled from it [see also Fig. 2.12]. Thus, the colloid stably levitates at a distance $D_{0,s}$ corresponding to a local minimum of the potential. The depth of this minimum ranges between a few k_BT [Fig. 2.14(a)] up to several k_BT [Fig. 2.14(b)]. Upon increasing ξ_+, $D_{0,s}$ increases as well, i.e., the colloid position is shifted away from the patterned substrate with the potential minimum becoming more shallow. In Fig. 2.14(a) $\lambda = 0.4$ and we find $\Psi^*(\lambda = 0.4) \simeq 4.65$ and $\Psi_0(\lambda = 0.4) \simeq 3.71$ [see Fig. 2.12(b)] so that for $\Psi < \Psi_0(\lambda = 0.4)$, i.e., for $\xi_+ \gtrsim 53.5\,\mathrm{nm}$ [Fig. 2.14(a)] the colloid does not exhibit stable levitation and the critical Casimir potential has a local maximum only. The levitation minimum moves to macroscopic values of D upon approaching the temperature corresponding to $\xi_+ \simeq 53.5\,\mathrm{nm}$. In Fig. 2.14(b) $\lambda = 0.65$ and one has $\Psi^*(\lambda = 0.65) \simeq 2.63$; here $\Theta_{0,s}$ remains finite for $\Psi \to 0$ in contrast to the case $\lambda < 0.545$ [Fig. 2.12(b)]. Thus, within the DA, for the case shown in Fig. 2.14(b) stable levitation of the colloid is preserved

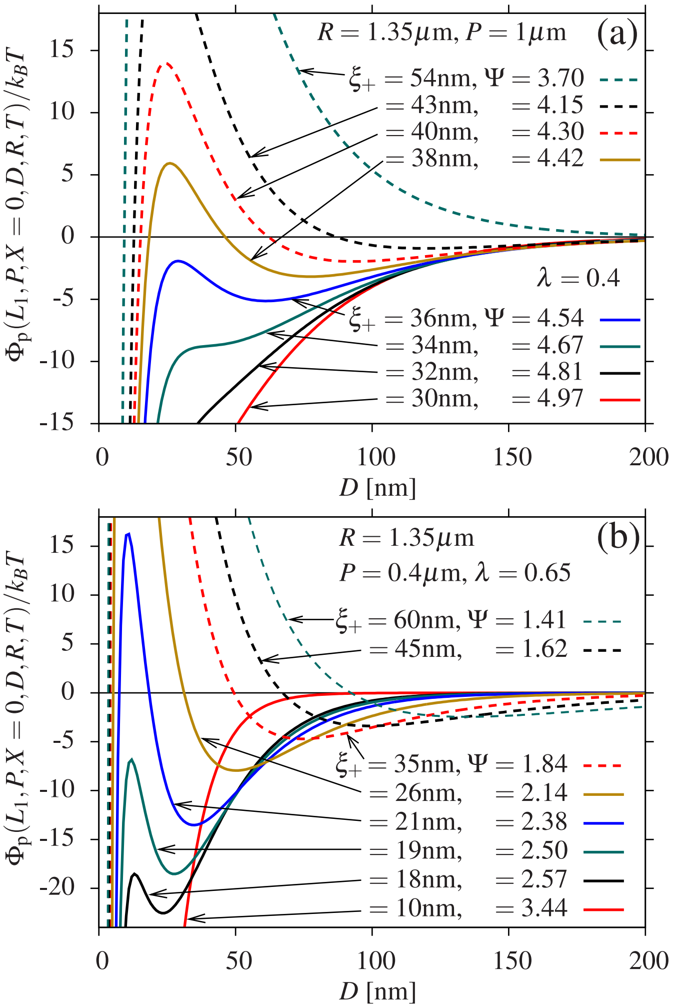

Figure 2.14: Critical Casimir potential Φ_p [Eq. (2.28)] in $d = 3$ of a colloid of radius $R = 1.35\,\mu$m close to a periodically patterned substrate as a function of D and for various values of ξ_+ for $P = 1\,\mu$m with $\lambda = 0.4$ in (a) and $P = 0.4\,\mu$m with $\lambda = 0.65$ in (b). The values of P, λ, and ξ_+ are chosen as to be experimentally accessible in a colloidal suspension exhibiting critical Casimir forces [20, 21, 35, 37]. The critical Casimir potential for the colloid close to a patterned substrate may exhibit — depending on the value of ξ_+, and, thus, on the temperature — a local minimum corresponding to stable levitation. (Note that (a) corresponds to case (iii) in Fig. 2.13, and (b) corresponds to case (ii) in Fig. 2.13.)

for all finite values of $\xi_+ > P^2/[R\,(\Psi^*(\lambda = 0.65))^2] \simeq 17\,\mathrm{nm}$. In this case upon approaching T_c the levitation minimum moves to macroscopic values of D proportional to the bulk correlation length ξ_+.

Additional forces

The discussion above focuses on the position of mechanical equilibrium of the colloid, corresponding to the point at which the forces acting on the particle vanish and the associated potential Φ has a local minimum Φ_{min}. However, due to the thermal fluctuations of the surrounding (near-) critical fluid at temperature T, the colloid undergoes a Brownian diffusion which allows it to explore randomly such regions in space where the potential Φ is typically larger than Φ_{min} for at most few k_BT. As a result, a position of mechanical equilibrium is stable against the effect of thermal fluctuations only if the potential depth of the minimum is larger than few k_BT. In particular, if the potential barrier $\Phi(L_1,P,0,D=D_{0,u},R,T) - \Phi(L_1,P,0,D=D_{0,s},R,T)$, which separates the position of the local minimum at distance $D = D_{0,s}$ (levitation) from the global one at $D = 0$ (stiction), is not sufficiently large [see, e.g., the curves corresponding to $\xi_+ = 36\,\mathrm{nm}$ in Fig. 2.14(a) or corresponding to $\xi_+ \lesssim 18\,\mathrm{nm}$ in Fig. 2.14(b)], a de facto irreversible transition from levitation to stiction may occur as a consequence of thermal fluctuations.

In Fig. 2.15 we show the resulting total potential of the forces acting on the colloid in the presence of an additional electrostatic repulsion which is experimentally practically unavoidable, in order to study its effect on critical Casimir levitation. We assume that the electrostatic repulsion is laterally homogeneous and that it can be simply added to the critical Casimir potential [21, 35] (see Sec. 3.2.2 below). Concerning the spatial dependence of the electrostatic repulsion we consider the one of Ref. [35], which corresponds to a colloid of radius $R = 1.35\,\mu\mathrm{m}$ immersed in a (near-) critical water-lutidine mixture and close to a substrate exhibiting critical adsorption of water or lutidine [35]:

$$\Phi_{\mathrm{el}}(D)/k_BT = \exp\{-\kappa(D - D_0)\}, \tag{2.41}$$

where $D_0 = 88\,\mathrm{nm}$ and $\kappa^{-1} = 11\,\mathrm{nm}$ [35]. (Formally, Φ_{el} in Eq. (2.41) is finite for $D \to 0$, and thus $\Phi_{\mathrm{p}} + \Phi_{\mathrm{el}}$ is negative for $D \lesssim 2\,\mathrm{nm}$ and has a global minimum at $D = 0$ because $\Phi_{\mathrm{p}} \to -\infty$ for $D \to 0$. However, Eq. (2.41) is actually the asymptotic form of the electrostatic interaction which is valid for distances larger than the electrostatic screening length, i.e., $D \gg \kappa^{-1}$. The corresponding total potential $\Phi_{\mathrm{p}} + \Phi_{\mathrm{el}}$ is therefore not accurate for small values of D and is reported in Fig. 2.15 for $D > 50\,\mathrm{nm}$ only.) As in Fig. 2.14(b) we choose $P = 0.4\,\mu\mathrm{m}$, $\lambda = 0.65$, and experimentally accessible values of ξ_+.

Figure 2.15 provides a realistic comparison of the critical Casimir potential with other forces as they typically occur in actual experimental systems. One can infer from the graph reported in Fig. 2.15 that for this choice of parameters the critical Casimir levitation exhibited by the colloid is rather pronounced even in the presence of electrostatic interaction. Far from the critical point ($\xi_+ = 10\,\mathrm{nm}$) the interaction of the colloid with the substrate is completely dominated

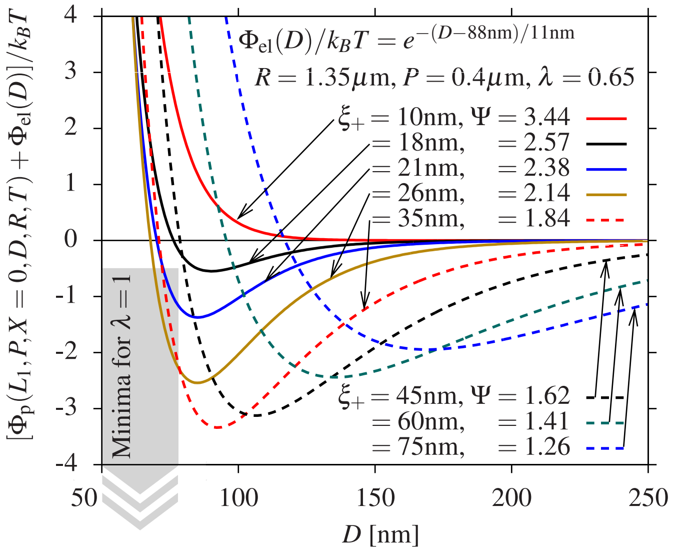

Figure 2.15: The same as in Fig. 2.14(b) but with an electrostatic potential $\Phi_{\rm el}$ [Eq. (3.10)] added to $\Phi_{\rm p}$, which refers to actual experimental data [35]. The shaded area indicates the ranges of the positions and the depths of the local minima of the total potential occurring if the substrate is laterally homogeneous and purely attractive, i.e., for $\lambda = 1$ ($(-,-)$ BC) for the range $14\,{\rm nm} < \xi_+ < 75\,{\rm nm}$ leading to potential depths between $0.5 k_BT$ and $70 k_BT$ (indicated by the shaded arrow); for $\lambda = 1$ the preferred colloid position is dictated by the electrostatic repulsion and restricted to the range of $50\,{\rm nm}$ to $75\,{\rm nm}$, whereas the colloid position $D_{0,s} = \Theta_{0,s}\xi_+$ due to critical Casimir levitation can be much larger and tuned by temperature. Moreover, whereas for $\lambda = 1$ and upon approaching T_c the minima monotonically become deeper, the levitation minima first deepen and move to smaller values of D followed by a decrease of the depth, by becoming more shallow, and moving to larger values of D. Reducing the range and strength of the electrostatic repulsion by adding salt to the solvent is expected to provide access to even more details of the critical Casimir levitation potential $\Phi_{\rm p}$ shown in Fig. 2.14(b).

by electrostatic repulsion. Upon approaching criticality ($10\,\mathrm{nm} \lesssim \xi_+ \lesssim 35\,\mathrm{nm}$) a minimum in the total potential develops and becomes deeper due to the increasing critical Casimir attraction working against the electrostatic repulsion. For this latter range of values of ξ_+ the local minimum of the critical Casimir potential corresponding to levitation is located at distances $D_{0,s} \lesssim 60\,\mathrm{nm}$ at which the electrostatic repulsion still strongly contributes to the resulting total potential [see Fig. 2.15]. Closer to the critical point ($\xi_+ \gtrsim 45\,\mathrm{nm}$) the levitation minimum of the critical Casimir potential occurs at distances $D_{0,s} \gtrsim 100\,\mathrm{nm}$ [see Fig. 2.14(b)] at which the electrostatic force acting on the colloid is weak. Thus, here the critical Casimir effect dominates and the position of the minimum of the total potential increases with increasing values of ξ_+, which allows for measurements of the critical Casimir potential for distances at which the precise form of Φ_{el} is not important. Moreover, the depth of the minimum *decreases* upon approaching criticality and the minimum becomes more shallow.

This behavior of the levitation minimum is distinct from the critical Casimir effect acting on a colloid close to a *homogeneous* substrate: a local minimum also occurs in the latter case if the critical Casimir force is purely attractive ($\lambda = 1$, $(-,-)$ BC) and works against the electrostatic repulsion [20, 21], due to the competition of different forces with opposite sign. (We note that the critical Casimir levitation described above emerges from the critical Casimir force alone, i.e., it is a feature of a *single* force contribution.) However, in this homogeneous case the preferred colloid position $D_{0,(-,-)}$ depends crucially on the form of the electrostatic interaction and is almost constant ($50\,\mathrm{nm} < D_{0,(-,-)} < 75\,\mathrm{nm}$). Moreover, the depths of these latter minima monotonically increase as a function of of ξ_+ and become much larger than those shown in Fig. 2.15 (see, e.g., Fig. 2(a) and Fig. 2(c) in Ref. [20] and Fig. 3 in Ref. [35]). In Fig. 2.15 this is indicated by the shaded area and the shaded arrow, which corresponds to the area of the graph within which minima of the total potential in the homogeneous case $\lambda = 1$ occur for $14\,\mathrm{nm} < \xi_+ < 75\,\mathrm{nm}$ corresponding to potential depths of $0.5k_BT$ up to $70k_BT$. On the other hand, the colloid position $D_{0,s}$ due to critical Casimir levitation can be much larger, can reach values of several ξ_+, and can be tuned by temperature according to $D_{0,s} = \Theta_{0,s}\xi_+$. In conclusion, the examples presented in Figs. 2.14 and 2.15 strongly suggest that the critical Casimir levitation of a colloid close to a patterned substrate is experimentally accessible.

2.6.3. Comparison with quantum electrodynamic Casimir levitation

By patterning the substrate, one introduces an additional (*lateral*) length scale into the system, which, according to our results presented above, can finally lead to stable levitation. Introducing an additional length scale along the *normal* direction by stacking different materials on top of each other may lead to levitation due to *quantum electrodynamic* Casimir forces [166]. The behavior of the stable levitation distance shows a bifurcation and irreversible transitions from separation to stiction [166] similarly to the ones described above [see Fig. 2.12]. In that context great importance has been given to the temperature dependence of the position $D_{0,s}$ of stable quantum Casimir levitation [166], which is quantified by the value of $\frac{d}{dT}D_{0,s}$. In the critical Casimir case presented here, for an estimate of $\frac{d}{dT}D_{0,s}$ we pick as an example the stable levitation positions for $\xi_+ = 18\,\mathrm{nm}$ and $\xi_+ = 60\,\mathrm{nm}$ as reported in Fig. 2.14 (a different choice would lead to similar results). The results reported in Fig. 2.14 correspond to the experimentally relevant water-lutidine mixture with $\xi_0^+ = 0.2\,\mathrm{nm}$ and $T_c \simeq 307\,\mathrm{K}$ [20, 21, 35]. Therefore, according to $\xi_+/\xi_0^+ = |(T-T_c)/T_c|^{-\nu}$, the difference in temperature required to move from $\xi_+ = 18\,\mathrm{nm}$ to $\xi_+ = 60\,\mathrm{nm}$ is $\Delta T \simeq 0.2\,\mathrm{K}$. Thus we find $\frac{d}{dT}D_{0,s} \simeq 560\,\mathrm{nm/K}$ for the average temperature dependence of critical Casimir levitation [Fig. 2.14(b)], and $\frac{d}{dT}D_{0,s} \simeq 230\,\mathrm{nm/K}$ by additionally taking electrostatics into account [Fig. 2.15]. We note that in the present critical case $\frac{d}{dT}D_{0,s}$ can become arbitrarily large at temperatures corresponding to the transition from separation to stiction and the emergence of the local minimum and the local maximum of the critical Casimir potential [see Fig. 2.12 and the curves for $\xi_+ = 34\,\mathrm{nm}$ and $\xi_+ = 36\,\mathrm{nm}$ in Fig. 2.14(a)]. This shows that the critical Casimir levitation is strongly temperature dependent, even near room temperature, with the variation of stable separation $\frac{d}{dT}D_{0,s}$ being two orders of magnitude larger than the one predicted for the *quantum electrodynamic* Casimir effect in Ref. [166]. In general the colloid will not only be exposed to the critical Casimir force and to an electrostatic force but also to gravity and to laser tweezers, which generate a linearly increasing potential contribution. This attractive contribution tends to reduce the potential barriers shown in Figs. 2.14 and 2.15 and can eliminate small barriers altogether. Thus these external forces can be used to switch levitation on and off (compare a similar discussion related to the quantum electrodynamic Casimir levitation in Ref. [164, 166]).

2.7. Cylindrical colloids

Currently, there is an increasing experimental interest in *elongated* colloidal particles which have a typical diameter of up to several $100\,\mathrm{nm}$ and a much larger length (see, e.g., Refs. [111, 167, 168] and references therein). These types of colloids resemble *cylinders* rather than spheres. The description of their behavior in confined critical solvents calls for a natural extension of the studies presented in Secs. 2.2–2.5. Hence, in the present section we consider the case of a $3d$ cylinder with $(-)$ BC which is adjacent and parallel aligned to a periodically chemically patterned substrate consisting of alternating $(-)$ and $(+)$ stripes as the ones discussed in Sec. 2.5. Accordingly, the axis of rotational invariance of the cylinder is perpendicular to both the x direction [Fig. 2.1] and the direction normal to the substrate, and it is parallel to the direction of spatial translational invariance of the chemical stripes forming the pattern. As compared with the case of the sphere the analysis for the cylinder is technically simpler because the system as a whole is invariant along all directions but two, the lateral one, x, and the one normal to the substrate. (For the sphere its finite extension in the second lateral direction, which is normal to the x-axis, matters and thus leads to a basically three-dimensional problem. Accordingly, here we do not consider short cylinders, for which this finite length matters, too.) This reduction of the number of relevant dimensions allows us to perform numerical calculations of adequate precision for a range of various pattern geometries which is wider than in the case of the sphere.[15] Even though the expressions derived in Appendix B.4 can be used to study the case of a cylinder having its axis laterally displaced by an arbitrary amount X from the chemical step, our numerical calculations for the case of a chemical stripe address only the case $X = 0$. This corresponds to a lateral position of the symmetry axis of the cylinder which coincides with the center of an attractive $(-)$ stripe.

In Appendix B.4 we briefly derive the scaling behavior of the normal critical Casimir force acting on the cylinder and compare it with the case of a sphere. Then, we adapt the Derjaguin approximation appropriate for the geometry of the cylinder. On this basis, we have calculated the scaling function of the normal critical Casimir force acting on the cylinder in $d = 3$ and $d = 4$ on the basis of the Monte Carlo simulation data for the film geometry (see footnote 14 on page 40) and of the analytic MFT expression for the critical Casimir force for the film geometry [117], respectively. In addition, in order to assess the performance of the DA, we compare our results with MFT scaling functions numerically calculated within the same approach as the one of Sec. 1.2.4 [170].

Here we focus on the comparison between the DA appropriate for the cylinder and the full numerical MFT data for the scaling function $K_{\mathrm{p}}^{\mathrm{cyl}}(\lambda,\Pi,\Xi = 0,\Theta,\Delta)$ which characterizes the normal critical Casimir force in the presence of a periodically patterned substrate; λ, Π, Ξ, Θ, and Δ are defined as in the case of the sphere [see Sec. 2.5 and Appendix B.4]. Figure 2.16 shows the scaling function of the normal critical Casimir force acting on a cylinder as a function of Θ as obtained from the DA ($\Delta \to 0$) in $d = 4$ and from the full numerical MFT calculations for $\Delta = 1/3$. Besides the quantitative differences in the scaling function as a function of Θ, the *qualitative* features of the behavior of the force acting on a cylinder, which is reported in Fig. 2.16 for various values of λ, are similar to the ones for the sphere [compare Figs. 2.10 and 2.11]. For $\Pi = 1.92$ [Fig. 2.16(a)] the DA describes the actual behavior of the critical Casimir force rather well, in particular for $\Theta \gtrsim 2$, even for most values of λ. As in Figs. 2.10 and 2.11, for a certain range of values of λ the normal critical Casimir force changes sign at $\Theta_0^{\mathrm{cyl}}(\Pi,\lambda,\Xi = 0,\Delta)$. On the other hand for small periodicities ($\Pi = 0.29$ in Fig. 2.16(b)) the DA in $d = 4$ fails to describe quantitatively the actual behavior of the force as obtained from the full numerical MFT calculations. These strong deviations from the DA [Fig. 2.16(b)] indicate the relevance of effects caused by the actual non-additivity of critical Casimir forces.

For $\lambda \gtrsim 0.6$ the scaling function $K_{\mathrm{p}}^{\mathrm{cyl}}$ of the normal critical Casimir force obtained numerically and represented by symbols in Fig. 2.16(b) is very close (much closer than within the DA)

---

[15] Here, we do not consider a cylindrical colloid which is not perfectly aligned with the pattern and which would, therefore, experience a critical Casimir torque; this has been studied in detail in Ref. [169]. (The case of an elongated particle aligning parallel or perpendicular opposite to a homogeneous substrate has been studied in Ref. [111].)

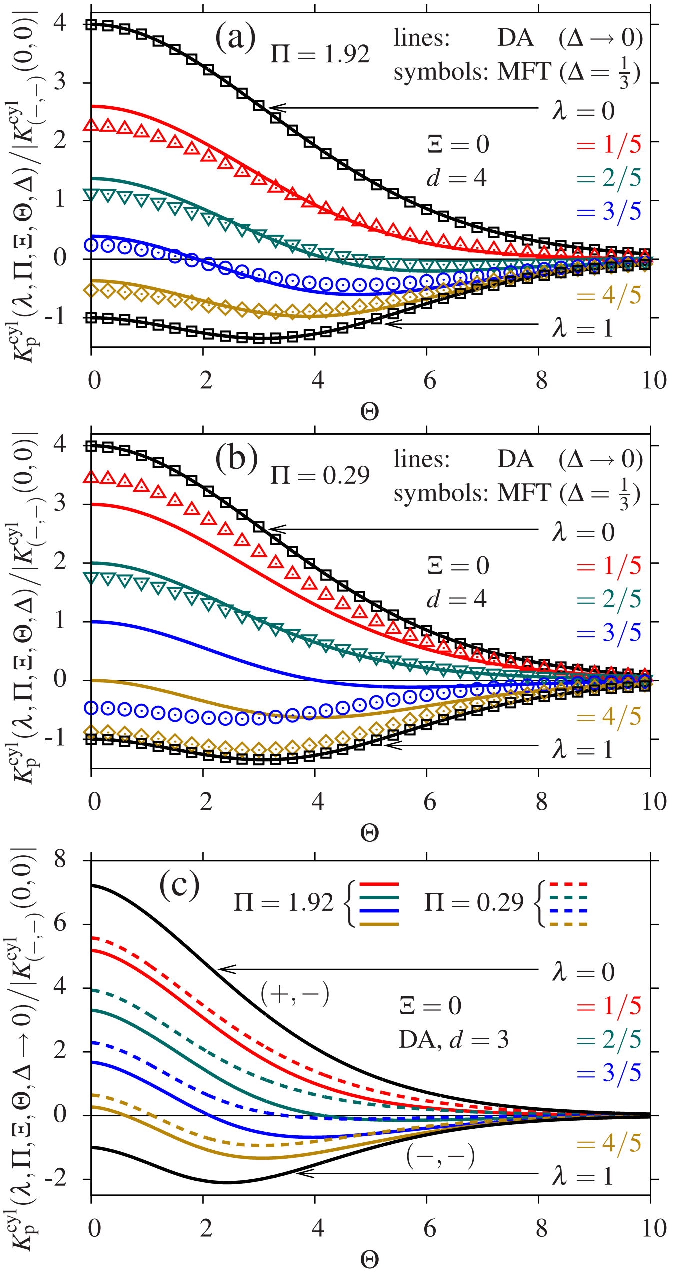

Figure 2.16: Normalized scaling function $K_{\mathrm{p}}^{\mathrm{cyl}}$ [see Appendix B.4, including expressions for $K_{(-,-)}^{\mathrm{cyl}}(0,0)$] of the normal critical Casimir force acting on a *cylindrical* colloid close to and parallel to a periodically patterned substrate. The cylinder axis is aligned with the striped pattern and positioned above the center of a $(-)$ stripe which has the same adsorption preference as the cylinder (analogous to Fig. 2.10 for a spherical colloid). In (a) for $\Pi = 1.92$ the appropriate DA describes the actual MFT data [170] rather well, and for $0.3 \lesssim \lambda \lesssim 0.7$ there is a change of sign of the force. In (b), instead, apart from the limiting homogeneous cases $\lambda = 0$ and $\lambda = 1$, for $\Pi = 0.29$ the DA fails to describe quantitatively the actual MFT data [170]. In (c) $K_{\mathrm{p}}^{\mathrm{cyl}}$ is shown for $d = 3$ within the DA based on the Monte Carlo simulation data for the film geometry (see footnote 14 on page 40) for the two cases $\Pi = 0.29$ and $\Pi = 1.92$. We expect that also in $d = 3$ the DA for $\Pi = 0.29$ is not quantitatively reliable.

to the one corresponding to the homogeneous case with $(-,-)$ BC (corresponding to $\lambda = 1$) and does not show a change of sign. This means that, even if the substrate is not homogeneous but chemically patterned — but such that the larger part of the surface still corresponds to $(-)$ BC, i.e., $\lambda \gtrsim 0.5$ — the resulting critical Casimir force acting on the colloid with $(-)$ BC resembles the behavior for laterally homogeneous $(-,-)$ BC. This can be understood in terms of the fixed point Hamiltonian in Eq. (1.6) which penalizes spatial variations of the order parameter at short scales. Thus the system tries to smooth out spatial inhomogeneities of the order parameter profile, biased by the preference of the colloidal particle. If the pattern is very finely structured, i.e., $\Pi = (L_1 + L_2)/\sqrt{RD} \ll 1$, regions with a positive order parameter close to the narrow $(+)$ stripes ($\lambda \simeq 1^-$, i.e., $L_2 \ll L_1$) extent only very little into the direction normal to the substrate and the resulting order parameter profile at a distance from the substrate remains negative only [171], so that the force resembles the one corresponding to the homogeneous case. (Note that within the DA, the corresponding order parameter profile would simply consist of a patchwork of the order parameter profiles corresponding to the film geometry, with no smoothing taking place at the edges of the various spatial regions.) Similarly, but in a weaker manner due to the opposite order parameter preference at the colloid, the curves in Fig. 2.16(b) for $\lambda \lesssim 0.5$ approach the corresponding homogeneous one for the case $(+,-)$ (i.e., $\lambda = 0$). Thus, the fact that both in Fig. 2.16(a) and Fig. 2.16(b) the curves for $\lambda = 1/5$ are less close to their limiting ones for $\lambda = 0$ than the curves for $\lambda = 4/5$ are close to the ones for $\lambda = 1$ — although the portions of the minority part of the surface are the same — is due to the fact that an order parameter profile with $(+,-)$ boundary conditions is energetically less preferred than the one with $(-,-)$ boundary conditions because in the $(+,-)$ case an interface emerges between the two phases. For broad stripes, i.e., in contrast to the case $\Pi \to 0$, the energy costs for a similar behavior are seemingly larger: the full numerical MFT data for $\lambda = 1/5$ and $\lambda = 4/5$ are less close to the corresponding limiting homogeneous cases $\lambda = 0$ and $\lambda = 1$, respectively, for $\Pi = 1.92$ than for $\Pi = 0.29$.

Figure 2.16(c) shows the scaling function $K_{\mathrm{p}}^{\mathrm{cyl}}$ of the normal critical Casimir force for $d = 3$ within the DA as obtained by using Monte Carlo simulation data for the film geometry (see footnote 14 on page 40). One can infer from Fig. 2.16(c) that the qualitative features of the MFT scaling function as described above, such as the change of sign, are carried over to $d = 3$.

As discussed in the previous section, the vanishing of the normal critical Casimir force corresponds to a stable levitation of the colloid at a distance D_0 from the substrate only if $\partial_D F_{\mathrm{p}}^{\mathrm{cyl}}|_{D=D_0} < 0$. Within the DA and at the laterally stable position $\Xi = 0$ the sign of $\partial_D F_{\mathrm{p}}^{\mathrm{cyl}}$ is given by Eq. (2.39) with K_{p} replaced by $K_{\mathrm{p}}^{\mathrm{cyl}}$. The behavior of Θ_0^{cyl} as a function of Ψ and the demarcation of the regions where levitation is stable against perturbations of D is shown in Fig. 2.17, where the solid and the dashed lines correspond to stable and unstable levitation, respectively. The behavior for the normal critical Casimir force acting on the cylinder is qualitatively similar to the one for the sphere shown in Fig. 2.12. Analogously to the case of a sphere discussed in Sec. 2.6, no stable levitation is found at $T = T_c$ or for

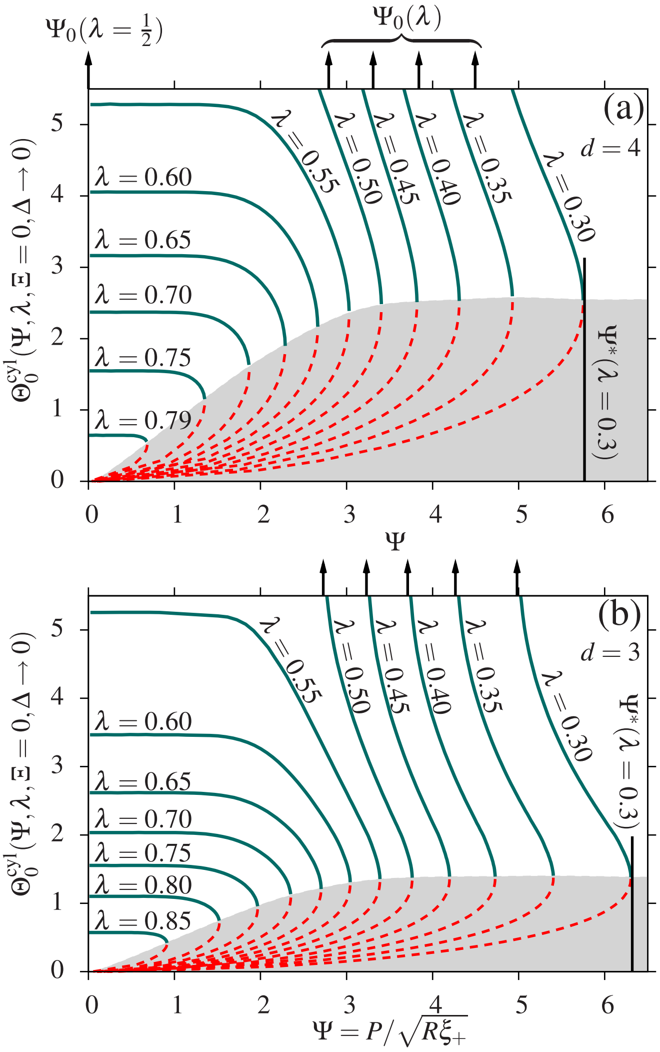

Figure 2.17: Values of the scaling variable $\Theta_0^{\rm cyl}$ at which the normal critical Casimir force $K_{\rm p}^{\rm cyl}$ acting on a cylinder close to a periodically patterned substrate vanishes as a function of $\Psi=P/\sqrt{R\xi_+}$ [compare Fig. 2.12 for the case of a sphere] within the DA. The region indicated by solid lines corresponds to the one in which the levitation of the cylinder at a height $D=D_0=\Theta_0\xi_+$ is stable against small perturbations of D, wheres in the shaded region indicated by dashed lines there is no such stable levitation although the normal critical Casimir force acting on the colloid vanishes. For $\lambda>\lambda_0$ with $\lambda_0(d=4)=4/5$ and $\lambda_0(d=3)\simeq 0.88$, $\Theta_0^{\rm cyl}$ ceases to exist, i.e., $K_{\rm p}^{\rm cyl}$ does not exhibit a zero. For $\lambda<\lambda_1$ with $\lambda_1(d=4)=1/2$ and $\lambda_1(d=3)\simeq 0.545$, $\Theta_0^{\rm cyl}(\Psi\searrow\Psi_0(\lambda))$ diverges. (The values for $\Psi_0(\lambda)$ are indicated by upward arrows.) For any $\lambda<\lambda_0$, $\Theta_0^{\rm cyl}$ exists for $\Psi<\Psi^*(\lambda)$. We expect the DA to be quantitatively reliable only for $\Psi/\sqrt{\Theta_0}\gtrsim 2$ for $\Theta_0\lesssim 4$ and for $\Psi/\sqrt{\Theta_0}\gtrsim 0.5$ for $\Theta_0\gtrsim 4$.

$\lambda > \lambda_0 = \Delta_{(+,-)}/(\Delta_{(+,-)} - \Delta_{(-,-)})$, where $\lambda_0 = 0.80$ in $d = 4$ and $\lambda_0 \simeq 0.88$ in $d = 3$. On the other hand, for $\Theta > 0$, and $\lambda < \lambda_0$, it is always possible to find values of P and R such that stable levitation of the cylinder occurs at a certain distance from the substrate. The values of λ_1 below which one has a finite value $\Psi_0(\lambda)$ at which Θ_0 diverges remain the same as for the case of a sphere, i.e., $\lambda_1(d = 4) = 1/2$ and $\lambda_1(d = 3) \simeq 0.545$; also the corresponding values of $\Psi_0(\lambda)$ remain the same [see Eq. (2.40)].

2.8. Summary

We have investigated the universal properties of the normal and lateral critical Casimir forces acting on a spherical or cylindrical colloidal particle close to a chemically structured substrate with laterally varying adsorption preferences for the species of a (near-) critical classical binary liquid mixture (at its critical composition) in which the colloid is immersed. Within the Derjaguin approximation (DA) [see Fig. B.6 in the Appendix] in spatial dimensions $d = 3$ and $d = 4$ we have derived analytic expressions for the corresponding universal scaling functions of the forces and the potentials for general fixed-point boundary conditions (BC) in terms of the scaling function of the critical Casimir force acting on two parallel, homogeneous plates. These expressions are given explicitly analytically at the bulk critical point $T = T_c$ and – for symmetry breaking boundary conditions — far away from the critical point. These relations enable one to obtain predictions for actual three-dimensional systems with a sphere-inhomogeneous plate geometry (for which currently computations are not possible) based on the scaling function for the parallel homogeneous plate geometry, for which, e.g., Monte Carlo simulation data in $d = 3$ are available. Moreover, results within mean-field theory (MFT, corresponding to $d = 4$) and symmetry-breaking boundary conditions [Sec. 1.2.4] have been obtained fully numerically and have been compared with the approximate results of the DA, which allows us to explore the limits of validity of the latter. We have studied several relevant situations [see Fig. 2.1] and our main findings are the following:

1. First, we have studied a spherical colloid immersed in a binary liquid mixture close to a chemically *homogeneous* substrate which has, compared to the colloid, the same $(-)$ or a different $(+)$ adsorption preference for one of the species of the mixture [Sec. 2.2]. Close to the bulk critical point at $T = T_c$ the critical Casimir force induced by the confinement of the order parameter (e.g., the concentration difference in a binary liquid mixture) can be described in terms of universal scaling functions depending on the surface-to-surface distance D of the colloid from the substrate scaled by the bulk correlation length, $\Theta = \mathrm{sign}((T - T_c)/T_c)D/\xi_\pm$, and its ratio with the radius of the colloid, $\Delta = D/R$ [Eqs. (2.1) and (2.2)]. The scaling functions obtained within the DA [Eqs. (2.6) and (2.7)] are valid for $\Delta \to 0$. From the comparison with the full numerical MFT results [Fig. 2.2] we find that in $d = 4$ the DA describes the actual behavior quite well for $\Delta \lesssim 0.4$. Based on

Monte Carlo simulation data for the scaling function of the critical Casimir force between parallel, homogeneous plates and within the DA we have obtained also the scaling function for the critical Casimir force on a spherical colloid close to a homogeneous substrate in $d = 3$ [Fig. 2.2].

2. The basic building block of a chemically patterned substrate is a *chemical step*, which we have studied in Sec. 2.3. Due to the broken translational invariance in one lateral direction (x) the critical Casimir forces and potentials acquire a dependence on the additional scaling variable $\Xi = X/\sqrt{RD}$, which corresponds to the lateral distance X of the center of the spherical colloid from the position of the chemical step along the plane [Eqs. (2.8), (2.10), and (2.17)]. Due to the different boundary conditions on both sides of the chemical step a *lateral* critical Casimir force emerges, which leads to a laterally varying potential for the colloid [Fig. 2.3]. In the limit $\Delta \to 0$ both the scaling function for the potential and for the lateral critical Casimir force as obtained within the DA are in agreement with the full numerical data [Fig. 2.4]. We have derived the corresponding scaling functions within the DA also in $d = 3$ by using Monte Carlo data for the parallel plate geometry [Figs. 2.3 and 2.4].

3. Section 2.4 deals with the critical Casimir forces and the corresponding potential acting on a spherical colloid in front of a *single chemical lane* of width $2L$, which additionally depends on a fourth scaling variable $\Lambda = L/\sqrt{RD}$ [Eqs. (2.21) and (2.22)]. It turns out that within the DA the scaling functions for the critical Casimir force and the critical Casimir potential across a chemical lane can be expressed in terms of the ones for the chemical step [Eqs. (2.25) and (2.26)]. For large values of Λ the resulting potential can be described as a suitable superposition of chemical steps, whereas for $\Lambda \lesssim 3$ one has explicitly to account for the finite width of the chemical stripe [Fig. 2.5]. Comparing the results of the DA with the ones obtained by a full numerical analysis, one finds that the DA describes the actual behavior quite well for $\Delta \lesssim 0.4$, even for small Λ. Seemingly, in this respect, the nonlinearities inherent in the critical Casimir effect and edge effects do not considerably affect the resulting scaling functions [Fig. 2.6].

4. On the basis of the results of Sec. 2.4, in Sec. 2.5 we have studied the universal scaling functions of the critical Casimir force and the corresponding potential for a sphere opposite to a *periodically patterned substrate* with laterally alternating chemical stripes of different adsorption preferences [Sec. 2.5]. These scaling functions [Eqs. (2.27) and (2.28)] depend, besides the scaling variables Θ, Δ, and Ξ, on two additional scaling variables $\Pi = P/\sqrt{RD}$ and $\lambda = L_1/P$, which correspond to the period $P = L_1 + L_2$ of the pattern and to the width $L_1 \leq P$ of the stripes with the same adsorption preference as the colloid. The scaling function for the normal critical Casimir force obtained within the DA can be expressed in terms of the one for the chemical step and describes the ac-

tual behavior well for $\Pi \gtrsim 2$ [Eq. (2.31) and Figs. 2.7, 2.8(a) and 2.10(a)]. However, for $\Pi \to 0$ [Eq. (2.33)] the DA fails to capture quantitatively the numerically obtained behavior within MFT, reflecting the importance of nonlinearities and edge effects in this context, which are not accounted for by the DA [Figs. 2.7, 2.8(a) and 2.10(b)]. The failure of the DA in the limit $\Pi \to 0$ can be traced back to the fact that for the *film* geometry of a patterned wall next to a laterally homogeneous flat wall, additivity of the critical Casimir forces does not hold [Fig. 2.9].

5. The MFT scaling function of the normal critical Casimir force acting on a colloid close to a periodically patterned substrate shows a remarkable behavior as a function of $\Theta = D/\xi_+$. Within a certain range of values of Π and λ the critical Casimir force vanishes at Θ_0 corresponding to a distance $D = D_0$ between the colloid and the substrate. We have analyzed the sign of the derivative of the critical Casimir force with respect to D at D_0, which is negative if for $D < D_0 = D_{0,s}$ the colloid is repelled from the substrate whereas for $D > D_0 = D_{0,s}$ it is attracted to the substrate [Fig. 2.12]. This means that in the absence of other forces the colloid can levitate above the substrate at a stable distance which can be tuned by temperature. Stable levitation points are found also in $d = 3$, within the DA and on the basis of the Monte Carlo data for the parallel plate geometry [Figs. 2.8(b), 2.11, and 2.12(b)]. Our analysis shows that *at* the critical point $T = T_c$ levitation is not possible, whereas off criticality a geometrical configuration leading to stable levitation can always be found [Fig. 2.13]. For fixed geometrical parameters, the critical Casimir potential as a function of D changes from a monotonic behavior to a non-monotonic one upon approaching criticality; a local maximum and a local minimum, the latter corresponding to stable levitation, occur [Fig. 2.14(a) and (b)]. Experimentally, this corresponds to a de facto irreversible transition from separation to stiction of a colloid and a patterned substrate. The depths of these potential minima can be up to several $k_B T$ so that the levitation is stable against Brownian motion of the colloid. The critical Casimir levitation can be rather pronounced and robust even in the presence of electrostatic interactions [Fig. 2.15]. The levitation height is proportional to the bulk correlation length and thus can be tuned by varying temperature. Depending on the geometric parameter λ we have identified two distinct types of temperature dependences of the levitation height $D_{0,s}$ [Fig. 2.13]. In both cases it exhibits a high temperature sensitivity $\frac{d}{dT} D_{0,s}$ which, for realistic examples at ambient temperature, is of the order of several $100\,\mathrm{nm/K}$. These results show that the periodic patterning of the substrate enables one to design critical Casimir forces over a wide range of properties.

6. This behavior is also observed for a *cylindrical* colloid which lies parallel to the substrate such that its axis is aligned with the translationally invariant direction of the stripes [Sec. 2.7 and Appendix B.4]. The main features of the scaling function for the corresponding normal critical Casimir force are similar to the ones for the spherical colloid:

the DA describes well the actual behavior as obtained from full numerical MFT calculations for large values of Π, but fails quantitatively for $\Pi \lesssim 2$ [Fig. 2.16]. The numerical studies for $\Pi \to 0$ indicate that a substrate with a very fine pattern, dominated by one of the two BC as far as the corresponding covered area is concerned, leads to a normal critical Casimir force which resembles the one for a homogeneous substrate characterized by the dominating BC [Fig. 2.16(b)]. Based on Monte Carlo data for the parallel plate geometry we calculated within the DA the critical Casimir force acting on a cylinder in $d = 3$ [Fig. 2.16(c)]. Above a chemically patterned substrate, also for a cylinder stable levitation is possible for a wide range of parameters [Fig. 2.17].

3. Comparison with experiments

3.1. Introduction

The critical Casimir effect acting on colloidal particles immersed in a binary liquid mixture of water and 2,6-lutidine and close to substrates which are chemically patterned with stripes of antagonistic adsorption preferences obtained via different surface preparation techniques has been investigated experimentally by *Florian Soyka et al.* [37, 38] and by *Dominik Vogt et al.* [39, 40]. Their measurements provide strong evidence for the occurrence of *lateral* critical Casimir forces in addition to ones along the normal direction. Upon approaching the critical point of the solvent, laterally confining potentials for the colloids are generated by the critical Casimir effect.

Here,[16] we analyze theoretically in detail the rich behavior of the spherical colloids close to such substrates, including also background forces in excess to the critical Casimir forces. As shown below, our theoretical analysis provides accurate information also about the vertical probability distribution of the positions of the colloidal particles which, however, cannot be resolved by the kind of video microscopy used in the aforementioned experiments. In comparing the measured data with our theoretical predictions it turns out that the critical Casimir potential resulting from a chemical pattern depends rather strongly on its geometrical details and it provides a sensitive tool to probe these microscopic features, which might not be easily accessible otherwise. Indeed, the experimental data obtained for the substrates prepared via a focused ion beam [37, 38] compare only with our corresponding theoretical predictions when assuming that the chemical steps between two subsequent stripes within the pattern are not microscopically sharp due to the fluctuations inherent to the preparation process of the structures. On the other hand, the measurements of the critical Casimir potentials for the colloids close to substrates prepared via microcontact printing [39, 40] agree with the corresponding theoretical predictions for all substrates that were analyzed. Since the strength of these confining potentials can be tuned by minute temperature changes, this provides a new technique for "trapping" and controlling colloids as model systems, opening encouraging perspectives for applications.

In both experiments [37, 40], a dilute suspension of charged spherical colloids, imposing $(-)$ BC to the order parameter of the (near-) critical solvent, is exposed to a chemically patterned substrate, the surface of which consists of alternating stripes, which impose $(-)$ and $(+)$ BC.

---

[16] Parts of this chapter have been published in advance in Refs. [40, 51].

The equilibrium spatial distribution of colloids was measured via digital video microscopy and from it one can define an effective potential for a single colloid, which varies laterally due to critical Casimir forces. In the experimental setups described below, the lower critical demixing point of the water-lutidine mixture is always approached from the homogeneous (mixed) phase at temperatures $T < T_c$ upon increasing T at *fixed critical composition* of the mixture. Thus, in the following we ignore the difference of the behavior of the correlation length above and below T_c, and do not keep track of the subscripts "$\pm$" for $\xi_\pm$, because we are exclusively dealing with $\tau > 0$, and the bulk correlation length ξ is always associated with ξ_+. Moreover, we do not consider bulk fields, which would correspond to an off-critical composition of the binary liquid mixture.

3.2. Theory

3.2.1. Critical Casimir potential

As described in Chapters 1 and 2, according to renormalization group theory, in the vicinity of the critical point at $T = T_c$ the normal and lateral critical Casimir forces as well as the corresponding potential can be described by universal scaling functions. The relevant thermodynamic properties which emerge upon approaching the point of the continuous phase transition can be understood and analyzed in terms of the fluctuations of the order parameter ϕ of the phase transition. For the consolute point of phase segregation of a binary liquid mixture ϕ is given by the difference between the local and the mean concentration of one of the two components of the mixture; the corresponding bulk universality class is of the so-called Ising type (see Sec. 1.2). The local enhancement of the order parameter at the confining surfaces is effectively described by symmetry-breaking surface fields and it is denoted by $(+)$ and $(-)$ boundary conditions corresponding to having a preference for $\phi > 0$ and $\phi < 0$, respectively, at the surface. For the water-lutidine mixture we are interested in, one conventionally indicates the preferential adsorption for lutidine and water as $(+)$ and $(-)$ BC, respectively (see also Refs. [20, 21]). From the experimental point of view it is rather difficult to quantify the strength of the adsorption preference exhibited by the different portions of the surfaces. Therefore the comparison with theoretical predictions requires assumptions, which can be verified *a posteriori*. In the present case we have qualitative experimental evidence that the chemical treatment of the surfaces results in rather pronounced adsorption preferences and therefore we shall assume that the surfaces are characterized by the *strong critical adsorption* fixed point (see Sec. 1.2). Thus, for the comparison with the experimental data, we consider neither the case of weak adsorption at the surfaces (see, e.g., Refs. [33, 35]) nor the effects due to off-critical compositions of the mixture, which might lead to a bridging transition analogous to capillary condensation (see, e.g., Refs. [21, 44, 172–176]).

In Sec. 2.5, for a spherical colloid with $(-)$ BC opposite to a chemically patterned substrate with alternating $(+)$ and $(-)$ BC the critical Casimir potential has been calculated both numerically within full mean-field theory (corresponding to $d=4$) and by resorting to the so-called Derjaguin approximation exploiting the full knowledge of $k_{(+,\pm)}$ in the film geometry for $d=3$. Accordingly, the critical Casimir force and the critical Casimir potential for a colloid close to a chemically patterned wall can be expressed in terms of universal scaling functions which take the geometry into account and which depend on the following scaled quantities:[17]

- $\Theta = z/\xi$, where z is the surface-to-surface distance between the colloid and the substrate and ξ is the bulk correlation length of the (near-) critical binary liquid mixture,
- $\Delta = z/R$, where R is the radius of the spherical colloid,
- $\Xi = x/\sqrt{Rz}$, where x is the lateral coordinate of the center of the colloid such that $x=0$ corresponds to the colloid being located opposite to the center of a stripe with $(-)$ BC,
- $\Pi = P/\sqrt{Rz}$, where P is the periodicity of the stripe pattern along the x-direction,
- $\lambda = L_-/P$, where L_- is the width of the stripes with $(-)$ BC.

According to Eq. (2.28) in $d=3$ the critical Casimir potential Φ_C can be written as

$$\Phi_\mathrm{C}(L_-,P,x,z,R,T) = k_BT\frac{R}{z}\vartheta_\mathrm{p}(\lambda,\Pi,\Xi,\Theta,\Delta), \tag{3.1}$$

where ϑ_p is a universal scaling function [Eq. (2.30)]. The realization of the present geometrical setup of a sphere facing a plane still represents a challenge for lattice based Monte Carlo simulations. Accordingly, up to now it is not possible to obtain accurate numerical data for this three-dimensional geometry and therefore one has to rely on the *Derjaguin approximation*, based on the assumption of additivity, in order to calculate approximately the critical Casimir potential. Within the Derjaguin approximation, the scaling function ϑ_p can be expressed in terms of the known scaling functions $k_{(\pm,-)}$ for the film geometry [Eq. (1.3)] via Eqs. (2.30), (2.7), (2.14), and (B.43):

$$\vartheta_\mathrm{p}(\lambda,\Pi,\Xi,\Theta,\Delta\to 0) = \frac{\vartheta_{(+,-)}(\Theta)+\vartheta_{(-,-)}(\Theta)}{2} + \frac{\vartheta_{(+,-)}(\Theta)-\vartheta_{(-,-)}(\Theta)}{2}\omega(\lambda,\Pi,\Xi,\Theta), \tag{3.2}$$

where

$$\vartheta_{(\pm,-)}(\Theta) = 2\pi\int_1^\infty \mathrm{d}\beta\,(\beta-1)\,\beta^{-3}k_{(\pm,-)}(\beta\Theta) \tag{3.3}$$

---

[17] See also Fig. 2.1. Note that, since we include in the following also gravity and in order to make explicit that the colloids are vertically positioned *above* the substrate, here we denote the surface-to-surface distance between the colloid and the substrate as "z", which in Chapter 2 was denoted as "D". For convenience, in the following the lateral position of the colloidal particle is denoted as "x", which in Chapter 2 was denoted as "X".

are the scaling functions of the critical Casimir potential of a colloid in front of a homogeneous wall as calculated within the Derjaguin approximation [20], and

$$\omega_{\mathrm{p}}(\lambda,\Pi,\Xi,\Theta) = 1 + \sum_{n=-\infty}^{\infty} \left\{ \omega_{(+|-,-)}(\Xi+\Pi(n+\tfrac{\lambda}{2}),\Theta) - \omega_{(+|-,-)}(\Xi+\Pi(n-\tfrac{\lambda}{2}),\Theta) \right\} \tag{3.4}$$

with $\omega_{(+|-,-)}$ given by

$$\omega_{(+|-,-)}(\Xi \gtrless 0,\Theta) = \mp 1 \pm \frac{\Xi^4 \int_1^\infty \mathrm{d}s \frac{s\arccos\left(s^{-1/2}\right)-\sqrt{s-1}}{(1+\Xi^2 s/2)^d} \Delta k\left(\Theta[1+\Xi^2 s/2]\right)}{\vartheta_{(+,-)}(\Theta)-\vartheta_{(-,-)}(\Theta)}, \tag{3.5}$$

where $\Delta k(\Theta) = k_{(+,-)}(\Theta) - k_{(-,-)}(\Theta)$. For $\Theta = 0$ and $\Theta \gg 1$ the analytic expressions for $\omega_{(+|-,-)}$ given in Eqs. (2.15) and (2.16) hold. In Chapter 2 the accuracy of the Derjaguin approximation has been checked numerically within mean-field theory and it has turned out that this approximation describes quantitatively the actual behavior of those numerical data which correspond to $\Theta \gtrsim 4$ for $\Delta \lesssim 1$ and $\Pi \gtrsim 0.5$, as well as to $0 \leq \Theta \lesssim 4$ with $\Delta \lesssim 0.3$ and $\Pi \gtrsim 2$. In the experiments discussed further below the corresponding values of Θ, Δ, and Π vary within these ranges so that, assuming that the previous quantitative conclusions extend to $d = 3$, we expect the Derjaguin approximation to be quantitatively reliable.

3.2.2. Background forces

In addition to the critical Casimir force due to the critical fluctuations of the solvent, the colloidal particles of the suspension are subjected to additional effective forces which are characterized by a smooth and rather mild dependence on temperature. Typical background forces acting within the colloidal suspensions of present interest are due to (screened) electrostatic and dispersion interactions and to the gravitational field. In a first approximation, which neglects possible mutual influences of these forces,[18] their total potential is given by the sum of the corresponding contributions: (i) the electrostatic potential Φ_{el}, (ii) the gravitational potential Φ_{g}, (iii) the van der Waals interaction Φ_{vdW}, and (iv) the effective critical Casimir potential Φ_{C}.

Electrostatics

This interaction originates from the fact that, due to the formation of charge double-layers (see, e.g., Ref. [92] and references therein), the surface of the colloids and of the substrate acquire a surface charge once immersed in the liquid solvent. As a result, the polystyrene colloids of radius $R = 1.2\,\mu\mathrm{m}$ and $(-)$ BC immersed in water-lutidine mixtures experience an electrostatic repulsion from the substrate. The screened electrostatic potential of the colloid at a surface-to-surface distance z from a *homogeneous* substrate with $(\pm)$ BC is well approximated by

$$\Phi_{\mathrm{el},\pm}(z)/(k_B T) = \exp\{-\kappa(z - z_0^{\pm})\}, \tag{3.6}$$

---

[18] Note that the interplay between critical phenomena and electrostatics is rather subtle when the salt density is much higher than the one for the experiments discussed here (see Chap. 5).

where κ^{-1} is the screening length and $z_0^{\pm}$ describes the strength of the electrostatic repulsion from the substrate with $(\pm)$ BC. Although the values of these parameters are determined by the surface charge of the colloid, the dielectric constant of the mixture etc. [177], here they will be treated as fitting parameters of the actual experimental data for $\Phi_{\mathrm{el},\pm}$. In experimental conditions similar to the present ones as far as the mixture and the colloids are concerned, one finds $\kappa^{-1} \simeq 12\,\mathrm{nm}$ [20, 21, 35] and $z_0^{\pm} \simeq 0.1\,\mu\mathrm{m}$ to $0.2\,\mu\mathrm{m}$ [20, 21, 35] as typical values at $T \simeq T_c \simeq 307K$. In view of a possible difference between z_0^{+} and z_0^{-}, the resulting electrostatic potential of a colloid close to a *patterned* substrate such as the one described above depends on the lateral position x of the colloid. Such a dependence can be accounted for theoretically within the Derjaguin approximation (by repeating the calculations described in Appendix B for Φ_{C}), which is expected to be particularly accurate due to the exponential decay of $\Phi_{\mathrm{el},\pm}$ in Eq. (3.6) as a function of the distance z from the substrate. For this electrostatic potential $\Phi_{\mathrm{el}}(x,z)$ one therefore finds (for a colloid facing the center of a $(-)$ stripe at $x=0$)

$$\Phi_{\mathrm{el}}(x,z) = \frac{\Phi_{\mathrm{el},+}(z)+\Phi_{\mathrm{el},-}(z)}{2} + \frac{\Phi_{\mathrm{el},+}(z)-\Phi_{\mathrm{el},-}(z)}{2}\Omega(x), \tag{3.7}$$

where

$$\Omega(x) = 1 + \sum_{n=-\infty}^{\infty} \left\{ \mathrm{erf}([x+nP-L_-/2]/\Lambda) - \mathrm{erf}([x+nP+L_-/2]/\Lambda) \right\}, \tag{3.8}$$

with $\Lambda = \sqrt{2R\kappa^{-1}} \simeq 0.17\,\mu\mathrm{m}$. Ω and Φ_{el} depend on the geometric parameters L_- and P describing the pattern.

Dispersion forces

For the particular choice of materials and conditions used in the present experiments, van der Waals forces turn out to be negligible compared with the other contributions [20, 21, 178]. In addition, the dielectric permittivity $\varepsilon(T)$ of the water-lutidine mixture is temperature dependent. Upon approaching the critical point, $\varepsilon(T)$ exhibits a weak cusplike singularity $\varepsilon(T)-\varepsilon(T_c) \propto |\tau|^{1-\alpha}$, where $\alpha \simeq 0.11$ is the critical exponent of the specific heat for the three-dimensional Ising universality class [179]. This weak variation of $\varepsilon(T)$ might affect the strength of the van der Waals forces, as well as the range of the electrostatic interaction Φ_{el} [20]. However, in the (near-) critical mixture of water and lutidine, the permittivity $\varepsilon(T)$ turns out to vary less than 1% for $|T_c - T| < 1\,\mathrm{K}$ [180], and therefore the van der Waals forces as well as the electrostatic interaction are expected to be not affected significantly.

Gravity

Due to buoyancy the colloid immersed in the solvent above the patterned substrate experiences a gravitational potential given by

$$\Phi_{\mathrm{g}}(z) = (\rho_{\mathrm{PS}} - \rho_{\mathrm{WL}})g\frac{4\pi}{3}R^3\, z \equiv Gz, \tag{3.9}$$

where $\rho_{\mathrm{PS}} \simeq 1.055\,\mathrm{g/cm^3}$ and $\rho_{\mathrm{WL}} \simeq 0.988\,\mathrm{g/cm^3}$ [181] are the mass densities of the polystyrene colloid and of the water-lutidine mixtures at the critical composition and near T_c, respectively, and $g \simeq 9.81\,\mathrm{m\,s^{-2}}$ is the gravitational acceleration. Accordingly, at $T \simeq 307\,\mathrm{K}$ one has $G \simeq 1.12\,k_BT\,\mu\mathrm{m}^{-1}$ and therefore, compared to the other contributions, it turns out that the gravitational potential depends rather mildly on the distance z because it varies only over a few k_BT on the relevant length scale of a few microns. The expression in Eq. (3.9) assumes that the colloidal particle of mass density ρ_{PS} is floating in a homogeneous medium of mass density ρ_{WL}. However, the laterally varying adsorption preferences of the substrate induce the formation of alternating water-rich or lutidine-rich regions close to the surface of the patterned substrate, which laterally alter the resulting mass density of the solvent as a consequence of water and lutidine having different mass densities. This implies that the effective gravitational constant G acquires a dependence on x. In addition, the preferential adsorption of the colloid, with the ensuing formation of an adsorption profile around it, can lead to a modification of the effective density ρ_{PS} of the colloid itself. However, on the basis of our estimates, we expect all these effects to be negligible for the present experimental conditions [182].

3.2.3. Total potential

The total potential Φ of the sum of the forces acting on the colloid is given by

$$\Phi(x,z,T) = \Phi_{\mathrm{C}}(L_-,P,x,z,R,T) + \Phi_{\mathrm{el}}(x,z) + \Phi_{\mathrm{g}}(z), \tag{3.10}$$

where the theoretical expressions for the individual contributions are given by Eqs. (3.1), (3.7), and (3.9). Here and in the following we do not indicate the dependence of Φ on L_-, P, and R, because the values of these parameters are fixed for each individual experiment. Figure 3.1 shows the total potential $\Phi(x,z,T)$ of a single colloid with $(-)$ BC opposite to a chemically patterned substrate, as a function of both x and z and for three values of the temperature T close to the critical value T_c. These three values correspond to different correlation lengths ξ, as indicated in the figure. The gray area in the x-z plane indicates the vertical projection of the stripe with $(-)$ BC, the center of which corresponds to $x = 0$. In Fig. 3.1 the white part of the x-z plane corresponds to the projection of the stripe with $(+)$ BC, the center of which is located at $x = P/2 = 0.9\,\mu\mathrm{m}$. The potential of the forces acting on the colloid is translationally invariant along the y-direction which is not shown in Fig. 3.1. $\Phi(x,z,T)$ in Fig. 3.1 has been calculated by using geometrical and interaction parameters which mimic the actual experimental conditions and by using values of the correlation length ξ which are experimentally available. As anticipated above, Fig. 3.1 clearly shows that the gravitational tail of the potential, which characterizes $\Phi(x,z,T)$ at large values of z, is indeed rather flat on the scales of k_BT and of hundreds of nm. As a consequence of thermal fluctuations — which cause the colloid to explore a region of space within which the total potential Φ differs from its minimum by a few k_BT — the particle is expected to display large fluctuations $\Delta z \simeq k_BT/G$ along the vertical direction.

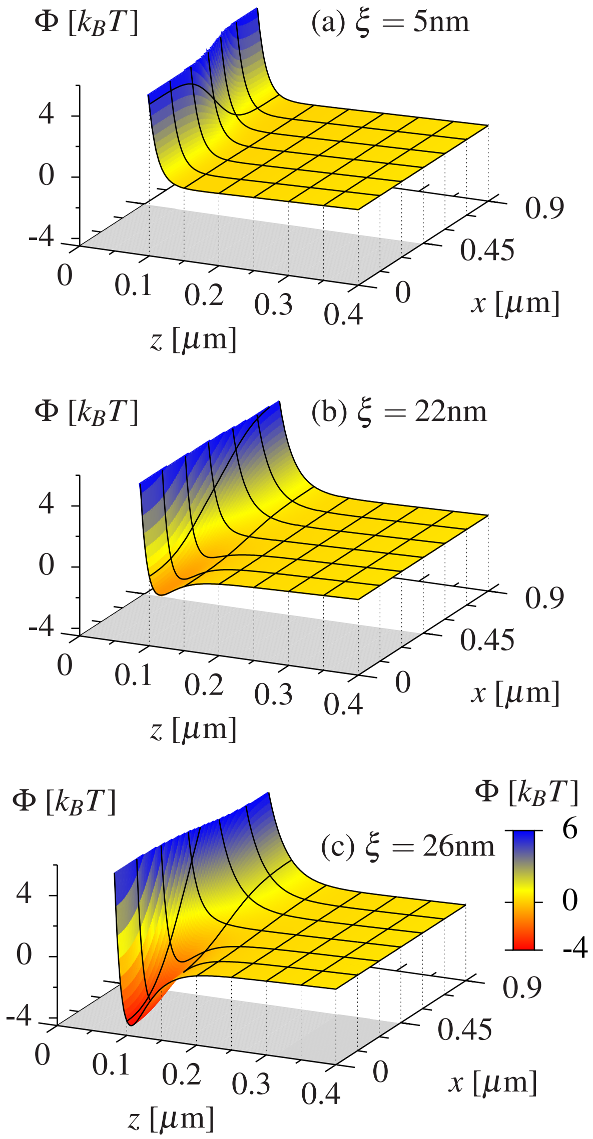

Figure 3.1: Total potential $\Phi(x,z,T)$ of a colloid with radius $R = 1.2\,\mu\text{m}$ opposite to a chemically patterned substrate with $L_- = 0.9\,\mu\text{m}$ and $P = 1.8\,\mu\text{m}$ for three temperatures corresponding to (a) $\xi = 5\,\text{nm}$, (b) $\xi = 22\,\text{nm}$, and (c) $\xi = 26\,\text{nm}$, respectively. The electrostatic potential corresponds to $z_0^- = 0.12\,\mu\text{m}$, $z_0^+ = 0.08\,\mu\text{m}$, and $\kappa^{-1} = 12\,\text{nm}$ (see the main text for details). At small separations $z \lesssim z_0^\pm$, the colloid is strongly repelled from the substrate due to electrostatics. The effective gravitational potential associated with buoyancy is rather flat, with a spatial slope $G \simeq 1.12\,k_BT\mu\text{m}^{-1}$. Accordingly, the surface-to-surface particle-substrate distance z exhibits large thermal fluctuations of the order of $k_BT/G \simeq 1\,\mu\text{m}$ as long as ξ is small. Upon approaching the critical point [from (a) to (c)], ξ increases and a deep, local potential minimum arises rapidly as a function of ξ above that part of the substrate (indicated by the shaded area) with the same preferential adsorption as the colloid. The colloid is eventually confined in this deep potential well at a distance $z \simeq z_0^-$ with almost no vertical fluctuations. The black lines correspond to cuts through the potential surface at constant values of z and x, respectively.

At small particle-substrate distances electrostatic forces are responsible for the strong repulsion of the colloid from the substrate. In Fig. 3.1 we allowed for a lateral inhomogeneity of the electrostatic potential (i.e., $z_0^+ \neq z_0^-$), which might occur due to different surface charges on the different stripes. This is clearly visible in panel (a) of Fig. 3.1, which corresponds to a rather small value of the correlation length ξ so that, within the range $z \simeq 0.1\,\mu\text{m}$ Fig. 3.1(a) refers to, the contributions of the critical Casimir force are negligible. In this case, the x-dependent electrostatic contribution dominates at small values of z, whereas the laterally homogeneous gravitational potential dominates at larger distances. However, upon approaching the critical point [Figs. 3.1(b) and 3.1(c)], the correlation length ξ increases and the critical Casimir force acting on the colloid builds up; it is repulsive within the region with $(+)$ BC whereas it is attractive within the region with $(-)$ BC. In the latter case the behavior of the colloid is eventually determined by the electrostatic repulsion and the attractive critical Casimir force, whereas in the former case it is determined by gravitation and the repulsive Casimir effect. Above a certain threshold value of ξ, which depends on the specific choice of the various geometrical and physical parameters, a very deep and steep potential well develops rapidly close to the stripe with $(-)$ BC, which therefore confines the vertical motion of the colloid at much smaller values of z than before with very limited thermal fluctuations of the particle-wall distance. In contrast, the vertical repulsive critical Casimir force, which the colloid experiences above the stripe with $(+)$ BC, pushes it further away from the surface, but the corresponding fluctuations of the vertical position z (still limited only by the gravitational tail) are not significantly affected. Thus, the full theoretical analysis of the various forces at play reveals a rather interesting energy landscape which is strongly temperature dependent.

3.2.4. Measured potential

In order to measure experimentally the total potential Φ of the forces acting on a colloid a very effective approach consists in monitoring the equilibrium Brownian motion of a *single* particle and inferring from the sampled probability distribution function $\bar{P}(x,y,z) \propto \exp(-\Phi(x,z,T)/k_BT)$ the potential as $\Phi/(k_BT) = -\ln\bar{P} + const$, where x and y are the lateral coordinates of the projection of the colloid center onto the substrate surface. This approach forms the basis of total internal reflection microscopy, which has been used in Refs. [20, 21, 35] to study critical Casimir forces. Alternatively, one can study a colloidal *suspension* which is sufficiently dilute so that the inter-particle interaction is negligible. In this case, the mean equilibrium number density $\rho(x,y,z)$ of the colloids at position (x,y,z) is proportional to the single-colloid probability distribution function $\bar{P}$ and therefore it is again given by $\rho(x,y,z) \propto \exp(-\Phi(x,z,T)/k_BT)$. In the experimental setup described below, the positions of the centers of the colloids are monitored via a digital video camera positioned below the substrate. Accordingly, the surface-to-surface distances z of the colloids from the substrate are not resolved and the camera records only the projected number density $\rho_\mathrm{P}(x,y) \equiv \int_0^\infty \mathrm{d}z\, \rho(x,y,z)$.

Due to the translational invariance of the chemical pattern along the y direction of length $l \gg P, R$, the density $\rho_{\mathrm{P}}(x,y)$ can be conveniently projected further onto the x-axis, resulting in an effective number density $\hat{\rho}(x) = l^{-1}\int_0^l \mathrm{d}y\, \rho_{\mathrm{P}}(x,y) = l^{-1}\int_0^l \mathrm{d}y \int_0^\infty \mathrm{d}z\, \rho(x,y,z)$, which depends only on x. This projection increases the statistics and therefore the accuracy with which this projected density can be determined experimentally. Subsequently, an effective potential $\hat{V}(x)$ (up to an irrelevant additive constant) can be associated with $\hat{\rho}(x)$ such that $\hat{\rho}(x) \propto \exp(-\hat{V}(x)/(k_B T))$. (Note that due to the thermal fluctuations of the colloids along the vertical direction, even if one knows the average distance $z_{\mathrm{avg}}(x)$ of the colloid from the substrate at a certain lateral position x, the effective potential $\hat{V}(x)$ is not simply given by $\Phi(x, z_{\mathrm{avg}}(x), T) + const$, as it was implicitly assumed in Ref. [37].) The measured potential

$$\delta\hat{V}(x) = \hat{V}(x) - \hat{V}(P/2) = -k_B T \ln(\hat{\rho}(x)/\hat{\rho}(P/2)) \tag{3.11}$$

is eventually defined such that it vanishes for a colloid opposite to the center of a repulsive $(+)$ stripe at $x = P/2$. We emphasize that $\delta\hat{V}(x)$ contains universal ingredients stemming from the scaling function associated with Φ_{C} (see Eq. (3.10)) as well as nonuniversal contributions due to Φ_{el} and Φ_{g}.

3.2.5. Non-ideal stripe patterns

Due to the preparation process (see below) the actual position $x = x_s(y)$ of each chemical step separating two adjacent stripes might vary smoothly along the y-axis. This variation affects the measured effective potential $\hat{V}$ of the colloids as long as it occurs on a length scale which is comparable or smaller than the typical distance ℓ_{msd} along the y-axis which each particle explores during the acquisition of the images by the camera. The images aquired during the experiments allow one to estimate such a mean-square displacement ℓ_{msd} to be of the order of tens of µm [37, 39, 40]. The projection along the y-axis, which yields the density $\hat{\rho}(x)$, effectively causes a broadening of $\hat{\rho}(x)$ compared to the case of straight (ideal) chemical steps with $x_s(y) = const$. In addition, locally a smooth intrinsic chemical gradient of the step leads to such an effect, too. For illustration purposes, we first consider a single chemical step, which is ideally located at $x = 0$ and which generates a potential $\Phi(x,z,T)$. (This reasoning can be extended to the periodic chemical pattern we are presently interested in by assuming additivity of the forces, analogously as presented in Chap. 2.) In order to estimate the effect of these variations of the actual position of the step along the y-axis, we assume that the local position $x_s(y)$ of the step does not change significantly along the y-axis on the scale of the radius R of the colloid, so that on this scale it can be considered as ideal and therefore generates a potential $\Phi(x - x_s(y), z, T)$. For $x_s(y)$ we assume an effective Gaussian distribution $p(x_s)$ along the y-axis, with zero average and standard deviation Δx. Accordingly, the projection $l^{-1}\int_0^l \mathrm{d}y$ along the y-axis turns into $\int_{-\infty}^{\infty} \mathrm{d}x_s p(x_s)$ and affects the resulting projected density $\hat{\rho}(x)$ and the resulting potential $\hat{V}(x)$ [see Eq. (3.11)].

3.2.6. Particle-substrate distance

The theoretical knowledge of the total potential $\Phi(x,z,T)$ [see Eq. (3.10)] allows one to predict the particle-substrate distance z as a function of the lateral variable x and temperature, a quantity which is not accessible to the experiments discussed below. As anticipated above, the rather small value of G in Eq. (3.9) is responsible for rather large fluctuations of the particle-substrate distance z around the position $z = z_{\mathrm{min}}(x)$ at which the potential $\Phi(x,z,T)$ has a minimum as a function of z for a fixed lateral position x of the particle and which corresponds to the position of mechanical equilibrium. In the presence of these large fluctuations it is convenient to consider the x-dependent mean particle-substrate distance $z_{\mathrm{avg}}(x)$, which is determined by the probability distribution function $\bar{P}$ of the colloid, i.e., by the total potential as[19]

$$z_{\mathrm{avg}}(x) = \frac{1}{N(x)} \int\limits_0^\infty \mathrm{d}z\, z \,\exp\{-\Phi(x,z,T)/(k_BT)\}, \tag{3.12}$$

where $N(x) = \int_0^\infty \mathrm{d}z\, \exp\{-\Phi(x,z,T)/(k_BT)\}$ is the normalization. In order to describe the thermal fluctuations of the vertical position of the colloid it is convenient to consider the probability $\bar{P}_<(z;x)$ that for a fixed lateral position x the colloid has a surface-to-surface distance from the substrate smaller than a given z:

$$\bar{P}_<(z;x) = \frac{1}{N(x)} \int\limits_0^z \mathrm{d}z' \,\exp\{-\Phi(x,z',T)/(k_BT)\}. \tag{3.13}$$

In order to generalize the notion of “standard deviation” to the present case of an asymmetric distribution of the particle-substrate distances at fixed lateral position, we define a lower value $z_{\mathrm{low}}(x)$ and an upper value $z_{\mathrm{upp}}(x)$ of the particle-substrate distances such that

$$\bar{P}_<(z_{\mathrm{low}}(x);x) = 0.159 \qquad \text{and} \qquad \bar{P}_<(z_{\mathrm{upp}}(x);x) = 1-0.159, \tag{3.14}$$

so that the probability of the colloid to be at a distance z with $z_{\mathrm{low}}(x) < z < z_{\mathrm{upp}}(x)$ is $\simeq 68\%$, whereas the probability to find it at distances smaller (larger) than $z_{\mathrm{low}}(x)$ ($z_{\mathrm{upp}}(x)$) is $\simeq 16\%$; these two properties define the standard deviation for a Gaussian distribution.

Figure 3.2 shows the behavior of the colloid with $(-)$ BC above a chemically patterned substrate for the two lateral positions (a) $x = 0$ and (b) $x = P/2$ at which the colloid is floating

---

[19] Note that the Derjaguin approximation holds only for distances which are small on the scale of the particle size (a detailed analysis of its applicability for the system under consideration is given in Ref. [52]). However, in Eq. (3.12) also large values of z occur. But at these large particle-wall distances the critical Casimir force as well as the electrostatic force are negligibly small compared to the gravitational force, so that using this approximation is nonetheless not detrimental. In principle, the integration in Eq. (3.12) is limited by the vertical extension of the experimental sample cell of around 200 μm. However, due to the gravitational contribution to the potential, de facto no colloidal particle moves out of the vertical field of view of the camera. Thus the integration in Eq. (3.12) can be taken to run up to infinity without quantitatively relevant consequences because contributions from large z are strongly suppressed.

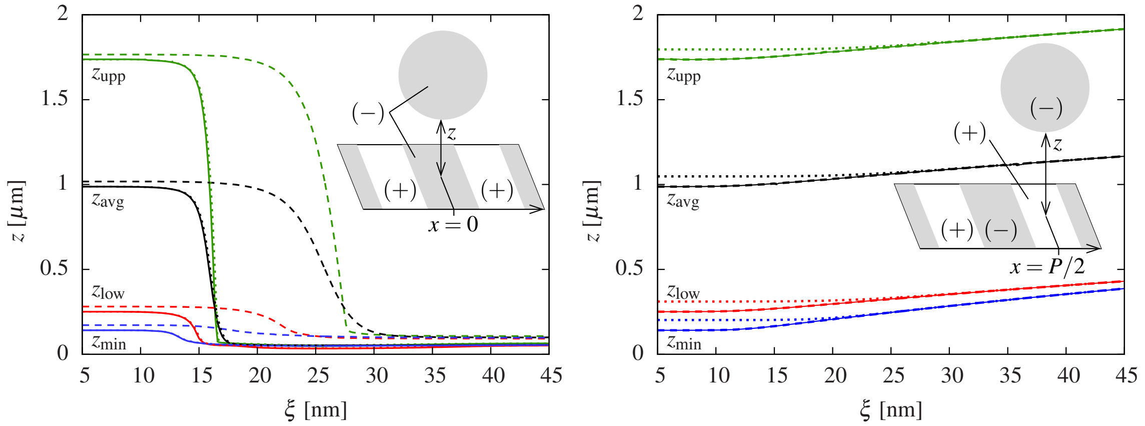

(a) $x = 0$ **(b)** $x = P/2$

Figure 3.2: Distances of the colloid from the substrate, for a fixed lateral position (a) $x = 0$ and (b) $x = P/2$, as a function of the bulk correlation length ξ. Here, $P = 1.8\,\mu\mathrm{m}$, $R = 1.2\,\mu\mathrm{m}$, $L_- = 0.9\,\mu\mathrm{m}$, whereas z_{upp}, z_{avg}, z_{low}, and z_{min} indicate the upper, average, lower, and potential-minimum distances of the colloid, respectively (see the main text). The solid lines correspond to the choice $z_0^- = z_0^+ = 0.09\,\mu\mathrm{m}$, the dashed lines to $z_0^- = 0.12\,\mu\mathrm{m}$ and $z_0^+ = 0.09\,\mu\mathrm{m}$, and the dotted lines to $z_0^- = 0.09\,\mu\mathrm{m}$ and $z_0^+ = 0.15\,\mu\mathrm{m}$. As expected, the fluctuations of the particle-substrate distance z for a colloid opposite to an attractive stripe [$x = 0$, panel (a)] decrease significantly upon increasing the correlation length ξ, due to the fact that the particle is mainly localized around the deep potential well which forms as a consequence of the action of the critical Casimir force. In fact, $z_{\mathrm{upp,avg,low,min}} \simeq z_0^-$ for large ξ. The actual value of z_0^- strongly affects the behavior of the particle, both in determining the values of $z_{\mathrm{upp,avg,low,min}}$ close to the critical point and in setting the threshold value ξ^* of ξ at which one observes such a sharp transition towards strong spatial confinement for $\xi > \xi^*$. From panel (a) one infers, e.g., that $\xi^* \simeq 17\,\mathrm{nm}$ and $\xi^* \simeq 27\,\mathrm{nm}$ for the solid and dashed curves, respectively. On the other hand, the dependence on z_0^+ is not pronounced and indeed in panel (a) the dotted lines practically coincide with the solid ones. For a colloid opposite to a repulsive stripe [$x = P/2$, panel (b)], due to the repulsive nature of both the electrostatic and the critical Casimir force and the very weak gravitational attraction one has $z_{\mathrm{min}} < z_{\mathrm{low}}$ and the average position is typically of the order of $1\,\mu\mathrm{m}$ with fluctuations of the same order. As anticipated, also in this case the actual value of z_0^+ is not very relevant, in particular for large values of ξ. Analogously, the behavior of the colloid at $x = P/2$ is not affected by the choice of z_0^- and in panel (b) the dashed lines practically coincide with the solid ones.

above the center of a $(-)$ and of a $(+)$ stripe, respectively, as a function of the correlation length ξ. In Fig. 3.2 the values of the geometrical parameters (P, R, L_-) are chosen to correspond to the actual experimental conditions, whereas the parameters $z_0^\pm$ governing the electrostatic repulsion from the substrate are varied within a range which was determined by previous independent experiments. Panel (a) clearly demonstrates that the fluctuations of z for a colloid opposite to an attractive stripe decrease significantly upon increasing the correlation length ξ above a certain threshold value ξ^* which depends on z_0^-. This reflects the emergence of the deep potential well shown in Fig. 3.1 which results from the competition between an increasingly attractive critical Casimir force and a repulsive electrostatic repulsion, the former being always overwhelmed by the latter around $z = z_0^-$. Indeed, for small values of ξ the average position $z_{\text{avg}}(x = 0)$ is typically determined by the competition between the electrostatic repulsion and the gravitational part, such that $z_{\text{avg}}(x = 0) \simeq z_0^- + k_BT/G \simeq 1\,\mu\text{m}$ with fluctuations of the order of $k_BT/G \simeq 1\,\mu\text{m}$. On the other hand, for larger values of ξ, one has $z_{\text{upp,avg,low,min}}(x = 0) \simeq z_0^-$ and there are only very small thermal fluctuations of the particle-substrate distance, at most a few tens of nm. Depending on the relative strength of the electrostatic repulsion and the critical Casimir attraction, one can have $z_{\text{min}} < z_{\text{low}}$ if the former dominates the latter, i.e., at small values of ξ or the opposite at large values of ξ. From Fig. 3.2(a) one concludes that the choice of z_0^- strongly affects the behavior of the particle, both in determining the values of $z_{\text{upp,avg,low,min}}$ and in setting the threshold value ξ^* of ξ above which the particle becomes strongly confined, whereas the dependence on z_0^+ is negligible for the behavior at $x = 0$, because z_0^+ controls the electrostatic interaction with the adjacent stripe. Analogously, the behavior of a colloid at $x = P/2$ as shown in Fig. 3.2(b), i.e., opposite to a repulsive stripe is not affected by the choice of z_0^-. However, for this configuration, also the actual value of z_0^+ does not affect significantly the resulting behavior of the particle-substrate distance at $x = P/2$, in particular for large values of ξ. Indeed, due to the repulsive nature of both the electrostatic and the critical Casimir force and the weak gravitational attraction, the average position is typically of the order of $z_{\text{avg}}(x = P/2) \simeq z_0^+ + k_BT/G \simeq k_BT/G$ (with an additional linear contribution $\propto \xi$ for large values of ξ) allowing fluctuations of the order of $k_BT/G \simeq 1\,\mu\text{m}$.

In Fig. 3.3 the particle-substrate distance (characterized via $z_{\text{avg,upp,low}}$) and the position of mechanical equilibrium z_{min} are reported as functions of the lateral coordinate of the colloid within the period P and for two different temperatures, i.e., two different values of ξ. In Fig. 3.3, the choice of the parameters corresponds to actually experimentally accessible values. Figure 3.3 clearly shows that for $\xi = 10\,\text{nm}$ (dashed lines) the particle-substrate distance is laterally constant and the colloid does not react to the presence of the chemical pattern on the substrate, apart for a possible effect due to a change in the electrostatic interaction (which here is taken to be the same on the different stripes). On the other hand, for $\xi = 20\,\text{nm}$ (solid line) the colloid is strongly attracted to that part of the substrate with the same preferential adsorption (in Fig. 3.3 indicated by a shaded background), as a consequence of the emerging critical Casimir forces. Indeed for $|x| \lesssim L_-/2$ the particle is abruptly localized at a distance $z \simeq z_0^-$, which is

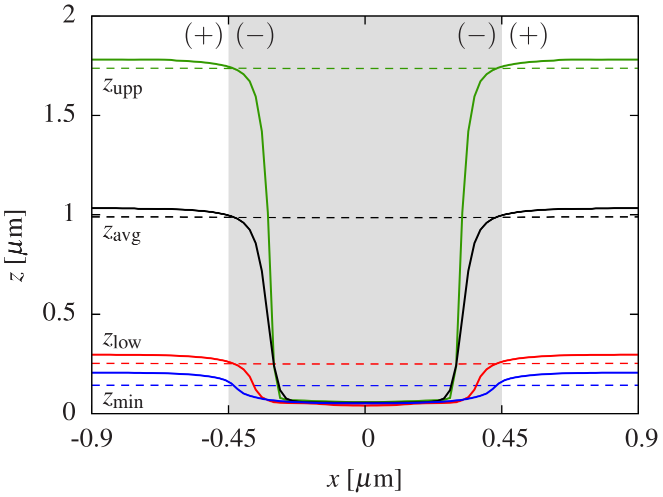

Figure 3.3: Particle-substrate distance z (characterized via $z_{\mathrm{upp,avg,low}}$, see the main text) and position of mechanical equilibrium z_{min} as functions of the lateral coordinate of the particle for $\xi = 10\,\mathrm{nm}$ (dashed curves) and $\xi = 20\,\mathrm{nm}$ (solid curves). Here, $z_0^- = z_0^+ = 0.09\,\mu\mathrm{m}$, $P = 1.8\,\mu\mathrm{m}$, $R = 1.2\,\mu\mathrm{m}$, and $L_- = 0.9\,\mu\mathrm{m}$. For small values of the correlation length ξ the various characteristic distances are almost independent of the lateral coordinate, whereas above a certain threshold value ξ^* of ξ (see also Fig. 3.2) the colloid opposite to the attractive stripe is strongly confined close to the wall at a distance $z \simeq z_0^-$ with almost no fluctuations.

primarily set by the electrostatic repulsion and which corresponds to the position $z_{\mathrm{min}}(0)$ of the minimum of the potential, with almost no thermal fluctuations. In the region above the repulsive stripes (in Fig. 3.3 indicated by a white background) and within the temperature range considered here, instead, the repulsive critical Casimir force pushes the colloid only slightly further away from the substrate, by a distance of the order of the increasing correlation length ξ. But the amplitude of the thermal fluctuations of the particle-substrate distance are barely affected by the onset of the repulsive critical Casimir force.

The analysis of the particle-substrate distance shows that the behavior of the colloidal particle and the resulting potential are drastically influenced by the strong attraction of the colloid close to an attractive stripe. Accordingly, the electrostatic repulsion from this stripe, i.e., the value of z_0^-, affects significantly the total potential and has therefore to be considered carefully in the comparison between theoretical predictions with the experimental data. On the contrary, the actual value of z_0^+ as well as the actual value of κ do not significantly affect the resulting behavior of the potentials as long as they are within the range appropriate for the present experiment which can be inferred from previous, independent measurements [21].

3.3. Comparison with the experimental data

3.3.1. Description of the experiments

Here, we shall provide a brief description of the two different experimental setups used by *Soyka et al.* and *Vogt et al.* described in detail in Refs. [37–40]. In both experimental setups, in order to measure the critical Casimir forces which act on a colloidal particle exposed to the patterned substrates, polystyrene (PS) probe particles with radius $R = 1.2\,\mu\text{m}$ have been used. Their surface charge is $10\,\mu\text{C}/\text{cm}^2$ which renders them hydrophilic, realizing $(-)$ boundary conditions [37, 40]. The particles were dissolved in a critical water-2,6-lutidine mixture which has a lower critical demixing point at a lutidine mass fraction of $c_L^c \cong 0.286$ and a critical temperature of $T_c = 307\,\text{K}$. In both experiments [37, 40] particle positions were monitored by digital video microscopy which allows one to track the projection of their centers onto the substrate plane with a spatial resolution of about 50 nm. While several particle trajectories were recorded at the same time, the particle density was sufficiently small in order to to exclude the presence of forces among neighboring colloids, such that only the single particle interaction with the patterned substrate has been probed during the measurements [37, 40].

A temperature control which stabilizes temperatures close to T_c within only 10 mK over several hours, has been realized [37, 40]. However, in contrast to temperature *changes*, which could be resolved within mK accuracy, larger errors occurred in the determination of *absolute* temperatures (in particular the measured critical temperature), due to the fact, that the thermometer could not be placed within the sample cell but it was instead attached outside [37, 40]. Indeed, the thermometer measures a temperature T^{out} lower than the actual temperature T inside the sample cell. The temperature $T^{\text{out}} = T_c^{\text{out}}$ has been associated with the critical temperature $T = T_c^{\text{exp}}$ of the solvent in the sample at that particular temperature for which critical opalescence is observed when shining a laser beam into the sample cell [37, 40]. This leads to systematic errors on the absolute temperature of T_c^{out} and T_c^{exp} of the order of 50 mK. Using the assumption that $T - T^{\text{out}} = const$ (this constant could not be determined experimentally and is inter alia dependent on the ambient temperature), the temperature difference $\Delta T = T_c^{\text{out}} - T^{\text{out}}$ has been measured and identified it with $T_c^{\text{exp}} - T \equiv \Delta T$ [37, 40]. Since the comparison with the theoretical predictions depends crucially on the actual value $T_c \simeq 307\,\text{K}$ of the critical temperature, in the analysis below we account for such a possible systematic error by considering $\Delta T_c^* = T_c - T_c^{\text{exp}}$ as an additional fitting parameter, where $T_c \simeq 307\,\text{K}$ is the actual critical temperature of the water-lutidine mixture.

The experiments by *Soyka et al.* and by *Vogt et al.* differ crucially in the preparation and the parameters of the chemical substrate pattern, as addressed below.

3.3.2. Comparison of theory with experiments

The total potential Φ of the forces [Eq. (3.10)] acting on the colloidal particle has been calculated on the basis of the Derjaguin approximation with $k_{(\pm,-)}$ [see Eqs. (1.3) and (3.5)] obtained from Monte Carlo simulations. In the following we shall use for the scaling functions $k_{(\pm,-)}$ of the critical Casimir force between two planar walls with $(\pm,-)$ BC the numerical estimate referred to as "approximation (*i*)" in Figs. 9 and 10 of Ref. [100]. We have checked that different [100] or more recent and accurate [106] estimates for $k_{(\pm,-)}$ actually lead to essentially the same effective potentials, the only difference being a small additional overall shift of the resulting fitted value of the critical temperature. In Chapter 2 we have presented an detailed analysis in spatial dimension $d = 4$ which suggests that the Derjaguin approximation we have used in our theoretical predictions for $d = 3$ should be rather accurate in describing the actual potential of the colloid within the range of parameters experimentally studied here. As anticipated above, in order to predict the effective potential $\hat{V}$ we need to fix also the value of the parameters which determine the electrostatic interaction. For the comparison between theory and experiment we fix the screening length to the value $\kappa^{-1} = 12\,\text{nm}$ which has been reported from independent measurements on the same system (see, e.g., Ref. [21]). In order to fit our theoretical predictions to the experimental data, we vary instead the unknown values of the parameters $z_0^{\pm}$ [Eqs. (3.6) and (3.7)] within the range $0.08\,\mu\text{m}$ to $0.15\,\mu\text{m}$, which can be reasonably expected on the basis of previous measurements on homogeneous substrates [21]. However, the results for $\delta\hat{V}(0)$ are hardly affected by the particular choice of z_0^+ so that in the following we keep it fixed at $z_0^+ = 0.10\,\mu\text{m}$ for the comparison with the experiments by *Soyka et al.* and $z_0^+ = 0.09\,\mu\text{m}$ for the comparison with the experiments by *Vogt et al.*, respectively. The amplitude ξ_0^+ of the correlation length has been determined by independent experiments as $\xi_0^+ \simeq 0.20 \pm 0.02\,\text{nm}$ (see, e.g., Tab. III in Ref. [21]) so that we vary ξ_0^+ within the range $0.18\,\text{nm}$ to $0.22\,\text{nm}$ in order to obtain the best fit to the experimental data by the theoretical scaling functions. Moreover, as mentioned above, the experimental uncertainty in the determination of the absolute value of the critical temperature T_c^{exp} is taken into account by considering as an additional fitting parameter the shift $\Delta T_c^* = T_c - T_c^{\text{exp}}$ of up to $|\Delta T_c^*| \simeq 100\,\text{mK}$. (The values of ΔT_c^* may be different for the individual stripe widths L_- which characterize the substrates investigated in independent experiments.) However, the *relative* uncertainty in the determination of the temperature within a single experimental run is smaller than $\pm 10\,\text{mK}$ (see above). Thus, for the comparison carried out below, we are left with ΔT_c^*, z_0^-, ξ_0^+, and Δx (see Subsec. 3.2.5) as fitting parameters which, however, are all limited to rather small ranges of values in order to be in accordance with independent and previous experimental results.

3.3.3. Experiment by *Soyka et al.*

First[20], the theoretically predicted curves are compared with the experimental data for the critical Casimir potential for a single colloid obtained in Ref. [37]. The substrate surface confining the colloidal suspension consists of equally spaced stripes along the y-axis which impose $(-)$ and $(+)$ BC alternating along the x-axis, and have a width $L_- = 2.6\,\mu\mathrm{m}$ and $L_+ = 5.2\,\mu\mathrm{m}$, resulting in a periodicity $P = L_- + L_+ = 7.8\,\mu\mathrm{m}$. The chemical patterns were created by removing locally a hydrophobic monolayer of HMDS particles from a hydrophilic glass surface with a focused ion beam (FIB). Although under ideal conditions the resolution of FIB is within the range of several nanometers, in the case of non-conducting surfaces distortions/deflections of the ion beam due to an electrostatic charging of the glass surface have been observed, leading to deviations of the chemical steps from straight lines (see Sec. 3.2.5).

A detailed analysis of the potentials adopted to the experimental conditions show that for $|x| < L_-/2$ the contribution of Φ_C to Φ_tot is significant only for distances from the substrate $z \lesssim \xi$, which corresponds to $\Delta = z/R \lesssim 0.03$, whereas for $P/2 + L_+/2 > |x| > L_-/2$ the typical distance is $z \simeq z_0^-$ and therefore $\Delta \simeq 0.12$ with $\Theta = z/\xi \gtrsim 4$. In addition, the relevant geometrical parameters are $P/\sqrt{RD} \simeq 7 \div 20$ and $L_-/\sqrt{RD} \simeq 2 \div 7$, such that, based on our theoretical analysis of the range of validity of the DA, we expect the latter to be accurate for the potentials Φ_el and Φ_C. Moreover, the values of Θ, $P/\sqrt{RD}$, and $L_-/\sqrt{RD}$ are such that the resulting critical Casimir potential is adequately described by the superposition of a sequence of single chemical steps.

The depths of the measured potentials are given by $\Delta\hat{V} = -\delta\hat{V}(0) > 0$ [see Eq. (3.11)]. From the experimental data $\Delta\hat{V}$ is determined as the difference of the potential between its value at the center of a repulsive stripe and at the center of an attractive stripe with an uncertainty of around $\pm 0.15 k_B T$ near the critical temperature $T_c \simeq 307\,\mathrm{K}$. From our analysis we find that keeping the value of ξ_0^+ restricted to the range $0.20 \pm 0.02\,\mathrm{nm}$, the resulting predictions for the depths of the potentials do not compare very well with the experimental data [182]. This is shown in Fig. 3.4, where the dashed lines corresponds to one of the best fits obtained for ξ_0^+ restricted to this range (other, equally well fits are almost equal to this curve). However, the comparison improves significantly if one allows for a change in the value of ξ_0^+ within a broader range (see the solid line in Fig. 3.4). Accordingly, the values $z_0^- \simeq 0.136\,\mu\mathrm{m}$, $\xi_0^+ \simeq 0.42\,\mathrm{nm}$, and $\Delta T_c^* \simeq 27\,\mathrm{mK}$ yield a very good fit to the experimental data for $\Delta\hat{V}$ (Fig. 3 of Ref. [37]). Whereas ΔT_c^* is within the experimental accuracy, ξ_0^+ is significantly larger than previous estimates $\xi_0^+ = 0.20 \pm 0.02\,\mathrm{nm}$ [20], suggesting that for the rather small corresponding values of $\xi \simeq 20\,\mathrm{nm}$ to $36\,\mathrm{nm}$ corrections to the leading scaling behavior might still be relevant.

In Fig. 3.5 we compare the experimental data with the resulting theoretical predictions for $\delta\hat{V}(x)$ (dasehd lines) across the $(-)$ stripe (grey). As anticipated, the effects of the chemical steps at $x = 0$ and L_- do not interfere in the actual range of parameters. The theoretical curves

---

[20] This comparison has been performed together with *Andrea Gambassi* [182] and presented in Ref. [51].

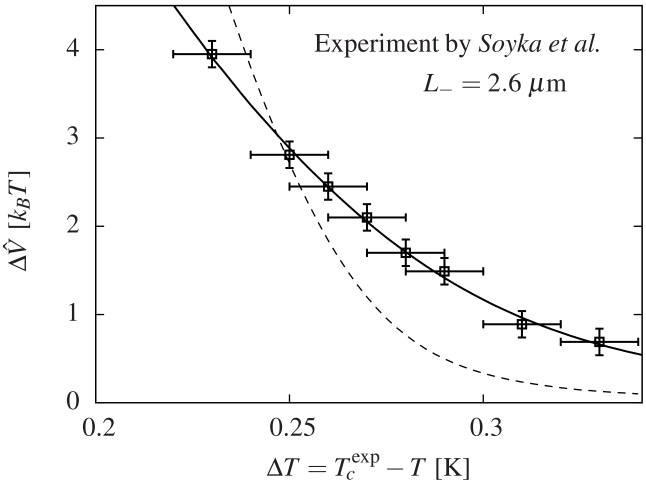

Figure 3.4: $\Delta\hat{V}$ as a function of $\Delta T = T_c^{\mathrm{exp}} - T$ (see also Ref. [182]). The symbols represent the experimental data obtained for the depth of the potential of colloids close to chemical stripes obtained via the focused ion beam technique [37]. They are affected by an experimental uncertainty as indicated by the errorbars (see the main text). The dashed line corresponds to one of the best fits obtained when varying the value of ξ_0^+ within the range $\xi_0^+ = 0.20 \pm 0.02\,\mathrm{nm}$ known from independent results (the resulting parameters are $\xi_0^+ = 0.22\,\mathrm{nm}$, $z_0^- = 0.110\,\mu\mathrm{m}$, and $\Delta T_c^* = -78\,\mathrm{mK}$). The solid line corresponds to the best fit when allowing ξ_0^+ to vary within a broader range (the corresponding parameters are $\xi_0^+ = 0.42\,\mathrm{nm}$, $z_0^- = 0.136\,\mu\mathrm{m}$, and $\Delta T_c^* = 27\,\mathrm{mK}$).

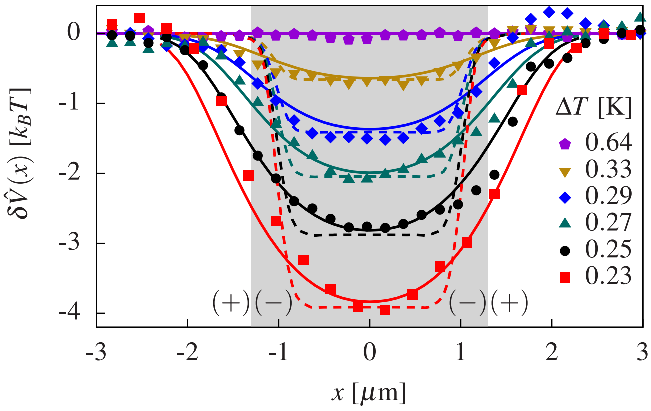

Figure 3.5: Lateral variation of the effective potential $\delta\hat{V}$ [see the main text] of a colloidal particle $(-)$ facing a chemically patterned substrate and immersed in a binary liquid mixture at critical concentration for various temperatures $T_c - \Delta T$. Symbols indicate the experimental data of Ref. [37], whereas the solid and the dashed lines are theoretical predictions for the same values of parameters for an ideal and non-ideal stripe pattern, respectively.

— in *qualitative* disagreement with the experimental data — display a sharp transition between the plateau values 0 and $-\Delta\hat{V}$. In order to test the robustness of this distinctive feature we varied λ within the plausible range 8 nm to 18 nm, considered polydispersity ($R = 1.2\,\mu\text{m}$ to $1.8\,\mu\text{m}$), and allowed for a possible inhomogeneous buoyancy $\Phi_g(z,x)$ induced by laterally varying fluid layers adsorbed on the colloid and on the substrate. Moreover, due to their fabrication process, the $(-)$ stripes might have a rather weak preferential adsorption as compared to the $(+)$ stripes, which we tried to capture by reducing the amplitude of $k_{(-,-)}$ by up to 70%. Consequently, the values of $z_0^- \simeq 0.10$—$0.14\,\mu\text{m}$, $\xi_0^+ \simeq 0.3$—$0.4\,\text{nm}$, and $\Delta T_c \simeq -0.1$—$0.1\,\text{K}$, which yield the best agreement with the experimental data for $\Delta\hat{V}$, are affected by these changes[21] but the sharpness of the variation *is not*. In addition, our analysis shows that the effect of the periodic spatial arrangement of the stripes – which would smoothen the potential for relatively small periodicities P — is negligible for the experimental conditions used in Ref. [37]. On the same basis, we expect the DA to be sufficiently accurate and that the non-linearities inherent in the critical Casimir interaction, which actually invalidate the assumption of additivity of the forces and might cause a smoothening, *do not* affect significantly the potential shown in Fig. 3.5.

However, if the chemical step between two adjacent chemical strips is not ideal (see Sec. 3.2.5), this results in a pronounced modification of the resulting potentials. Even though there is no direct measurement of such a variation of the position of the step, it is reasonable to assume that it occurs due to the fabrication process and due to the projection of the data onto one dimension without independent knowledge of the alignment of the chemical stripes. In order to estimate the consequences, we have we have assumed the actual position of the chemical step to be characterized by a Gaussian distribution with zero average and standard deviation $\Delta x = 0.5\,\mu\text{m}$ as described in Sec. 3.2.5. The resulting $\delta\hat{V}(x)$, which basically correspond to a convolution of the original almost square-well-like potentials with a Gaussian of width Δx, are shown as dashed curves in Fig. 3.5. The agreement with the experimental data is significantly improved. In view of the pronounced modifications of the resulting potential our analysis demonstrates that critical Casimir forces respond sensitively to geometrical details of the chemical pattern, which could not be checked independently in Ref. [37].

3.3.4. Experiment by *Vogt et al.*

In a recent experiment — following the one of Ref. [37] — performed by *Dominik Vogt et al.* [39, 40], surfaces with a periodic pattern of alternating stripes with opposite adsorption preferences for the two components of the binary mixture of water and lutidine were obtained by *micro-contact printing* (μCP) of alkanethiols. Elastic stamps have been prepared by casting polydimethylsiloxane onto a master which was topographically structured by a lithographic process [40]. The stamps have been wetted with a solution of nonpolar thiols and brought into mechanical contact with a gold-coated glass substrate, which results in hydrophobic stripes on the substrate surface [40]. Finally, the substrate has been dipped into a solution of another type of thiols in order to render the remaining bare gold surface hydrophilic [40]. With this technique periodic arrays of hydrophilic and hydrophobic stripes of widths between $0.9\,\mu\text{m}$ and $3\,\mu\text{m}$ over a typical total extension of $0.5\,\text{cm}^2$ and a typical lateral edge resolution of the order of $50\,\text{nm}$ to $100\,\text{nm}$ have been produced [39, 40]. In contrast to the focused ion beam technique used in Ref. [37] (Sec. 3.3.3) charging effects are basically absent in μCP; thus, one has an improved control of the geometrical structure of the imprinted chemical pattern [40].

---

[21] As the amplitude of $k_{(-,-)}$ is reduced, the fitted value of ξ_0^+ moves closer to 0.20 nm, suggesting that indeed the preferential adsorption of the $(-)$ stripes might be effectively rather weak.

Depth of the potential

Figure 3.6(a) shows the depth of the measured laterally confining potential $\Delta\hat{V} = -\delta\hat{V}(0)$ [Eq. (3.11)] as a function of the deviation $\Delta T = T_c^{\text{exp}} - T$ of the temperature from the experimentally determined critical demixing temperature T_c^{exp}, for various stripe widths L_- and measured in independent experimental runs as described above. The periodicities P of the various patterns the stripes belong to are determined from the photolithography mask and are given in Tab. 3.1. The potential depth $\Delta\hat{V}$ is determined as the difference of the potential between its value at the center of a repulsive stripe and at the center of an attractive stripe, carrying an uncertainty of $\pm 0.15 k_B T$ near the critical temperature $T_c \simeq 307\,\text{K}$. Upon approaching T_c, for a stripe width $L_- \lesssim 1.5\,\mu\text{m}$ the effects of two adjacent chemical steps interfere, which results in an effectively reduced potential depth compared to the case of a very wide stripe (see the dashed curves in Fig. 3.6(b); in Fig. 3.6(a) the experimental uncertainty in determining the critical temperature T_c^{exp} is responsible for the relative displacements among the various curves). The effect of non-ideal chemical steps may result in an effectively reduced potential depth as well (see, for example, Fig. 3.6(b) and, c.f., Fig. 3.8(b)). Accordingly, in comparing the experimental data for $\Delta\hat{V}$ with the theoretical predictions we allow for an uncertainty in the local position of the boundary between adjacent stripes, as described in Subsec. 3.2.5. However, as will be shown below, we are able to determine Δx rather precisely from the lateral variation of the potential. The values of Δx, which yield the best agreement and which are used for the comparison shown in Fig. 3.6, are given in Tab. 3.1. On the basis of our theoretical analysis, it turns out that the temperature dependence of the potential depth becomes independent of the stripe width when the latter is sufficiently large. Adopting for the geometrical and physical parameters the values corresponding to the present experimental conditions, this is expected to occur for $L_- \gtrsim 2\,\mu\text{m}$. From Fig. 3.6 one can see, however, that the experimentally determined data for individual experimental runs are shifted along the temperature axis with respect to each other, which reflects the uncertainty of up to $100\,\text{mK}$ in measuring the absolute value of the critical temperature. On the other hand, within a single individual experimental run corresponding to a certain stripe width, the temperature difference between the various data points can be measured with the high accuracy of less than $10\,\text{mK}$. Upon comparing the experimental data shown as symbols in

Figure 3.6: Depth $\Delta\hat{V}$ of the effective potentials of a colloid close to patterned substrates, with periods $P = L_- + L_+$ and $(-)$ stripe widths L_- given in Tab. 3.1, as a function of the temperature deviation from the critical temperature. The symbols represent the experimental data which are affected by an experimental uncertainty of $\pm 0.15 k_B T$ for the potential depth and of $\pm 0.01\,\mathrm{K}$ for the temperature differences between the various data points belonging to one and the same value for L_-.

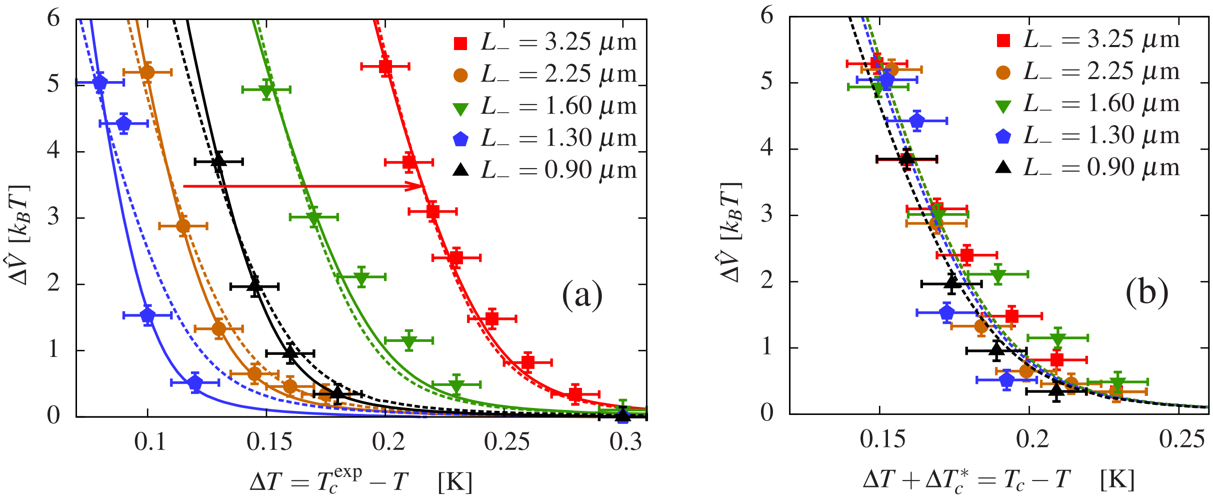

(a) $\Delta\hat{V}$ as a function of $\Delta T = T_c^{\mathrm{exp}} - T$. (For better visibility, the data for $L_- = 3.25\,\mu\mathrm{m}$ are shifted by $0.1\,\mathrm{K}$ along the ΔT axis, as indicated by the red arrow.) The solid lines represent the best fit of the theory to the experimental data for each *individual* value of L_- with fixed parameters κ and z_0^+ which do not affect the resulting behavior significantly as discussed in the main text. ξ_0^+ has been varied within the reasonable range $0.18\,\mathrm{nm} \lesssim \xi_0^+ \lesssim 0.22\,\mathrm{nm}$ known from the literature. The values of all parameters corresponding to the solid lines are given in Tab. 3.1. Clearly, for each individual L_- the actual critical temperature T_c is shifted by $\Delta T_c^* = T_c - T_c^{\mathrm{exp}}$ from the value T_c^{exp} determined experimentally, with ΔT_c^* being within the experimental accuracy $|\Delta T_c^*| \lesssim 0.1\,\mathrm{K}$. The dashed curves represent a *common* fit to all data. For this latter fit we have assumed ξ_0^+ and z_0^- to be the same for the various independent experimental runs, independently of the corresponding value of L_-, whereas $\Delta T_c^* = T_c - T_c^{\mathrm{exp}}$ (besides Δx as determined below) is used for adjustment to the data for each individual L_-. The best fit for all these parameters renders $\xi_0^+ = 0.22\,\mathrm{nm}$, $z_0^- = 0.11\,\mu\mathrm{m}$, and the values reported in Tab. 3.2.

(b) $\Delta\hat{V}$ as a function of $\Delta T + \Delta T_c^* = T_c - T$ using the values of ΔT_c^* for the best common fit (see dashed lines in (a)) given in Tab. 3.2. This plot takes into account the experimental uncertainty of measuring the absolute value of T_c^{exp}. The data points, which have been shifted accordingly, basically fall on top of each other within their error bars. The dashed lines correspond to the dashed ones shown in (a) and represent the theoretical predictions. For $L_- \geq 1.60\,\mu\mathrm{m}$ the various curves are almost indistinguishable from each other, whereas for $L \leq 1.30\,\mu\mathrm{m}$ the potential depth is effectively reduced due to the interference of the effects of two neighboring steps and due to the fact that the steps are non-ideal.

Fig. 3.6 with our theoretical predictions we take this into account by introducing, for each value of L_-, a possible shift $\Delta T_c^*(L_-) = T_c - T_c^{\exp}(L_-)$ between the actual critical temperature T_c and the value $T_c^{\exp}$ determined in that particular experiment. Accordingly, for the data corresponding to a certain L_-, the actual distance from the critical point is given by $T_c - T = \Delta T + \Delta T_c^*(L_-)$.

The dashed curves in Fig. 3.6 correspond to the *common* fit to all experimental data which leads to the fitting parameters ξ_0^+ and z_0^- taking the same values $\xi_0^+ = 0.22\,\text{nm}$ and $z_0^- = 0.11\,\mu\text{m}$ for all L_- as obtained from the least-square method. On the other hand, the individual temperature shifts $\Delta T_c^*(L_-)$ are given in Tab. 3.2 for each data set corresponding to a single value of L_-. The values of ξ_0^+ and z_0^- are both in agreement with independent previous findings [21]. Figure 3.6(b) shows the depth of the potentials as a function of $\Delta T + \Delta T_c^*(L_-) = T_c - T$, i.e., shifted along the temperature axis by $\Delta T_c^*(L_-)$ as given in Tab. 3.2. This accounts for the uncertainty in determining experimentally the absolute value of the temperature, and indeed, as expected for significantly wide stripes $L_- \gg \xi$, the data overlap with each other within the error bars, reflecting that in this limit $\Delta\hat{V}$ is independent of L_-.

The solid lines in Fig. 3.6(a) correspond to fits of the theoretical predictions to each *individual* experiment dealing with a specific stripe width. Distinct from the previous common fit, here for each stripe width L_- we allow for a variation of the values of ξ_0^+ and z_0^- in addition to ΔT_c and Δx. On the basis of a least-square fit, best agreement is obtained for the values given in Tab. 3.1, which agree with those obtained in independent previous studies [21] within the corresponding experimental accuracy.

Shape of the potentials

Figures 3.7 and 3.8 show the total potential of the forces acting on the colloid as a function of its lateral position for various temperatures and for two stripe widths. Symbols represent the experimental data, whereas the solid and dashed lines are the corresponding theoretical predictions with ξ_0^+, z_0^-, and ΔT_c^* fixed to the values reported in Tab. 3.1, which have been determined from the fit of the depth $\Delta\hat{V}$ of the potential. In addition, for a few cases and as indicated in the figure captions, we use the leeway provided by the experimental uncertainty of $\pm 10\,\text{mK}$ for the temperature value. The dashed lines in Figs. 3.7 and 3.8 are based on the assumption that the stripe patterns are *ideal* whereas the solid ones refer to *non-ideal* patterns for which we fitted the parameters Δx (see Subsec. 3.2.5) in order to obtain the best agreement between theoretical predictions and the set of experimental data at distinct temperatures. The resulting values of Δx for the various widths of the pattern are reported in Tab. 3.1. In fact, the broadness of the transition regions across the chemical steps of $\delta\hat{V}(x)$ between its extremal values is affected practically exclusively by Δx. We have checked that the other parameters and potential additional effects such as polydispersity and weak adsorption cannot account for the discrepancies of the slopes of the dashed curves and the experimentally determined ones. Thus, Δx and L_- are determined de facto independently of the choice of ξ_0^+, z_0^-, and ΔT_c^* and in the

Table 3.1.: Values of the parameters for which best agreement is obtained between theory and the data for $\delta\hat{V}(x)$ for each individual experimental run, corresponding to a single value of L_- (see Fig. 3.6(a)). The values $\kappa^{-1} = 12\,\mathrm{nm}$ and $z_0^+ = 0.09\,\mu\mathrm{m}$ are fixed because their choice does not affect significantly the resulting theoretical curves in Fig. 3.6.

$P[\mu\mathrm{m}]$ [a]	$L_-^{\mathrm{exp}}[\mu\mathrm{m}]$ [b]	$L_-[\mu\mathrm{m}]$ [c]	$\xi_0^+[\mathrm{nm}]$	$z_0^-[\mu\mathrm{m}]$	$\Delta T_c^*[\mathrm{mK}]$	$\Delta x[\mu\mathrm{m}]$ [d]
6.0	3.0	3.25	0.22	0.103	86	0.15
5.4	2.7	2.25	0.21	0.128	-5	0.10
4.2	2.1	1.60	0.22	0.095	88	0.22
3.6	1.8	1.30	0.19	0.140	-18	0.19
1.8	0.9	0.90	0.20	0.121	-28	0.09

[a] Most of the experimental data for the potential $\delta\hat{V}(x)$ discussed here are not influenced by the actual value of P as long as $P \gtrsim 2L_-$. Accordingly, we assume the periodicity to be the one determined by the inscribed photolithographic mask pattern reported here.

[b] Width of the stripes of the photolithographic mask pattern. Due to the μCP stamping process we estimate the uncertainty of the actual width of the thiol stripes to be up to $\pm 0.5\,\mu\mathrm{m}$.

[c] Value of the stripe width for which best agreement between theory and experiment is obtained.

[d] Value of Δx for which best agreement between theory and experiment is obtained (see Figs. 3.7 and 3.8).

Table 3.2.: Values of the parameters for which best agreement is obtained between theory and all experimental data together (see Fig. 3.6(b)), so that the values of ξ_0^+ and z_0^- are the same, and ΔT_c^* (in addition to Δx determined from the shape of the potentials; see below) is the only parameter allowed to vary for the various stripe widths L_-. As in Tab. 3.1, the values of $\kappa^{-1} = 12\,\mathrm{nm}$ and $z_0^+ = 0.09\,\mu\mathrm{m}$ are fixed. (For a description of the parameter values P, L_-^{exp}, and L_- see the footnotes in Tab. 3.1.)

$P[\mu\mathrm{m}]$ [a]	$L_-^{\mathrm{exp}}[\mu\mathrm{m}]$	$L_-[\mu\mathrm{m}]$	$\xi_0^+[\mathrm{nm}]$	$z_0^-[\mu\mathrm{m}]$	$\Delta T_c^*[\mathrm{mK}]$	$\Delta x[\mu\mathrm{m}]$
6.0	3.0	3.25	0.22	0.110	49	0.15
5.4	2.7	2.25	0.22	0.110	54	0.10
4.2	2.1	1.60	0.22	0.110	0	0.22
3.6	1.8	1.30	0.22	0.110	72	0.19
1.8	0.9	0.90	0.22	0.110	29	0.09

Figure 3.7: Lateral variation of the effective potential $\delta\hat{V}(x)$ (see Eq. (3.11)) for a colloid opposite to a chemically patterned substrate and immersed in the water-lutidine binary liquid mixture at its critical concentration for various temperatures $T_c^{\mathrm{exp}} - \Delta T$. Symbols indicate experimental data, whereas the lines are the corresponding theoretical predictions for ideal (dashed lines) and non-ideal (solid lines) stripe patterns. The parameters used to calculate the theoretical curves are given in Tab. 3.1.

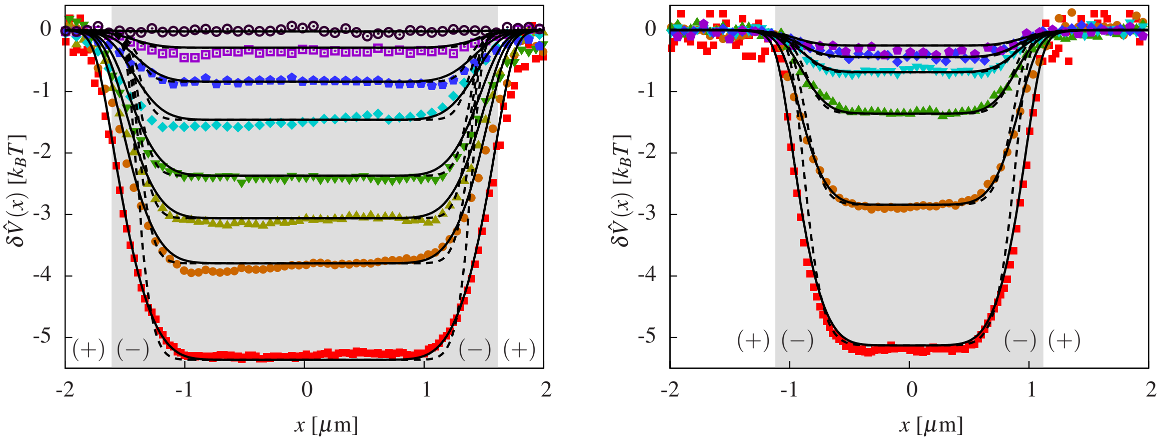

(a) $L_- = 3.25\,\mu\mathrm{m}$. From top to bottom the critical point is approached and the measured temperature deviations ΔT are 0.3, 0.18, 0.15 (0.153), 0.145 (0.14), 0.13 (0.128), 0.12, 0.11 (0.113), and 0.10 K with an uncertainty of up to $\pm 0.01\,\mathrm{K}$ with respect to each other. If indicated, the values in brackets are corrected values (but compatible within the experimental inaccuracy) which have been used for evaluating the theoretical predictions.

(b) Same as (a) for $L_- = 2.25\,\mu\mathrm{m}$ and $\Delta T = 0.175$ (0.165), 0.16 (0.152), 0.145 (0.143), 0.13, 0.115, and 0.10 K.

following they can be regarded fixed upon variation of the values of these latter parameters. In particular, this is important for narrow stripes as shown in Fig. 3.8, where even the depth of the potential depends on L_- and Δx, in contrast to broader stripes.

As anticipated, in the case of rather large stripe widths $L_- = 3.25\,\mu\mathrm{m}$ and $L_- = 2.25\,\mu\mathrm{m}$ shown in Fig. 3.7 and for the temperatures considered here the effects of two neighboring chemical steps do not interfere and the resulting potential across the center of the attractive chemical stripe is flat. Accordingly, from the comparison between the experimental data for the shapes of the potentials and the corresponding theoretical prediction we can infer the width L_- of the stripes — now treated as a fitting parameter — independently of its initially assumed value L_-^{exp} determined by the width of the photolithography mask. Indeed, the actual width of the stripe imprinted by the mask may differ by up to $\pm 0.5\,\mu\mathrm{m}$ from L_-^{exp} characterizing the mask itself. It is only L_-^{exp} which is controlled during the preparation process [39]. On the other hand, the actual value of P is the same as the one of the photolithography mask because the periodicity is not affected by the stamping process. (Note that, within the parameter range investigated in

Figure 3.8: Effective potential $\delta\hat{V}(x)$ (see Eq. (3.11)) for various temperatures $T_c^{\mathrm{exp}} - \Delta T$ and relatively small widths of the attractive stripes. Symbols indicate experimental data, whereas the lines are the corresponding theoretical predictions for ideal (dashed lines) and non-ideal (solid lines) stripe patterns. The parameters used to calculate the theoretical curves are given in Tab. 3.1.

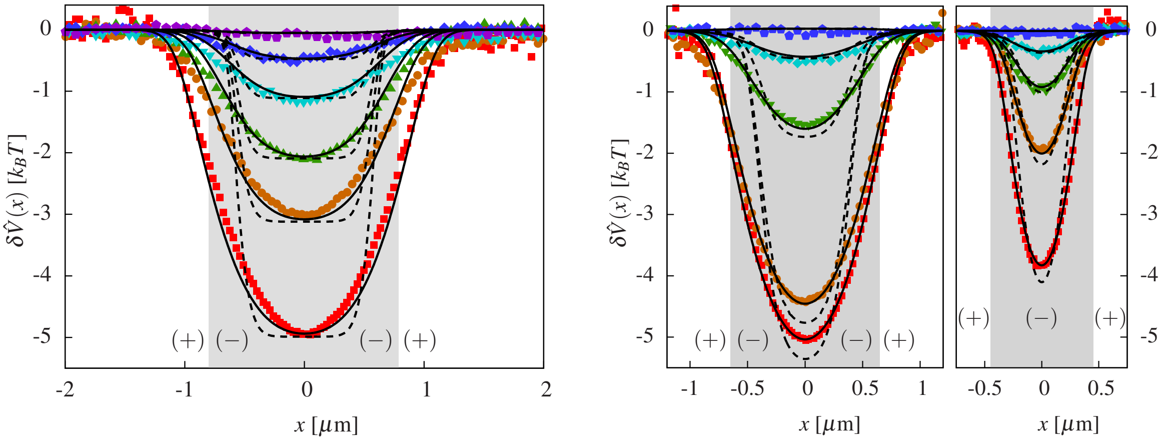

(a) Same as Fig. 3.7(a) for $L_- = 1.60\,\mu\mathrm{m}$ and $\Delta T = 0.3$, 0.23 (0.218), 0.21 (0.198), 0.19 (0.182), 0.17, 0.15 (0.153) K.

(b) Same as (a) for $L_- = 1.30\,\mu\mathrm{m}$ (left panel) and $L_- = 0.9\,\mu\mathrm{m}$ (right panel) with $\Delta T = 0.3$, 0.12, 0.1, 0.09 (0.083), 0.08 K for $L_- = 1.30\,\mu\mathrm{m}$ and $\Delta T = 0.3$, 0.18, 0.16, 0.145, 0.13 K for $L_- = 0.9\,\mu\mathrm{m}$.

Fig. 3.7, the effects of neighboring chemical steps do not influence each other and therefore the actual value of the periodicity P of the pattern does not affect the determination of L_-.) In agreement with this observation, the comparison with the theoretical predictions leads to fitted values L_- which are within the aforementioned range indicated in Tab. 3.1. From Fig. 3.7 we find that the experimental techniques described above lead to rather sharp chemical steps between two stripes with an uncertainty of only $\Delta x \leq 0.15\,\mu\mathrm{m}$.

The comparison for narrower stripe widths $L_- \lesssim 2\,\mu\mathrm{m}$ is shown in Fig. 3.8. Even for these cases, in which the effects of two neighboring chemical steps do interfere, the experimental data agree very well with the theoretical predictions obtained from the Derjaguin approximation. Whereas for $L_- = 1.6\,\mu\mathrm{m}$ and $L_- = 1.3\,\mu\mathrm{m}$ we have to take into account an uncertainty Δx of the position and associated with the shape of the chemical steps of about $0.2\,\mu\mathrm{m}$, for the smallest stripe width $L_- = 0.9\,\mu\mathrm{m}$ the chemical pattern turns out to be almost ideal with $\Delta x < 0.1\,\mu\mathrm{m}$ (see Tab. 3.1).

3.4. Summary

We have presented a detailed comparison between experimental measurements and corresponding theoretical predictions of critical Casimir forces acting on colloids suspended in a (near-) critical binary liquid mixture of water and 2,6-lutidine and close to chemically patterned substrates. Experimentally, chemical patterns of stripes of different widths and with laterally alternating adsorption preferences for either lutidine [$(+)$ boundary condition] or water [$(-)$ boundary condition] has been obtained via removing HDMS particles with a focused ion beam [37, 38] and by micro-contact printing of monolayers of thiols [39, 40], respectively. The solute colloidal particles — $2.4\,\mu$m diameter polystyrene spheres — were rendered hydrophilic, corresponding to $(-)$ boundary conditions, due to their surface charge. The key experimental findings, which have been analyzed theoretically here, were the following (see Refs. [37, 40]): At the fixed critical composition of the water-lutidine mixture, upon raising the temperature T towards its lower critical demixing point at $T = T_c$, *lateral* forces acting on the colloidal particles arise gradually. These critical Casimir forces cause the colloidal particles to be attracted to those chemical stripes which have the same adsorption preference as the particles and to be repelled from those stripes with the opposite adsorption preference. These lateral and normal contributions to the total effective forces (compare Subsec. 3.2.2) are negligible at temperatures T more than a few hundred mK away from the critical value T_c but they increase significantly upon approaching T_c. Eventually, they lead to laterally confining potentials for the colloidal particles with potential depths of several k_BT (see Figs. 3.4 and 3.6). These potentials can be reversibly tuned by minute temperature changes. In contrast to the case of surface patterns created by the focused ion beam, across a chemical step the critical Casimir potentials vary rather abruptly between two plateau values on a length scale of $\approx 0.8\,\mu$m for the case of patterns created by micro-contact printing (compare Figs. 3.5 and Fig. 3.7). This indicates that the microscopic structures of the chemical steps formed by imprinted layers of alkanethiols with different endgroups [40] are much sharper than those created by a focused ion beam [37]. For rather narrow stripes of widths $\lesssim 2\,\mu$m the effects of two neighboring chemical steps interfere and consequently reduce the potential depth and lead to rounded shapes of the effective potentials (see Fig. 3.8).

These experimental observations [37, 40] can be consistently interpreted in terms of the occurrence of the critical Casimir effect, and it is possible to quantitatively compare the measured potentials with the corresponding theoretical predictions. We have derived the effective potentials within the Derjaguin approximation (see Subsec. 3.2.1) based on universal scaling functions for the critical Casimir force between two plates with $(\pm,\pm)$ or $(+,-)$ boundary conditions as obtained from Monte Carlo simulation data.[22] In contrast to the present experimental measurements we are able to theoretically analyze the spatially fully resolved critical Casimir potential acting on a colloid. The resulting energy landscape for a colloidal particle is rather rich due to the interplay of several relevant forces, which we have taken into account (see Fig. 3.1). Typically, thermal fluctuations lead to large fluctuations of the lateral position and the distance between the colloidal particles and the substrate (see Fig. 3.2). Upon approaching T_c, however, strong normal and lateral critical Casimir forces abruptly localize the colloids very close to and above stripes exhibiting the same adsorption preference as the particles (see Fig. 3.3). Calculating the effectively one-dimensional, projected potentials for a single colloid, as they are obtained experimentally, we also take into account the possibility that the chemical pattern is not ideal, in addition to other experimental uncertainties.

---

[22] Differences in estimates for these scaling functions as obtained from various Monte Carlo simulations do not affect our results significantly.

Concerning the experiment by *Soyka et al.* [37], the assumption of non-ideal steps improves the agreement with the experimental data significantly. In view of the pronounced modifications of the resulting potential our analysis demonstrates that critical Casimir forces respond sensitively to geometrical details of the chemical pattern, which could not be checked independently in Ref. [37]. However, in spite of this improvement in the comparison between the *shapes* of the theoretical and experimental potentials, the analysis of the temperature dependence of the corresponding potential *depths* renders an amplitude ξ_0 of the correlation length ξ (treated as a fitting parameter) which is about twice as large as the one known from independent previous measurements.

This persisting discrepancy, together with the necessity to test independently the aforementioned assumption, called for a more detailed experimental study of the critical Casimir force acting in the presence of patterned substrates, which has been realized by *Vogt et al.* [39, 40]. Concerning the comparison with these experiments, not only the theoretical predictions for the potential depths agree with the experimental data (see Fig. 3.6) but also the correlation length ξ, as determined from our comparison, follows rather well the expected universal power law behavior and the associated non-universal amplitude ξ_0 is in agreement with previous independent experimental determinations (see Tab. 3.1). Moreover, the shapes of the potentials as a function of the lateral position of the colloid show good agreement between the theory and the experiments (see Figs. 3.7 and 3.8). Thus, we find that the chemical steps obtained by the experimental method used by *Vogt et al.* are sharp, with deviations of only a few percent in terms of the stripe width. From the detailed comparison with rather narrow chemical stripes (see Fig. 3.8(b)) we infer that even for such cases the Derjaguin approximation describes the actual behavior quite well, as expected from our corresponding theoretical analysis within mean-field theory in Chap. 2.

We conclude that the quantitatively successful comparison between the experimental data and the theoretical predictions demonstrates the significance and reliability of the critical Casimir effect for colloidal suspensions and reveals a new means of using them as model systems in soft-matter physics or in applications in integrated micro- or nano-devices.

4. Dynamic critical phenomena around colloidal particles

4.1. Introduction

CLOSE to criticality not only static properties of physical systems but also their dynamics is strongly altered and it obeys universal behavior (see Sec. 1.2.5). As for the static case, *surfaces* affect strongly the dynamical properties of a system, and their influence can be studied in terms of *dynamic surface universality classes* [183–186]. They depend on the boundary conditions and the representative, effective dynamical model [187–189]. Concerning the quantitative treatment, confining surfaces are accounted for by supplementing the Hamiltonian $\mathscr{H}$ in Eqs. (1.9) and (1.11) by the surface-Hamiltonian $\mathscr{H}_\mathrm{s}$ given in Eq. (1.7).

Critical dynamics in systems of *finite size* is a subject which is rather rarely explored and the corresponding studies have been mainly limited to the *film geometry* (see, e.g., Refs. [190–192] and references therein). In particular, spinodal decomposition with Model B dynamics has been studied numerically within the film geometry in detail [193–197]. The dynamical evolution of a *critical* system with Model A dynamics in a thin film geometry has been studied only recently [190, 192, 198–200].

In view of using colloidal suspensions for the study of critical phenomena and critical Casimir forces, knowledge about the influence of *curved* surfaces on critical dynamics is needed. Here, we extend previous studies of critical dynamics to systems which are confined by curved objects such as colloidal particles immersed in a fluid. Moreover, theoretically the question of the appropriate definition of the *dynamic* critical Casimir force raises, which is addressed below. In the following Sections we focus on the time evolution of the order parameter profile close to flat and curved surfaces.

4.2. Critical dynamics in systems confined by curved surfaces

Whereas the paradigmatic models for theoretical studies very often involve planar surfaces, most natural and experimental objects in soft matter, such as colloidal particles, have a *curved* surface. An obvious question concerns how the critical dynamics of the fluid surrounding such objects is affected due to non-zero curvature. In particular, one may ask how the effect of the surface propagates with time into the bulk, and whether the dynamical behavior is influenced by curvature as compared to the case of a planar wall.

Previous studies of critical phenomena close to curved objects *inter alia* include the theoretical [201, 202] and experimental [203] investigation of *static* critical adsorption at colloidal particles. The spatial order parameter profile turns out to depend strongly on the curvature and on the number of directions along which the object surface is bent [201]. The dynamics of Model A within the Ising universality class for curved surfaces has been studied on a *pseudosphere* in two dimensions (see, e.g., Refs. [204–207] and references therein). The pseudosphere is a geometric object with constant *negative* Gaussian curvature,[23] which — according to Ref. [205] — has been considered with respect to, e.g., quantum physics, string theory, or cosmology. In Refs. [208, 209] the phase ordering kinetics within Model A has been studied theoretically for surfaces implying all kinds of curvatures; in particular, the growth of the domain interfaces in time was studied. In Ref. [209] it has been shown that the domain growth dynamics depends strongly on the local Gaussian curvature and is qualitatively different from the one in flat systems. Basically, close to points with negative Gaussian curvature the dynamics becomes *faster* as compared to the planar case [205, 209], whereas close to points of positive Gaussian curvature the dynamics becomes slower [209]. In Ref. [210] conserved dynamics (Model B) has been studied numerically at spherical particles; however, for rigid spheres no deviation from the planar wall case has been seen — a fact which the authors of Ref. [209] attribute to the short evolution times performed in Ref. [210]. The qualitative changes induced by curvature as seen for the non-conserved Model A dynamics are expected to hold for Model B dynamics as well.

In order to extend previous considerations to the experimentally colloidal particles, here, we study the relaxation of the order parameter (Model A) next to a single colloid of cylindrical or spherical shape (zero or positive Gaussian curvature) immersed in a critical (binary) fluid. Model A dynamics amounts to replacing the kinetic coefficient $\hat{\Omega}$ in the general Langevin equation Eq. (1.9) by the scalar relaxation constant Ω; within mean field theory (MFT) it is given by $\Omega = (\xi_0^+)^2/t_{R,0}^+$ [190]. Here, we consider the Ising universality class, i.e., a scalar order parameter field $\phi(\mathbf{r},t)$. As for the static case, we are mainly interested in the case without bulk fields, $h = 0$. First, we briefly recall critical dynamics at planar walls and in thin films in Subsecs. 4.2.1 and 4.2.2 and test our numerical method described in App. A.3 with these well known systems. In Subsec. 4.2.3 we study critical dynamics at curved objects within MFT and derive a short-distance expansion in Subsec. 4.2.4 for several kinds of surface universality classes at the boundary of the curved surface. Finally in Subsec. 4.2.5 we numerically study the critical relaxation of the order parameter next to colloidal particles corresponding to the ordinary surface transition (Dirichlet BC).

---

[23] Every point on a surface (in $d = 3$) has two principal curvatures, κ_1 and κ_2, given by the maximum and the minimum value of the curvatures of the surface along the tangential directions of this point. The Gaussian curvature is defined as the product $K = \kappa_1\kappa_2 = 1/(R_1R_2)$, where R_1 and R_2 are the corresponding principal radii of curvature. The Gaussian curvature is positive, $K > 0$, whenever both centers of the circles corresponding to the principal curvature (radii) lie on the same side of the surface, e.g., on every point on top of or within a sphere surface. $K = 0$ whenever one of the principal curvatures vanishes, as for the case of a cylinder. Negative Gaussian curvature, $K < 0$, is exhibited when the centers of the curvature circles lie on different sides of the surface, e.g., on saddle points, or generally on hyperboloids.

The critical dynamics of the relaxation of the order parameter at planar surfaces and in thin films has been studied in Refs. [183–185, 188, 190, 192]. Due to the presence of a confining wall, in experiments and simulations very often one has to deal with finite values of the order parameter even in the homogeneous phase of the system. Thus, it is crucial to account for the nonlinear terms of the Hamiltonian Eq. (1.6) and the Langevin equation Eq. (1.9). The evolution equation for the mean field order parameter profile $m(\mathbf{r},t) = (u/3!)^{-1/2}\langle\phi(\mathbf{r},t)\rangle$ can be derived at lowest level ("zero loop expansion") from the Langevin equation given in Eq. (1.9) with the standard Landau-Ginzburg bulk and surface Hamiltonians given in Eqs. (1.6) and (1.7), respectively (see Secs. 1.2.4 and 1.2.5). Since the average of the stochastic noise vanishes, one finds for the mean field order parameter evolution in the bulk [156, 157, 190]

$$\partial_t m(\mathbf{r},t) + \Omega\left\{-\nabla^2 + \hat{\tau} + m^2(\mathbf{r},t)\right\} m(\mathbf{r},t) = 0. \tag{4.1}$$

In a confined system Eq. (4.1) has to be supplemented with equations for the values of m at the boundaries, depending on the boundary conditions at the surfaces and derived from Eq. (1.7).[24]

4.2.1. Nonlinear relaxation close to planar walls

Before considering the order parameter profile evolution close to a curved surface, we briefly recall the known results obtained for the semi-infinite geometry (i.e., a single planar wall) in Refs. [184, 185, 190]. For the semi-infinite system, the mean field order parameter spatially depends only on the distance $x_\perp$ from the wall located at $x_\perp = 0$. In the absence of bulk fields, from renormalization-group considerations one can infer the scaling form [184, 185, 190]

$$\begin{aligned} m(x_\perp,t) = {} & \frac{1}{\xi_0^+}\left(\frac{t}{t_{R,0}^+}\right)^{-\beta/(z\nu)} \\ & \times \Psi\left((x_\perp/\xi_0^+)(t/t_{R,0}^+)^{-1/z}, \mathrm{sign}(\hat{\tau})t/t_R, \{\xi_0^+ m(x'_\perp,0)(t/t_{R,0}^+)^{\beta/z\nu}\}\right), \end{aligned} \tag{4.2}$$

where the temperature enters via the relaxation time t_R [Eq. (1.8)]. Within MFT and Model A one has $\beta = \nu = 1/2$ and $z = 2$ (see above). The scaling function Ψ depends on the initial configuration $m(x_\perp,0)$ of the order parameter profile, which is assumed to be created via a bulk field which vanishes at $t = 0$ [184, 190]. For "large" initial order parameter values $m(x_\perp, 0)\xi_0^+ \gg (t/t_{R,0}^+)^{-\beta/z\nu}$, the dynamical evolution becomes independent of it and follows the scaling function $\Psi(u_\perp, w, \infty)$ [190].

---

[24] From Eq. (4.1) one can directly infer that the linear regime (*Gaussian approximation* of $\mathscr{H}$), is valid only for $|\hat{\tau}| \gg m^2$. Clearly at criticality ($\hat{\tau} = 0$), the linear approximation is not applicable and the dynamical behavior is dominated by the nonlinear contribution. For a more thorough discussion concerning the ranges of validity of the linear regime in confined geometries see, e.g., Ref. [190].

From a short-distance expansion (more precisely, $(x_\perp/\xi_0^+)(t/t_{R,0}^+)^{-1/z} \to 0$), one finds that $\Psi(u_\perp, w, \infty) \propto u_\perp^{(\beta_1-\beta)/\nu}$, where β_1 is the surface critical exponent of the order parameter which is in general different from β and depends on the surface universality class [190].[25] That is, close to the wall, the order parameter follows the behaviors $m \propto x_\perp^{(\beta_1-\beta)/\nu}$ with distance, and $m \propto t^{-\beta_1/\nu z}$ with time.

At a fixed distance $x_\perp$ from the wall (after a non-universal transient time due to the initial order parameter profile, but still at short times[26]), the order parameter first relaxes according to the universal bulk behavior $\Psi(\infty, w, \infty)$ [190]. At the critical point, i.e., $t_R \to \infty$, the bulk behavior is given by $\Psi(\infty, 0, \infty) = const$, i.e., $m \propto t^{-\beta/z\nu}$. As time goes by, $(x_\perp/\xi_0^+) < (t/t_{R,0}^+)^{1/z}$, and the surface affects also the behavior at a distance $x_\perp$ from the wall so that the order parameter relaxes according to the surface behavior $m \propto t^{-\beta_1/\nu z}$ [190]. Note that these properties of the order parameter relaxation are affected *off*-criticality only when m becomes small and the relaxation is exponential in time for $t \gg t_R$, and at distances from the surface much larger than the correlation length $x_\perp \gg \xi$ [190].

We have applied a finite element method described in detail in App. A.3 to the semi-infinite system with an ordinary transition at a flat surface (Dirichlet BC), i.e., $m(x_\perp = 0, t) = 0$. (This effectively one-dimensional problem is used for testing the numerical method which can deal with two spatial dimensions.) Inspired by Ref. [190] we chose an initial order parameter profile of the form $m(x_\perp, t = 0) = Kx_\perp/D$ for $x_\perp < D$ and $m(x_\perp, t = 0) = K$ for $x_\perp \geq D$, where K and D are constants. Figure 4.1 shows a typical spatio-temporal order parameter profile close to a single wall at $T = T_c$ as obtained within the finite element method for the values $K = 20/\xi_0^+$ and $D = 0.1\xi_0^+$.

Using the finite element method, we have been able to reproduce the dynamic critical behavior in an semi-infinite system. As can be inferred from Fig. 4.2, at fixed distance $x_\perp$, after a non-universal transient time which depends on the initial conditions, the order parameter profile m first decays as within the bulk $\propto t^{-\beta/z\nu} = t^{-1/2}$. After a crossover time $t/t_{R,0}^+ \simeq (x_\perp/\xi_0^+)^z$ the relaxation proceeds as at a surface $m \propto t^{-\beta_1/z\nu} = t^{-1}$.

---

[25] Within MFT, $\beta_1 = 1$ for the ordinary surface universality class and $\beta_1 = 1/2$ for the special universality class [66]. For the extraordinary (normal) universality class corresponding to critical adsorption, the order parameter at the surface and its derivative are continuous and a singularity occurs for its second derivative only. Thus, one identifies $\beta_1 = 2$; however, this singularity is so weak such that effectively the surface order parameter is constant for the extraordinary transition which would correspond to a vanishing exponent [68].

[26] Beyond the MFT discussed here, in the initial time regime the order parameter evolution is given according to a universal behavior characterized by the initial-slip exponent [186, 211].

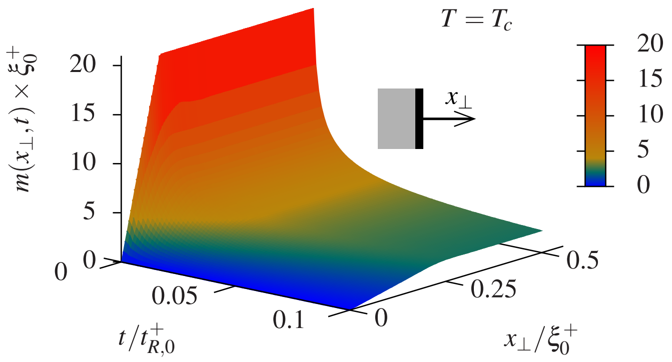

Figure 4.1: Order parameter profile $m(x_\perp, t) \times \xi_0^+$ [Eq. (4.2)] at $T = T_c$ as obtained numerically (see App. A.3) from Eq. (4.1). The order parameter exhibits Dirichlet BC at the wall (ordinary surface transition). Its initial value at distances $x_\perp > D = 0.1\xi_0^+$ has been chosen to be $K = 20/\xi_0^+$, so that for times $t/t_{R,0}^+ \gg (\xi_0/K)^z \simeq 0.003$, i.e., after a non-universal transient time, the profile evolution is universal (see the main text).

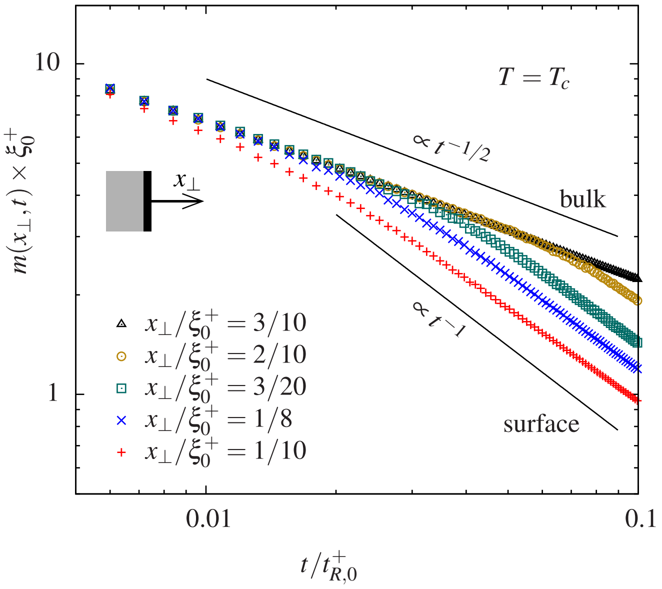

Figure 4.2: Cuts through the order parameter profile m shown in Fig. 4.1 at different distances $x_\perp$ from the wall, and as a double-logarithmic plot as function of t. Symbols correspond to numerical data obtained via the method described in App. A.3. As expected, at fixed position $x_\perp$ the order parameter first decays according to the bulk behavior $\propto t^{-1/2}$. After a waiting time which increases with distance from the wall, the profile decays according to the surface behavior $\propto t^{-1}$.

4.2.2. Critical dynamics in thin films

Thin films, i.e., slabs $\mathbf{R}^{d-1} \times [0,L]$ of finite thickness L, provide a paradigm for studying finite-size effects. Note that in the present context, L has to be considered much larger than the typical microscopic length scale ξ_0^+. Whereas critical phenomena and the occurrence of critical Casimir forces in thin films have been studied rather comprehensively as far as their equilibrium *static* properties are concerned, their *dynamics* is a less explored subject. In particular, the order parameter evolution within Model A dynamics in thin films has been studied recently [190, 192, 199, 200]. Here, we briefly review the MFT behavior given by Eq. (4.1) with appropriate boundary conditions, as presented in detail in Ref. [190].

Assuming translation invariance along the directions parallel to the film walls, the order parameter profile m depends on the film thickness L in addition to the distance $x_\perp \in [0,L]$ from one wall, to time, and to temperature, and its expected scaling behavior is given by (see also Eq. (4.2) for the semi-infinite system) [190]:

$$\begin{aligned} m(x_\perp,L,t) = {} & \frac{1}{\xi_0^+}\left(\frac{t}{t_{R,0}^+}\right)^{-\beta/(z\nu)} \\ & \times \hat{\Psi}\left(x_\perp/L,(L/\xi_0^+)(t/t_{R,0}^+)^{-1/z},\mathrm{sign}(\hat{\tau})t/t_R,\{\xi_0^+ m(x'_\perp,L,0)(t/t_{R,0}^+)^{\beta/z\nu}\}\right). \quad (4.3) \end{aligned}$$

For $T = T_c$ and for sufficiently large values of the initial order parameter $m(x_\perp,L,0)\xi_0^+ \gg (t/t_{R,0}^+)^{-\beta/z\nu}$ the scaling function $\hat{\Psi}(\hat{x},\hat{t}^{-1/z},0,\infty)$ depends only on the two scaling variables $\hat{x} \equiv x_\perp/L$ and $\hat{t} \equiv (t/t_{R,0}^+)/(L/\xi_0^+)^z$. Thus, for the dimensionless quantity $\hat{m}(\hat{x},\hat{t}) \equiv L \times m(x_\perp,L,t)$, Eq. (4.1) reduces to [190]

$$\partial_{\hat{t}}\hat{m}(\hat{x},\hat{t}) + \left\{-\partial_{\hat{x}}^2 + \hat{m}^2(\hat{x},\hat{t})\right\}\hat{m}(\hat{x},\hat{t}) = 0, \quad (4.4)$$

where the MFT values $\Omega = (\xi_0^+)^2/t_{R,0}^+$ and $z = 2$ have been used [190].

For the *ordinary surface transition* (i.e., Dirichlet BC and $\beta_1 = 1$) at both confining walls of the film, four distinct temporal regimes for the behavior of the order parameter $\hat{m}(\hat{x},\hat{t})$ at a fixed position $\hat{x} \in (0,1)$ have been predicted and numerically observed in Ref. [190]:

(i) First, the order parameter relaxes non-universally depending on the specific initial profile.

(ii) After a non-universal transient time, the early relaxation is determined by the bulk behavior, and therefore $\hat{m} \propto \hat{t}^{-\beta/z\nu}$.

(iii) For times $\hat{t} \gtrsim \hat{x}^z$ the effect of the presence of the surface has reached the points at a distance $\hat{x}$, and the order parameter relaxes according to the surface behavior $\hat{m} \propto \hat{t}^{-\beta_1/\nu z}$.

(iv) Within the late relaxation regime, the effects of the two surfaces of the film interfere, and the order parameter vanishes exponentially as $\hat{m} \propto \exp(-\pi^2\hat{t})$.

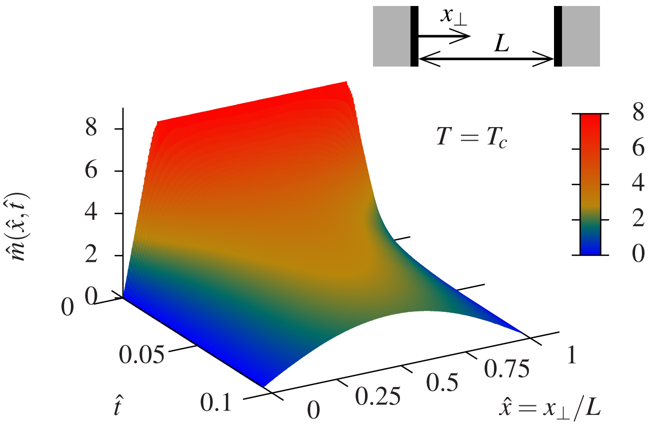

Figure 4.3: Numerically obtained order parameter $\hat{m}(\hat{x},\hat{t})$ in a film of thickness L with ordinary (Dirichlet) BC at the two confining walls. At $T = T_c$, $\hat{m} = L \times m$ is only a function of $\hat{x} = x_\perp/L$ and $\hat{t} = (t/t^+_{R,0})(L/\xi^+_0)^{-z}$. The initial profile $\hat{m}(\hat{x},\hat{t}=0)$ has a trapezoidal shape (see the main text). Upon increasing time $\hat{t}$, the order parameter approaches a universal shape independent of the initial conditions. For late times, $\hat{m}$ decays exponentially with $\hat{t}$ and has a sinusoidal shape as function of $\hat{x}$.

The various crossover times between these regimes have been defined operatively and studied in Ref. [190]. Whereas the first three regimes are analogous to the semi-infinite system, the latest time regime (iv), occurs at $T = T_c$ only for a finite size system. That is, the crossover time from regime (iii) to (iv) diverges with $(L/\xi^+_0)^z$ [190]. This is related to the fact, that in finite systems the actual critical point is shifted from the bulk one. Time regime (iv) is in agreement with the solution of the linear Langevin equation valid for relatively small $\hat{m}$, where the quadratic term in Eq. (4.4) can be neglected; this solution reads [190]

$$\hat{m}_{(iv)}(\hat{x},\hat{t}) = \sum_{n=1}^{\infty} \alpha_n \exp(-\pi^2 n^2 \hat{t}) \sin(\pi\hat{x}), \qquad (4.5)$$

where the coefficients α_n depend on the initial profile [190]. If $\alpha_1 \neq 0$, the first term of the series dominates for large $\hat{t}$.

We have applied the numerical method described in App. A.3 to the film geometry with ordinary transitions at both confining surfaces (Dirichlet BC), i.e., $\hat{m}(\hat{x}=0,t) = \hat{m}(\hat{x}=1,t) = 0$. Analogously to Ref. [190] we have chosen an initial order parameter profile of the form $\hat{m}(\hat{x},\hat{t}=0) = \hat{K}\hat{x}/\hat{D}$ for $\hat{x} < \hat{D}$, $\hat{m}(\hat{x},\hat{t}=0) = \hat{K}$ for $\hat{D} \le \hat{x} \le 1-\hat{D}$, and $\hat{m}(\hat{x},\hat{t}=0) = \hat{K}(1-\hat{x})/\hat{D}$ for $\hat{x} > 1-\hat{D}$, where $\hat{K}$ and $\hat{D}$ are constants. Under these assumptions, $\hat{m}$ is symmetric across the axis $\hat{x} = 1/2$. In Fig. 4.3 the order parameter profile $\hat{m}(\hat{x},\hat{t})$ obtained within the finite element method is shown for the film geometry at $T = T_c$ with $\hat{K} = 8$ and $\hat{D} = 0.125$. According to the considerations above, one expects universal behavior after a transient time depending on the initial conditions, i.e., for $\hat{t} \gg 1/[\hat{m}(\hat{x},\hat{t}=0)]^2$. In the particular case shown in Fig. 4.3 this

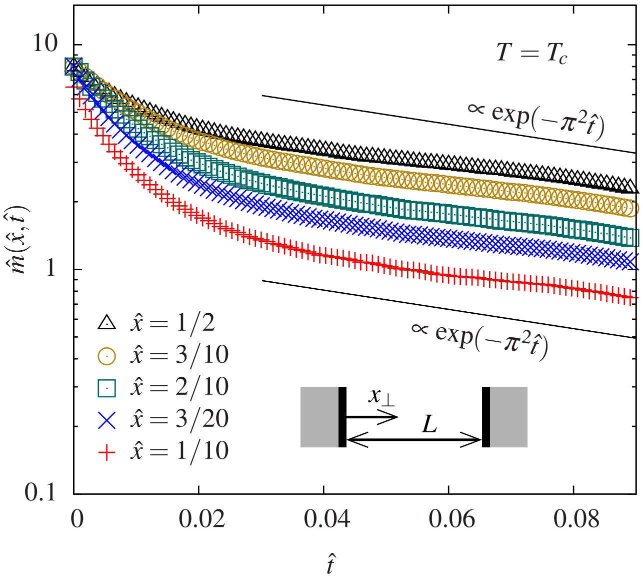

Figure 4.4: Order parameter profile $\hat{m}$ in the film geometry as shown in Fig. 4.3 as a function of $\hat{t}$ for various values of $\hat{x}$. The order parameter profile decays exponentially $\propto \exp(-\pi^2\hat{t})$ for values of $\hat{t} \gtrsim 0.05$.

occurs for $\hat{t} \gg 0.015$.

The finite element method used here is able to reproduce the feature which distinguishes the film geometry from the semi-infinite system, i.e., the exponential decay of $\hat{m}$ at $T = T_c$. This is shown in Fig. 4.4, where at fixed distance $\hat{x}$ the order parameter profile $\hat{m}$ decays after some time as $\propto \exp(-\pi^2\hat{t})$ (see, also Fig. 16 of Ref. [190]).

In Fig. 4.5 the order parameter $\hat{m}$ is shown as a function of $\hat{x}$ for various times $\hat{t}$. Whereas for small $\hat{t}$, the space-dependence of $\hat{m}$ shown in Fig. 4.5 resembles its nonuniversal initial condition (i.e., a trapezoidal shape here), for $\hat{t} \gtrsim 0.05$, $\hat{m}$ approaches a sinusoidal shape as predicted in Ref. [190]. The black, solid lines in Fig. 4.5 correspond to the functions $A\sin(\pi\hat{x})$, where we have chosen $A = \hat{m}(\hat{x} = 1/2, \hat{t})$.

4.2.3. Dynamic critical phenomena around colloidal particles

Here we consider the relaxation of the order parameter with Model A dynamics close to a d_s-dimensional hypercylinder in infinite space, where $d_s - 1$ is the number of directions along which the surface (of dimension $d-1$) of the curved object is bound, whereas along the remaining directions it is infinitely extended. In particular, $d_s = 2$ corresponds to a cylinder, $d_s = 3$ corresponds to a sphere, and $d_s = 4$ corresponds to a hypersphere in $d = 4$. This extends the case of a planar wall (which corresponds to $d_s = 1$) and provides the suitable treatment for colloidal particles of rodlike or spherical shape (see, e.g., Refs. [201, 202] for equilibrium critical order parameter profiles next to colloidal particles). Note that the extension of d_s to values larger than

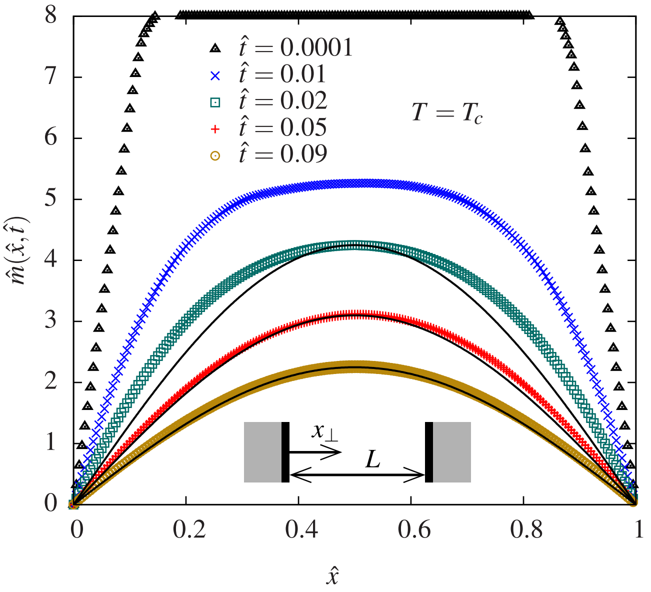

Figure 4.5: Order parameter $\hat{m}$ shown as function of $\hat{x}$ at different times $\hat{t}$. For small $\hat{t}$ the shape of the order parameter profile across the slab is dominated by its nonuniversal initial condition. For $\hat{t} \gtrsim 0.05$ the sinusoidal shape predicted for the late time behavior (see the main text) is approached: the black, solid lines correspond to $A\sin(\pi\hat{x})$ with $A = \hat{m}(\hat{x} = 1/2, \hat{t})$.

three is mainly due to technical reasons because the upper critical dimension of the system we are primarily interested in is four, which corresponds to MFT. The mean field scaling function for the order parameter profile around the colloid depends on the distance $r_\perp$ from the surface of the cylindrical hypersphere and on the radius of the latter in addition to time, i.e., $m(r_\perp, R, t)$, whereas it is translationally invariant along the tangential directions and the directions $r_\parallel$ parallel to the cylinder axis (for $d_s < d$).

It is convenient to introduce the dimensionless quantities $\bar{R} \equiv R/\xi_0^+$, $\bar{r} \equiv r_\perp/\xi_0^+$, $\bar{t} \equiv t/t_{R,0}^+$, $\bar{\tau} \equiv \hat{\tau}(\xi_0^+)^2$, and $\bar{m} \equiv \xi_0^+ m$. Then, the dynamical evolution equation reads

$$\partial_{\bar{t}}\bar{m}(\bar{r},\bar{R},\bar{t}) + \left\{-\partial_{\bar{r}}^2 - \frac{d_s - 1}{\bar{r}+\bar{R}}\partial_{\bar{r}} + \bar{\tau} + \bar{m}^2(\bar{r},\bar{R},\bar{t})\right\}\bar{m}(\bar{r},\bar{R},\bar{t}) = 0, \tag{4.6}$$

which is obtained from Eq. (4.1) by using the fact that within MFT the relaxation constant can be expressed in terms of the non-universal amplitudes as $\Omega = (\xi_0^+)^2/t_{R,0}^+$ [190]. Equation (4.6) has to be supplemented with a boundary condition for $\bar{m}$ or $\partial_{\bar{r}}\bar{m}$ at $\bar{r} = 0$. Analogous to the reasoning above, one obtains the following scaling behavior for $\bar{m}$:

$$\bar{m}(\bar{r},\bar{R},\bar{t}) = \bar{t}^{-\beta/(z\nu)}\bar{\Psi}\left(\bar{r}/\bar{t}^{1/z}, \bar{r}/\bar{R}, \operatorname{sign}(\bar{\tau})|\bar{\tau}|^{\nu z}\bar{t}, \{\bar{m}(\bar{r}',\bar{R},0)(\bar{t})^{\beta/z\nu}\}\right). \tag{4.7}$$

For large initial values of $\bar{m}$ or at late times (as long initially the order parameter is finite), the universal scaling function $\bar{\Psi}$ becomes independent of the initial conditions of the system.

In the following we restrict ourselves to the case just described, i.e., $\bar{m}(\bar{r},\bar{R},0)(\bar{t})^{\beta/z\nu} \gg 1$, and focus on the behavior at the critical temperature. Then, Eq. (4.6) becomes

$$\partial_{\bar{t}}\bar{m} - \partial_{\bar{r}}^2\bar{m} - \frac{d_s-1}{\bar{r}+\bar{R}}\partial_{\bar{r}}\bar{m} + \bar{m}^3 = 0, \tag{4.8}$$

and the order parameter profile takes the simplified scaling form:

$$\bar{m}(\bar{r},\bar{R},\bar{t}) = \bar{t}^{-\beta/(z\nu)} M\left(\bar{r}\bar{t}^{-1/z}, \frac{\bar{r}}{\bar{R}}\right), \tag{4.9}$$

where $M(u,v) = \bar{\Psi}(u,v,0,\infty)$.

4.2.4. Critical dynamics at curved objects

The curvature of a cylindrical or spherical particle influences significantly the critical behavior of the medium surrounding it. Here we calculate the curvature contribution by means of a short-distance expansion. To this end, it is convenient to separate the spatial dependencies of the order parameter $\bar{m}$ and to introduce a generalized amplitude function $g(\bar{r}/\bar{R})$ for the curvature contribution [201]. Moreover, we take into account an additional amplitude function $h(w)$ depending on the scaling variable $w = \bar{R}\bar{t}^{-1/z}$, which describes the influence of the curvature on the characteristic time evolution of the system. Thus, we heuristically consider the following *ansatz*:

$$M\left(\bar{r}\bar{t}^{-1/z}, \frac{\bar{r}}{\bar{R}}\right) = h(\bar{R}\bar{t}^{-1/z}) \times f\left(\bar{r}\bar{t}^{-1/z}\right) \times g\left(\frac{\bar{r}}{\bar{R}}\right), \tag{4.10}$$

where by definition $g(v \to 0) \equiv 1$, with $v \equiv \bar{r}/\bar{R}$. The ansatz in Eq. (4.10), which we have chosen in order to separate the different contributions does *not* capture all possible forms of the scaling function M. For the case of a planar wall ($d_s = 1$) one has $g(v) = h(w) = 1$.

In order to obtain an expansion for $u \equiv \bar{r}\bar{t}^{-1/z} \to 0$, which corresponds to short distances or to late times, we expand f around $u = 0$:

$$f(u \to 0) = \sum_{i=-1}^{\infty} a_i u^i. \tag{4.11}$$

For $i < -1$, we do not find a non-zero solution of the resulting equations. After inserting Eq. (4.11) into Eq. (4.10) one obtains differential equations for g and h corresponding to the leading behavior via power counting of u (see App. C).

Ordinary transition — Dirichlet BC

Within the ordinary surface universality class (corresponding to $c > 0$ and $h_1 = 0$ in Eq. (1.7)) the surface is less ordered than the bulk. Since for the ordinary transition $\beta_1 > \beta$, M vanishes at $\bar{r} = 0$, and the order parameter asymptotically satisfies a *Dirichlet boundary condition* [66].

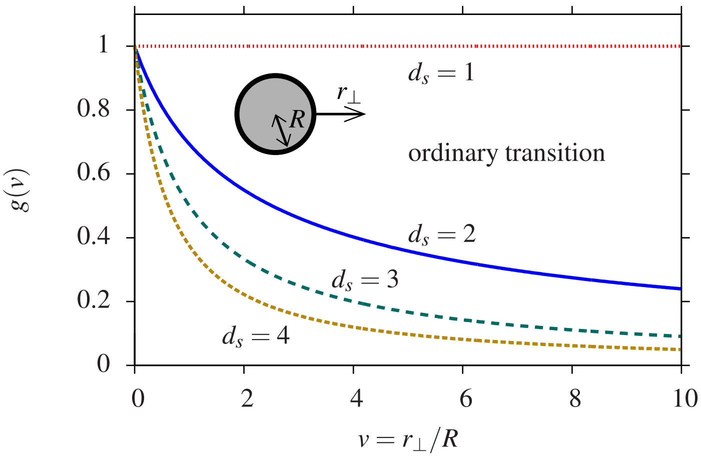

Figure 4.6: Scaling function $g(v)$ in mean field approximation and as a function of $v = \bar{r}/\bar{R} = r_\perp/R$ as obtained from an expansion for $u = \bar{r}\bar{t}^{-1/2} \to 0$ (see Eq. (4.10)). Here $g(v)$ is shown for the ordinary surface transition, i.e., Dirichlet BC at the confining curved surface and for different dimensionality d_s of the curved object. For $v \to 0$ all curves approach the value 1 which corresponds to the case of a planar wall. For $d_s \geq 2$ $g(v)$ vanishes for large v.

Accordingly, the two first terms in the expansion of f in Eq. (4.11) vanish, i.e., $a_{-1} = 0$ and $a_0 = 0$.

The leading term for Dirichlet BC is thus $a_1 u^1$ [Eq. (4.11)], and we find that $a_{2i} = 0$ for all $i \in \mathbf{N}$. From Eq. (4.8) one obtains to leading order (see Eq. (C.4)) the following equation for $g(v)$:

$$(d_s - 1)g(v) + (2 + v + d_s v)g'(v) + v(1 + v)g''(v) = 0. \tag{4.12}$$

Accordingly, $g(v)$ is *independent* of the amplitude function $h(\bar{R}\bar{t}^{-1/z})$ and of a_1. Equation (4.12) is solved for the different geometries by the functions

$$d_s = 1: \qquad g(v) = 1, \tag{4.13}$$

$$d_s = 2: \qquad g(v) = \frac{\ln(1+v)}{v} \simeq 1 - \frac{1}{2}v + \frac{1}{3}v^2 - \frac{1}{4}v^3 + \ldots, \tag{4.14}$$

$$d_s = 3: \qquad g(v) = \frac{1}{1+v} \simeq 1 - v + v^2 - v^3 + \ldots, \tag{4.15}$$

$$d_s = 4: \qquad g(v) = \frac{2+v}{2(1+v)^2} \simeq 1 - \frac{3}{2}v + 2v^2 - \frac{5}{2}v^3 + \ldots. \tag{4.16}$$

That is, close to a (curved) wall, for $v \to 0$, the order parameter profile first grows linearly with distance $\bar{r}$ from the surface and takes for finite values of v a curvature contribution given by Eqs. (4.14)–(4.16) and shown in Fig. 4.6. Note that there may be an additional dependence of the order parameter on time via the scaling function $h(\bar{R}\bar{t}^{-1/2})$.

From Eq. (4.13) we recover the case of a planar wall ($d_s = 1$) [184, 190], i.e., asymptotically $M(u, v = 0) \propto u$, which is in agreement with the expected behavior $\propto u^{(\beta_1 - \beta)/\nu}$ with $\beta_1 = 1$

valid for the ordinary transition [66]. For $d_s = 1$ we find the following subleading terms for the behavior close to a planar wall:

$$a_3 = -\frac{1}{6}a_1, \qquad a_5 = \frac{1}{20}\left(a_1^3 - \frac{1}{3}a_1\right), \dots . \tag{4.17}$$

Special surface universality class — Neumann boundary conditions

At the special surface transition ($c = h_1 = 0$ in Eq. (1.7)) the order at the surface is changed just as within the bulk. Consequently, within MFT, $\beta_1 = \beta = 1/2$ and one has *Neumann boundary conditions* at the confining surface. The leading term a_0 [Eq. (4.11)] for Neumann boundary conditions is independent of u. Moreover, one has $a_{-1} = a_1 = 0$, leading to $a_{2i-1} = 0$ for all $i \in \mathbf{N}$. To leading order the behavior of g is determined from Eq. (C.3) and *independent* of $h(w)$:

$$(d_s - 1)g'(v) + (1+v)g''(v) = 0, \tag{4.18}$$

which is solved by

$$d_s = 1: \qquad g(v) = 1, \tag{4.19}$$

$$d_s = 2: \qquad g(v) = 1, \tag{4.20}$$

$$d_s = 3: \qquad g(v) = \frac{1}{1+v} \simeq 1 - v + v^2 - v^3 + \dots, \tag{4.21}$$

$$d_s = 4: \qquad g(v) = \frac{1}{(1+v)^2} \simeq 1 - 2v + 3v^2 - 4v^3 + \dots . \tag{4.22}$$

The scaling functions $g(v)$ for the special surface transition are shown in Fig. 4.7 for the various values of d_s. In the case of a planar wall, this is in agreement with the expected behavior $M(u \to 0, 0) \propto u^{(\beta_1 - \beta)/\nu} = const$ for the special transition.

Normal (extraordinary) surface universality class — Critical adsorption

Finally, we consider the case of (strong) critical adsorption, corresponding to $(\pm)$ BC, which belongs to the normal (extraordinary) surface universality class [66]. For the normal surface transition, the corresponding leading behavior is determined by the term $a_{-1}u^{-1}$ in Eq. (4.11). This leading behavior determines g from Eq. (4.8) via Eq. (C.2):

$$vg''(v) - \frac{(d_s-3)v-2}{1+v}g'(v) + \frac{(d_s-3)v-2}{v(1+v)}g(v) + \frac{a_{-1}^2 h^2(w)}{v}g^3(v) = 0, \tag{4.23}$$

where $w = \bar{R}\bar{t}^{-1/z}$. For $g(v)$ we find solutions to Eq. (4.23) for $a_{-1} = \pm\sqrt{2}$ and $h(w) \equiv 1$. Then, Eq. (4.23) for $g(v)$ is identical to the ones obtained for the curvature part of the *static* MFT

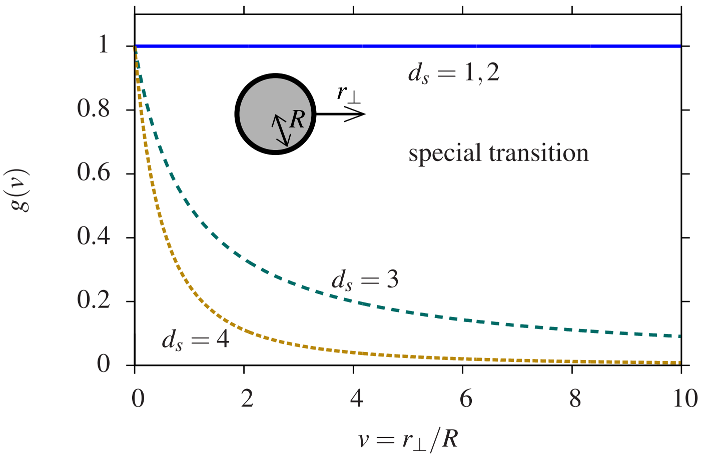

Figure 4.7: Scaling function $g(v)$ (see Eq. (4.10)) within MFT and as function of $v = \bar{r}/\bar{R} = r_\perp/R$ as obtained from an expansion for $\bar{r}\bar{t}^{-1/2} \to 0$ for the case of the special surface transition, i.e., Neumann BC at the curved wall. $g(v \to \infty)$ vanishes for $d_s > 2$, whereas it takes the planar wall value 1 for the marginal case $d_s = 2$.

equation of critical adsorption (see Sec. IV in Ref. [201]):

$$d_s = 1: \qquad g(v) = 1, \tag{4.24}$$

$$d_s = 5/2: \qquad g(v) = \frac{\frac{1}{2}v}{1 + v - \sqrt{1+v}}, \tag{4.25}$$

$$d_s = 4: \qquad g(v) = \frac{1}{1 + \frac{1}{2}v}. \tag{4.26}$$

Note that in Eq. (4.25) the value of d_s is extended to an unphysical non-integer value basically due to technical reasons. Numerical solutions for $d_s = 2, 3$ are presented in Ref. [201]. An expansion for $d_s = 3$ and small values of v can be found in Refs. [201, 212].

The resulting dynamical behavior for the extraordinary transition at a planar wall is given by $M(u \to 0, 0) \propto u^{-\beta/\nu}$. This is formally not in agreement with the one discussed above, i.e., $\propto u^{(\beta_1 - \beta)/\nu}$ [190], because $\beta_1 = 2$ for the extraordinary transition. However, at the extraordinary transition, the order parameter and its derivative are continuous at the surface and at the critical point, so that $\beta_1 = 2$ has been obtained only for the *singular* part of the order parameter [66, 68]. Effectively, it is therefore reasonable to assume a constant behavior of the order parameter at the surface corresponding to a vanishing exponent β_1, so that both expressions effectively agree.

It is not surprising that the curvature contribution $g(v)$ of the MFT scaling function $M(u, v)$ coincides with the corresponding *static* contributions in the limit $u \to 0$ because the latter limit corresponds to the asymptotic behavior for either short distances at all times *or* late stages of relaxation at all distances, i.e., the equilibrated system.

Small-sphere expansion

The curvature contributions g obtained for $d_s = 1, \dots, 4$ for the extraordinary transition (see, e.g., Fig. 7 in Ref. [213]) differ significantly from the ones obtained for the ordinary transition and the special transition shown in Fig. 4.6 and Fig. 4.7, respectively. For the ordinary transition $g(v \to \infty) = 0$ for all $d_s \geq 2$ and for the special transition $g(v \to \infty) = 0$ for all $d_s > 2$, whereas for the extraordinary transition $g(v \to \infty)$ approaches a finite value for $d_s < 3$, and vanishes asymptotically only above the marginal value $d_s = 3$ [201]. This difference can be understood in terms of a small-sphere expansion [41–43, 201].

Whenever the radius of the (hyper-)cylinder is small compared to $r_\perp$ (but still large on a microscopic scale), the statistical weight $\exp(-\delta\mathscr{H})$ due to its presence can be systematically expanded in a series with increasing powers of ϕ, i.e., [43, 201]

$$\exp(-\delta\mathscr{H}) \propto 1 + \varepsilon^{\phi}_{d_s,d} R^{(x_\phi + d_s - d)} \omega^{\phi}_{d_s,d} + \varepsilon^{\phi^2}_{d_s,d} R^{(x_{\phi^2} + d_s - d)} \omega^{\phi^2}_{d_s,d} + \dots, \tag{4.27}$$

where $\varepsilon^{\phi^i}_{d_s,d}$ are amplitudes, $i = 1, 2$, and

$$\omega^{\phi^i}_{d_s,d} = \begin{cases} \displaystyle\int\limits_{\mathbf{R}^{d-d_s}} \mathrm{d}^{d-d_s} r_\parallel \phi^i(r_\perp = 0), & d_s < d, \\ \phi^i(0), & d_s = d. \end{cases} \tag{4.28}$$

In Eq. (4.27) the corresponding exponents are given by $x_\phi = \beta/\nu$ and $x_{\phi^2} = d - \nu^{-1}$ [41]. For symmetry-breaking BC at the (hyper-)cylinder such as the extraordinary transition, the term corresponding to ϕ in Eq. (4.27) is crucial, because it is not invariant under a transformation $\phi \leftrightarrow -\phi$. On the other hand, for symmetry-preserving BC, such as the ordinary and the special transitions, $\varepsilon^{\phi}_{d_s,d} = 0$ and the term corresponding to ϕ^2 (invariant under a transformation $\phi \leftrightarrow -\phi$) is the leading one [42]. However, this systematic small-sphere expansion is only meaningful for positive exponents of R [201] so that the "insertion" of a small object into the bulk can be treated as perturbation, the influence of which vanishes upon $R \to 0$. On the other hand, for negative exponents of R in Eq. (4.27), even an infinitely small object generates a non-vanishing perturbation which becomes independent of R in the limit $R \to 0$ [201]. That is, one can infer from the value of $x_{\phi^i} + d_s - d$ ($i = 1, 2$) the marginal dimensionality of the generalized cylinder above which a small object perturbation is — in the renormalization group sense — "irrelevant" (i.e., $g(v \to \infty) = 0$) and below which it is "relevant" (i.e., $g(v \to \infty) \neq 0$) [201]. Since for the symmetry-breaking extraordinary transition x_ϕ is the relevant exponent, one finds that the marginal cylinder dimensionality in $d = 4$ (MFT) is given by $d - \beta/\nu = 3$ [201]. Analogously, for the symmetry-preserving ordinary transition the exponent x_{ϕ^2} leads to the marginal dimensionality $\nu^{-1} = 2$ within MFT. Accordingly, $g(v \to \infty)$ vanishes for $d_s \geq 2$ for the ordinary transition, but only for $d_s \geq 3$ for the extraordinary transition, as observed in the analysis above. For the special transition g does not vanish for the marginal case $d_s = 2$ but only for $d_s > 2$.

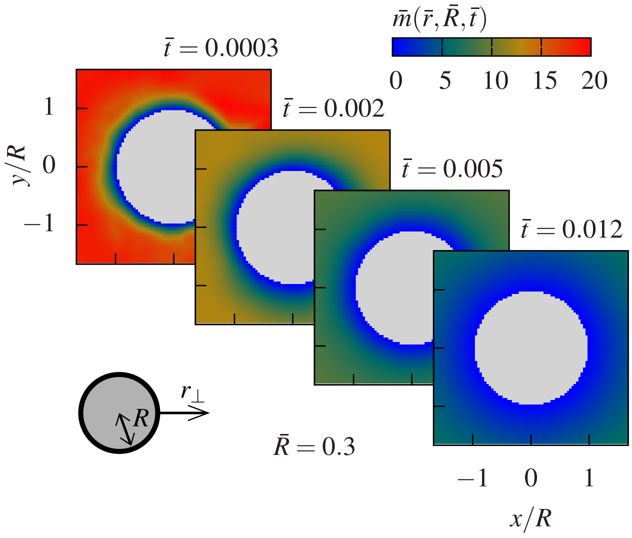

Figure 4.8: Order parameter profile $\bar{m}(\bar{r},\bar{R},\bar{t})$ (see Eq. (4.7)) around a cylindrical particle ($d_s = 2$) shown as contour plots within the (x,y) plane perpendicular to the cylinder axis and at various times $\bar{t}$. $\bar{m}$ has been obtained using the finite element method for $\bar{R} = 0.3$ and for the initial conditions $\bar{K} = 20$ and $\bar{D} = 0.001$ (see the main text).

4.2.5. Relaxation phenomena around colloids for the ordinary transition

In this subsection we study numerically the critical relaxation of the order parameter profile around curved objects, the surface of which implies an ordinary boundary condition (Dirichlet BC) on the order parameter. In the following we focus on the particular case $T = T_c$ and initial configurations $\bar{m}(\bar{r},\bar{R},\bar{t} = 0)$ of the order parameter profile assumed to be created via a bulk field which vanishes at $t = 0$.

Results from finite element method

First, we have used the finite element method described in App. A.3 in order to calculate the spatio-temporal evolution of the order parameter profile close to a cylinder ($d_s = 2$). (Although this problem is effectively only one-dimensional, the finite element method has been applied in view of future extensions of this analysis to actual two-dimensional situations.) Analogously to the cases presented above, we chose an initial profile of the form $m(\bar{r},\bar{R},t = 0) = \bar{K}\bar{r}/\bar{D}$ for $\bar{r} \leq \bar{D}$ and $m(\bar{r},\bar{R},t = 0) = \bar{K}$ for $\bar{r} > \bar{D}$ where the constants $\bar{K}$ and $\bar{D}$ are chosen carefully in order to ensure numerical stability.

Figure 4.8 shows the order parameter profile $\bar{m}$ as obtained from the finite element method at different times for the specific case $\bar{R} = 0.3$ and the initial conditions $\bar{K} = 20$ and $\bar{D} = 0.001$. In Fig. 4.8 the order parameter profile is shown within the (x,y) plane perpendicular to the cylinder axis. One can infer that the order parameter relaxes towards its equilibrium value more rapidly

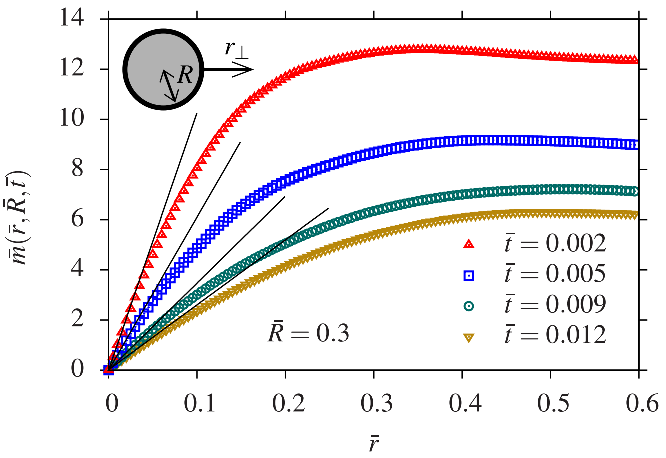

Figure 4.9: Order parameter profile $\bar{m}(\bar{r},\bar{R},\bar{t})$ around a cylinder and for the ordinary transition as obtained via the finite element method shown as function of $\bar{r}$ at different times. The graph is shown for the specific case $\bar{R}=0.3$ and the initial conditions $\bar{K}=20$ and $\bar{D}=0.001$ (see the main text). For small values of $\bar{r}$ the order parameter increases linearly as expected from the short distance expansion (black lines) discussed in Subsec. 4.2.4. For large values of $\bar{r}$ the profile becomes flat and it approaches the bulk behavior $m \propto t^{-1/2}$.

close to the surface with Dirichlet BC than within the bulk.

In Fig. 4.9 the order parameter profile is shown as a function of $\bar{r}$ for the same values of the parameter $\bar{R}$ and of times $\bar{t}$ as in Fig. 4.8. From an expansion for small values of $u=\bar{r}\bar{t}^{-1/2}$ one obtains for the ordinary surface transition the leading behavior $\bar{m} \propto \bar{u} \times \bar{t}^{1/2} g(\bar{r}/\bar{R}) h(\bar{R}\bar{t}^{-1/2})$ (see Eq. (4.10) and Subsec. 4.2.4). Since the expansion is valid for small u, it holds for short distances at all times, i.e., for a fixed radius $\bar{R}$ the order parameter increases linearly. This feature is reproduced by the numerical data shown in Fig. 4.9, where a linear behavior is indicated as black solid lines (note that the initial profile used here corresponds to an almost step-like function along $\bar{r}$). For large values of $\bar{r}$ the order parameter becomes constant and attains the corresponding bulk values $m \propto t^{-1/2}$. Note however, that according to the analysis discussed above, a universal behavior is approached only after a non-universal transient time which depends crucially on the initial profile. Accordingly, universal behavior is expected for times $\bar{t} \gg 1/[\bar{m}(\bar{r},\bar{R},0)]^2$; for the present case shown in Figs. 4.8 and 4.9 this corresponds to $\bar{t} \gg 0.003$. Thus, due to the short time scales reached, the results presented in Figs. 4.8 and 4.9 and in Fig. 4.10 below may depend significantly on the chosen initial profile.

We are particularly interested in the contribution due to the curvature in difference compared to the case of a planar wall. In order to highlight this contribution and according to the expansion discussed in Subsec. 4.2.4, Fig. 4.10 shows the value of $\bar{m}(\bar{r},\bar{R},\bar{t})$ divided by its linear behavior at $\bar{r}=0$, i.e., $\bar{r} \times \partial_{\bar{r}} \bar{m}(\bar{r},\bar{R},\bar{t})|_{\bar{r}=0}$, as a function of $v=\bar{r}/\bar{R}$. The data shown in Fig. 4.10 correspond to the numerical data presented in Fig. 4.9. Indeed, according to Eq. (4.10) this

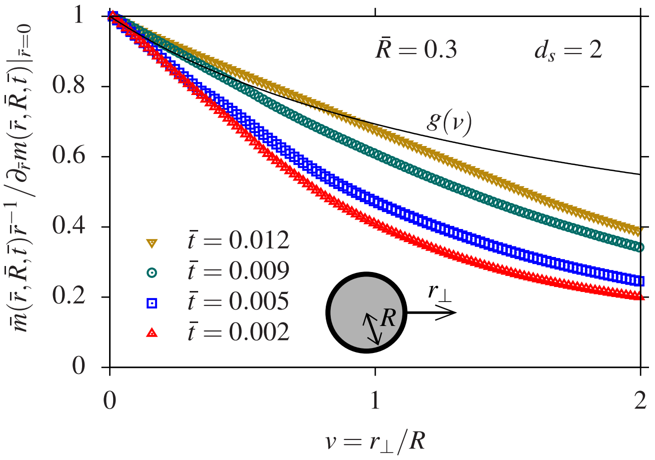

Figure 4.10: Order parameter profile $\bar{m}$ around a cylinder of radius $\bar{R} = 0.3$ with Dirichlet boundary conditions (as shown in Fig. 4.9) divided by its linear behavior at $\bar{r} = 0$, i.e., $\bar{r} \times \partial_{\bar{r}} \bar{m}(\bar{r},\bar{R},\bar{t})|_{\bar{r}=0}$, and shown as function of $v = \bar{r}/\bar{R}/r_\perp/R$ at different times $\bar{t}$. According to our analysis in Subsec. 4.2.4, for $u = \bar{r}\bar{t}^{-1/2} \to 0$, the curves should tend towards the scaling function $g(v)$ (see Eqs. (4.10) and (4.14)). Since we have been able to study early regimes only, i.e., small values of $\bar{t}$, we expect the data to approach $g(v)$ for $v \ll 1$.

should tend towards the scaling function $g(v)$ [Eq. (4.14)] for $u = \bar{r}\bar{t}^{-1/2} \to 0$.

Results from numerical calculations

Using the numerical finite element method for critical dynamics presented in App. A.3 we have faced severe numerical difficulties, and, therefore, we have not been able to numerically calculate the order parameter relaxation close to a cylinder on large time scales within a reasonably small numerical error. Moreover, it turned out that the results obtained via the finite element method are subject to a rather large numerical error, as may be seen, e.g., from Figs. 4.9 and 4.10. We attribute these numerical errors to numerical difficulties in finding the minimal order parameter profile within reasonable computing time. In addition, as discussed above, for the case of the ordinary surface transition, the cylinder $d_s = 2$ constitutes the marginal case in the renormalization group sense; i.e., for $d_s < 2$ the bulk is perturbed by the presence of a cylinder even in the case $R \to 0$, whereas for $d_s > 2$ its influence vanishes for vanishing radius. That is, finding the order parameter profile is numerically particularly challenging for the case $d_s = 2$ because the effect of the cylinder is long-ranged, which constitutes a potential source for the severe numerical difficulties we have faced using the finite element method.

Since we are interested in the universal behavior at time scales $\bar{t} \gg 1/[\bar{m}(\bar{r},\bar{R},0)]^2$ and also in the limit $u = \bar{r}\bar{t}^{-1/2} \to 0$, we have gone beyond the finite element method discussed above. Accordingly, the mean field results presented in the following were obtained using a computational software program [214] which solves the differential equation Eq. (4.6) numerically. Using this

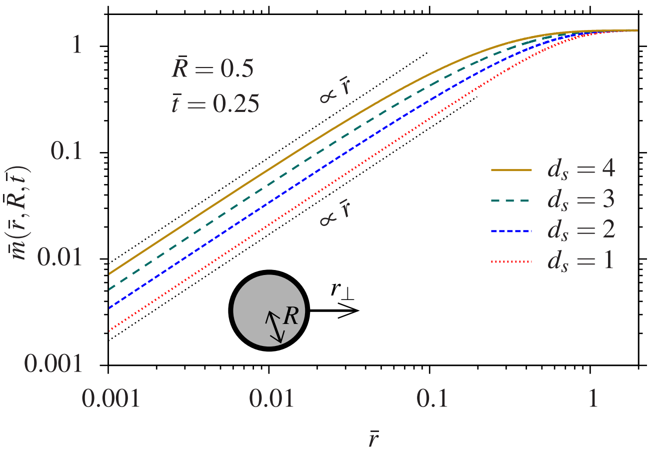

Figure 4.11: Order parameter profile $\bar{m}(\bar{r},\bar{R},\bar{t})$ around a curved object with dimensionality d_s and for the ordinary surface transition for $\bar{R} = 0.5$ and $\bar{t} = 0.25$ as function of $\bar{r}$. Close to the curved surface $\bar{m}$ increases linearly $\propto \bar{r}$. For $\bar{r} \to \infty$ the bulk value is approached. The effect of the (curved) surface reaches a given distance $\bar{r}$ later for increasing values of d_s.

effectively one-dimensional method, we expect a numerical error of at most few percent for the results presented below.

The analysis has been restricted to the ordinary surface transition, but we have extended the analysis based on the finite element method to all values $d_s = 1,2,3,4$. For the initial order parameter profile we have conveniently chosen $\bar{m}(\bar{r},\bar{R},\bar{t} = 0) = \bar{K}\tanh(\bar{\delta}\bar{r})$, where $\bar{K}$ and $\bar{\delta}$ are constants. As discussed above, after some nonuniversal transient time depending on the initial profile, i.e., $\bar{t} \gg 1/[\bar{m}(\bar{r},\bar{R},0)]^2$, the relaxation is expected to become independent of the actual initial configuration. Typical choices of $\bar{K}$ and $\bar{\delta}$ are around the value 20 for both, $\bar{K}$ and $\bar{\delta}$, so that for $\bar{t} \gg 0.003$ the behavior becomes independent of the actual initial profile.

Indeed, from the analysis of the numerical data we find that the order parameter close to the curved surface at which $\bar{m} = 0$ increases first linearly as function of the distance $\bar{r}$ from the surface for all values of d_s. This is shown in Fig. 4.11, where results obtained for the specific case $\bar{R} = 0.3$ and $\bar{t} = 0.25$ are presented (analogous results have been obtained for all values considered $\bar{R} = 0.1$ to 1, and $\bar{t} \leq 4$). From Fig. 4.11 one can infer that the bulk value is approached for $\bar{r} \to \infty$ differently for different values of d_s. At a given time $\bar{t}$, for a planar wall ($d_s = 1$) the effect of the surface has propagated much deeper into the bulk as for a curved surface; in particular, for a cylinder ($d_s = 2$) the surface affects the behavior at fixed distance $\bar{r}$ at later times than for a planar wall, but at earlier times than for a sphere ($d_s = 3$) or a hypersphere ($d_s = 4$). This is in agreement with what one would expect, because with increasing dimensionality d_s of the curved surface there are less “planar” contributions from the $d - d_s$ directions along which the curved object is translationally invariant (i.e., the “effective surface” decreases with increasing d_s).

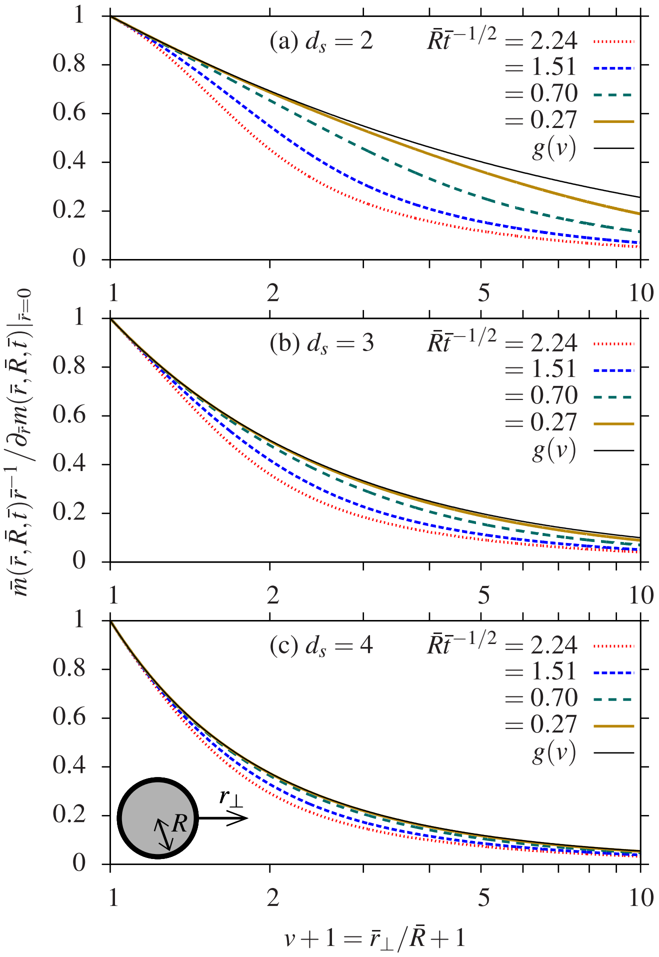

Figure 4.12: Value of $\bar{m}(\bar{r},\bar{R},\bar{t})/[\bar{r} \times \partial_{\bar{r}}\bar{m}(\bar{r},\bar{R},\bar{t})|_{\bar{r}=0}]$ around (a) a cylinder, (b) a sphere, and (c) a hypersphere for the ordinary surface transition as a function of $v+1 = \bar{r}/\bar{R}+1$ obtained from calculations performed using a computational software program. (Panel (a) corresponds to Fig. 4.10, which was obtained via the finite element method for shorter time scales.) The curves are shown for various values of the scaling parameter $w = \bar{R}\bar{t}^{-1/2}$. For $w \to 0$ the curves approach the scaling functions $g(v)$ given in Eqs. (4.14)–(4.16).

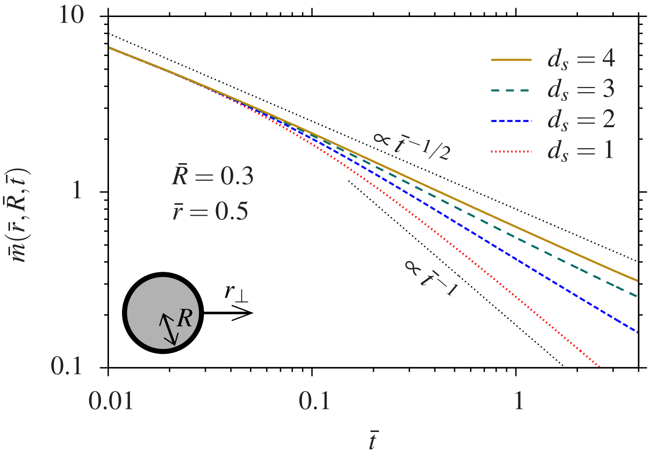

Figure 4.13: Order parameter $\bar{m}(\bar{r},\bar{R},\bar{t})$ around a curved object and for the ordinary surface transition for $\bar{R} = 0.3$ at fixed distance $\bar{r} = 0.5$ as function of time $\bar{t}$. First, for $\bar{t} \lesssim 0.1$ the order parameter decays according to the bulk behavior $\propto \bar{t}^{-1/2}$, whereas for times $\bar{t} \gtrsim 0.25$ the order parameter decays according to $\bar{m} \propto \bar{t}^{-s}$ (see the main text). For $d_s = 1$ (which is independent of $\bar{R}$) s takes the planar wall value 1, whereas for $d_s \geq 2$, s decreases for increasing d_s towards the bulk value $1/2$.

In order to separate the geometrical contribution due to the curvature, in Fig. 4.12 the value of $\bar{m}(\bar{r},\bar{R},\bar{t})/[\bar{r} \times \partial_{\bar{r}}\bar{m}(\bar{r},\bar{R},\bar{t})|_{\bar{r}=0}]$ is shown as a function of $v = \bar{r}/\bar{R}$ for different values of $\bar{R}\bar{t}^{-1/2}$. According to Eq. (4.10), for $\bar{r}\bar{t}^{-1/2} \to 0$ this quantity approaches the scaling functions $g(v)$ given in Eqs. (4.14)–(4.16). As can be inferred from Fig. 4.12 the curves indeed do so at late times ($w = \bar{R}\bar{t}^{-1/2} \to \infty$) or short distances ($v \to 0$). For $d_s = 4$ the scaling function is approached already at earlier stages (Fig. 4.12(c)) compared to $d_s = 3$ and $d_s = 2$ (Fig. 4.12(b) and (a)). (Note that the curves shown in Fig. 4.12 have been obtained from calculations for various values of $\bar{R}$; that is, scaling via the additional variable $w = \bar{R}\bar{t}^{-1/2}$ holds.)

The discussion in the preceding paragraphs deals with corrections to the planar wall behavior due to the *static* curvature contribution $g(v)$. However, we find that the time evolution is altered as well by the presence of curvature and the characteristic exponent describing the dynamics close to the surface depends on d_s. Figure 4.13 shows the order parameter for $\bar{R} = 0.3$ at the fixed distance $\bar{r} = 0.5$ as function of time $\bar{t}$ (clearly, the results for $d_s = 1$ are independent of $\bar{R}$). After a non-universal transient time (expected at time scales smaller than the ones shown in the graph; see the discussion above), first the profile decays according to the bulk behavior $\bar{m} \propto \bar{t}^{-\beta/z\nu} = \bar{t}^{-1/2}$. After times $\bar{t} \gtrsim \bar{r}^z$ the effect of the surface reaches at distance $\bar{r}$ and the profile decays according to $\bar{m} \propto \bar{t}^{-s}$, where s is the corresponding exponent. For the semi-infinite geometry ($d_s = 1$) one has $s = -\beta_1/z\nu = 1$, i.e., close to a planar wall the profile decays faster than within the bulk due to the presence of the Dirichlet BC at the surface. We find that the corresponding exponent s differs significantly from the planar wall case when considering *curved* walls. From Fig. 4.13 we infer that $1/2 \leq s < 1$ for $d_s \geq 2$, and s decreases for increasing

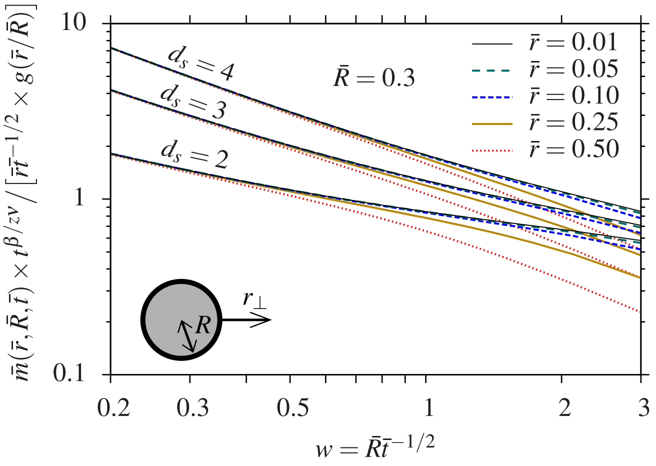

Figure 4.14: Value of $\bar{m}(\bar{r},\bar{R},\bar{t}) \times t^{\beta/z\nu} / \left[\bar{r}\bar{t}^{-1/2} \times g(\bar{r}/\bar{R})\right]$ (see the main text) for $\bar{R} = 0.3$ as function of $w = \bar{R}\bar{t}^{-1/2}$ for various distances $\bar{r}$ from the curved wall with Dirichlet boundary conditions and for $d_s = 2,3,4$. For $u = \bar{r}\bar{t}^{-1/2} \to 0$ (i.e., $w \to 0$ or $\bar{r} \to 0$), the curves approach a universal behavior $h(w)$ which indicates a characteristic universal dynamical behavior different from the one of a planar wall.

d_s towards the bulk value $1/2$. This agrees with what one would expect: due to “less” amount of surface present for increasing d_s the behavior tends towards the bulk behavior and the dynamics becomes slower as compared to the case of a planar wall. Within the numerically sampled time ranges we do not find a crossover towards another regime.

In Fig. 4.14 we show the value of the order parameter divided by its behavior extracted from the expansion for $u = \bar{r}\bar{t}^{1/2} \to 0$ derived in Subsec. 4.2.4, i.e., $\bar{m}(\bar{r},\bar{R},\bar{t}) \times t^{\beta/z\nu} / \left[\bar{r}\bar{t}^{-1/2} \times g(\bar{r}/\bar{R})\right]$ [Eqs. (4.9) and (4.10)]. For $u \to 0$ the curves should approach the scaling function $h(w)$, where $w = \bar{R}\bar{t}^{-1/2}$ (see Eq. (4.10)). We have not been able to derive an approximation to $h(w)$ within the approach presented in Subsec. 4.2.4. The numerical data reported in Fig. 4.14 for the particular case $\bar{R} = 0.3$ indeed approach a common behavior either at large times (i.e., small values of w) or close to the surface (i.e., small values of $\bar{r}$); both these limits correspond to $u \to 0$.

From Fig. 4.15 one can infer that this behavior is common to all values of $\bar{R}$ considered and the curves approach a universal function $h(w)$ independent of $\bar{R}$. Figure 4.15 shows the same as Fig. 4.14 but for various values of $\bar{R}$ and only at distance $\bar{r} = 0.01$ from the curved wall. (Note that — for the purpose of comparison — we show in Fig. 4.15 also the behavior for $d_s = 1$ which is independent of $\bar{R}$ as function of $\bar{t}^{-1/2}$ so that deviations from the constant behavior indicate the times at which the $u \to 0$ behavior is not reached for the case of a planar wall.) We find that upon decreasing w towards zero, $h(w)$ increases as a power law $h(w \to 0) \propto w^{-y(d_s)}$. From a least square fit the values $y(1) = 0$, $y(2) = 0.66(5)$, $y(3) = 0.93(5)$, and $y(4) = 0.99(5)$ are found. We conclude that in the presence of curvature of a surface the dynamics of the order parameter is significantly slower as compared to a planar wall. This is in agreement with earlier

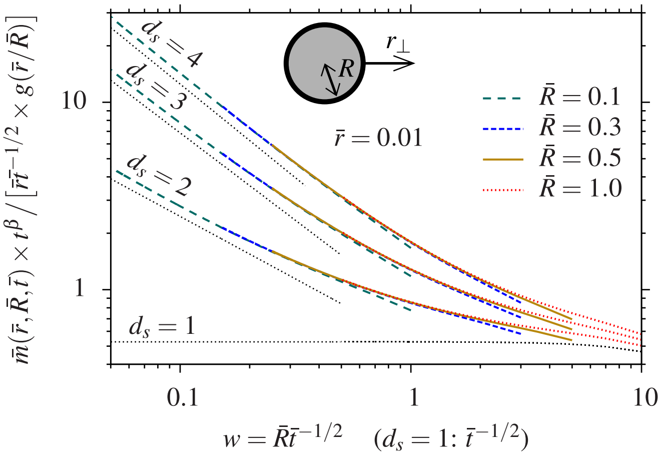

Figure 4.15: Same as Fig. 4.14 but shown for different radii $\bar{R}$ and fixed distance, $\bar{r} = 0.01$. All numerical data approach for small values w a universal behavior $h(w)$. For $w \to 0$ the scaling function h increases as a power law $h(w \to 0) \propto w^{-y(d_s)}$, where we have found from a least square fit the values $y(1) = 0$, $y(2) = 0.66(5)$, $y(3) = 0.93(5)$, and $y(4) = 0.99(5)$ shown as dotted lines. (Note that we do not have further indication about the specific values of the exponents.) For the sake of completeness we show also the case $d_s = 1$ for which the plotted quantity is independent of $\bar{w}$. Deviations of the curve for $d_s = 1$ from a constant value indicate deviations from the short-distance planar wall behavior $\propto \bar{r}\bar{t}^{-1}$.

studies for the domain interface dynamics [209].

4.3. Dynamic critical Casimir force — state of the art

The fluctuation-induced Casimir forces which occur in finite size systems and act on the confining boundaries depend on time because of the temporal fluctuations of thermal nature of the medium in between the walls. The dynamics of critical Casimir forces is determined by the corresponding non-equilibrium behavior of the order parameter of the confined fluid and of the boundary conditions at the confinement. For example, after a sudden quench towards the critical point, critical Casimir forces build up in time and tend towards their equilibrium value [198]. The dynamics of Casimir forces has been studied in few cases recently [190, 198–200, 215–220].

However, whereas in statics the Casimir force is given by the spatial derivative of a suitable equilibrium effective free energy, this is no longer a *bona fide* definition in non-equilibrium situations. Accordingly, it is necessary to define the dynamic Casimir force on a different basis. Currently, two different definitions of the dynamic Casimir force have been proposed and used in literature: one relies on the *stress tensor* [190, 198, 215, 216, 220], whereas the other on taking the spatial derivative of the effective Hamiltonian [199, 200]. An alternative approach for calculating the dynamic Casimir forces, still essentially based on the stress tensor, is considered in Refs. [217–219], where the local pressure of the fluid at the surface of an embedded object is integrated. The definition of the non-equilibrium Casimir force is important also for the calculation of fluctuations of Casimir forces (see Refs. [86, 221], where the stress tensor was used) and drag forces (see Refs. [222–224], where the derivative of the effective Hamiltonian was used). In view of the fact that these different approaches do not always yield the same result, a clarification of their differences and of their domains of application is needed.

Recently, the authors of Ref. [225] have investigated in more detail this question, when studying the variance of the Casimir force acting on inclusions embedded in a fluctuating membrane. Their results are rather general and apply also to various instances of non-equilibrium Casimir forces [225]. In particular, they argue that both approaches mentioned above are suitable but they apply in different physical situations [225], as the possible variation of the order parameter field upon a virtual displacement of the boundary is crucial. Depending on the actual physical coupling of the order parameter at the boundary, the corresponding order parameter field may remain constant or its value may be affected. Moreover, one may think of combinations of the two cases of order parameter variations considered in Ref. [225]. For fluids, the order parameter is actually defined via a suitable coarse-grained spatial density (or density difference) of molecules. Obviously, the fluid molecules close to a wall are displaced upon movement of the wall. Thus, the order parameter undergoes the transformation [Eq. (A.6)] which is underlying the definition of the force based on the stress tensor (see App. A.2). Consequently, for objects *included* in a fluctuating medium — as it is the generic case for confining bodies in a fluid — the stress tensor provides the physically motivated expression for the Casimir force [225].

Indeed, the fluid in between the confining objects plays an active role and can “transport” stress [198]. This may lead to interesting situations for which one has dynamic critical Casimir forces of *different* strength, which act on the two walls confining a fluid film [198]. Such a "violation" of *Newton's* action-reaction-principle (actually, the counteractive forces are acting within the medium in between or surrounding the confining objects) may occur out of equilibrium within asymmetric setups such as the ones considered in Ref. [198], and objects may exhibit "self-forces" or "self-propulsion" [218, 219, 226].

4.4. Summary

In this Chapter dynamic critical phenomena close to colloidal particles have been studied. The evolution in time is the given by a Langevin equation [Eq. (4.1)]. Here, we have studied Model A dynamics corresponding to pure relaxation of the order parameter m within mean field theory and within the non-linear regime. We have mainly considered the situation where a non-zero order-parameter profile has been suitably prepared within the system and we investigate its time evolution at the critical temperature T_c. Dynamics of critical phenomena results in splitting up each static universality class into subclasses corresponding to different effective, representative dynamical models. These subclasses are further split up according to the type of boundary conditions at a confining surface.

Within the bulk, critical slowing down induces a slow relaxation of the order parameter towards its equilibrium value according to a power law $t^{-\beta/z\nu}$ as a function of time t, where z is the universal dynamic exponent, and β and ν are the standard static critical exponents. Within MFT and Model A dynamics $z = 2$ and $\beta = \nu = 1/2$. In a semi-infinite system with a planar boundary this picture is modified due to the occurrence of a second characteristic decay of the order parameter according to $t^{-\beta_1/z\nu}$ sufficiently close to the boundary. As a function of time, the surface behavior propagates into the bulk. This well-known behavior of critical dynamics for the case of the ordinary surface transition [184, 190] (Dirichlet boundary conditions) could be reproduced by a finite element method (see Figs. 4.1 and 4.2).

For the film geometry, in addition to the surface effects observed in the semi-infinite system, the confining surfaces start to affect each other at sufficiently large times and consequently the order parameter profile decays exponentially even at T_c (see Figs. 4.3 and 4.4). These well-known features of finite-size critical dynamics [190] were reproduced by our numerical algorithm described in detail in Appendix A.3. Within the latest stage of relaxation, for the case of the ordinary surface transition the order parameter profile attains a sinusoidal shape along the film (see Fig. 4.5) as already predicted in Ref. [190] and confirmed by our analysis.

We have extended these previous studies to the experimentally relevant case of confinements due to colloidal particles by considering curved surfaces in Secs. 4.2.3 — 4.2.5. Different dimensionalities d_s of the curved body of radius R have been studied. They correspond to a planar wall ($d_s = 1$), a cylinder ($d_s = 2$), a sphere ($d_s = 3$) and a hypersphere ($d_s = 4$), so that the corresponding Langevin equation depends *inter alia* on d_s [Eq. (4.6)]. We have restricted the present analysis to cases which are angular symmetric around the body axes of the curved objects. Close to criticality, the order parameter attains a scaling form given by Eq. (4.7), which depends on the scaling variables $u = (r_\perp/\xi_0^+)(t/t_{R,0}^+)^{-1/z}$, $v = r_\perp/R$, and $\mathrm{sign}(\hat{\tau})|\hat{\tau}/(\xi_0^+)^2|^{\nu z}(t/t_{R,0}^+)$, where $r_\perp$ is the distance from the curved surface. Additionally, at early times regimes the order parameter depends significantly on its initial profile [Eq. (4.7)].

For $T = T_c$ and the within the universal time regime which is independent of the initial order parameter profile, in Sec. 4.2.4 we have performed an expansion of the order parameter scaling function for small values u (i.e., short distances or late times) and for various values of d_s. We find that different boundary conditions correspond to different leading behaviors of the scaling function in terms of a power series in the scaling variable u: whereas for the ordinary surface transition the order parameter profile $\propto u^1$, the special transition corresponds to u^0, and the extraordinary transition to u^{-1}. Accordingly, the scaling functions $g(v)$ describing the effect of curvature are different for the various surface universality classes (Figs. 4.6 and 4.7). For the extraordinary surface transition $g(v)$ agrees with the results of the available studies for static critical phenomena — reflecting, indeed, the fact that $u \to 0$ corresponds to a system relaxed to equilibrium. In addition, the scaling functions $g(v)$ depend on the dimensionality d_s of the curved surface and they show qualitative differences with respect to the boundary conditions. Whereas for the symmetry-preserving ordinary and special surface transitions $g(v \to \infty)$ vanishes for $d_s > 2$, for the symmetry-breaking extraordinary surface transition $g(v \to \infty) = 0$ for $d_s > 3$. This is in agreement with a small-sphere expansion from which one can derive the marginal values of the dimensionalities d_s, so that for dimensionalities below this value an object affects the bulk even for $R \to 0$. For symmetry-preserving BC, at the marginal value $d_s = 2$, $g(v \to \infty)$ vanishes for the ordinary transition but not for the special transition. For the extraordinary transition (symmetry-breaking BC), $g(v \to \infty) = 0$ at the marginal value $d_s = 3$.

We have implemented a finite element method in order to calculate the time evolution of the order parameter around a cylindrical particle for the case of the ordinary surface transition and for $T = T_c$ (Sec. 4.2.5). For short distances $r_\perp$ from the surface, the order parameter profiles grows linearly as function of $r_\perp$ in agreement with the short-distance expansion (Figs. 4.8 and 4.9). However, using the finite element method, we have been able to calculate the order parameter profile only at early times so that the limiting function $g(v)$ is not yet approached (Fig. 4.10).

In order to overcome the numerical limitations of the two-dimensional finite element approach we have performed an effectively one-dimensional numerical calculation for various values of d_s. We have focused on the ordinary surface transition, and for $d_s = 2, 3, 4$ the corresponding linear behavior $m \propto r_\perp$ close to the surface has been obtained also numerically (Fig. 4.11). Moreover, we have found that the curvature contribution to the order parameter profile indeed approaches the limiting scaling function $g(v)$ (Fig. 4.12).

The presence of a curved surface does not only affect the order parameter profile as compared to the case of a planar surface in a static sense, i.e., via the scaling function $g(v)$, but also its characteristic dynamics. For $T = T_c$, we have found that depending on the dimensionality d_s of the curved surface, the decay of the order parameter m as a function of time at a fixed distance from the surface first decays $m \propto t^{-1/2}$ as within the bulk, whereas at later times it follows a power law $m \propto t^{-1/2(2-y(d_s))}$. For the ordinary surface transition $0 \leq y(d_s) \leq 1$ (Fig. 4.13). For $u \to 0$ the critical dynamical behavior is characterized by a universal scaling function $h(w)$, where $w = u/v = (R/\xi_0^+)(t/t_{R,0}^+)^{-1/z}$ (Fig. 4.14). That is, the different characteristic dimensionalities of surface curvature described by d_s affect the dynamical behavior. The behavior of $h(w)$ depends on d_s and follows a characteristic power law for $w \to 0$. Accordingly, from fits to the numerical data we find the corresponding exponents $y(1) = 0$, $y(2) = 0.66(5)$, $y(3) = 0.93(5)$, and $y(4) = 0.99(5)$ (Fig. 4.15).

The critical Casimir forces acting on two or more objects confining a critical medium are subject to dynamic processes as well. However, in systems out of thermodynamic equilibrium, the dynamic critical Casimir force has to be *defined*, which is a matter of current debate in literature. In Sec. 4.3, we have briefly reviewed the state of the art concerning the definition the dynamic critical Casimir force. We conclude, that for the experimentally relevant fluidic systems, the stress tensor (Appendix A.2) constitutes an appropriate definition of the dynamic critical Casimir force.

5. Outlook

In the following, a brief outlook is given over recent development in the field of research of this thesis, which has experienced a pronounced scientific activity during the last years. This concerns theoretical as well as experimental investigations which have demonstrated a rather rich variety of phenomena related to the critical Casimir effect.

First, we note, however, that the validity of the Derjaguin approximation *inter alia* used here is of rather general interest. In this context, it seems to be important to differentiate between forces due to surface effects only, and forces which also depend on the body of the object. Recently, an approach for calculating the force between a body and a planar wall has been presented based on the assumption of additivity of pairwise forces [227]. The authors of Ref. [227] present a surface integration approach in which they argue that the summation of the forces acting on point-like objects constituting the body and a wall reduces to an integral over the surface of the body of the force between two planar walls. For the case of a spherical body close to a wall they derive an expression of the force which differs from our approach presented in Eqs. (2.3)–(2.5) in Sec. 2.2.1 only in the limits of integration; whereas we sum up the forces acting on "rings" (see also Fig. B.6) belonging to the semi-spherical cap next to the wall, the approach of Ref. [227] integrates also over the rings of the upper semi-spherical cap. This difference of the two approaches stems from the type of forces. In Ref. [227] body forces are considered, whereas here we consider critical Casimir forces which are due to the presence of surfaces and depend only on the surface geometry and surface properties but not on the body "behind" the surfaces. In the Derjaguin limit, i.e., $R/D \to 0$ (see Fig. 2.1) the two approaches both tend to the same expression [227]. Moreover, there is pronounced interest also in the field of quantum electrodynamic Casimir forces in studying the corrections to the Derjaguin approximation [228, 229]. However, our assessment of the range of validity of the Derjaguin approximation revealed that the latter is applicable within the range of parameters used in the experiments that we have compared with in Chap. 3.

In Sec. 2.7 we have studied a *cylindrical* colloid opposite to a patterned substrate parallel to chemical stripes. A natural extension concerns the behavior of cylindrical colloids which are *tilted* with respect to the chemical stripes. A cylinder opposite to a chemical step has been studied in Ref. [169]. It turns out that close to the critical point a *critical Casimir torque* acting on the cylindrical particle approaching the chemical step emerges. Depending on the ratio of length and radius of the cylinder, the critical Casimir torque aims in aligning the cylinder axis parallel or perpendicular with respect to the chemical step [169]. In view of potential applications, a generalization of Ref. [169] to a variety of substrate patterns as discussed within this work seems to be rewarding.

Instead of structuring the substrate, it is possible to endow the colloid particles with a chemical pattern. Such *Janus particles* infer different kinds of boundary conditions at the colloid surface. Thus, in the presence of a homogeneous substrate, one expects a critical Casimir torque acting on Janus particles. Two or more Janus particles are expected to exhibit self-assembly due to critical Casimir forces. Janus particles are experimentally feasible and exhibit promising phenomena such as “self-propulsion” [230].

Moreover, many-body effects due to critical Casimir forces open a new variety of phenomena. Recently, it has been observed that the critical Casimir effect may induce a demixing of two kinds of colloidal particles with opposite boundary conditions for the binary liquid mixture they were immersed in [231]. Thus, the demixing of the binary liquid mixture at its critical point is transferred from the molecular scale to the length scales of visible light [231]. A phase transition on the colloidal scale induced by the critical Casimir interaction may also occur for a suspension of only one species of colloidal particles; in this case, one may identify a phase diagram which has colloid-rich and colloid-poor phases [232].

In view of present research efforts and potential applications, it is important to study the effect of *weak* critical adsorption of the fluid at the confining surfaces, corresponding to *finite* surface fields. Such weak surface fields can be realized by applying suitable surface chemistry and they influence the resulting behavior of the critical Casimir effect strongly [33, 35]. Another approach to create an effective reduction of the surface adsorption is to create fine periodic chemical patterns with different (strong) adsorption preferences as discussed here. However, our results for $\Pi \to 0$ [Figs. 2.10(b) and 2.16(b)] show that a fine patterning of the substrate with alternating boundary conditions does not necessarily lead to an effective reduction of the surface adsorption at *short* distances because in this range the critical Casimir force for a inhomogeneous adsorption preference resembles the one for a *homogeneous* substrate corresponding to strong adsorption. On the other hand, at *large* distances a periodically patterned substrate does lead to an effective BC corresponding to a weak adsorption preference, and for $\lambda = 1/2$ the surface fields even cancel out, leading to an effective BC resembling the so-called ordinary BC [47]. This offers the interesting perspective to study, at least asymptotically, critical Casimir forces with Dirichlet BC by using classical fluids instead of superfluid quantum fluids [26–28, 93–95, 233]. A patterning on the *molecular* scale is *not* captured by the continuous approach pursued here, which gives the universal features of the critical Casimir effect. Nonetheless, a molecular patterning of the substrates may provide another means for an effective reduction of the adsorption of the corresponding fluid at the surface. However, on a molecular scale the patterning is more likely to lead to randomly distributed surface fields which opens a new challenge in the context of critical Casimir forces.

By adding salt to the solvent of the colloidal suspension the electrostatic repulsion between the substrate and a colloid is strongly screened; this provides the possibility to explore the spatial variation of critical Casimir forces over a much wider range of distances. Moreover, a rather complex behavior of the resulting forces acting on the colloid emerges because electrostatic forces induced by ions lead to rather delicate physical features. Recently, measurements have shown a rich and novel behavior of a colloid immersed in a salt-rich solvent upon approaching the critical point [36]. Strong attractive forces set on even several K below the critical temperature and, in addition, these forces are found to remain attractive, independent of the boundary conditions, $(\pm,\pm)$ or $(+,-)$, throughout a large temperature range. It turns out that the coupling between electrostatic interactions and critical fluctuations has to be considered in understanding this phenomenon [234–236]. The ion-solvent coupling can turn a repulsive electrostatic force into an attractive one upon approaching the critical point [234]. However, eventually these forces are dominated by the universal critical Casimir effect [234]. This allows for a interpretation of the experimental data of Ref. [36].

Using these intriguing effects together with a chemical patterning of surfaces may open a new field of phenomena with potential applications in colloid science.

Appendix

A. Numerics - `f3dm`

For the various geometries under consideration (see Fig. 2.1, *inter alia*, we have minimized the Hamiltonian Eq. (1.6) with the appropriate boundary condition implied by Eq. (1.7) using a three-dimensional finite element method (for an introduction to the finite element method, see, e.g., Ref. [237]). Moreover, we have solved Eq. (1.9) for Model A dynamics within the finite element method in the film geometry and around a cylinder. For the calculation of the order parameter profile, here we have used and extended the "`f3dm`" library developed mainly by *Svyatoslav Kondrat* [238, 239].

The `f3dm`-library for C/C++ [240] encompasses the `f3dm`-geom package which implements a three-dimensional mesh with arbitrary boundaries based on the *GNU Triangulated Surface library* (GTS) [241], the 3d-mesh creator *Tetgen* [242], and the *Gnome library* (GLIB) [243]. The `f3dm`-lib package provides tools to assign one or more fields, external potentials, and boundary conditions to the three-dimensional mesh and to perform *inter alia* a routine based on the *GNU scientific library* (GSL) [244] which minimizes a functional of these fields.

Using additional programs and bash scripts based on the `f3dm`-geom and the `f3dm`-lib packages the mean-field theoretical approach discussed within this work has been implemented numerically for static and dynamic critical phenomena and the calculation of critical Casimir forces for the various problems considered. The programs have been running mainly on computer clusters operated via the *Oracle®grid engine* and with *Intel®Xeon*™*E5450* 2.6 GHz quad-core CPUs ("Casimir" cluster at the Max-Planck-Institute for Intelligent Systems) or with *AMD Opteron*™*252/852* 2.6 GHz processors ("Gibbs" cluster at the Max-Planck-Institute for Intelligent Systems).

A.1. Numerical calculation of static critical behaviour

The basic idea of the finite element method is to subdivide complex geometries into small "finite" elements. In three dimensional space, these elements typically are small tedrahedra, so that the boundaries of the domain are formed by small triangles. On each element the actual continuous field is replaced by an *ansatz* based on a set of discrete values of the field.

The basic form is a *linear* finite element, i.e., the *ansatz* of the function replacing the field f is linear and interpolates in between values of the actual field at the four nodes at the edges

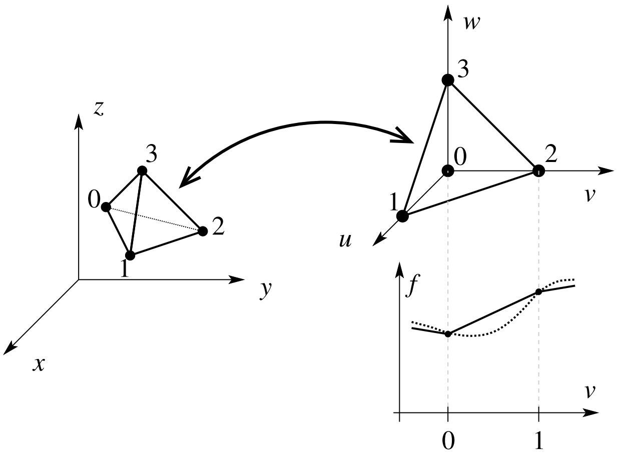

Figure A.1: Sketch of the linear finite element method. The (x,y,z) space is discretized into tetrahedral elements defined by four edge nodes (left figure). These finite elements are parametrized into (u,v,w) space, where $u,v,w \in [0,1]$ (upper right figure). The field f is approximated by a linear function which interpolates between its actual values on the edges (lower right figure).

of the tedrahedron; this is sketched in Fig. A.1. The three-dimensional elements in (x,y,z)-space are parametrized into (u,v,w)-space so that the tedrahedron is spanned by the tree unit vectors $\mathbf{e}_{u,v,w}$, and the interpolation nodes are located at $(0,0,0)$, $(1,0,0)$, $(0,1,0)$, and $(0,0,1)$, respectively (see Fig. A.1). On these "standard" tedrahedra, the field can be easily replaced by its discretized version based on the linear ansatz, i.e.,

$$f(u,v,w) = f_0 + u(f(1,0,0) - f_0) + v(f(0,1,0) - f_0) + w(f(0,0,1) - f_0), \tag{A.1}$$

where $f_0 = f(0,0,0)$ and the values of the field f at the edge nodes are the same as on the edge nodes of the original element. The first derivatives of f along the (x,y,z) directions are obtained in terms of the inverse Jacobian matrix $[J]$, i.e., [237]

$$\begin{pmatrix} \partial_x \\ \partial_y \\ \partial_z \end{pmatrix} = \Big[J\Big]^{-1} \begin{pmatrix} \partial_u \\ \partial_v \\ \partial_w \end{pmatrix} . \tag{A.2}$$

For the tedrahedron used in the finite element method the Jacobian is given by

$$\Big[J\Big] = \begin{bmatrix} x_1 - x_0 & y_1 - y_0 & z_1 - z_0 \\ x_2 - x_0 & y_2 - y_0 & z_2 - z_0 \\ x_3 - x_0 & y_3 - y_0 & z_3 - z_0 \end{bmatrix} , \tag{A.3}$$

where (x_i, y_i, z_i) are the coordinates of the nodes depicted in Fig. A.1 and $\det(J) = 6V$, where V is the volume of the original element [237]. (Note that all elements have to be ordered with the same "right handed" orientation [237].)

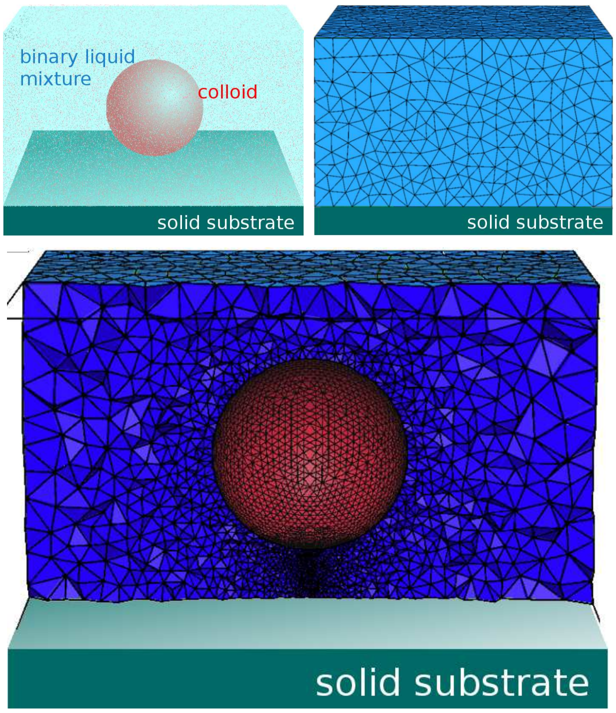

Figure A.2: Example of finite element mesh which numerically represents a spherical colloid close to a substrate and immersed in a binary liquid mixture. The fluid is transferred to a mesh of finite tedrahedral elements which vary in size in order to efficiently decrease the numerical error within regions of strongly varying order parameter. As can be seen in the lowermost picture, which is a cut through the finite element mesh, the colloid corresponds to a spherical hole in the mesh; the nodes at the boundaries underlie a boundary constraint given by the BC of the surface of the colloid. The lower surface of the box containing the finite elements underlies a boundary condition as well, whereas the other sides of the box are “free” (in actual calculations we have used smaller finite elements and larger boxes than the one depicted here in order to exclude a potential influence of the finite box size). The visualization of the mesh data has been obtained via *TetView* [245].

Figure A.2 shows a typical example for a mesh generated for a spherical colloid opposing a wall. The advantage of the finite element method is that space can be subdivided into elements of arbitrary and different sizes so that regions with a complex boundary and regions with rapidly spatially varying fields can be occupied with rather small elements, whereas regions with a very smoothly varying field can be“filled” with rather large elements. Thus, finite computer memory and computing time can be efficiently used to enhance the quality of the approximation at the regions of interest (e.g., the space in between the colloid and the wall, as shown in Fig. A.2).

Within the finite element approach the integrand of the Hamilitonian $\mathscr{H}[\phi]$ given in Eq. (1.6), which contains terms in ϕ and $\nabla\phi$ can be suitably (numerically) integrated, so that the summation over all parametrized elements yields the total functional. Starting with a random initialization profile[27] across the mesh and applying the appropriate boundary conditions[28], we have minimized $\mathscr{H}[\phi]$ using a multidimensional numerical minimization procedure [246]. A method based on the vectorial *Broyden-Fletcher-Goldfarb-Shanno* (BFGS) algorithm [244, 247] has been used, which varied the values of ϕ at each of the nodes within the mesh apart from the ones fixed by the boundary conditions. Moreover, multiple minimization runs have been performed for a given configuration with increasing mesh quality (i.e., smaller elements) within regions of strongly varying ϕ, in order to minimize the numerical error of the method. Typical meshes for numerical data with reasonably small expected errors[29] have been consisting of several 100.000 nodes.

It is worthwhile to note that the discrete approximation of the order parameter field via the finite element method may lead to the existence of various numerical “local” minima of $\mathscr{H}[\phi]$ which do not correspond to the order parameter profile which minimizes $\mathscr{H}$ in a global sense. Typically, the minimization mechanisms lead to a relatively fast convergence towards to globally minimizing profile. However, in particular situations, the minimization routines in use do not efficiently overcome this problem within reasonable computer time on a large mesh as used here so that the results obtained may not be reliable. We have observed that $\mathscr{H}$ given in Eq. (1.6) can be well globally minimized within our approach and the meshes under consideration for $\hat{\tau} \geq 0$, whereas for $\hat{\tau} < 0$, reliable results were only obtained within reasonable computing time for homogeneous boundary conditions $(\pm,\pm)$. This is due to the fact that for $\hat{\tau} < 0$ the order parameter minimum attains two different (“competing”) values $\pm a|\tau|^{\beta}$ within the bulk, biased by the boundary conditions $(\pm)$ at the confining walls. For different boundary conditions $(\pm,\mp)$ regions with different minimizing ϕ occur within the space between the colloid and the wall, which are separated by a (smooth) interface. It turns out that finding the precise location of this interface is subjected to a large numerical error. Thus, we do not present results for $\tau < 0$ and boundary conditions different from $(\pm,\pm)$ (see, e.g., Fig. 2.2) because we focus on the experimentally relevant regime $\tau \geq 0$.

---

[27] For a given geometrical configuration, calculations for different temperatures (i.e., values of $\hat{\tau}$ in Eq. (1.6)) have been performed not only with random initialization profiles but also with order parameter profiles minimizing $\mathscr{H}$ for a value $\hat{\tau} \pm \delta\hat{\tau}$ corresponding to a nearby temperature in order to improve the numerical performance.

[28] For $(\pm)$ BC corresponding to $\phi \to \infty$ at the boundary, which is clearly not numerically feasible, we have used the *short-distance expansion* close to the confining planar wall and the spherical colloid (see, e.g., [50, 201, 202] and references therein). However, we have chosen the “short distance” ε from the boundaries such that the resulting data for the universal scaling functions were not affected by the particular choice of ε.

[29] The expected numerical error of the finite element method used here in order to obtain the MFT scaling functions for the systems under consideration are at most of the range of few percent and indicated in the corresponding figures via the size of the points of the numerically obtained MFT data.

A.2. Stress tensor

The normal and lateral critical Casimir forces can be calculated directly from the order parameter profile via the stress tensor. Numerically, this has the advantage, that one avoids difficult calculations of differences of free energies, which here are connected to numerical errors of small differences of large numbers (due to the presence of the $(\pm)$ boundary conditions at the walls) with finite accuracy.

The stress tensor originates from quantum field theory and describes the variation of the action $\mathscr{S}[\varphi]$ under a transformation of the field φ [128]. The stress tensor is connected to *Noether's theorem* and associated with the constants of classical motion, namely energy and momentum [128]. Accordingly, we consider the variation of the action given by

$$\mathscr{S}[\phi] = \int\limits_V \mathrm{d}^d r \, \mathscr{L}(\varphi(\mathbf{r}), \nabla\varphi(\mathbf{r})), \tag{A.4}$$

where the Langrangean density $\mathscr{L}$ depends on the field $\varphi(\mathbf{r})$ and its derivatives $\nabla\varphi$, and V indicates the domain of the system. Upon performing an infinitesimal translation of the system by $\varepsilon(\mathbf{r})$

$$\mathbf{r} \mapsto \tilde{\mathbf{r}} = \mathbf{r} + \varepsilon(\mathbf{r}), \tag{A.5}$$

the field is transformed as

$$\varphi(\mathbf{r}) \mapsto \tilde{\varphi}(\tilde{\mathbf{r}}) = \varphi(\mathbf{r}), \tag{A.6}$$

so that to first order in ε one has (see, e.g., also Refs. [128, 225])

$$\tilde{\varphi}(\mathbf{r}) = \varphi(\mathbf{r}) - \varepsilon(\mathbf{r}) \cdot \nabla\varphi(\mathbf{r}). \tag{A.7}$$

For the derivatives of φ analogous statements hold. Then, the variation of the action $\delta\mathscr{S} = \mathscr{S}[\tilde{\varphi}] - \mathscr{S}[\varphi]$ is given by [128, 212]

$$\delta\mathscr{S} = -\int\limits_V \mathrm{d}^d r \, (\partial_j \varepsilon_i(\mathbf{r})) T_{ij} \tag{A.8}$$

where ε_i is the ith component of ε, and where the components of the stress tensor $\mathbf{T}$ are

$$T_{ij} = \mathscr{L}\delta_{ij} - \frac{\partial\mathscr{L}[\varphi]}{\partial(\partial_j\varphi)}\partial_i\varphi. \tag{A.9}$$

Via *Gauss' theorem* Eq. (A.8) can be written as

$$\delta\mathscr{S} = \int_V \mathrm{d}^d r\, \varepsilon_i(\mathbf{r})\partial_j T_{ij} - \oint_S \mathrm{d}^{d-1} r\, \varepsilon_i(\mathbf{r}) T_{ij} n_j, \tag{A.10}$$

where n_j is the jth component of the normal unit vector $\mathbf{n}$ (pointing outside) on the boundary S of the volume V. For fields φ which fulfil the corresponding *Euler-Lagrange equation*, i.e., the classical equation of motion for the action $\mathscr{S}$, the stress tensor is divergence free, and the first term on the rhs of Eq. (A.10) vanishes [128].

This formalism can be transferred to statistical physics via identifying the action with the free energy Hamiltonian, i.e., $\mathscr{S}[\varphi] \leftrightarrow \mathscr{H}[\phi]$. Correspondingly, within MFT, $\delta\mathscr{H}/\delta\phi = 0$, and $\partial_j T_{ij} = 0$. Then, one can relate the stress tensor to the force $\mathbf{F}$ acting on the volume enclosed by the surface S upon considering the translation $\varepsilon(\mathbf{r}) \equiv \mathbf{e}_i \ell_i$; Eq. (A.10) yields

$$\mathbf{F} = -\mathbf{e}_i \frac{\partial\mathscr{H}}{\partial\ell_i} = \oint_S \mathrm{d}^{d-1} r\, \mathbf{e}_i T_{ij} n_j. \tag{A.11}$$

Within MFT, the force on a colloidal particle is given by an integral over *any* surface surrounding the colloid. Note that this identification can also be constructed from the definition of continuum mechanics (see, e.g., Appendix B of Ref. [225]). Within the view of continuum mechanics Eq. (A.6) corresponds to the assumption that each particle displaced from $\mathbf{r}$ to $\tilde{\mathbf{r}}$ keeps its value of the order parameter ϕ during the translation [225].

According to Eq. (A.9) for the *Ginzburg-Landau-Wilson* fixed point Hamiltonian given in Eq. (1.6) one has [117]

$$T_{ij} = -\partial_i\phi\partial_j\phi + \delta_{ij}\left(\frac{1}{2}(\nabla\phi)^2 + \frac{\hat{\tau}}{2}\phi^2 + \frac{u}{4!}\phi^4\right). \tag{A.12}$$

For the normal force (along the z-direction) acting on the colloid one integrates T_{zz} over any surface surrounding the colloid, whereas for the lateral force (along the x-direction) the corresponding stress tensor component is given by T_{zx}. Note that one may add divergence-free terms to the stress-tensor in order to make it renormalizable or to ensure its conformal invariance [47, 212, 248, 249]. However, these so called *improvement terms* do not contribute to $\mathbf{F}$ in Eq. (A.11) because *Gauss' theorem* applies (this has been shown in Ref. [50] for the film geometry and in Ref. [111] for colloidal particles).

Numerically, we calculate the normal and lateral critical Casimir forces acting on the colloidal particle by integrating the stress tensor over a connected set of triangular surfaces of the tetrahedral finite elements. The resulting connected closed surface may be of any shape, however, it turned out to be numerically convenient to resemble a spherical shape as well: Within the linear finite element method the first derivatives of ϕ are assumed to be constant within each element [Eqs. (A.1) and (A.2)]. Thus, the relative numerical error of the value of $\nabla\phi$ is larger than the corresponding relative error of ϕ. Since within the stress tensor given in Eq. (A.9)

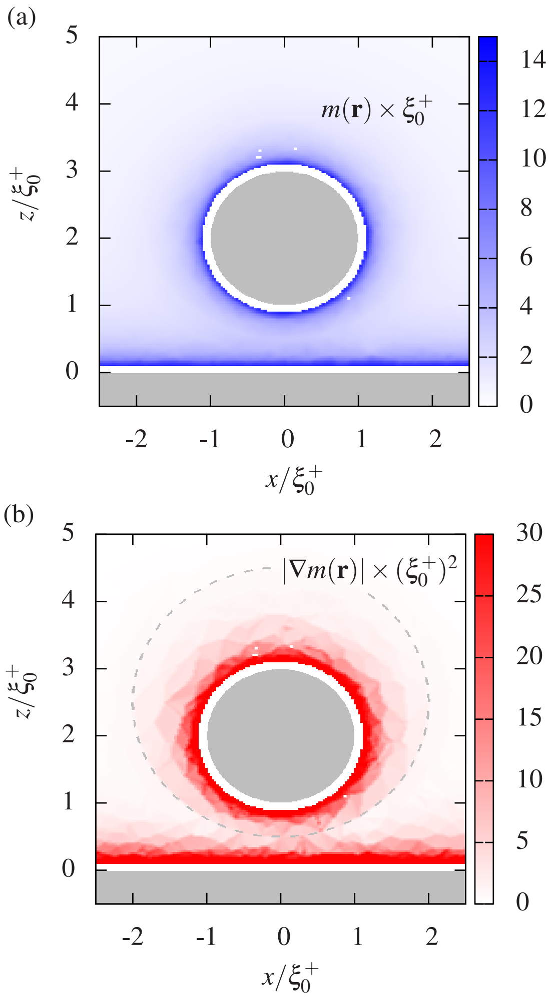

Figure A.3: (a) Numerically minimized order parameter profile $m(\mathbf{r}) \times \xi_0^+$ for a spherical colloid opposite to a homogeneous substrate with $(+,+)$ BC and at $T = T_c$ shown as contour plot along the plane $y = 0$. The graph indicates the particular case $R = D = \xi_0^+$ and is shown for illustration purposes only. (Note that the universal scaling functions obtained numerically are independent of ξ_0^+.) The white layers next to the colloid and the substrate (shaded areas) indicate the regions where the short-distance expansion for the order parameter profile was assumed to hold. Panel (b) shows the absolute value of the gradient, $|\nabla m(\mathbf{r})| \times (\xi_0^+)^2$ as obtained from the linear finite element method. Clearly, $|\nabla m(\mathbf{r})|$ obeys a much larger numerical uncertainty than $m(\mathbf{r})$ due to the assumption of linearity of m within one finite element (see the main text). Since the value of $|\nabla m|$, however, affects the stress tensor we calculate the latter one on surfaces on which $|\nabla m|$ is small (dashed line) in order to reduce the numerical error for the critical Casimir force.

terms containing derivatives of ϕ occur, this numerical error applies to the stress tensor as well. However, the freedom in choosing the actual surface domain over which one integrates T_{ij} allows for a integrating over a particular surface at which the value of $|\nabla\phi|$ is comparably small. We have checked that choosing such surfaces significantly improves the quality of the numerical data for the critical Casimir forces. Typically, the average absolute value of $\nabla\phi$ for the order parameter minimizing $\mathscr{H}$ around a sphere close to a wall is rather small on a surface of another sphere with a radius which is 1.5 to 3 times larger than the one of the sphere and symmetrically located along the xy-direction around the original sphere such its distance from the wall is half of the original sphere-wall distance. This is indicated in Fig. A.3 which shows an example of $m(\mathbf{r}) = (u/3!)^{1/2}\langle\phi(\mathbf{r})\rangle$ and $|\nabla m(\mathbf{r})|$ as obtained numerically for a colloid opposite to a substrate. Thus, in order to obtain the MFT numerical data of the normal and lateral critical Casimir forces acting on colloids we have integrated the stress tensor given in Eq. (A.12) over spherical surfaces at which we expect $|\nabla\phi|$ to be small so that its rather large relative error compared to the numerical error of ϕ does not affect the result for the scaling functions of the critical Casimir force significantly.

A.3. Numerical calculation of critical dynamics

One of the aims of the present work is the application and extension of present numerical routines to dynamic critical phenomena. Since typical experimental setups for the determination of Casimir forces, such as a colloid opposite to a wall, involve rather complex geometries, it is viable to use tools being able to deal with arbitrary geometries, such as the finite element method (see App. A.1). For numerically calculating the timtimeion of a given system one can either observe the state after certain iteration steps, or one can use one dimension of the mesh of finite elements as a time axis. Here, we have used the latter method in order to calculate the dynamical critical order parameter evolution of the Ising universality class with Model A dynamics (see Sec. 1.2.5 and Chap. 4) within MFT around cylindrically shaped colloidal particles and for the film and semi-infinite geometry.

In order to extend the minimization routine for the finite element method described above and implemented for static critical phenomena to dynamics one has to define the appropriate functional to be minimized. However, the dynamical functional S given in Eq. (1.11) obtained within the response functional formalism is not suited for the purpose here because it the corresponding "partition function" is always unity and therefore the corresponding "free energy" vanishes (see the discussion below Eq. (1.11) on page 34). Here, we *indirectly* solve the dynamical Langevin equation for the order parameter by minimizing the squared lhs of Eq. (4.1) (or Eq. (4.6), respectively)

$$H_{\text{eff}}[m] \equiv \int\limits_V \mathrm{d}^d r \int \mathrm{d}t \, \left[\partial_t m(\mathbf{r},t) + \Omega\left\{-\nabla^2 + \hat{\tau} + m^2(\mathbf{r},t)\right\} m(\mathbf{r},t)\right]^2, \tag{A.13}$$

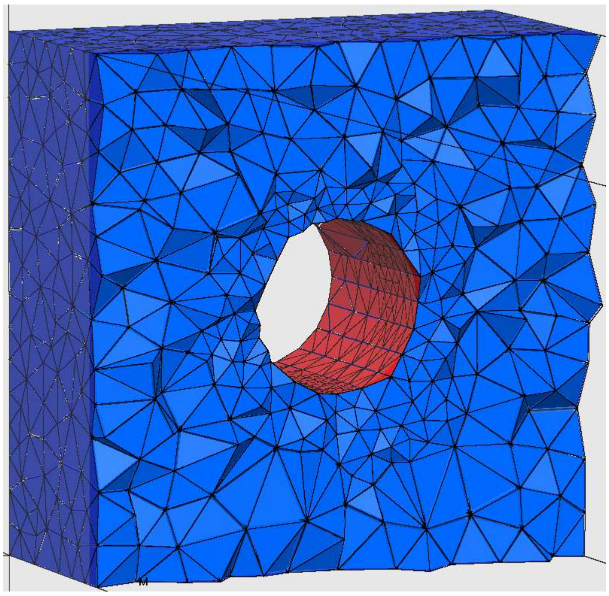

Figure A.4: Example of a mesh of finite elements used for the numerical calculation of dynamic critical phenomena visualized via TetView [245] (actually much finer-grained meshes have been used). The axis parallel to the cylinder axis corresponds to the time axis, whereas the two axes perpendicular to it correspond to two spatial dimensions. Here, one aims at calculating the order parameter profile around a cylindrical colloid (circle) at a fixed position along the time axis.

and apply the appropriate boundary conditions. The existence of a solution $m(\mathbf{r},t)$ for Eq. (4.1) implies that H_{eff} vanishes and is minimal for the correct spatio-temporal order parameter profile $m(\mathbf{r},t)$, and the integrand in Eq. (A.13) vanishes for each space-time point. We have extended the present finite element method by assigning two space axes and one time axis to the three-dimensional mesh in order to being able to also capture the time evolution within complex two-dimensional geometries beyond the semi-infinite or the film geometry.

Figure A.4 sketches a finite element mesh for a cylindrical colloidal particle immersed in a fluid in two spatial dimensions and along the time axis. Here, it is assumed that the colloid does not change its position (or shape) during time evolution. Accordingly the cylindrical “hole” in the mesh on the surface of which one applies some boundary conditions, is translated along the time axis.

Since in H_{eff} [Eq. (A.13)] also second derivatives of m occur, one needs a *quadratic* finite element method (the linear finite element method used above for static critical phenomena may allow for the calculation of second derivatives only indirectly). To this end we have used *complete quadratic Langrangean finite elements* with tetrahedral shape and ten nodes, as shown in Fig. A.5 [237]. In contrast to the linear elements, six additional nodes are introduced at the center of each connection line between two edge nodes. Within the quadratic finite element method one assumes a quadratic form of the approximative field replacing the actual field within

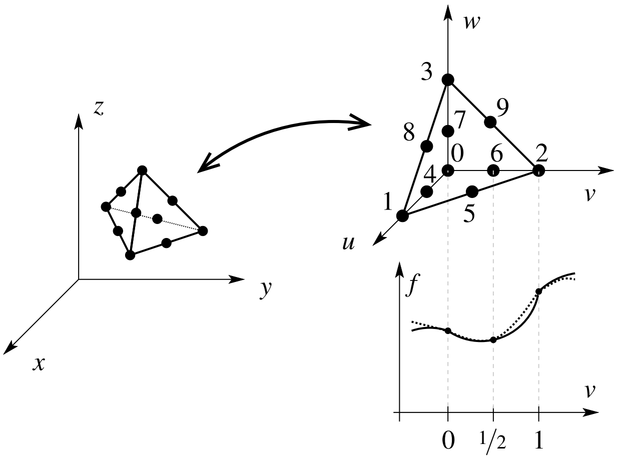

Figure A.5: Sketch of the quadratic finite element method, for which the finite elements of the linear finite element method (Fig. A.1) are extended by six additional nodes located at the center of each connection line between two edge nodes. The field f is approximated by a quadratic function which interpolates between the actual values of f at the ten nodes. Therefore, one can also calculate second derivatives needed for the description of dynamic critical phenomena (see the main text).

the tetrahedral elements, i.e., the field f on the parametrized coordinate (u,v,w) is approximated by

$$\begin{aligned} f(u,v,w) = f_0 &+ 2(f_0+f_1-2f_4)u^2 + 2(f_0+f_2-2f_6)v^2 + 2(f_0+f_3-2f_7)w^2 \\ &+ 4(f_0-f_6-f_4+f_5)uv + 4(f_0-f_7-f_6+f_9)vw + 4(f_0-f_7-f_4+f_8)uw \\ &+ (-3f_0-f_1+4f_4)u + (-3f_0-f_2+4f_6)v + (-3f_0-f_3+4f_7)w, \end{aligned} \tag{A.14}$$

where f_i are the values of the actual field on the nodes $i=0,\ldots,9$ as shown in Fig. A.5. The first derivatives of f are given by Eq. (A.2) with the Jacobian matrix Eq. (A.3). They are no longer constant within a single element but depend on the coordinates (u,v,w). The (constant) second derivatives of f are given by [237]

$$\begin{pmatrix} \partial_x^2 \\ \partial_y^2 \\ \partial_z^2 \\ \partial_x\partial_y \\ \partial_y\partial_z \\ \partial_x\partial_z \end{pmatrix} = \begin{bmatrix} T_1 \end{bmatrix} \begin{pmatrix} \partial_u \\ \partial_v \\ \partial_w \end{pmatrix} + \begin{bmatrix} T_2 \end{bmatrix} \begin{pmatrix} \partial_u^2 \\ \partial_v^2 \\ \partial_w^2 \\ \partial_u\partial_v \\ \partial_v\partial_w \\ \partial_u\partial_w \end{pmatrix}. \tag{A.15}$$

For a constant Jacobian as used here (non-curvilinear elements), $[T_1]=0$ in Eq. (A.15) and the first term on the rhs vanishes [250]. The second term on the rhs of Eq. (A.15) is determined by the elements $j_{ij} \equiv J^{-1}_{ij}$ of the inverse Jacobian matrix, i.e., [237]

$$\left[T_2\right] = \begin{bmatrix} j_{11}^2 & j_{12}^2 & j_{13}^2 & 2j_{11}j_{12} & 2j_{12}j_{13} & 2j_{13}j_{11} \\ j_{21}^2 & j_{22}^2 & j_{23}^2 & 2j_{21}j_{22} & 2j_{22}j_{23} & 2j_{23}j_{21} \\ j_{31}^2 & j_{32}^2 & j_{33}^2 & 2j_{31}j_{32} & 2j_{32}j_{33} & 2j_{33}j_{31} \\ j_{11}j_{21} & j_{12}j_{22} & j_{13}j_{23} & j_{11}j_{22}+j_{12}j_{21} & j_{12}j_{23}+j_{13}j_{22} & j_{11}j_{23}+j_{13}j_{21} \\ j_{21}j_{31} & j_{22}j_{32} & j_{23}j_{33} & j_{21}j_{32}+j_{22}j_{31} & j_{22}j_{33}+j_{23}j_{32} & j_{21}j_{33}+j_{23}j_{31} \\ j_{31}j_{11} & j_{32}j_{12} & j_{33}j_{13} & j_{31}j_{12}+j_{32}j_{11} & j_{32}j_{13}+j_{33}j_{12} & j_{31}j_{13}+j_{33}j_{11} \end{bmatrix} . \quad \text{(A.16)}$$

Analogous to the static case, depending on the boundary conditions, it is useful to replace the actual BC by fixing nodes at the confining surfaces with values obtained via a short distance expansion. We have used the expansion for a planar wall ($d_s = 1$) and for a cylinder ($d_s = 2$), respectively, as derived in Sec. 4.2.4, in particular for ordinary surface transition (Dirichlet BC).

Failure of numerical approach

It turned out, that the method presented here, is rather slowly converging towards the actual order parameter profile solving Eq. (4.1). This can be attributed to pronounced numerical difficulties in minimizing $H_{\text{eff}}[m]$ given in Eq. (A.13). Moreover, in order to determine the evolution of the order parameter on a long time scale accurately, one needs quite large numerical meshes extended along the time axis.

B. Calculation of the Derjaguin approximation for patterned substrates

The calculation of a Derjaguin-like approximation for the critical Casimir force acting on a colloid in the presence of a chemically patterned substrate presented in the following have been performed together with *Andrea Gambassi* [251, 252].

B.1. Derjaguin approximation for a chemical step

In this appendix we first calculate within the DA the normal critical Casimir force $F_\mathrm{s}(X,D,R,T)$ [Eq. (2.8)] acting on a spherical colloid of radius R facing a chemical step by using the DA. (We cannot directly calculate the lateral critical Casimir force $F_\mathrm{s}^{\|}(X,D,R,T)$ within the DA because for two parallel homogeneous plates such a force vanishes.) In a second step we derive the critical Casimir potential $\Phi_\mathrm{s}(X,D,R,T) = \int_D^\infty \mathrm{d}z\, F_\mathrm{s}(X,z,R,T)$ by integrating this result for the normal critical Casimir force. In a third step the lateral critical Casimir force is obtained as $F_\mathrm{s}^{\|}(X,D,R,T) = -\partial_X \Phi_\mathrm{s}(X,D,R,T) = -\int_D^\infty \mathrm{d}z\, \partial_X F_\mathrm{s}(X,z,R,T)$ [see Sec. 2.3.2].

In the spirit of the DA, the surface of the spherical colloid with (b) BC is thought of as being made of a pile of (infinitely thin) rings parallel to the opposing substrate and with an area $\mathrm{d}S(\rho) = 2\pi\rho\,\mathrm{d}\rho$, where ρ is the radius of the ring. Each of these rings is partly facing (in normal direction) the surface with $(a_<)$ BC, with an extension $\mathrm{d}S_<(\rho)$, and partly facing the surface with $(a_>)$ BC on the other side of the chemical step [Fig. B.6], with an extension $\mathrm{d}S_>(\rho)$, such that $\mathrm{d}S(\rho) = \mathrm{d}S_<(\rho) + \mathrm{d}S_>(\rho)$. For an assigned ρ, $\mathrm{d}S_\gtrless(\rho)$ depend, *inter alia*, on the lateral position X of the colloid. Using the *assumption of additivity* of the forces underlying the DA we suppose that the contribution $\mathrm{d}F_\mathrm{s}(\rho)$ of the ring to the total critical Casimir force F_s is given by the *sum* of the critical Casimir forces which would act, in a film, on portions of areas $\mathrm{d}S_<$ and $\mathrm{d}S_>$ in the presence of $(a_<,b)$ and $(a_>,b)$ BC, respectively. According to Eq. (1.3) this leads to the following expression for the force acting on a single ring:

$$\frac{\mathrm{d}F_\mathrm{s}(\rho)}{k_B T} = \frac{\mathrm{d}S_<(\rho)}{L^d(\rho)} k_{(a_<,b)}(\mathrm{sign}(\tau)\, L(\rho)/\xi_\pm) + \frac{\mathrm{d}S_>(\rho)}{L^d(\rho)} k_{(a_>,b)}(\mathrm{sign}(\tau)\, L(\rho)/\xi_\pm), \tag{B.1}$$

where $L(\rho)$ is the substrate-ring distance [Fig. B.6] as given in Eq. (2.3), and $k_{(a_\gtrless,b)}$ are the scaling functions of the critical Casimir force in the film geometry with $(a_>,b)$ and $(a_<,b)$ BC, respectively [see Eq. (1.3)]. This assumption neglects all edge effects along the boundary between the areas $\mathrm{d}S_>(\rho)$ and $\mathrm{d}S_<(\rho)$, which might actually be relevant in view of the spatial variation of the order parameter profile. It is therefore important to test the validity of this assumption at least in some relevant cases. This is carried out in Sec. 2.3 for $d = 4$, i.e., within MFT.

Without loss of generality in the following we assume $X > 0$, i.e., that the normal projection of the center of the sphere falls on the part of the substrate with $(a_>)$ BC [Figs. 2.1 and B.6].

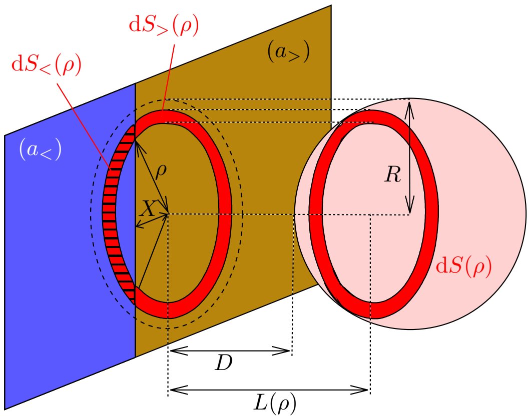

Figure B.6: Sketch concerning the Derjaguin approximation for the critical Casimir force acting on a colloid opposite to a chemical step. The critical Casimir force is subdivided into contributions from rings parallel to the substrate. The projection of the area $dS(\rho)$ of a ring onto the substrate is separated into the areal contributions $dS_<$ and $dS_>$ which emerge as the intersection of the projected ring with the half-planes carrying $(a_<)$ and $(a_>)$ BC, respectively [see the main text]. The sphere has a surface-to-surface distance D from the substrate and its center has a lateral distance X from the chemical step.

The results for $X < 0$ are obtained by exchanging in the formulas below $a_< \leftrightarrow a_>$ and $X \leftrightarrow -X$. Taking into account that $dS(\rho) = dS_<(\rho) + dS_>(\rho)$ one can rewrite Eq. (B.1) as

$$\frac{dF_s(\rho)}{k_BT} = \frac{dS(\rho)}{L^d(\rho)} k_{(a_>,b)}(\text{sign}(\tau)L(\rho)/\xi_\pm) + \frac{dS_<(\rho)}{L^d(\rho)} \Delta k(\text{sign}(\tau)L(\rho)/\xi_\pm), \tag{B.2}$$

where $\Delta k(\Theta) = k_{(a_<,b)}(\Theta) - k_{(a_>,b)}(\Theta)$. Summing up all force contributions from the rings of different radii ρ, one finds for the *total* normal force acting on the sphere

$$F_s(X,D,R,T) = F_{(a_>,b)}(D,R,T) + \Delta F(X,D,R,T), \tag{B.3}$$

where $F_{(a_>,b)}$ is the force acting on a sphere close to a *homogeneous* substrate with $(a_>)$ BC and is given by Eq. (2.5) or by Eqs. (2.1) and (2.6). This term does not contribute to the *lateral* critical Casimir force experienced by the colloid near the chemical step, because it does not depend on the lateral coordinate of the colloid. The second term ΔF in Eq. (B.3) corresponds to the integration of the force differences Δk in the region of overlap between the projection of the sphere onto the substrate plane and that part of the substrate with $(a_<)$ BC. For each ring this area is given by [see Fig. B.6]

$$dS_<(\rho) = \begin{cases} 0, & \rho < X, \\ 2\arccos(X/\rho)\rho d\rho, & X \le \rho \le R. \end{cases} \tag{B.4}$$

This leads to

$$\frac{\Delta F(X,D,R,T)}{k_BT} = 2\int_X^R d\rho\, \rho \arccos\left(\frac{X}{\rho}\right) \frac{\Delta k(\text{sign}(\tau)L(\rho)/\xi_\pm)}{L^d(\rho)}. \tag{B.5}$$

In the spirit of the DA, the radius of the sphere is taken to be large compared to its distance to the substrate, i.e., $\Delta = D/R \ll 1$, and the contributions from the rings closest to the substrate dominate. Therefore, it is well justified and in accordance with the DA to assume $X/R \ll 1$ because the contributions of rings with large radii do not change the behavior of the force in the Derjaguin limit. Within these two limits we can use the *parabolic* approximation for the distance of the rings to the substrate [Eq. (2.3)], $L(\rho) \simeq D\alpha$, with $\alpha = 1 + \rho^2/2RD$. Changing the integration variable in Eq. (B.5) we directly find

$$\Delta F(X,D,R,T) = k_B T \frac{R}{D^{d-1}} \Delta K(\Xi,\Theta,\Delta), \tag{B.6}$$

where ΔK is a universal scaling function given by

$$\Delta K(\Xi,\Theta,\Delta \to 0) = 2 \int\limits_{1+\Xi^2/2}^{\infty} \mathrm{d}\alpha\, \alpha^{-d} \arccos\left(\frac{\Xi}{\sqrt{2(\alpha-1)}}\right) \Delta k(\alpha\Theta). \tag{B.7}$$

Note that the relevant scaling variable $\Xi = X/\sqrt{RD}$ can take on arbitrary values, irrespective of the two assumptions $D/R \ll 1$ and $X/R \ll 1$. From Eq. (B.7) one finds with Eqs. (2.6) and (2.9) directly the expression for the scaling function $\psi_{(a_<|a_>,b)}$ given in Eq. (2.12).

The critical Casimir potential $\Phi_\mathrm{s}(X,D,R,T) = \int_D^\infty \mathrm{d}l F_\mathrm{s}(X,l,R,T)$ can be separated analogously to Eq. (B.3), i.e.,

$$\Phi_\mathrm{s}(X,D,R,T) = \Phi_{(a_>,b)}(D,R,T) + \Delta\Phi(X,R,D,T) \tag{B.8}$$

with

$$\Delta\Phi(X,R,D,T) = \int\limits_{D}^{\infty} \mathrm{d}l \Delta F(X,l,R,T) =: k_B T \frac{R}{D^{d-2}} \Delta\vartheta(\Xi,\Theta,\Delta). \tag{B.9}$$

Using Eq. (B.7), the scaling function $\Delta\vartheta$ is given by

$$\Delta\vartheta(\Xi,\Theta,\Delta) = 2 \int\limits_{1}^{\infty} \mathrm{d}y \frac{1}{y^{d-1}} \int\limits_{1+\Xi^2/(2y)}^{\infty} \mathrm{d}\alpha\, \frac{1}{\alpha^d} \arccos\left(\frac{\Xi}{\sqrt{2y(\alpha-1)}}\right) \Delta k(y\alpha\Theta). \tag{B.10}$$

By changing the integration variable $\alpha \mapsto z \equiv 2y(\alpha-1)/\Xi^2$ followed by $y \mapsto v \equiv y + \Xi^2 z/2$ one obtains

$$\Delta\vartheta(\Xi,\Theta,\Delta) = \Xi^2 \int\limits_{1}^{\infty} \mathrm{d}z \int\limits_{1+z\Xi^2/2}^{\infty} \mathrm{d}v \frac{1}{v^d} \arccos(1/\sqrt{z}) \Delta k(v\Theta). \tag{B.11}$$

After changing the order of integration

$$\int\limits_{1}^{\infty} \mathrm{d}z \int\limits_{1+z\Xi^2/2}^{\infty} \mathrm{d}v = \int\limits_{1+\Xi^2/2}^{\infty} \mathrm{d}v \int\limits_{1}^{2(v-1)/\Xi^2} \mathrm{d}z, \tag{B.12}$$

and using the primitive[30]

$$\int \mathrm{d}z \arccos(1/\sqrt{z}) = z \arccos(1/\sqrt{z}) - \sqrt{z-1} + c, \tag{B.13}$$

one obtains after a final change of variables $v \mapsto w \equiv 2(v-1)/\Xi^2$

$$\Delta\vartheta(\Xi,\Theta,\Delta) = \frac{\Xi^4}{2} \int_1^\infty \mathrm{d}s \frac{1}{(1+\Xi^2 s/2)^d} \left[s \arccos(s^{-1/2}) - \sqrt{s-1} \right] \Delta k(\Theta[1+\Xi^2 s/2]). \tag{B.14}$$

From Eq. (B.14) together with Eq. (2.7) one obtains the final expression for the scaling function of the critical Casimir potential as given in Eq. (2.14).

Bulk critical point: $\Theta = 0$

In order to calculate the critical Casimir force acting on the colloid at the *bulk critical point* one inserts Eq. (1.4) into Eq. (B.7) and obtains

$$\begin{aligned} \Delta K(\Xi,\Theta=0,\Delta) &= 2\left(\Delta_{(a_<,b)} - \Delta_{(a_>,b)}\right) \int_{1+\Xi^2/2}^{\infty} \mathrm{d}\alpha\, \alpha^{-d} \arccos\left(\frac{\Xi}{\sqrt{2\alpha-2}}\right) \qquad \text{(B.15)} \\ &=: \Xi^2 \left(\Delta_{(a_<,b)} - \Delta_{(a_>,b)}\right) I_d(\Xi^2/2), \end{aligned}$$

where $\Delta_{(a,b)} = k_{(a,b)}(0)$ [see Eq. (1.4)], and with the substitution $\alpha \mapsto z = \Xi/\sqrt{2(\alpha-1)}$ for $d > 1$,

$$I_d(a) = 2 \int_0^1 \mathrm{d}z \frac{z^{2d-3}}{(z^2+a)^d} \arccos(z). \tag{B.16}$$

For $I_d(a)$ the recursion relation

$$I_{d+1}(a) = \frac{1}{d} a^{1-d} \frac{\mathrm{d}}{\mathrm{d}a} [a^d I_d(a)] \tag{B.17}$$

holds, so that I_4 and I_3 can be expressed in terms of I_2. Performing the integration we find[31]

$$I_2(a) = \frac{\pi}{2a} \left[1 - \frac{a^{1/2}}{(1+a)^{1/2}} \right], \tag{B.18}$$

and therefore with Eq. (B.17)

$$I_3(a) = \frac{\pi}{4a} \left[1 - \frac{\frac{3}{2} a^{1/2} + a^{3/2}}{(1+a)^{3/2}} \right], \tag{B.19}$$

---

[30] See Eq. 7.8.3 on p. 168 in *Tables of indefinite integrals*, edited by Y. A. Brychkov, O. I. Marichev, and A. P. Prudnikov (Gordon and Breach, New York, 1989), with the substitution $z \mapsto x = 1/\sqrt{z}$.

[31] See Eq. (4) of Tab. 234 in *Nouvelles tables d'intégrales définies*, edited by D. B. De Haan (P. Engels, Leide, 1867); note that there is a misprint in Eq. 4.521.8 in *Table of Integrals, Series, and Products*, Sixth edition, edited by I. S. Gradshteyn and I. M. Ryzhik (Academic, London, 2000). The correct expression is $\int_0^1 \mathrm{d}x\, x\big(\arccos(x)\big)/(1+qx^2)^2 = \pi(\sqrt{1+q}-1)/(4q\sqrt{1+q})$ for $q > -1$.

and

$$I_4(a) = \frac{\pi}{6a}\left[1 - \frac{\frac{15}{8}a^{1/2} + \frac{5}{2}a^{3/2} + a^{5/2}}{(1+a)^{5/2}}\right]. \tag{B.20}$$

Thus, from Eqs. (B.16), (B.19), and (B.20) together with the expression for $K_{(a_{\gtrless},b)}(0,0) = 2\pi\Delta_{(a_{\gtrless},b)}/(d-1)$ [Sec. 2.2.1] and Eq. (2.9), one finds the expression for the scaling function $\psi_{(a_<|a_>,b)}$ given in Eq. (2.13). The critical Casimir potential at $\Theta = 0$ for $d = 3$ and 4 can be found from Eq. (B.10) together with Eq. (B.16):

$$\Delta\vartheta(\Xi, \Theta = 0, \Delta) = \Xi^2 \left(\Delta_{(a_<,b)} - \Delta_{(a_>,b)}\right) \int\limits_1^\infty \mathrm{d}y\, y^{-d} I_d\left(\tfrac{\Xi^2}{2y}\right), \tag{B.21}$$

and from a change of variable $y \mapsto a = \Xi^2/(2y)$ one finds

$$\Delta\vartheta(\Xi, 0, \Delta) = \frac{2^{d-2}}{\Xi^{2d-4}} \left(\Delta_{(a_<,b)} - \Delta_{(a_>,b)}\right) \int\limits_0^{\Xi^2/2} \mathrm{d}a\, a^{d-2} I_d(a). \tag{B.22}$$

Using Eq. (B.17) and the limiting behavior $I_d(a \to 0) = \pi/(2(d-1)a)$, we find

$$\Delta\vartheta(\Xi, 0, \Delta) = \frac{\Xi^2}{2(d-1)} \left(\Delta_{(a_<,b)} - \Delta_{(a_>,b)}\right) I_{d-1}(\Xi^2/2). \tag{B.23}$$

From Eqs. (B.18), (B.19), and (B.23) together with $\vartheta(0,0)$ as given in Sec. 2.2.1 one obtains Eq. (2.15) for the scaling function of the critical Casimir potential at T_c.

Far from criticality: $\Theta \gg 1$

Far from the critical point, i.e., for $\Theta \gg 1$, and for *symmetry breaking* boundary conditions $(a_<) = (+)$, $(a_>) = (-)$, and $(b) = (-)$ Eq. (1.5) holds and the integrals in Eqs. (B.7) and (B.14) can be calculated analytically. For $\Theta \gg 1$ Eq. (B.7) turns into

$$\Delta K(\Xi, \Theta \gg 1, \Delta) = 2(A_- - A_+)\Theta^d \int\limits_{1+\Xi^2/2}^{\infty} \mathrm{d}\alpha \arccos\left(\frac{\Xi}{\sqrt{2(\alpha-1)}}\right) e^{-\alpha\Theta}. \tag{B.24}$$

Substituting $\alpha \mapsto \beta = 2(\alpha - 2)/\Xi^2$ one has

$$\Delta K(\Xi, \Theta \gg 1, \Delta) = \Xi^2 (A_- - A_+)\Theta^d e^{-\Theta} \int\limits_1^\infty \mathrm{d}\beta \arccos(\beta^{-1}) e^{-\Xi^2\Theta\beta/2}. \tag{B.25}$$

Integrating by parts leads to

$$\Delta K(\Xi, \Theta \gg 1, \Delta) = (A_- - A_+)\Theta^{d-1} e^{-\Theta} \int\limits_1^\infty \mathrm{d}\beta \frac{1}{\beta\sqrt{\beta - 1}} e^{-\Xi^2\Theta\beta/2}. \tag{B.26}$$

By using the relation[32]

$$\int_1^\infty \mathrm{d}\beta \frac{1}{\beta\sqrt{\beta-1}} e^{-a^2\beta} = \pi\,\mathrm{erfc}(a), \tag{B.27}$$

where $a > 0$ and $\mathrm{erfc}(a) = 1 - \mathrm{erf}(a) = 2\pi^{-1/2}\int_a^\infty \mathrm{d}w \exp(-w^2)$ is the complementary error function, we finally arrive at

$$\Delta K(\Xi, \Theta \gg 1, \Delta) = \pi(A_- - A_+)\Theta^{d-1} e^{-\Theta}\,\mathrm{erfc}(\Xi\sqrt{\Theta/2}). \tag{B.28}$$

The scaling function $K_{(\mp,-)}$ for $\Theta \gg 1$ in the homogeneous case [Sec. 2.2] is given by [21]

$$K_{(\mp,-)}(\Theta \gg 1, \Delta \to 0) = 2\pi A_\pm \Theta^{d-1} e^{-\Theta} \tag{B.29}$$

and from Eqs. (2.9), (B.28), and (B.29) one obtains the expression for $\psi_{(-|+,-)}$ as given in Eq. (2.16). Similarly, after rewriting Eq. (B.14) for $\Theta \gg 1$ as

$$\Delta\vartheta(\Xi, \Theta \gg 1, \Delta) = (A_- - A_+)\Theta^d e^{-\Theta}\frac{\Xi^4}{2}\int_1^\infty \mathrm{d}s \left(s \arccos(s^{-1/2}) - \sqrt{s-1}\right) e^{-\Xi^2\Theta s/2}, \tag{B.30}$$

one can integrate by parts, which yields

$$\Delta\vartheta(\Xi, \Theta \gg 1, \Delta) = (A_- - A_+)\Theta^{d-2} e^{-\Theta}\int_1^\infty \mathrm{d}s \frac{1}{\sqrt{s-1}}\left[\frac{1}{s} + \frac{\Theta\Xi^2}{2}\left(1 + \Theta\Xi^2\right) - \frac{\Theta^2\Xi^4}{2}s\right] e^{-\Xi^2\Theta s/2}. \tag{B.31}$$

Using Eq. (B.27) and the relations [which follow from taking successive derivatives $-d/d(a^2)$ of Eq. (B.27)]

$$\int_1^\infty \mathrm{d}s \frac{1}{\sqrt{s-1}} e^{-a^2 s} = \frac{\sqrt{\pi}}{a} e^{-a^2}, \qquad \int_1^\infty \mathrm{d}s \frac{s}{\sqrt{s-1}} e^{-a^2 s} = \frac{\sqrt{\pi}}{2a^3}\left(1 + 2a^2\right) e^{-a^2}, \tag{B.32}$$

one ends up with

$$\Delta\vartheta(\Xi, \Theta \gg 1, \Delta) = \pi(A_- - A_+)\Theta^{d-2} e^{-\Theta}\,\mathrm{erfc}(\Xi\sqrt{\Theta/2}). \tag{B.33}$$

Together with the expression for the homogeneous case [see Sec. 2.2 and Ref. [21]],

$$\vartheta_{(\mp,-)}(\Theta \gg 1, \Delta \to 0) = 2\pi A_\pm \Theta^{d-2} e^{-\Theta}, \tag{B.34}$$

one obtains the expression for $\omega_{(-|+,-)}$ given in Eq. (2.16).

---

[32] See Eq. (26) on p. 136 in *Tables of Integrals Transforms*, Vol. I, Bateman Manuscript Project, edited by H. Erdelyi (McGraw-Hill, New York, 1954).

B.2. Derjaguin approximation for a single chemical lane

Based on the assumption of additivity which underlies the Derjaguin approximation one can use the results presented in Sec. 2.3 for a chemical step in order to study a chemical lane. The chemical lane configuration can be regarded as the superposition of two chemical steps, one (A) being a chemical step located at $x = -L$ with $(a|a_\ell)$ BC, and the other one (B) being a chemical step located at $x = L$ with $(a_\ell|a)$ BC. This superposition overcounts a contribution corresponding to a homogeneous substrate with (a_ℓ) BC which must be subtracted [see Eq. (2.9)]:

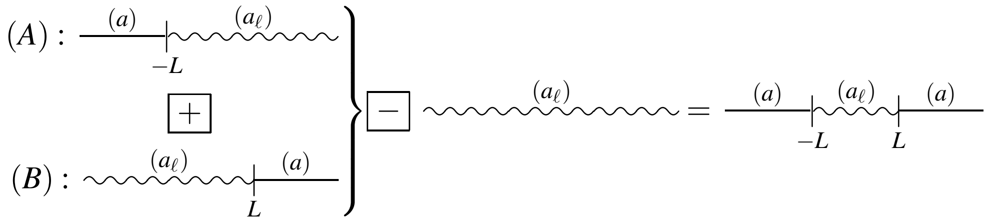

$$K_s^{(A)} + K_s^{(B)} \quad - \quad K_{(a_\ell,b)} \quad = \quad K_\ell, \tag{B.35}$$

where

$$K_s^{(A)}(\Lambda,\Xi,\Theta,\Delta) = \frac{K_{(a,b)} + K_{(a_\ell,b)}}{2} + \frac{K_{(a,b)} - K_{(a_\ell,b)}}{2} \psi_{(a|a_\ell,b)}(\Xi + \Lambda,\Theta,\Delta) \tag{B.36}$$

and

$$K_s^{(B)}(\Lambda,\Xi,\Theta,\Delta) = \frac{K_{(a,b)} + K_{(a_\ell,b)}}{2} + \frac{K_{(a_\ell,b)} - K_{(a,b)}}{2} \psi_{(a_\ell|a,b)}(\Xi - \Lambda,\Theta,\Delta). \tag{B.37}$$

Since within the DA $\psi_{(a_\ell|a,b)} = \psi_{(a|a_\ell,b)}$, Eqs. (B.35)–(B.37) and Eq. (2.23) lead directly to Eq. (2.25). The procedure for calculating the critical Casimir potential is analogous to the one discussed here for the force and leads to Eq. (2.26).

B.3. Derjaguin approximation for periodic chemical patterns

In order to obtain the scaling function for the critical Casimir force and the potential of a sphere close to a periodic chemical pattern one can follow a procedure analogous to the one presented in Appendix B.2. Indeed, in order to form a lane ℓ' with (a_1) BC on an otherwise homogeneous *portion* of a substrate with (a_2) BC and lateral extension P, one can proceed as follows:

(A): superimpose onto the substrate the single chemical lane ℓ studied in Sec. 2.4, with $a_\ell = a_1$, $a = a_2$, suitably positioned in space such that it coincides with the lane ℓ' to be formed.

(B): subtract the contribution of a homogeneous substrate with (a_2) BC, which is overcounted in the previous superposition. After this subtraction, the contribution to the force resulting from that part — marked by (?) in Eq. (B.38) — of the original substrate which is not affected by the formation of the extra lane is unchanged.

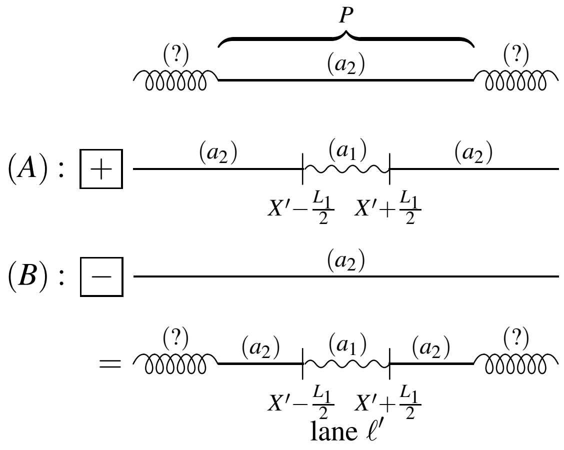

(B.38)

The contribution ΔF to the critical Casimir force experienced by a colloid close to such a substrate and due to the addition of the lane is characterized by the scaling function [see Eq. (2.23)]

$$\Delta K(\lambda,\Pi,\Xi-\Xi',\Theta,\Delta\to 0)=K_\ell(\Pi\tfrac{\lambda}{2},\Xi-\Xi',\Theta)-K_{(a_2,b)}=\frac{K_{(a_2,b)}-K_{(a_1,b)}}{2}$$
$$\times\left[\psi_{(a_1|a,b)}(\Xi-\Xi'+\Pi\tfrac{\lambda}{2},\Theta,\Delta\to 0)-\psi_{(a_1|a,b)}(\Xi-\Xi'-\Pi\tfrac{\lambda}{2},\Theta,\Delta\to 0)\right] \quad (B.39)$$

where we have used the relation $(L_1/2)/\sqrt{RD}=\Pi\lambda/2$ and have introduced $\Xi'\equiv X'/\sqrt{RD}$, with X' as the position of the center of the added lane ℓ'. The force resulting from a periodic pattern can now be obtained by starting out with a homogeneous substrate with (a_2) BC and by iterating the procedure discussed above which adds progressively displaced lanes at positions $X'=nP$, i.e., $\Xi'=n\Pi$, with $n\in\mathbb{Z}$. The resulting force is characterized by the scaling function

$$K_\mathrm{p}(\lambda,\Pi,\Xi,\Theta,\Delta\to 0)=K_{(a_2,b)}+\sum_{n=-\infty}^{+\infty}\Delta K(\lambda,\Pi,\Xi-n\Pi,\Theta,\Delta\to 0) \quad (B.40)$$

which, together with Eq. (2.29), yields immediately Eq. (2.31) for ψ_p.

For $\lambda=0$ or $\lambda=1$ one recovers from Eq. (2.31) the homogeneous cases with (a_2,b) BC or (a_1,b) BC, respectively. Obviously, for $\lambda=0$, the sum in Eq. (2.31) vanishes, and one is left with $\psi_\mathrm{p}(\lambda=0,\Pi,\Xi,\Theta,\Delta\to 0)=1$, corresponding to (a_2,b) BC. On the other hand for $\lambda=1$, the sum in Eq. (2.31) can be easily evaluated [see Eq. (2.12) for $|\Xi|\to\infty$]:

$$\lim_{M,N\to\infty}\sum_{n=-M}^{N}\left\{\psi_{(a_1|a_2,b)}(\Xi+\Pi(n+\tfrac{1}{2}),\Theta,\Delta)-\psi_{(a_1|a_2,b)}(\Xi+\Pi(n-\tfrac{1}{2}),\Theta,\Delta)\right\}$$
$$=\lim_{M,N\to\infty}\left\{\psi_{(a_1|a_2,b)}(\Xi+\Pi(N+\tfrac{1}{2}),\Theta,\Delta)-\psi_{(a_1|a_2,b)}(\Xi+\Pi(-M-\tfrac{1}{2}),\Theta,\Delta)\right\}=-2, \quad (B.41)$$

where we have used the fact that $\psi_{(a_1|a_2,b)}(\Xi=\pm\infty,\Theta,\Delta)=\mp 1$. Accordingly, $\psi_\mathrm{p}(\lambda=1,\Pi,\Xi,\Theta,\Delta\to 0)=-1$, which corresponds to the homogeneous case with (a_1,b) BC.

In the limit $\Pi \to 0$ (i.e., for very fine patterns compared with $\sqrt{RD}$), the sum in Eq. (2.31) turns into an integral:

$$\begin{aligned}
&\sum_{n=-\infty}^{\infty} \left\{ \psi_{(a_1|a_2,b)}(\Xi + \Pi(n + \tfrac{\lambda}{2}), \Theta, \Delta) - \psi_{(a_1|a_2,b)}(\Xi + \Pi(n - \tfrac{\lambda}{2}), \Theta, \Delta) \right\} \\
&\quad \xrightarrow[\Pi \to 0]{} \frac{1}{\Pi} \int_{-\infty}^{\infty} \mathrm{d}\eta \left\{ \psi_{(a_1|a_2,b)}(\Xi + \eta + \tfrac{\Pi\lambda}{2}, \Theta, \Delta) - \psi_{(a_1|a_2,b)}(\Xi + \eta - \tfrac{\Pi\lambda}{2}, \Theta, \Delta) \right\} \\
&\quad = \int_{-\infty}^{\infty} \mathrm{d}\eta \, \lambda \, \frac{\mathrm{d}}{\mathrm{d}\eta} \psi_{(a_1|a_2,b)}(\Xi + \eta, \Theta, \Delta) \\
&\quad = \lambda \left\{ \psi_{(a_1|a_2,b)}(+\infty, \Theta, \Delta) - \psi_{(a_1|a_2,b)}(-\infty, \Theta, \Delta) \right\} = -2\lambda,
\end{aligned} \tag{B.42}$$

and finally one finds Eq. (2.32).

For completeness, we provide the corresponding expression for the scaling function of the critical Casimir potential ω_p within the DA:

$$\begin{aligned}
&\omega_\mathrm{p}(\lambda, \Pi, \Xi, \Theta, \Delta \to 0) = \\
&1 + \sum_{n=-\infty}^{\infty} \left\{ \omega_{(a_1|a_2,b)}(\Xi + \Pi(n + \tfrac{\lambda}{2}), \Theta, \Delta \to 0) - \omega_{(a_1|a_2,b)}(\Xi + \Pi(n - \tfrac{\lambda}{2}), \Theta, \Delta \to 0) \right\}.
\end{aligned} \tag{B.43}$$

In the limit $\Pi \to 0$, ω_p reduces to

$$\omega_\mathrm{p}(\lambda, \Pi \to 0, \Xi, \Theta, \Delta \to 0) = 1 - 2\lambda. \tag{B.44}$$

Accordingly, within the DA and in the limit $\Pi \to 0$ the critical Casimir potential is the average of the ones corresponding to the two boundary conditions, weighted with the corresponding relative stripe width:

$$\vartheta_\mathrm{p}(\lambda, \Pi \to 0, \Xi, \Theta, \Delta \to 0) = \lambda \vartheta_{(a_1,b)}(\Theta, \Delta \to 0) + (1 - \lambda)\vartheta_{(a_2,b)}(\Theta, \Delta \to 0). \tag{B.45}$$

B.4. Cylinder close to a patterned substrate

Derjaguin approximation for a homogeneous substrate

Similarly to the case of a sphere discussed before, the critical Casimir force $F^{\mathrm{cyl}}_{(a,b)}$ per unit length acting on a (three-dimensional) cylinder of radius R with (b) BC close to and parallel to a substrate with (a) BC at a surface-to-surface distance D can be expressed in terms of a universal scaling function K^{cyl}:

$$F^{\mathrm{cyl}}_{(a,b)}(D, R, T) = k_B T \frac{R^{1/2}}{D^{d-1/2}} K^{\mathrm{cyl}}_{(a,b)}(\Theta, \Delta), \tag{B.46}$$

with $\Theta = \mathrm{sign}(\tau) D/\xi_\pm$ and $\Delta = D/R$ as before. Equation (B.46) describes a force divided by a length and per D^{d-3} which for $d = 4$ corresponds to considering $F^{\mathrm{cyl}}_{(a,b)}$ per length of its axis and per length of the *extra* translationally invariant direction of a hypercylinder [compare Eq. (2.1)]. The geometric prefactor in Eq. (B.46), however, differs from the one for the sphere [Eq. (2.1)] because it is chosen such that within the DA ($\Delta \to 0$) the scaling function $K^{\mathrm{cyl}}_{(a,b)}$ attains a nonzero and finite limit, as discussed before. The DA can be implemented along the lines of Sec. 2.2.1 for the sphere. Here the surface of the cylindrical colloid is decomposed into pairs of infinitely narrow stripes of combined area $\mathrm{d}S = 2M\mathrm{d}\rho$, positioned parallel to the substrate at a distance $L(\rho)$ from it [Eq. (2.3)] and each at a distance ρ from the symmetry plane of the configuration. M is the length of the cylinder and drops out from $F^{\mathrm{cyl}}_{(a,b)}$ which follows analogously from Eqs. (2.4) and (2.5):

$$F^{\mathrm{cyl}}_{(a,b)}(D,R,T)/k_BT \simeq 2\int_0^R \mathrm{d}\rho\,[L(\rho)]^{-d}\,k_{(a,b)}(\mathrm{sign}(\tau)\,L(\rho)/\xi_\pm), \tag{B.47}$$

where $L(\rho)$ is given in Eq. (2.3). Finally, in the limit $\Delta \to 0$ we obtain

$$K^{\mathrm{cyl}}_{(a,b)}(\Theta,\Delta\to 0) = \sqrt{2}\int_1^\infty \mathrm{d}\alpha\,(\alpha-1)^{-\frac{1}{2}}\,\alpha^{-d}\,k_{(a,b)}(\Theta\alpha). \tag{B.48}$$

At the bulk critical point $\Theta = 0$ one finds $K^{\mathrm{cyl}}_{(a,b)}(0,0) = \sqrt{2\pi}[\Gamma(d-\frac{1}{2})/\Gamma(d)]\Delta_{(a,b)}$ so that $K^{\mathrm{cyl}}_{(a,b)}(0,0) = [3\pi/(4\sqrt{2})]\Delta_{(a,b)} \simeq 1.66\times\Delta_{(a,b)}$ for $d=3$ and $K^{\mathrm{cyl}}_{(a,b)}(0,0) = [5\pi/(8\sqrt{2})]\Delta_{(a,b)} \simeq 1.38\times\Delta_{(a,b)}$ for $d=4$.

Derjaguin approximation for a chemical step

Here, we assume that the axis of the cylinder is parallel to the chemical step, i.e., perpendicular to the x direction [Fig. 2.1], as well as parallel to the substrate. The projection of the position of the axis of the cylinder with respect to the x direction is denoted by X, so that at $X=0$ the cylinder is positioned directly above the chemical step [Fig. 2.1]. Accordingly, the problem is effectively two-dimensional and the corresponding DA can be performed much easier than in Appendix B.1. Following an approach analogous to the one adopted for the sphere in Sec. 2.3 and in Appendix B.1, we rewrite the normal critical Casimir force per unit length acting on the cylinder as in Eq. (B.3):

$$F^{\mathrm{cyl}}_{\mathrm{s}}(X,D,R,T) = F^{\mathrm{cyl}}_{(a_>,b)}(D,R,T) + \Delta F^{\mathrm{cyl}}(X,D,R,T). \tag{B.49}$$

Within the DA we find for $\Delta\to 0$ [compare Eq. (B.6)]

$$\Delta F^{\mathrm{cyl}}(X,D,R,T) = k_BT\frac{R^{1/2}}{D^{d-1/2}}\Delta K^{\mathrm{cyl}}(\Xi,\Theta,\Delta\to 0), \tag{B.50}$$

where [compare Eq. (B.7)]

$$\Delta K^{\mathrm{cyl}}(\Xi,\Theta,\Delta\to 0) = \sqrt{2}\int_{1+\Xi^2/2}^{\infty} \mathrm{d}\alpha\,(\alpha-1)^{-\frac{1}{2}}\,\alpha^{-d}\Delta k(\Theta\alpha). \tag{B.51}$$

Using Eq. (B.51) and Eq. (B.48) we find for the whole range of values of Ξ the scaling function $\psi^{\mathrm{cyl}}_{(a_<|a_>,b)}$ which is defined completely analogous to Eq. (2.9) [compare Eq. (2.12)]:

$$\psi^{\mathrm{cyl}}_{(a_<|a_>,b)}(\Xi \gtrless 0, \Theta, \Delta \to 0) = \mp 1 \pm \frac{\sqrt{2}\int_{1+\Xi^2/2}^{\infty} \mathrm{d}\alpha\,(\alpha-1)^{-\frac{1}{2}}\,\alpha^{-d}\Delta k(\Theta\alpha)}{K^{\mathrm{cyl}}_{(a_<,b)}(\Theta,\Delta\to 0) - K^{\mathrm{cyl}}_{(a_>,b)}(\Theta,\Delta\to 0)}. \tag{B.52}$$

Derjaguin approximation for a periodic chemical pattern

The derivation of the scaling function for the critical Casimir force acting on the cylinder close to and aligned with a periodic chemical pattern as studied in Sec. 2.7 is analogous to the one for the sphere described in Appendix B.3. The final formula for $\psi^{\mathrm{cyl}}_{\mathrm{p}}$ is the same as in Eq. (2.31) with $\psi_{(a_1|a_2,b)}$ replaced by $\psi^{\mathrm{cyl}}_{(a_1|a_2,b)}$ given by Eq. (B.52). This renders the critical Casimir force per unit length

$$F^{\mathrm{cyl}}_{\mathrm{p}}(L_1, P, X, D, R, T) = k_B T \frac{R^{1/2}}{D^{d-1/2}} K^{\mathrm{cyl}}_{\mathrm{p}}(\lambda, \Pi, \Xi, \Theta, \Delta) \tag{B.53}$$

where $K^{\mathrm{cyl}}_{\mathrm{p}}$ is defined as in Eq. (2.29) with $K_{(a_1,b)}$ and $K_{(a_2,b)}$ replaced by $K^{\mathrm{cyl}}_{(a_1,b)}$ and $K^{\mathrm{cyl}}_{(a_2,b)}$, respectively, which are given by Eq. (B.48), and with ψ_{p} replaced by $\psi^{\mathrm{cyl}}_{\mathrm{p}}$. The corresponding results are shown in Fig. 2.16.

C. Short distance expansion for critical dynamics

In order to obtain an expansion for small values of $u = \bar{r}\bar{t}^{-1/2}$ the ansatz given in Eq. (4.10) for the order parameter is inserted into the corresponding Langevin equation Eq. (4.8). Replacing β, ν, and z with their MFT values one obtains

$$\begin{aligned}\bar{t}^{-3/2}\Bigg\{ h(w)\Bigg[-\frac{1}{2}f(u)g(v) - \left[\frac{1}{2}u + \frac{d_s-1}{1+v}\frac{v}{u}\right] f'(u)g(v) - f''(u)g(v) - 2\frac{v}{u}g'(v)f'(u) \\ - \frac{d_s-1}{1+v}\frac{v^2}{u^2}g'(v)f(u) - \frac{v^2}{u^2}g''(v)f(u)\Bigg] - \frac{w}{2}f(u)g(v)h'(w) + \left(f(u)g(v)h(w)\right)^3 \Bigg\} = 0. \quad \text{(C.1)}\end{aligned}$$

According to Eq. (4.11) we replace the scaling function f by a power series in terms of u; for general values of d_s from we find from power counting (in u) the following differential equations for g

$$\begin{aligned} u^{-3}: \quad & \frac{a_{-1}h(w)}{1+v}\Big[((d_s-3)v-2)g(v) + (a_{-1}h(w))^2(1+v)g^3(v) - \\ & v\left((d_s-3)v-2\right)g'(v) + v^2(1+v)g''(v)\Big] = 0, \quad \text{(C.2)}\end{aligned}$$

$$u^{-2}: \quad a_0 h(w)\left\{3(a_{-1}h(w))^2 g^3(v) - \frac{v^2}{1+v}\left[(d_s-1)g'(v) + (1+v)g''(v)\right]\right\} = 0, \quad \text{(C.3)}$$

$$\begin{aligned} u^{-1}: \quad & 3a_{-1}(a_0^2 + a_1 a_{-1})h^3(w)g^3(v)\frac{a_{-1}}{2}wh'(w)g(v) \\ & - a_1\frac{vh(w)}{1+v}\Big[(d_s-1)g(v) + \left(2+(d_s+1)v\right)g'(v) + v(1+v)g''(v)\Big] = 0. \quad \text{(C.4)}\end{aligned}$$

These equations apply for different boundary conditions corresponding to suitable choices of the constants a_{-1}, a_0, and a_1 as given in Sec. 4.2.4.

Bibliography

[1] H. G. B. Casimir, *On the attraction between two perfectly conducting plates*, Proceedings of the Koninklijke Nederlandse Akademie van Wetenschappen **51**, 793 (1948).

[2] W. Heisenberg, *Über den anschaulichen Inhalt der quantentheoretischen Kinematik und Mechanik*, Zeitschrift für Physik **43**, 172 (1927).

[3] M. Planck, *Zur Theorie des Gesetzes der Energieverteilung im Normalspektrum*, Verhandlungen der Deutschen Physikalischen Gesellschaft **2**, 237 (1900).

[4] A. Einstein, *Über einen die Erzeugung und Verwandlung des Lichtes betreffenden heuristischen Gesichtspunkt*, Annalen der Physik **322**, 132 (1905).

[5] M. Kardar and R. Golestanian, *The "friction" of vacuum, and other fluctuation-induced forces*, Rev. Mod. Phys. **71**, 1233 (1999).

[6] S. K. Lamoreaux, *Demonstration of the Casimir Force in the 0.6 to* $6\mu m$ *Range*, Phys. Rev. Lett. **78**, 5 (1997).

[7] R. Brown, *A brief account of microscopical observations made in the months of June, July and August, 1827, on the particles contained in the pollen of plants; and on the general existence of active molecules in organic and inorganic bodies*, Phil. Mag. **4**, 161 (1828).

[8] A. Einstein, *Über die von der molekularkinetischen Theorie der Wärme geforderte Bewegung von in ruhenden Flüssigkeiten suspendierten Teilchen*, Annalen der Physik **322**, 549 (1905).

[9] A. Einstein, *Zur Theorie der Brownschen Bewegung*, Annalen der Physik **324**, 248 (1906).

[10] M. von Smoluchowski, *Zur kinetischen Theorie der Brownschen Molekularbewegung und der Suspensionen*, Annalen der Physik **326**, 756 (1906).

[11] J. Perrin, *Les atomes*, Félix Alcan, Paris, 1913.

[12] T. Graham, *Liquid Diffusion Applied to Analysis*, Philosophical Transactions of the Royal Society of London **151**, pp. 183 (1861).

[13] H. R. Kruyt, G. H. Jonker, and J. T. G. Overbeek, *Colloid Science*, volume I, Elsevier, New York, 1952.

[14] R. J. Hunter, *Foundations of colloid science*, volume I, Clarendon Press, Oxford, 1986.

[15] I. W. Hamley, *Introduction to soft matter*, Wiley and Sons, Chichester, 2000.

[16] L. Boltzmann, *Studien über das Gleichgewicht der lebendigen Kraft zwischen bewegten materiellen Punkten*, Wiener Berichte **58**, 517 (1868).

[17] J. C. Maxwell, *On Boltzmann's theorem on the average distribution of energy in a system of material points*, Cambridge Philosophical Society's Transactions **XII** (1879).

[18] T. Andrews, *On the Continuity of the Gaseous and the Liquid States of Matter*, Philosophical Transactions of the Royal Society of London **159**, 575 (1869).

[19] M. E. Fisher and P. G. de Gennes, *Phénomènes aux parois dans un mélange binaire critique*, Comptes Rendus de l'Académie des Sciences, Paris, Série B **287**, 207 (1978).

[20] C. Hertlein, L. Helden, A. Gambassi, S. Dietrich, and C. Bechinger, *Direct measurement of critical Casimir forces*, Nature **451**, 172 (2008).

[21] A. Gambassi, A. Maciołek, C. Hertlein, U. Nellen, L. Helden, C. Bechinger, and S. Dietrich, *Critical Casimir effect in classical binary liquid mixtures*, Phys. Rev. E **80**, 061143 (2009).

[22] A. Gambassi, *The Casimir effect: From quantum to critical fluctuations*, J. Phys.: Conf. Ser. **161**, 012037 (2009).

[23] A. Gambassi, C. Hertlein, L. Helden, C. Bechinger, and S. Dietrich, *The critical casimir effect: universal fluctuation-induced forces at work*, Europhysics News **40/1**, 18 (2009).

[24] M. Krech, *The Casimir Effect in Critical Systems*, World Scientific, Singapore, 1994.

[25] J. G. Brankov, D. M. Danchev, and N. S. Tonchev, *Theory of critical phenomena in finite size systems*, World Scientific, Singapore, 2000.

[26] M. Krech and S. Dietrich, *Finite-size scaling for critical films*, Phys. Rev. Lett. **66**, 345 (1991).

[27] M. Krech and S. Dietrich, *Free energy and specific heat of critical films and surfaces*, Phys. Rev. A **46**, 1886 (1992).

[28] M. Krech and S. Dietrich, *Specific heat of critical films, the Casimir force, and wetting films near critical end-points*, Phys. Rev. A **46**, 1922 (1992).

[29] R. Evans and J. Stecki, *Solvation force in two-dimensional Ising strips*, Phys. Rev. B **49**, 8842 (1994).

[30] H. W. Diehl, D. Grüneberg, and M. A. Shpot, *Fluctuation-induced forces in periodic slabs: Breakdown of ε-expansion at the bulk critical point and revised field theory*, EPL **75**, 241 (2006).

[31] R. Zandi, A. Shackell, J. Rudnick, M. Kardar, and L. P. Chayes, *Thinning of superfluid films below the critical point*, Phys. Rev. E **76**, 030601 (2007).

[32] F. M. Schmidt and H. W. Diehl, *Crossover from Attractive to Repulsive Casimir Forces and Vice Versa*, Phys. Rev. Lett. **101**, 100601 (2008).

[33] T. F. Mohry, A. Maciołek, and S. Dietrich, *Crossover of critical Casimir forces between different surface universality classes*, Phys. Rev. E **81**, 061117 (2010).

[34] J. N. Munday, F. Capasso, and V. A. Parsegian, *Measured long-range repulsive Casimir-Lifshitz forces*, Nature **457**, 170 (2009).

[35] U. Nellen, L. Helden, and C. Bechinger, *Tunability of critical Casimir interactions by boundary conditions*, EPL **88**, 26001 (2009).

[36] U. Nellen, J. Dietrich, L. Helden, S. Chodankar, K. Nygard, J. Friso van der Veen, and C. Bechinger, *Salt-induced changes of colloidal interactions in critical mixtures*, Soft Matter **7**, 5360 (2011).

[37] F. Soyka, O. Zvyagolskaya, C. Hertlein, L. Helden, and C. Bechinger, *Critical Casimir forces in colloidal suspensions on chemically patterned substrates*, Phys. Rev. Lett. **101**, 208301 (2008).

[38] F. Soyka, *Kritischer Casimir Effekt in kolloidalen Suspensionen*, diploma thesis, Universität Stuttgart (2008).

[39] D. Vogt, *Kritischer Casimir Effekt auf chemisch strukturierten Oberflächen*, diploma thesis, Universität Stuttgart (2009).

[40] M. Tröndle, O. Zvyagolskaya, A. Gambassi, D. Vogt, L. Harnau, C. Bechinger, and S. Dietrich, *Trapping colloids near chemical stripes via critical Casimir forces*, Molecular Physics **109**, 1169 (2011).

[41] T. W. Burkhardt and E. Eisenriegler, *Casimir interactions of spheres in a fluid at the critical point*, Phys. Rev. Lett. **74**, 3189 (1995), ibid **78**, 2867 (1997).

[42] E. Eisenriegler and U. Ritschel, *Casimir forces between spherical particles in a critical fluid and conformal invariance*, Phys. Rev. B **51**, 13717 (1995).

[43] A. Hanke, F. Schlesener, E. Eisenriegler, and S. Dietrich, *Critical Casimir forces between spherical particles in fluids*, Phys. Rev. Lett. **81**, 1885 (1998).

[44] F. Schlesener, A. Hanke, and S. Dietrich, *Critical Casimir Forces in Colloidal Suspensions*, J. Stat. Phys. **110**, 981 (2003).

[45] F. Schlesener, *Colloidal Particles in Critical Fluids*, PhD thesis, Universität Stuttgart (2004).

[46] E. Eisenriegler, *Anisotropic colloidal particles in critical fluids*, J. Chem. Phys. **121**, 3299 (2004).

[47] M. Sprenger, F. Schlesener, and S. Dietrich, *Forces between chemically structured substrates mediated by critical fluids*, J. Chem. Phys. **124**, 134703 (2006).

[48] M. Sprenger, *Kritische Phänomene auf chemisch strukturierten Substraten*, PhD thesis, Universität Stuttgart (2006).

[49] M. Tröndle, L. Harnau, and S. Dietrich, *Critical adsorption and critical Casimir forces for geometrically structured confinements*, J. Chem. Phys. **129**, 124716 (2008).

[50] M. Tröndle, *Critical Adsorption and Critical Casimir Forces for Geometrically Structured Confinements*, master thesis, Universität Stuttgart (2007).

[51] M. Tröndle, S. Kondrat, A. Gambassi, L. Harnau, and S. Dietrich, *Normal and lateral critical Casimir forces between colloids and patterned substrates*, EPL **88**, 40004 (2009).

[52] M. Tröndle, S. Kondrat, A. Gambassi, L. Harnau, and S. Dietrich, *Critical Casimir effect for colloids close to chemically patterned substrates*, J. Chem. Phys. **133**, 074702 (2010).

[53] S. Dietrich, *Thermostatistics*, Lecture notes (unpublished), Universität Stuttgart, 2006.

[54] L. E. Reichl, *A Modern Course in Statistical Physics*, John Wiley & Sons, New York, second edition, 1998.

[55] F. Reif, *Fundamentals of Statistical and Thermal Physics*, McGraw-Hill Book Company, 1965.

[56] C. Domb, *The Critical Point*, Taylor&Francis, London, 1996.

[57] M. E. Fisher, *The theory of equilibrium critical phenomena*, Rep. Prog. Phys. **30**, 615 (1967).

[58] M. E. Fisher, *Scaling, Universality and Renormalization Group Theory*, in *Lecture Notes in Physics - Critical Phenomena (Proceedings, Stellenbosch, South Africa)*, edited by F. J. W. Hahne, volume 186, Springer, Berlin, 1982.

[59] W. Gebhardt and U. Krey, *Phasenübergänge und kritische Phänomene*, Vieweg, Braunschweig, 1980.

[60] H. E. Stanley, *Introduction to Phase Transitions and Critical Phenomena*, Oxford University Press, 1971.

[61] R. B. Griffiths, *Dependence of Critical Indices on a Parameter*, Phys. Rev. Lett. **24**, 1479 (1970).

[62] A. Pelissetto and E. Vicari, *Critical phenomena and renormalization-group theory*, Phys. Rep. **368**, 549 (2002).

[63] H. W. Diehl, *Field-theoretical Approach to Critical Behaviour at Surfaces*, in *Phase Transitions and Critical Phenomena*, edited by C. Domb and J. L. Lebowitz, volume 10, page 75, Academic, London, 1986.

[64] B. M. Law, *Wetting, adsorption and surface critical phenomena*, Prog. Surf. Sci. **66**, 159 (2001).

[65] T. C. Lubensky and M. H. Rubin, *Critical phenomena in semi-infinite systems. II. Mean-field theory*, Phys. Rev. B **12**, 3885 (1975).

[66] H. W. Diehl, *The theory of boundary critical phenomena*, Int. J. Mod. Phys. B **11**, 3503 (1997).

[67] M. E. Fisher and P. J. Upton, *Fluid interface tensions near critical end points*, Phys. Rev. Lett. **65**, 3405 (1990).

[68] A. J. Bray and M. A. Moore, *Critical behaviour of semi-infinite systems*, J. Phys. A **10**, 1927 (1977).

[69] T. W. Burkhardt and H. W. Diehl, *Ordinary, extraordinary, and normal surface transitions: Extraordinary-normal equivalence and simple explanation of* $|T-T_c|^{2-\alpha}$ *singularities*, Phys. Rev. B **50**, 3894 (1994).

[70] H. W. Diehl, *Critical adsorption of fluids and the equivalence of extraordinary and normal surface transitions*, Ber. Bunsenges. Phys. Chem. **98**, 466 (1994).

[71] M. E. Fisher and H. Nakanishi, *Scaling theory for the criticality of fluids between plates*, J. Chem. Phys. **75**, 5857 (1981).

[72] H. Nakanishi and M. E. Fisher, *Critical point shifts in films*, J. Chem. Phys. **78**, 3279 (1983).

[73] K. Binder, *Critical Behavior at Surfaces*, in *Phase Transitions and Critical Phenomena*, edited by C. Domb and J. L. Lebowitz, volume 8, page 1, Academic, London, 1983.

[74] F. Capasso, J. N. Munday, D. Iannuzzi, and H. B. Chan, *Casimir forces and Quantum Electrodynamical Torques: Physics and Nanomechanics*, IEEE J. Quantum Electron. **13**, 400 (2007).

[75] E. M. Lifshitz, *The theory of molecular attractive forces between solids*, Sov. Phys. JETP **2** (1956).

[76] P. Ball, *Feel the Force*, Nature **447**, 772 (2007).

[77] A. Ajdari, L. Peliti, and J. Prost, *Fluctuation-induced long-range forces in liquid crystals*, Phys. Rev. Lett. **66**, 1481 (1991).

[78] P. Ziherl, R. Podgornik, and S. Žumer, *Pseudo-Casimir Structural Force Drives Spinodal Dewetting in Nematic Liquid Crystals*, Phys. Rev. Lett. **84**, 1228 (2000).

[79] F. Karimi Pour Haddadan, D. W. Allender, and S. Žumer, *Pseudo-Casimir effect in untwisted chiral nematic liquid crystals*, Phys. Rev. E **64**, 061701 (2001).

[80] F. K. P. Haddadan and S. Dietrich, *Lateral and normal forces between patterned substrates induced by nematic fluctuations*, Phys. Rev. E **73** (2006).

[81] H. Lehle, M. Oettel, and S. Dietrich, *Effective forces between colloids at interfaces induced by capillary wavelike fluctuations*, Europhys. Lett. **75**, 174 (2006).

[82] F. Bresme, H. Lehle, and M. Oettel, *Solvent-mediated interactions between nanoparticles at fluid interfaces*, The Journal of Chemical Physics **130**, 214711 (2009).

[83] M. Goulian, R. Bruinsma, and P. Pincus, *Long-Range Forces in Heterogeneous Fluid Membranes*, EPL **22**, 145 (1993).

[84] R. Golestanian, M. Goulian, and M. Kardar, *Fluctuation-induced interactions between rods on a membrane*, Phys. Rev. E **54**, 6725 (1996).

[85] D. S. Dean and M. Manghi, *Fluctuation-induced interactions between domains in membranes*, Phys. Rev. E **74**, 021916 (2006).

[86] A.-F. Bitbol, P. G. Dommersnes, and J.-B. Fournier, *Fluctuations of the Casimir-like force between two membrane inclusions*, Phys. Rev. E **81**, 050903 (2010).

[87] F. Oosawa, *A theory on the effect of low molecular salts on the dissociation of linear polyacids*, Biopolymers **6**, 135 (1968).

[88] P. Attard, D. J. Mitchell, and B. W. Ninham, *Beyond Poisson–Boltzmann: Images and correlations in the electric double layer. I. Counterions only*, J. Chem. Phys. **88**, 4987 (1988).

[89] P. A. Pincus and S. A. Safran, *Charge fluctuations and membrane attractions*, EPL **42**, 103 (1998).

[90] R. Podgornik and V. A. Parsegian, *Charge-Fluctuation Forces between Rodlike Polyelectrolytes: Pairwise Summability Reexamined*, Phys. Rev. Lett. **80**, 1560 (1998).

[91] H. Boroudjerdi, Y.-W. Kim, A. Naji, R. Netz, X. Schlagberger, and A. Serr, *Statics and dynamics of strongly charged soft matter*, Phys. Rep. **416**, 129 (2005).

[92] R. H. French et al., *Long range interactions in nanoscale science*, Rev. Mod. Phys. **82**, 1887 (2010).

[93] R. Garcia and M. H. W. Chan, *Critical Fluctuation-Induced Thinning of* $4He$ *Films near the Superfluid Transition*, Phys. Rev. Lett. **83**, 1187 (1999).

[94] R. Garcia and M. H. W. Chan, *Critical Casimir Effect near the* $^3He-^4He$ *Tricritical Point*, Phys. Rev. Lett. **88**, 086101 (2002).

[95] A. Ganshin, S. Scheidemantel, R. Garcia, and M. H. W. Chan, *Critical casimir force in He-4 films: Confirmation of finite-size scaling*, Phys. Rev. Lett. **97**, 075301 (2006).

[96] M. Fukuto, Y. F. Yano, and P. S. Pershan, *Critical Casimir effect in three-dimensional Ising systems: Measurements on binary wetting films*, Phys. Rev. Lett. **94**, 135702 (2005).

[97] S. Rafai, D. Bonn, and J. Meunier, *Repulsive and attractive critical Casimir forces*, Physica A **386**, 31 (2007).

[98] A. Hucht, *Thermodynamic Casimir effect in He-4 films near T_λ: Monte Carlo results*, Phys. Rev. Lett. **99**, 185301 (2007).

[99] O. Vasilyev, A. Gambassi, A. Maciołek, and S. Dietrich, *Monte Carlo simulation results for critical Casimir forces*, EPL **80**, 60009 (2007).

[100] O. Vasilyev, A. Gambassi, A. Maciołek, and S. Dietrich, *Universal scaling functions of critical Casimir forces obtained by Monte Carlo simulations*, Phys. Rev. E **79**, 041142 (2009), ibid **80**, 039902(E) (2009).

[101] M. Hasenbusch, *Another method to compute the thermodynamic Casimir force in lattice models*, Phys. Rev. E **80**, 061120 (2009).

[102] M. Hasenbusch, *The thermodynamic Casimir effect in the neighbourhood of the λ-transition: a Monte Carlo study of an improved three-dimensional lattice model*, J. Stat. Mech. **2009**, P07031 (2009).

[103] M. Hasenbusch, *Specific heat, internal energy, and thermodynamic Casimir force in the neighborhood of the λ transition*, Phys. Rev. B **81**, 165412 (2010).

[104] M. Hasenbusch, *Finite size scaling study of lattice models in the three-dimensional Ising universality class*, Phys. Rev. B **82**, 174433 (2010).

[105] M. Hasenbusch, *Universal amplitude ratios in the three-dimensional Ising universality class*, Phys. Rev. B **82**, 174434 (2010).

[106] M. Hasenbusch, *Thermodynamic Casimir effect for films in the three-dimensional Ising universality class: Symmetry-breaking boundary conditions*, Phys. Rev. B **82**, 104425 (2010).

[107] M. Hasenbusch, *Thermodynamic Casimir force: A Monte Carlo study of the crossover between the ordinary and the normal surface universality class*, Phys. Rev. B **83**, 134425 (2011).

[108] A. W. Rodriguez, F. Capasso, and S. G. Johnson, *The Casimir effect in microstructured geometries*, Nat Photon **5**, 211 (2011).

[109] F. Parisen Toldin and S. Dietrich, *Critical Casimir forces and adsorption profiles in the presence of a chemically structured substrate*, J. Stat. Mech. **2010**, P11003 (2010).

[110] F. Parisen Toldin and S. Dietrich, *Critical Casimir forces involving a chemically structured substrate*, in *Proceedings of the Ninth Conference on Quantum Field Theory Under the Influence of External Conditions (QFEXT09)*, edited by K. A. M. Milton and M. Bordag, page 355, World Scientific, Singapore, 2010.

[111] S. Kondrat, L. Harnau, and S. Dietrich, *Critical Casimir interaction of ellipsoidal colloids with a planar wall*, J. Chem. Phys. **131**, 204902 (2009).

[112] M. N. Barber, *Finite-size Scaling*, in *Phase Transitions and Critical Phenomena*, edited by C. Domb and J. L. Lebowitz, volume 8, page 145, Academic, London, 1983.

[113] V. Privman, *Finite-Size Scaling Theory*, in *Finite Size Scaling and Numerical Simulation of Statistical Systems*, edited by V. Privman, pages 1–98, World Scientific, Singapore, 1990.

[114] V. Privman, P. C. Hohenberg, and A. Aharony, *Universal Critical-Point Amplitude Relations*, in *Phase Transitions and Critical Phenomena*, edited by C. Domb and J. L. Lebowitz, volume 14, page 1 and p. 364, Academic, London, 1991.

[115] H. B. Tarko and M. E. Fisher, *Critical Scattering in a Field and Below T_c*, Phys. Rev. Lett. **31**, 926 (1973).

[116] H. B. Tarko and M. E. Fisher, *Theory of critical point scattering and correlations. III. The Ising model below T_c and in a field*, Phys. Rev. B **11**, 1217 (1975).

[117] M. Krech, *Casimir forces in binary liquid mixtures*, Phys. Rev. E **56**, 1642 (1997).

[118] Z. Borjan and P. J. Upton, *Off-Critical Casimir Effect in Ising Slabs with Symmetric Boundary Conditions in $d = 3$*, Phys. Rev. Lett. **101**, 125702 (2008).

[119] L. Landau, *Zur Theorie der Phasenumwandlungen I*, Physikalische Zeitschrift der Sowjetunion **11**, 26 (1937).

[120] L. Landau, *Zur Theorie der Phasenumwandlungen II*, Physikalische Zeitschrift der Sowjetunion **11**, 545 (1937).

[121] Landau, *Collected Papers of L. D. Landau*, Pergamon Press, Oxford, 1965.

[122] V. L. Ginzburg, *Some remarks on phase transitions of the second kind and the microscopic theory of ferroelectric materials*, Soviet Physics / Solid State **2**, 1824 (1960).

[123] K. G. Wilson, *Renormalization Group and Strong Interactions*, Phys. Rev. D **3**, 1818 (1971).

[124] K. G. Wilson, *Renormalization Group and Critical Phenomena. I. Renormalization Group and the Kadanoff Scaling Picture*, Phys. Rev. B **4**, 3174 (1971).

[125] K. G. Wilson, *Renormalization Group and Critical Phenomena. II. Phase-Space Cell Analysis of Critical Behavior*, Phys. Rev. B **4**, 3184 (1971).

[126] K. Binder and P. C. Hohenberg, *Phase Transitions and Static Spin Correlations in Ising Models wit Free Surfaces*, Phys. Rev. B **6**, 3461 (1972).

[127] H. W. Diehl and M. Smock, *Critical behavior at supercritical surface enhancement: Temperature singularity of surface magnetization and order-parameter profile to one-loop order*, Phys. Rev. B **47**, 5841 (1993), ibid **48**, 6740 (1993).

[128] J. Zinn-Justin, *Quantum Field Theory and Critical Phenomena*, Clarendon Press, Oxford, fourth edition, 2002.

[129] L. Van Hove, *Time-Dependent Correlations between Spins and Neutron Scattering in Ferromagnetic Crystals*, Phys. Rev. **95**, 1374 (1954).

[130] P. C. Hohenberg and B. I. Halperin, *Theory of dynamic critical phenomena*, Rev. Mod. Phys. **49**, 435 (1977).

[131] R. Folk and G. Moser, *Critical dynamics: a field-theoretical approach*, J. Phys. A **39**, (2006).

[132] J. Cardy, *Scaling and renormalization in statistical physics*, Cambidge University Press, 1996.

[133] U. Täuber, *Critical Dynamics*, Textbook (work in progress), downloaded on July 19, 2011, available at http://www.phys.vt.edu/ tauber/.

[134] R. A. Ferrell, N. Menyhárd, H. Schmidt, F. Schwabl, and P. Szépfalusy, *Dispersion in Second Sound and Anomalous Heat Conduction at the Lambda Point of Liquid Helium*, Phys. Rev. Lett. **18**, 891 (1967).

[135] R. A. Ferrell, N. Menyhárd, H. Schmidt, F. Schwabl, and P. Szépfalusy, *Fluctuations and lambda phase transition in liquid helium*, Annals of Physics **47**, 565 (1968).

[136] B. I. Halperin and P. C. Hohenberg, *Generalization of Scaling Laws to Dynamical Properties of a System Near its Critical Point*, Phys. Rev. Lett. **19**, 700 (1967), ibid **19**, 940 (1967).

[137] B. I. Halperin and P. C. Hohenberg, *Scaling Laws for Dynamic Critical Phenomena*, Phys. Rev. **177**, 952 (1969).

[138] B. I. Halperin, P. C. Hohenberg, and S.-K. Ma, *Calculation of Dynamic Critical Properties Using Wilson's Expansion Methods*, Phys. Rev. Lett. **29**, 1548 (1972).

[139] B. I. Halperin, P. C. Hohenberg, and S.-K. Ma, *Renormalization-group methods for critical dynamics: I. Recursion relations and effects of energy conservation*, Phys. Rev. B **10**, 139 (1974).

[140] K. Kawasaki, *Kinetic equations and time correlation functions of critical fluctuations*, Annals of Physics **61**, 1 (1970).

[141] B. I. Halperin, P. C. Hohenberg, and E. D. Siggia, *Renormalization-Group Calculations of Divergent Transport Coefficients at Critical Points*, Phys. Rev. Lett. **32**, 1289 (1974).

[142] E. D. Siggia, B. I. Halperin, and P. C. Hohenberg, *Renormalization-group treatment of the critical dynamics of the binary-fluid and gas-liquid transitions*, Phys. Rev. B **13**, 2110 (1976).

[143] J. Santos and U. Täuber, *Non-equilibrium behavior at a liquid-gas critical point*, EPJ B **28**, 423 (2002).

[144] K. Binder and H. L. Frisch, *Dynamics of surface enrichment: A theory based on the Kawasaki spin-exchange model in the presence of a wall*, Z. Phys. B **84**, 403 (1991).

[145] S. Puri and K. Binder, *Surface-directed spinodal decomposition: Phenomenology and numerical results*, Phys. Rev. A **46**, R4487 (1992).

[146] S. Puri and H. L. Frisch, *Surface-directed spinodal decomposition: modelling and numerical simulations*, J. Phys. Condens. Matter **9**, 2109 (1997).

[147] S. Puri and K. Binder, *Power Laws and Crossovers in Off-Critical Surface-Directed Spinodal Decomposition*, Phys. Rev. Lett. **86**, 1797 (2001).

[148] S. Puri and K. Binder, *Surface-directed phase separation with off-critical composition: Analytical and numerical results*, Phys. Rev. E **66**, 061602 (2002).

[149] P. Calabrese and A. Gambassi, *Ageing properties of critical systems*, J. Phys. A **38**, R133 (2005).

[150] P. C. Martin, E. D. Siggia, and H. A. Rose, *Statistical Dynamics of Classical Systems*, Phys. Rev. A **8**, 423 (1973).

[151] H.-K. Janssen, *On a Lagrangean for classical field dynamics and renormalization group calculations of dynamical critical properties*, Z. Phys. B **23**, 377 (1976).

[152] C. De Dominicis, E. Brézin, and J. Zinn-Justin, *Field-theoretic techniques and critical dynamics. I. Ginzburg-Landau stochastic models without energy conservation*, Phys. Rev. B **12**, 4945 (1975).

[153] C. De Dominicis, *Technique de renormalisation de la théorie des champs et dynamique des phénomènes critiques*, J. Phys. (Paris) Colloq. **37**, C1 (1976).

[154] R. Bausch, H. K. Janssen, and H. Wagner, *Renormalized field theory of critical dynamics*, Z. Phys. B **24**, 113 (1976).

[155] F. Langouche, D. Roekaerts, and E. Tirapegui, *Functional integral methods for stochastic fields*, Physica A **95**, 252 (1979).

[156] R. Bausch and H. K. Janssen, *Equation of motion and nonlinear response near the critical point*, Z. Phys. B **25**, 275 (1976).

[157] R. Bausch, E. Eisenriegler, and H. K. Janssen, *Nonlinear critical slowing down of the one-component Ginzburg-Landau field*, Z. Phys. B **36**, 179 (1979).

[158] U. Leonhardt and T. G. Philbin, *Quantum levitation by left-handed metamaterials*, New J. Phys. **9**, 254 (2007).

[159] A. W. Rodriguez, J. N. Munday, J. D. Joannopoulos, F. Capasso, D. A. R. Dalvit, and S. G. Johnson, *Stable Suspension and Dispersion-Induced Transitions from Repulsive Casimir Forces Between Fluid-Separated Eccentric Cylinders*, Phys. Rev. Lett. **101**, 190404 (2008).

[160] A. W. Rodriguez, A. P. McCauley, D. Woolf, F. Capasso, J. D. Joannopoulos, and S. G. Johnson, *Non-touching nanoparticle diclusters bound by repulsive and attractive Casimir forces*, Phys. Rev. Lett. **104**, 160402 (2010).

[161] S. J. Rahi, M. Kardar, and T. Emig, *Constraints on stable equilibria with fluctuation-induced forces*, Phys. Rev. Lett. **105**, 070404 (2010).

[162] S. J. Rahi and S. Zaheer, *Stable Levitation and Alignment of Compact Objects by Casimir Spring Forces*, Phys. Rev. Lett. **104**, 070405 (2010).

[163] R. Zhao, J. Zhou, T. Koschny, E. N. Economou, and C. M. Soukoulis, *Repulsive Casimir Force in Chiral Metamaterials*, Phys. Rev. Lett. **103**, 103602 (2009).

[164] J. Varela, A. W. Rodriguez, A. P. McCauley, and S. G. Johnson, *Casimir microsphere diclusters and three-body effects in fluids*, Phys. Rev. A **83**, 042516 (2011).

[165] B. Derjaguin, *Untersuchungen über die Reibung and Adhäsion - Theorie des Anhaftens kleiner Teilchen*, Kolloid Z. **69**, 155 (1934).

[166] A. W. Rodriguez, D. Woolf, A. P. McCauley, F. Capasso, J. D. Joannopoulos, and S. G. Johnson, Phys. Rev. Lett. **105**, 060401 (2010).

[167] M. Hoffmann, Y. Lu, M. Schrinner, M. Ballauff, and L. Harnau, *Dumbbell-Shaped Polyelectrolyte Brushes Studied by Depolarized Dynamic Light Scattering*, J. Phys. Chem. B **112**, 14843 (2008).

[168] M. Hoffmann et al., *Thermoresponsive colloidal molecules*, Soft Matter **6**, 1125 (2010).

[169] M. Labbé-Laurent, *Critical Casimir interaction between a cylindrical particle and a chemically structured substrate*, bachelor thesis, Universität Stuttgart (2010).

[170] L. Harnau, *Numerical calculations of the critical Casimir force between cylinders and patterned substrates*, private communication.

[171] M. Sprenger, F. Schlesener, and S. Dietrich, *Critical adsorption at chemically structured substrates*, Phys. Rev. E **71**, 056125 (2005).

[172] A. Drzewiński, A. Maciołek, and R. Evans, *Influence of Capillary Condensation on the Near-Critical Solvation Force*, Phys. Rev. Lett. **85**, 3079 (2000).

[173] A. Maciołek, A. Drzewiński, and R. Evans, *Near-critical confined fluids and Ising films: Density-matrix renormalization-group study*, Phys. Rev. E **64**, 056137 (2001).

[174] R. Evans, *Fluids adsorbed in narrow pores: phase equilibria and structure*, J. Phys. Cond. Mat. **2**, 8989 (1990).

[175] T. Bieker and S. Dietrich, *Wetting of curved surfaces*, Physica A **252**, 85 (1998).

[176] C. Bauer, T. Bieker, and S. Dietrich, *Wetting-induced effective interaction potential between spherical particles*, Phys. Rev. E **62**, 5324 (2000).

[177] J. Israelachvili, *Intermolecular and Surface Forces, 2nd ed.*, Academic, New York, 1992.

[178] D. Dantchev, F. Schlesener, and S. Dietrich, *Interplay of critical Casimir and dispersion forces*, Phys. Rev. E **76**, 011121 (2007).

[179] J. V. Sengers, D. Bedeaux, P. Mazur, and S. C. Greer, *Behavior of the dielectric constant of fluids near a critical point*, Physica A: Statistical and Theoretical Physics **104**, 573 (1980).

[180] U. Kaatze and D. Woermann, *Dielectric study of a binary aqueous mixture with a lower critical point*, The Journal of Physical Chemistry **88**, 284 (1984).

[181] Y. Jayalakshmi, J. S. Van Duijneveldt, and D. Beysens, *Behavior of density and refractive index in mixtures of 2,6-lutidine and water*, J. Chem. Phys. **100**, 604 (1994).

[182] A. Gambassi, *Patterned substrates: comparison with experiments*, unpublished notes (2009).

[183] S. Dietrich and H. W. Diehl, *The effects of surfaces on dynamic critical behavior*, Z. Phys. B **51**, 343 (1983).

[184] H. Riecke, *Nichlineare Relaxation in halbunendlichen Systemen*, Diploma thesis, Ludwigs-Maximilian-Universität München (1982).

[185] H. Riecke, S. Dietrich, and H. Wagner, *Field theory for nonlinear critical relaxation near a surface*, Phys. Rev. Lett. **55**, 3010 (1985).

[186] U. Ritschel and P. Czerner, *Universal Short-Time Behavior in Critical Dynamics near Surfaces*, Phys. Rev. Lett. **75**, 3882 (1995).

[187] H. W. Diehl and H. K. Janssen, *Boundary conditions for the field theory of dynamic critical behavior in semi-infinite systems with conserved order parameter*, Phys. Rev. A **45**, 7145 (1992).

[188] H. W. Diehl, *Universality classes for the dynamic surface critical behavior of systems with relaxational dynamics*, Phys. Rev. B **49**, 2846 (1994).

[189] F. Wichmann and H. W. Diehl, *Dynamic surface critical behavior of systems with conserved bulk order parameter: Detailed RG analysis of the semi-infinite extensions of model B with and without nonconservative surface terms*, Z. Phys. B **97**, 251 (1995).

[190] A. Gambassi and S. Dietrich, *Critical Dynamics in Thin Films*, J. Stat. Phys. **123**, 929 (2006).

[191] M. Barmatz, I. Hahn, J. A. Lipa, and R. V. Duncan, *Critical phenomena in microgravity: Past, present, and future*, Rev. Mod. Phys. **79**, 1 (2007).

[192] H. W. Diehl and H. Chamati, *Dynamic critical behavior of model A in films: Zero-mode boundary conditions and expansion near four dimensions*, Phys. Rev. B **79**, 104301 (2009).

[193] S. Puri and K. Binder, *Surface-directed spinodal decomposition in a thin-film geometry: A computer simulation*, J. Stat. Phys. **77**, 145 (1994).

[194] S. K. Das, S. Puri, J. Horbach, and K. Binder, *Kinetics of phase separation in thin films: Simulations for the diffusive case*, Phys. Rev. E **72**, 061603 (2005).

[195] S. K. Das, S. Puri, J. Horbach, and K. Binder, *Molecular Dynamics Study of Phase Separation Kinetics in Thin Films*, Phys. Rev. Lett. **96**, 016107 (2006).

[196] S. K. Das, J. Horbach, and K. Binder, *Kinetics of phase separation in thin films: Lattice versus continuum models for solid binary mixtures*, Phys. Rev. E **79**, 021602 (2009).

[197] K. Binder, S. K. Das, and J. Horbach, *Surface Directed Spinodal Decomposition: Lattice Model versus Ginzburg Landau Theory*, Modern Physics Letters B **23**, 549 (2009).

[198] A. Gambassi, *Relaxation phenomena at criticality*, The European Physical Journal B - Condensed Matter and Complex Systems **64**, 379 (2008).

[199] D. S. Dean and A. Gopinathan, *The non-equilibrium behavior of pseudo-Casimir forces*, J. Stat. Mech. , L08001 (2009).

[200] D. S. Dean and A. Gopinathan, *Out-of-equilibrium behavior of Casimir-type fluctuation-induced forces for free classical fields*, Phys. Rev. E **81**, 041126 (2010).

[201] A. Hanke and S. Dietrich, *Critical adsorption on curved objects*, Phys. Rev. E **59**, 5081 (1999).

[202] S. Kondrat, L. Harnau, and S. Dietrich, *Critical adsorption on nonspherical colloidal particles*, J. Chem. Phys. **126**, 174902 (2007).

[203] R. A. Omari, C. A. Grabowski, and A. Mukhopadhyay, *Effect of Surface Curvature on Critical Adsorption*, Phys. Rev. Lett. **103**, 225705 (2009).

[204] B. Doyon and P. Fonseca, *Ising field theory on a pseudosphere*, J. Stat. Mech. **2004**, P07002 (2004).

[205] H. Shima and Y. Sakaniwa, *The dynamic exponent of the Ising model on negatively curved surfaces*, J. Stat. Mech. **2006**, P08017 (2006).

[206] H. Shima and Y. Sakaniwa, *Geometric effects on critical behaviours of the Ising model*, J. Phys. A **39**, 4921 (2006).

[207] H. Shima, Y. Sakaniwa, and I. Hasegawa, *Short-time relaxation of the Ising model on curved surfaces*, J. Magn. Magn. Mater. **310**, e465 (2007).

[208] O. Schönborn and R. C. Desai, *Phase-ordering kinetics on curved surfaces*, Physica A **239**, 412 (1997).

[209] O. L. Schoenborn, *Phase-Ordering Kinetics on Curved Surfaces*, PhD thesis, University of Toronto (1998).

[210] T. Taniguchi, *Shape Deformation and Phase Separation Dynamics of Two-Component Vesicles*, Phys. Rev. Lett. **76**, 4444 (1996).

[211] H. K. Janssen, B. Schaub, and B. Schmittmann, *New universal short-time scaling behaviour of critical relaxation processes*, Z. Phys. B **73**, 539 (1989).

[212] F. Schlesener, *Kritische Casimirkräfte in Geometrien mit gekrümmten Oberflächen*, diploma thesis, Universität Wuppertal (1997).

[213] A. Hanke, M. Krech, F. Schlesener, and S. Dietrich, *Critical adsorption near edges*, Phys. Rev. E **60**, 5163 (1999).

[214] Wolfram, *Mathematica®*, http://www.wolfram.com/mathematica/.

[215] D. Bartolo, A. Ajdari, and J.-B. Fournier, *Effective interactions between inclusions in complex fluids driven out of equilibrium*, Phys. Rev. E **67**, 061112 (2003).

[216] A. Najafi and R. Golestanian, *Forces induced by nonequilibrium fluctuations: The Soret-Casimir effect*, EPL (Europhysics Letters) **68**, 776 (2004).

[217] R. Brito, U. M. B. Marconi, and R. Soto, *Generalized Casimir forces in nonequilibrium systems*, Phys. Rev. E **76**, 011113 (2007).

[218] P. R. Buenzli and R. Soto, *Violation of the action-reaction principle and self-forces induced by nonequilibrium fluctuations*, Phys. Rev. E **78**, 020102 (2008).

[219] P. R. Buenzli, *Fluctuation-induced self-force and violation of action–reaction in a nonequilibrium steady state fluid*, J. Phys.: Conf. Ser. **161**, 012036 (2009).

[220] P. Rodriguez-Lopez, R. Brito, and R. Soto, *Dynamical approach to the Casimir effect*, Phys. Rev. E **83**, 031102 (2011).

[221] D. Bartolo, A. Ajdari, J.-B. Fournier, and R. Golestanian, *Fluctuations of Fluctuation-Induced Casimir-Like Forces*, Phys. Rev. Lett. **89**, 230601 (2002).

[222] V. Démery and D. S. Dean, *Drag Forces in Classical Fields*, Phys. Rev. Lett. **104**, 080601 (2010).

[223] V. Démery and D. Dean, *Drag forces on inclusions in classical fields with dissipative dynamics*, EPJ E **32**, 377 (2010).

[224] V. Démery and D. S. Dean, *Thermal Casimir drag in fluctuating classical fields*, Phys. Rev. E **84**, 010103 (2011).

[225] A.-F. Bitbol and J.-B. Fournier, *Forces exerted by a correlated fluid on embedded inclusions*, Phys. Rev. E **83**, 061107 (2011).

[226] Krüger, M., Emig, T., Bimonte, G., and Kardar, M., *Non-equilibrium Casimir forces: Spheres and sphere-plate*, EPL **95**, 21002 (2011).

[227] D. Dantchev and G. Valcheva, *Surface Integration Approach: A New Technique for Evaluating Geometry Dependent Forces between Objects of Various Geometry and a Plate*, (2011), preprint submitted to Adv. Coll. Int. Sci.

[228] C. D. Fosco, F. C. Lombardo, and F. D. Mazzitelli, *The proximity force approximation for the Casimir energy as a derivative expansion*, preprint arXiv:1109.2123 (2011).

[229] G. Bimonte, T. Emig, R. L. Jaffe, and M. Kardar, *Casimir forces beyond the proximity approximation*, preprint arXiv:1110.1082 (2011).

[230] G. Volpe, I. Buttinoni, D. Vogt, H.-J. Kummerer, and C. Bechinger, *Microswimmers in patterned environments*, Soft Matter **7**, 8810 (2011).

[231] O. Zvyagolskaya, A. J. Archer, and C. Bechinger, *Criticality and phase separation in a two-dimensional binary colloidal fluid induced by the solvent critical behavior*, EPL **96**, 28005 (2011).

[232] T. F. Mohry, A. Maciołek, and S. Dietrich, *Phase behavior of colloidal suspensions with critical solvents in terms of effective interactions*, preprint (2012).

[233] A. Maciołek, A. Gambassi, and S. Dietrich, *Critical Casimir effect in superfluid wetting films*, Phys. Rev. E **76**, 031124 (2007).

[234] M. Bier, A. Gambassi, M. Oettel, and S. Dietrich, *Electrostatic interactions in critical solvents*, EPL **95**, 60001 (2011).

[235] D. Bonn, J. Otwinowski, S. Sacanna, H. Guo, G. Wegdam, and P. Schall, *Direct Observation of Colloidal Aggregation by Critical Casimir Forces*, Phys. Rev. Lett. **103**, 156101 (2009).

[236] A. Gambassi and S. Dietrich, *Colloidal Aggregation and Critical Casimir Forces*, Phys. Rev. Lett. **105**, 059601 (2010).

[237] G. Dhatt and G. Touzot, *The Finite Element Method Displayed*, Wiley and Sons, 1984.

[238] S. Kondrat, *F3DM - a numerical library for the 3d finite element method.*

[239] M. Tröndle, *Short documentation for the F3DM library and tools*, unpublished notes (2010).

[240] B. Stroustrup, *The C++ Programming Language*, Addison-Wesley Longman Publishing Co., Inc., Boston, MA, USA, 3rd edition, 2000.

[241] *The GNU Triangulated Surface library*, http://gts.sourceforge.net/.

[242] H. Si, *TetGen — a quality 3D mesh generator*, http://tetgen.berlios.de/.

[243] *Gnome library*, ftp://ftp.gtk.org/pub/glib/.

[244] *Gnu Scientific Library*, http://www.gnu.org/software/gsl/.

[245] H. Si, *TetView — A Tetrahedral Mesh and Piecewise Linear Complex Viewer*, http://tetgen.berlios.de/tetview.html.

[246] W. H. Press, S. A. Teukolsky, W. T. Vetterling, and B. P. Flannery, *Numerical Recipes in C - The Art of Scientific Computing*, Cambridge University Press, second edition, 1992.

[247] R. Fletcher, *Practical Methods of Optimization*, John Wiley & Sons, Chichester, 2nd edition, 1987.

[248] J. C. Collins, *Renormalization of the enery-momentum tensor in* ϕ^4 *theory*, Phys. Rev. D **14**, 1965 (1976).

[249] L. S. Brown, *Dimensional Regularization of Composite Operators in Scalar Field Theory*, Annals of Physics **126**, 135 (1980).

[250] J. E. Akin, *Finite element analysis with error estimators: an introduction to the FEM and adaptive error analysis for engineering students*, 2005.

[251] A. Gambassi, *Derjaguin approximation*, unpublished notes (2008).

[252] M. Tröndle, *Derjaguin approximation within mean field theory*, unpublished notes (2008).

Danksagung

MEIN großer Dank gilt **Prof. Dr. Siegfried Dietrich**, der mir nicht nur die Möglichkeit geboten hat in seiner Abteilung diese Arbeit anzufertigen, sondern der mit seinen Ideen und Anregungen und durch Diskussionen, Fragen und Antworten maßgeblich an der Entstehung dieser Arbeit beteiligt war. Ich möchte mich bei Prof. Dietrich besonders für das entgegengebrachte Vertrauen sowie für den Freiraum in der Forschung als auch abseits der Forschung bedanken. Ebenso ermöglichte mir Prof. Dietrich die Teilnahme an vielen Konferenzen und Workshops, von denen die ich viel profitiert und gelernt habe.

Weiter geht mein Dank an **Prof. Dr. Clemens Bechinger** für die Bereitschaft zur Übernahme des Zweitgutachtens sowie für Diskussionen über gemessene Casimir-Kräfte und die Bereitstellung von Bildern, Filmen und Daten für Präsentationen.

Ganz besonders möchte ich mich bei meinem Betreuer **Priv.-Doz. Dr. Ludger Harnau** bedanken, der meine Arbeit über Jahre bei Fragen zu Physik, Numerik und anderem intensiv begleitet hat. Ludger Harnau war wesentlich am Gelingen meiner Doktorarbeit beteiligt. Vielen Dank auch für das Korrekturlesen!

Grazie mille **Prof. Dr. Andrea Gambassi**! Mein großer Dank gilt Andrea Gambassi, der u.a. mit Derjaguin-Integralen und vielen physikalischen Diskussionen zu Statik, Dynamik und Kräften viel zur Entstehung dieser Arbeit beigetragen hat. Ganz besonders danken möchte ich ihm für die Interpretation experimenteller Daten, die einem Theoretiker Erfahrung und Ausdauer abnötigt. Vielen Dank auch für das Korrekturlesen.

Großer Dank gebührt auch dem Erfinder von `f3dm`, **Dr. Svyatoslav Kondrat**, der mich in die Tiefen der C-Programmierung (ohne “++”) geführt hat. Der Fußballmeister der Abteilung Dietrich war auf und neben “dem Platz” immer ein guter Gesprächs- und Diskussionspartner.

Für die Diskussion über Experimente und die Bereitstellung der Messungen bedanke ich mich besonders bei **Olga Zvyagolskaya** sowie bei **Dominik Vogt** und **Florian Soyka**. Mein Dank geht auch an weitere Mitglieder der Bechinger-Gruppe, **Dr. Laurent Helden** und **Ursula Nellen**.

Besonders möchte ich mich auch bei den weiteren “Casimir-Leuten” unserer Abteilung bedanken, die mir in vielen Diskussionen (nicht nur über Casimir) geholfen haben: **Dr. Ania Maciołek, Dr. Francesco Parisen Toldin, Dr. Oleg Vasilyev, Dr. Monika Sprenger** und **Thomas F. Mohry**. Bei Thomas Mohry bedanke ich mich besonders für die langjährige Zimmerteilung, die auch in Ringberg beibehalten wurde, und die vielen anregenden und auch heiteren Diskussionen über die Welt.

Für eine äußerst angenehme Atmosphäre auch abseits des Arbeitsplatzes bedanke ich mich bei allen (aktuellen und ehemaligen) Mitgliedern der Abteilung, insbesondere bei meinen zeitweiligen Zimmergenossinnen und Zimmergenossen. Bei **Anke Geigle** bedanke ich mich für die Hilfsbereitschaft bei organisatorischen Angelegenheiten aller Art.

Für ein perfektes Umfeld gilt mein Dank der Institutsleitung und der Max-Planck-Gesellschaft, den Mitarbeitern der EDV-Abteilung, die stets die Rechner und Cluster am Laufen halten, dem Betriebsrat, der u.a. für eine gute Essensversorgung sorgt, den hilfsbereiten Mitarbeiterinnen und Mitarbeitern des “Forscherbedarfslagers” und der Personalabteilung.

Ein besonderes Dankeschön möchte ich **Dr. h.c. Bernd Kretschmer** aussprechen, der als Lehrer in meiner Schulzeit mit seiner Physik-AG meine Leidenschaft für die Physik entfacht und befeuert hat.

Abschließend geht mein Dank an meine Eltern und meinen Bruder sowie insbesondere an meine Frau **Tabea** für die große moralische Unterstützung während der Zeit der Doktorarbeit.

Erklärung

Hiermit erkläre ich, dass ich die Dissertation, abgesehen von den ausdrücklich bezeichneten Hilfsmitteln und den Ratschlägen der jeweils namentlich aufgeführten Personen, selbständig verfasst habe.

Stuttgart, den 22.12.2011

Matthias Tröndle

Lebenslauf

Matthias Tröndle

*1981 in Lörrach

Fridinger Str. 12
70619 Stuttgart

mail@matthias-troendle.info

seit Jan. 2008	Doktorand Max-Planck-Institut für Intelligente Systeme, Stuttgart und Institut für Theoretische und Angewandte Physik, Universtität Stuttgart Prof. Dr. S. Dietrich
Nov. 2006 — Nov. 2007	Masterarbeit Max-Planck-Institut für Metallforschung, Stuttgart und Institut für Theoretische und Angewandte Physik, Universtität Stuttgart Prof. Dr. S. Dietrich “Critical adsorption and critical Casimir forces for geometrically structured confinements”
Okt. 2005 — Nov. 2007	Studiengang Master of Science in Physics Universität Stuttgart
Okt. 2002 — Sept. 2005	Studiengang Bachelor of Science in Physics Universität Basel (Schweiz)
Aug. 2001 — Juli 2002	Zivildienst Individuelle Schwerstbehindertenbetreuung Leben+Wohnen gGmbH Lörrach
Juni 2001	Abitur, Hans-Thoma-Gymnasium Lörrach

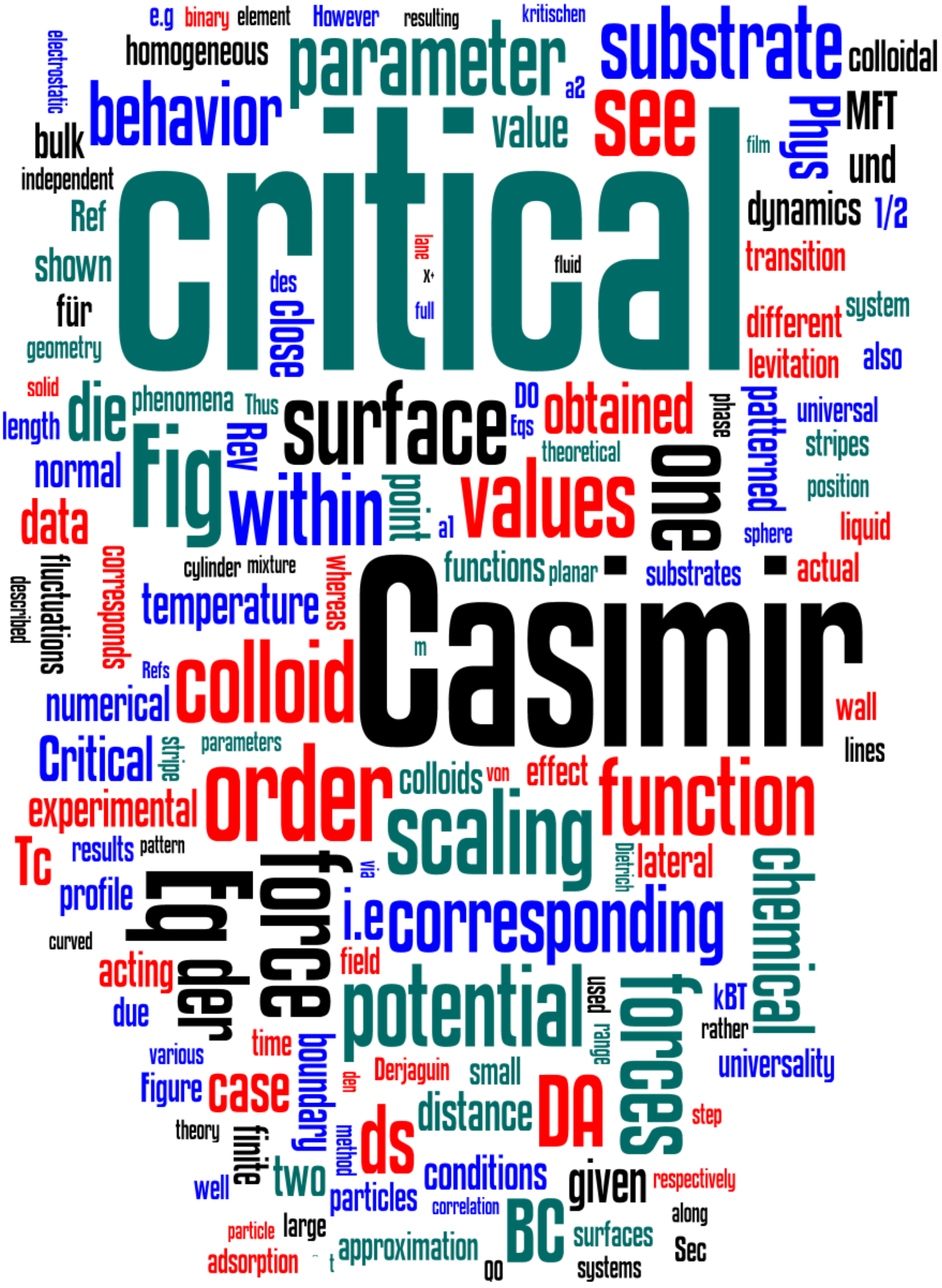
e.g
binary
element
However
resulting
kritischen
electrostatic
homogeneous
parameter
substrate
colloidal
a2
behavior
bulk
critical
value
see
Phys
MFT
film
und
independent
dynamics
1/2
Ref
transition
lane
x+
fluid
shown
des
close
full
für
system
different
geometry
levitation
also
solid
die
phenomena
Thus
surface
D0
Eqs
obtained
phase
patterned
universal
length
Rev
theoretical
one
stripes
normal
Fig
within
point
values
position
data
a1
sphere
liquid
functions
planar
substrates
actual
cylinder
mixture
whereas
corresponds
fluctuations
described
temperature
Casimir
m
Refs
colloid
numerical
wall
lines
Critical
stripe
parameters
colloids
von
effect
function
experimental
order
scaling
Tc
results
pattern
via
Dietrich
lateral
Eq
force
chemical
profile
i.e
corresponding
curved
field
acting
der
potential
used
forces
kBT
due
range
rather
time
boundary
various
den
Derjaguin
small
universality
figure
case
distance
DA
step
theory
finite
method
ds
two
conditions
given
respectively
well
particles
correlation
along
particle
large
BC
surfaces
adsorption
t
approximation
Sec
Q0
systems

Schlagwortwolke der 150 meist genutzten Wörter dieser Arbeit, gewichtet nach ihrem Vorkommen (erstellt mit “wordle.net”).